

Towards Digital Tomosynthesis-Guided Bronchoscopy Interventions

Dissertation

zur Erlangung des akademischen Grades

Doktoringenieur
(Dr.-Ing.)

von **M.Sc. Fatima Saad**

geb. am 18. November 1994 in Breikeh / Libanon

genehmigt durch die Fakultät für Elektrotechnik und Informationstechnik der
Otto-von-Guericke-Universität Magdeburg

Vorsitzender:

Prof. Dr.-Ing. habil. Martin Wolter

(FEIT/Institut für Elektrische Energiesysteme, Otto-von-Guericke-Universität Magdeburg)

Gutachter:

Prof. Dr. rer. nat. Georg Rose

(FEIT/Institut für Medizintechnik, Otto-von-Guericke-Universität Magdeburg)

Prof. Dr.-Ing. Andreas Nürnberger

(FIN/Institut für Technische und Betriebliche Informationssysteme,
Otto-von-Guericke-Universität Magdeburg)

Dr. Krish Bhadra

(CHI Memorial Rees Skillern Cancer Institute, Chattanooga, TN, USA)

Promotionskolloquium am **31. May 2024**

ABSTRACT

Navigational bronchoscopy has emerged as a safer and less invasive alternative to traditional lung nodule biopsy methods. However, its reported diagnostic yield is still suboptimal. This yield is ultimately dependent on the accurate location identification of the target nodule and the biopsy needle during the intervention. Current bronchoscopy procedures mainly rely on projective fluoroscopy for a real-time imaging, and, from time to time, cone-beam computed tomography (CBCT) scans are performed to provide a 3D overview. This navigational approach is challenging due to the superimposition of the different structures in fluoroscopy in a 2D image hindering the visualization of the target nodule. Moreover, the high radiation dose, long imaging time, and large footprints of CBCT are of great concern. Providing some depth information compared to projective fluoroscopy on the one hand, and posing lower radiation dose, shorter imaging time, and smaller footprints compared to CBCT on the other hand, digital tomosynthesis (DTS) appears as a potential alternative for guiding bronchoscopy interventions. DTS imaging involves acquiring limited sets of X-ray projection images over limited angular ranges, then reconstructing them to provide quasi-3D images. However, while promising, DTS imaging suffers from a low depth resolution due to incomplete data.

This dissertation seeks to improve DTS image quality at three levels: data acquisition, missing data replacement, and image reconstruction. At the data acquisition level, since multidirectional DTS scan orbits might improve image quality compared to unidirectional orbits, a novel C-arm-based spherical ellipse DTS scan orbit customized for bronchoscopy intervention guidance was proposed. Experiments using numerical phantoms and patient bronchoscopy data have shown that the proposed orbit provides a good compromise between image quality and workspace requirements compared to standard DTS orbits. To replace the missing data, preoperative computed tomography (CT) scans, which are often performed prior to interventions for diagnosis or to plan the intervention, represent a promising source of information. However, CT-to-body divergence is a significant barrier to the proper use of the CT data. To address this problem, a novel deformable 3D/3D CT-to-DTS registration algorithm aligning prior CT images to intraoperative DTS images was proposed. Experiments on simulated and real patient bronchoscopy data have demonstrated a registration accuracy sufficient-enough for guiding bronchoscopy interventions. At the image reconstruction level, a prior-aided iterative DTS reconstruction algorithm properly employing prior CT scans was proposed. Similarly, experiments on physical phantoms as well as on real patient bronchoscopy data have shown a significant improvement in DTS image quality using the proposed reconstruction algorithm and have demonstrated the benefits of incorporating prior knowledge into the DTS reconstruction algorithm.

The achieved results lay the cornerstone for DTS-guided bronchoscopy interventions and offer valuable insights and tools for researchers and medical practitioners to introduce DTS as an image guidance modality for bronchoscopy interventions.

ZUSAMMENFASSUNG

Navigationsbronchoskopie hat sich als sicherere und weniger invasive Alternative zu traditionellen Methoden der Lungenknötchenbiopsie etabliert. Die diagnostische Ausbeute ist jedoch immer noch suboptimal. Diese Ausbeute hängt letztendlich von einer genauen Lokalisierung des Zielknotens und der Biopsienadel während des Eingriffs ab. Gegenwärtige Bronchoskopieverfahren stützen sich hauptsächlich auf projektive Fluoroskopie für eine Echtzeitbildgebung und gelegentlich werden auch Cone-Beam-Computertomographie (CBCT)-Scans durchgeführt, die einen 3D-Überblick bieten. Dieser navigative Ansatz ist aufgrund der Überlagerung verschiedener Strukturen in der Fluoroskopie in einem 2D-Bild, die die Visualisierung des Zielknotens beeinträchtigt, herausfordernd. Darüber hinaus sind die hohe Strahlendosis, die lange Bildaufnahmezeit und der große Platzbedarf von CBCT-Systemen problematisch. Digital Tomosynthese (DTS) erscheint als potenzielle Alternative zur Führung von Bronchoskopieeingriffen, da sie im Vergleich zur projektiven Fluoroskopie einerseits Tiefeninformationen bietet und andererseits im Vergleich zu CBCT eine geringere Strahlendosis, kürzere Bildaufnahmezeit und kleinere Platzbedarf aufweist. DTS-Bildgebung besteht darin, eine begrenzte Anzahl von Röntgenprojektionsbildern über einen begrenzten Winkelbereich zu erfassen und diese dann zu quasi-3D-Bildern zu rekonstruieren. Allerdings leidet die DTS-Bildgebung trotz vielversprechender Ansätze unter einer geringen Tiefenaufklärung aufgrund unvollständiger Daten.

Diese Dissertation zielt darauf ab, die DTS-Bildqualität auf drei Ebenen zu verbessern: Datenerfassung, Ersatz fehlender Daten und Bildrekonstruktion. Auf der Datenerfassungsebene wurde aufgrund der Möglichkeit, dass multidirektionale DTS-Scanorbits im Vergleich zu unidirektionalen Orbits die Bildqualität verbessern könnten, ein neuartiger C-Bogen-basierter DTS-Scanorbit entlang einer sphärischen Ellipse, der für die Führung von Bronchoskopieeingriffen angepasst ist, vorgeschlagen. Experimente mit numerischen Phantomen und Patientenbronchoskopiedaten haben gezeigt, dass die vorgeschlagene Trajektorie einen guten Kompromiss zwischen Bildqualität und Platzbedarf bietet. Um fehlende Daten mit DTS zu ersetzen, stellen präoperative Computertomographie (CT)-Scans, die oft vor Eingriffen zur Diagnose oder zur Interventionsplanung durchgeführt werden, eine vielversprechende Informationsquelle dar. Allerdings ist die CT-zu-Körper-Divergenz ein signifikantes Hindernis für die ordnungsgemäße Verwendung der CT-Daten. Zur Bewältigung dieses Problems wurde ein neuartiger deformierend 3D/3D-CT-zu-DTS-Registrierungsalgorithmus vorgeschlagen, der vorherige CT-Bilder mit intraoperativen DTS-Bildern ausrichtet. Experimente mit echten Patientenbronchoskopiedaten haben eine ausreichende Registriergenauigkeit für die Führung von Bronchoskopieeingriffen gezeigt. Auf der Ebene der Bildrekonstruktion wurde ein vorwissensunterstützter iterativer DTS-Rekonstruktionsalgorithmus vorgeschlagen, der vorherige CT-Scans verwendet. Ebenso haben Experimente an physischen Phantomen sowie an echten Patientendaten eine signifikante Verbesserung der DTS-Bildqualität unter Verwendung des vorgeschlagenen Rekonstruktionsalgorithmus gezeigt und die Vorteile der Integration von Vorwissen in den DTS-Rekonstruktionsalgorithmus demonstriert.

Die erzielten Ergebnisse legen den Grundstein für DTS-geführte Bronchoskopieeingriffe und bieten wertvolle Einblicke und Werkzeuge für Forscher und Mediziner, um DTS als bildgebende Modalität für Bronchoskopieeingriffe einzuführen.

“THE SEEKER AFTER THE TRUTH IS NOT ONE WHO STUDIES THE WRITINGS OF THE ANCIENTS AND, FOLLOWING HIS NATURAL DISPOSITION, PUTS HIS TRUST IN THEM, BUT RATHER THE ONE WHO SUSPECTS HIS FAITH IN THEM AND QUESTIONS WHAT HE GATHERS FROM THEM, THE ONE WHO SUBMITS TO ARGUMENT AND DEMONSTRATION, AND NOT TO THE SAYINGS OF A HUMAN BEING WHOSE NATURE IS FRAUGHT WITH ALL KINDS OF IMPERFECTION AND DEFICIENCY. THUS THE DUTY OF THE MAN WHO INVESTIGATES THE WRITINGS OF SCIENTISTS, IF LEARNING THE TRUTH IS HIS GOAL, IS TO MAKE HIMSELF AN ENEMY OF ALL THAT HE READS, AND, APPLYING HIS MIND TO THE CORE AND MARGINS OF ITS CONTENT, ATTACK IT FROM EVERY SIDE. HE SHOULD ALSO SUSPECT HIMSELF AS HE PERFORMS HIS CRITICAL EXAMINATION OF IT, SO THAT HE MAY AVOID FALLING INTO EITHER PREJUDICE OR LENIENCY...”

– IBN AL HAYTHAM –

BOOK OF OPTICS

Contents

| | | |
|----------|---|-----------|
| 1 | Clinical Context | 1 |
| 1.1 | Cancer Overview | 2 |
| 1.2 | Lung Cancer | 3 |
| 1.2.1 | Pulmonary Nodules | 3 |
| 1.2.2 | Pulmonary Nodule Biopsy | 4 |
| 1.3 | Image-Guided Bronchoscopy Tools | 11 |
| 1.3.1 | Radial Probe Endobronchial Ultrasound | 11 |
| 1.3.2 | Virtual Bronchoscopy | 12 |
| 1.3.3 | Electromagnetic Navigational Bronchoscopy | 14 |
| 1.3.4 | CBCT-Guided Bronchoscopy | 15 |
| 1.4 | Conclusion | 19 |
| 2 | Problem Formulation and Aims of the Thesis | 21 |
| 2.1 | Problem Formulation and Research Questions | 21 |
| 2.2 | Motivation | 23 |
| 2.3 | Research Objectives | 23 |
| 2.4 | Contributions and Significance | 24 |
| 2.5 | Thesis Structure | 25 |
| 2.6 | List of Publications | 26 |
| 3 | Technical Background | 29 |
| 3.1 | X-ray Imaging | 30 |
| 3.1.1 | X-ray Generation | 31 |
| 3.1.2 | X-ray Transmission | 34 |
| 3.1.3 | X-ray Detection | 37 |
| 3.1.4 | X-ray Applications | 38 |
| 3.1.5 | Image Reconstruction | 40 |
| 3.2 | Digital Tomosynthesis: From Data Acquisition to Image Formation | 48 |
| 3.2.1 | History of Tomosynthesis | 49 |
| 3.2.2 | History of Tomosynthesis Reconstruction Methods | 51 |
| 3.2.3 | Data Acquisition | 55 |
| 3.2.4 | Acquisition Geometry Parameters | 57 |
| 3.2.5 | Artifacts | 58 |
| 3.3 | Conclusion | 61 |
| 4 | Spherical Ellipse Digital Tomosynthesis Scan Orbit | 63 |
| 4.1 | Motivation | 64 |
| 4.2 | Mathematical Definition of a Spherical Ellipse | 66 |
| 4.3 | Design of the Spherical Ellipse DTS Scan Orbit | 67 |
| 4.4 | Materials and Methods | 69 |
| 4.4.1 | Scan Orbits | 69 |
| 4.4.2 | Data | 71 |
| 4.4.3 | Reconstruction Algorithm | 72 |

| | | |
|----------|--|------------|
| 4.4.4 | Experiments | 73 |
| 4.5 | Results | 74 |
| 4.6 | Conclusion | 86 |
| 5 | Prior CT to Intraoperative Digital Tomosynthesis Image Registration | 87 |
| 5.1 | Motivation | 88 |
| 5.2 | Proposed Algorithm | 89 |
| 5.2.1 | Multistage Framework | 89 |
| 5.2.2 | Cost Functions and Multimetric Registration | 92 |
| 5.2.3 | Multiresolution Strategy | 93 |
| 5.3 | Experiments | 94 |
| 5.3.1 | Data | 94 |
| 5.3.2 | DTS Projection Generation | 95 |
| 5.4 | Evaluation Metrics | 97 |
| 5.5 | Results | 97 |
| 5.6 | Conclusion | 109 |
| 6 | Prior-Aided Digital Tomosynthesis Image Reconstruction | 111 |
| 6.1 | Motivation | 112 |
| 6.2 | Proposed Algorithm | 115 |
| 6.3 | Experiments | 116 |
| 6.3.1 | Physical Phantoms | 117 |
| 6.3.2 | Patient Bronchoscopy Data | 119 |
| 6.4 | Evaluation Metrics | 119 |
| 6.5 | Results | 119 |
| 6.6 | Conclusion | 127 |
| 7 | Alternative to Failed CT-Augmented Digital Tomosynthesis | 129 |
| 7.1 | Motivation | 129 |
| 7.2 | CBCT-to-DTS Registration Algorithm | 131 |
| 7.3 | CBCT-Aided DTS Reconstruction Algorithm | 131 |
| 7.4 | Results | 131 |
| 7.5 | Conclusion | 136 |
| 8 | Conclusion, Discussion, and Perspectives | 137 |
| 8.1 | Summary and Discussion | 137 |
| 8.2 | Limitations and Outlook | 141 |
| | References | 144 |

List of Figures

| | | |
|------|--|----|
| 1.1 | Estimated number of new cancer cases worldwide from 2020 to 2040 | 2 |
| 1.2 | Estimated number of cancer deaths worldwide from 2020 to 2040 | 2 |
| 1.3 | Causes of death by type of disease in Germany in 2022 | 3 |
| 1.4 | Estimated number of new cancer cases and cancer-related deaths in 2020 worldwide | 4 |
| 1.5 | Classification of pulmonary nodules | 5 |
| 1.6 | Image examples of the different types of pulmonary nodules | 5 |
| 1.7 | Various modalities currently available for the biopsy of peripheral pulmonary nodules (PPN) | 6 |
| 1.8 | Illustration of a surgical biopsy of a lung nodule | 6 |
| 1.9 | Illustration of a percutaneous transthoracic needle biopsy (PTNB) procedure | 8 |
| 1.10 | CT chest of a patient presenting a left pneumothorax | 8 |
| 1.11 | Illustration of a bronchoscopy procedure | 8 |
| 1.12 | Gustav Killian demonstrating bronchoscopy in a half-dissected frozen corpse | 10 |
| 1.13 | Ultrathin bronchoscope and standard bronchoscopes | 11 |
| 1.14 | A rEBUS image of a radial probe inserted in the center of a pulmonary lung nodule | 12 |
| 1.15 | Display of a virtual bronchoscopic navigation to a PPN | 13 |
| 1.16 | SuperDimension ENB-based navigational system | 15 |
| 1.17 | Bronchoscopy guidance using a C-arm CBCT system | 16 |
| 1.18 | Tool-in-lesion confirmation CBCT images | 17 |
| 1.19 | Representative room setup in a bronchoscopy procedure | 18 |
| 3.1 | One of the earliest X-ray images | 30 |
| 3.2 | Basic principles of X-ray imaging | 31 |
| 3.3 | Illustration of the electromagnetic spectrum | 31 |
| 3.4 | Illustration of the functional components of an X-ray tube | 32 |
| 3.5 | Bremsstrahlung X-ray generation | 33 |
| 3.6 | Characteristic X-ray generation | 34 |
| 3.7 | Example of an X-ray spectrum generated by an X-ray tube | 34 |
| 3.8 | X-ray photon interaction mechanisms with matter | 35 |
| 3.9 | Mathematical model of X-ray attenuation | 37 |
| 3.10 | Typical profile for the mass attenuation coefficient for bone and lung tissue as a function of X-ray energy | 38 |
| 3.11 | Chest X-ray image showing a lesion in the right lung lobe of the patient . . | 39 |
| 3.12 | Image example from a fluoroscopic sequence and a typical C-arm scanner used in minimally invasive interventions | 40 |
| 3.13 | Axial, coronal, and sagittal slice images of a chest CT scan | 40 |
| 3.14 | Illustration of the Radon transform and the formation of the sinogram . . | 41 |
| 3.15 | Line integral definition | 42 |
| 3.16 | Illustration of the Fourier slice theorem | 44 |
| 3.17 | Example of an image grid and some projection rays | 46 |
| 3.18 | Schematic of the ART cycle | 48 |

| | | |
|------|---|----|
| 3.19 | Comparison of a posterior-anterior PR image, a coronal CBCT slice, and a coronal DTS slice | 49 |
| 3.20 | Coded aperture tomosynthesis system | 50 |
| 3.21 | Principle of shift-and-add (SAA) tomosynthesis | 52 |
| 3.22 | Illustration of a linear tomosynthesis imaging geometry | 53 |
| 3.23 | Linear tomosynthesis motion geometry | 56 |
| 3.24 | Pseudo-linear tomosynthesis motion geometry | 57 |
| 3.25 | Circular tomosynthesis motion geometry | 57 |
| 3.26 | Illustration of the geometry parameters of a pseudo-linear scan acquisition . | 58 |
| 3.27 | Example of blurring artifacts in a DTS image | 59 |
| 3.28 | Example of ripple artifacts in a DTS image | 60 |
| 3.29 | Example of ghost artifacts in a DTS image | 60 |
| 3.30 | Example of metal artifacts in a DTS image | 60 |
| 4.1 | Region of Fourier’s space sampled with a pseudo-linear DTS acquisition geometry | 65 |
| 4.2 | Region of Fourier’s space sampled with a circular DTS acquisition geometry | 65 |
| 4.3 | An illustration of a spherical ellipse | 67 |
| 4.4 | Sampling of the spherical ellipse | 68 |
| 4.5 | Illustration of the different DTS scan orbits. | 70 |
| 4.6 | Illustration of visible and invisible singularities for each DTS scan protocol . | 72 |
| 4.7 | Ball phantom reconstructed images according to Experiment 1 | 75 |
| 4.8 | Line profiles in the y, x, and z directions through the center of the sphere . . | 75 |
| 4.9 | Ball phantom reconstructed coronal slices at 12.5 mm from the center of the phantom | 76 |
| 4.10 | Ball phantom axial slices reconstructed using different values of the large tomographic angle α | 76 |
| 4.11 | Line profiles in the y direction through the center of the sphere in the reconstructed axial slices shown in Figure 4.10 | 76 |
| 4.12 | Patient data DTS coronal slice reconstructions with the different scan trajectories | 78 |
| 4.13 | ROIs defined in the CBCT slice | 79 |
| 4.14 | Enlarged views around the spine (ROI#1) | 79 |
| 4.15 | Enlarged views around the needle tip and the target lesion (ROI#2) | 80 |
| 4.16 | Pearson correlation in ROI#1, ROI#2, and ROI#3 as a function of some acquisition parameters computed for the different scan orbits | 83 |
| 4.17 | Reconstructed coronal slices using a spherical ellipse (SE) scan orbit with different combinations of the number of projection views N and large tomographic angle α | 84 |
| 4.18 | Contour plots of the linear projection density and the Pearson correlation coefficients computed in different ROIs as a function of N and α | 85 |
| 5.1 | Illustration of the proposed deformable 3D/3D CT-to-DTS registration algorithm | 91 |
| 5.2 | Image examples of an intraoperative CBCT coronal slice and its associated masks | 95 |

| | | |
|------|---|-----|
| 5.3 | Image examples of a prior CT scan of a patient | 99 |
| 5.4 | Image examples of an intraoperative CBCT scan of a patient | 100 |
| 5.5 | Intraoperative DTS images used as fixed images for the registration algorithm | 101 |
| 5.6 | Prior DTS images used as moving images for the registration algorithm . . . | 101 |
| 5.7 | Registered prior DTS image at the different stages of the registration algorithm using the DTS_{sim_SE} data | 102 |
| 5.8 | Registered prior CT image at the different stages of the registration algorithm using the DTS_{sim_SE} data | 103 |
| 5.9 | Enlarged views of the ROIs surrounding the target lesion using the DTS_{sim_SE} data | 104 |
| 5.10 | Registered prior CT image at the different stages of the registration algorithm using the DTS_{sim_PL} data | 105 |
| 5.11 | Enlarged views of the ROIs surrounding the target lesion using the DTS_{sim_PL} data | 105 |
| 5.12 | Registered prior CT image at the different stages of the registration algorithm using the DTS_{real_PL} data | 106 |
| 5.13 | Enlarged views of the ROIs surrounding the target lesion using the DTS_{real_PL} data | 107 |
| 5.14 | DC and ASSD for different settings of α, β , and N | 108 |
| 6.1 | Illustration of the ART cycle in the case of a consistent square system having a unique solution | 114 |
| 6.2 | Illustration of the ART cycle in the cases of an ill-conditioned system and an underdetermined system | 115 |
| 6.3 | Flowchart of the proposed prior-aided DTS reconstruction method | 116 |
| 6.4 | Quant CT-training phantom | 117 |
| 6.5 | Anthropomorphic Lungman thoracic phantom | 119 |
| 6.6 | Quant phantom prior CT and intraoperative CBCT images | 120 |
| 6.7 | Quant phantom reconstruction results | 121 |
| 6.8 | Lungman phantom prior CT and intraoperative CBCT images | 122 |
| 6.9 | Experiment 2 reconstruction results using DTS_{sim_SE} | 123 |
| 6.10 | Experiment 2 reconstruction results using DTS_{sim_PL} | 123 |
| 6.11 | Experiment 2 reconstruction results using DTS_{real_PL} | 124 |
| 6.12 | Patient bronchoscopy data prior CT and intraoperative CBCT images . . . | 125 |
| 6.13 | Patient bronchoscopy data reconstruction results using DTS_{sim_SE} | 126 |
| 6.14 | Patient bronchoscopy data reconstruction results using DTS_{sim_PL} | 126 |
| 6.15 | Patient bronchoscopy data reconstruction results using DTS_{real_PL} | 127 |
| 7.1 | Alternative CBCT-coupled DTS-guided bronchoscopy protocol | 130 |
| 7.2 | Image examples of patient data where CT-to-DTS image registration might fail (Case A) | 132 |
| 7.3 | Registration results of Case A | 133 |
| 7.4 | Reconstruction results of Case A | 134 |
| 7.5 | Image examples of patient data where CT-to-DTS image registration might fail (Case B) | 134 |
| 7.6 | Registration results of Case B | 135 |

7.7 Reconstruction results of Case B 135

List of Tables

| | | |
|-----|---|-----|
| 5.1 | Downsampling factors f and control point grid spacings s (in mm) used at the different stages and different resolution levels | 94 |
| 5.2 | Patient demographics and lesion characteristics of each case | 95 |
| 5.3 | Acquisition parameters for the prior CT images and for the intraoperative CBCT images of each of the six patients. The duration in days between the two image acquisitions is shown for each patient. | 98 |
| 5.4 | DC and ASSD for each of the six patients' data | 108 |
| 6.1 | Acquisition and reconstruction parameters used in the simulation of DTS data in Experiment 1 | 118 |
| 6.2 | Experiment 1 quantitative results | 120 |
| 6.3 | Experiment 2 quantitative results | 122 |
| 6.4 | Patient bronchoscopy data quantitative results | 127 |

Acronyms

| | |
|----------------|---|
| ART | Algebraic Reconstruction Technique |
| ASSD | Average Symmetric Surface Distance |
| CBCCT | Cone-Beam Computed Tomography |
| CT | Computed Tomography |
| CTL | Computed Tomography Library |
| DC | Dice Coefficient |
| dPIRPLE | Deformable Prior Image Registration Penalized-Likelihood Estimation |
| DRRs | Digitally Reconstructed Radiographs |
| DTS | Digital Tomosynthesis |
| ENB | Electromagnetic Navigational Bronchoscopy |
| FBP | Filtered Backprojection |
| FDK | Feldkamp–Davis–Kress algorithm |
| FOV | Field of View |
| FPD | Flat Panel Detector |
| FWHM | Full-Width at Half-Maximum |
| GGN | Ground Glass Nodules |
| GS | Guide Sheath |
| GT | Ground Truth |
| LG | Locatable Guide |
| MITs | Matrix Inversion Tomosynthesis |
| MLEM | Maximum Likelihood Expectation Maximization |
| PBIR | Prior-Based Image Reconstruction |
| PC | Pearson Correlation |
| PICCS | Prior Image Constraint Compressed Sensing |
| PIRPLE | Prior-Image-Registered Penalized-Likelihood Estimator |
| PPN | Peripheral Pulmonary Nodules |
| PR | Projective Radiography |
| PrIDICT | Prior Image Dynamic Interventional Computed Tomography |
| PSN | Part-Solid Nodules |
| PTNB | Percutaneous Transthoracic Needle Biopsy |
| rEBUS | Radial Probe Endobronchial Ultrasound |
| ROC | Region of Change |
| RoD | Reconstruction of Difference |
| ROI | Region of Interest |

| | |
|-------------|---|
| SAA | Shift-and-Add |
| SART | Simultaneous Algebraic Reconstruction Technique |
| SN | Solid Nodules |
| SSN | Sub-Solid Nodules |
| TACT | Tuned Aperture CT |
| TBBx | Transbronchial Needle Biopsy |
| VATS | Video-Assisted Thoracoscopy Surgery |
| VCN | Virtual Bronchoscopic Navigation |

1

Clinical Context

Contents

| | | |
|------------|---|-----------|
| 1.1 | Cancer Overview | 2 |
| 1.2 | Lung Cancer | 3 |
| 1.2.1 | Pulmonary Nodules | 3 |
| 1.2.2 | Pulmonary Nodule Biopsy | 4 |
| 1.3 | Image-Guided Bronchoscopy Tools | 11 |
| 1.3.1 | Radial Probe Endobronchial Ultrasound | 11 |
| 1.3.2 | Virtual Bronchoscopy | 12 |
| 1.3.3 | Electromagnetic Navigational Bronchoscopy | 14 |
| 1.3.4 | CBCT-Guided Bronchoscopy | 15 |
| 1.4 | Conclusion | 19 |

THIS chapter is dedicated to introducing the clinical context of this doctoral work. It delves into the current state of lung cancer worldwide, the different techniques used for the biopsy of lung nodules, and, most importantly, the relevance of bronchoscopy in the diagnosis process. Furthermore, it provides in-depth coverage of various imaging techniques utilized for guiding bronchoscopy interventions and highlights the challenges encountered in today's image-guided bronchoscopy procedures. Readers interested in diving straight into the problems addressed by this doctoral work and the research questions it seeks to answer are invited to skip this chapter and proceed to Chapter 2.

1.1 Cancer Overview

Over the last few decades, cancer has become a leading cause of death worldwide [1]. Globally, one in five people develop cancer during their lifetime. With over 19 million new cancer cases estimated in 2020, over 30 million new cases and over 16 million deaths are expected by 2040 due to the population growth and aging (Figure 1.1 and Figure 1.2). In Germany, according to the latest data available from the Federal Statistical Office (Destatis), deaths due to cancer represent 22.4% of the total reported deaths in 2021, which ranks cancer second only to cardiovascular diseases in terms of causes of death (Figure 1.3). While this represents a considerably heavy burden worldwide, the impact is notably substantial in low- and middle-income countries.

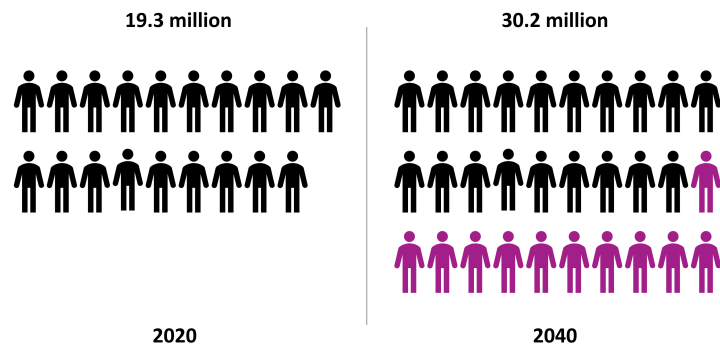


Figure 1.1: Pictogram representing the estimated number of new cancer cases worldwide from 2020 to 2040 [1]. Each icon represents one million individuals. Violet icons represent demographic changes.

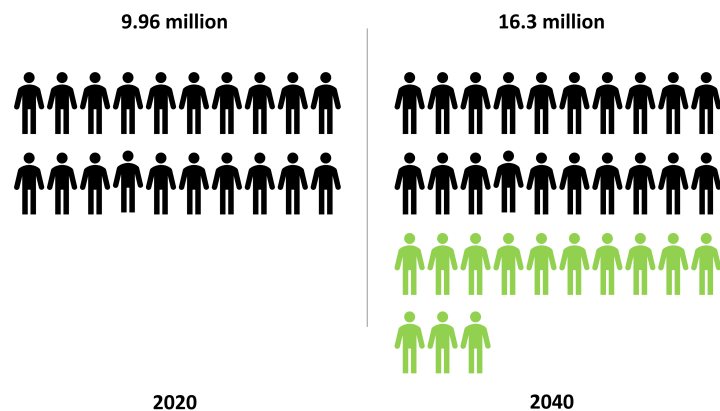


Figure 1.2: Pictogram representing the estimated number of cancer deaths worldwide from 2020 to 2040 [1]. Each icon represents 500 000 individuals. Green icons represent demographic changes.

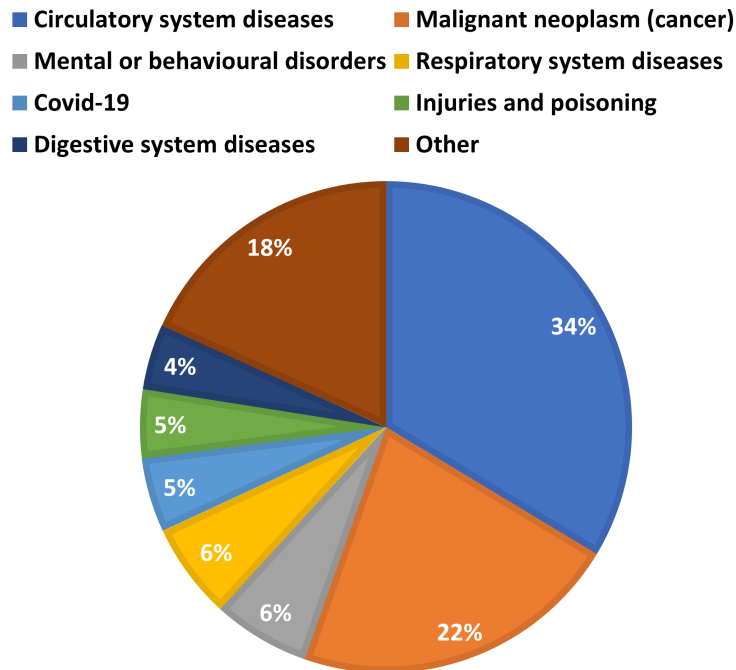


Figure 1.3: Causes of death by type of disease in Germany in 2022. Data source: Federal Statistical Office (Destatis).

1.2 Lung Cancer

While lung cancer ranks as the second most prevalent cancer worldwide (12.5% of the total estimated new cancer cases in 2020), it maintains its status as the primary cause of cancer-related mortality globally, primarily due to its poor prognosis (Figure 1.4) [2]. Its fatality rate is even higher than the one associated to the subsequent three most common cancers (colon, breast, and prostate). Despite significant advancements in diagnostic and therapeutic approaches, it continues to impose a major public health and economic challenge with a spirally growing global burden.

A higher likelihood of successful treatment of lung cancer is linked to an early-stage diagnosis [3]. If it is found when it is still small and before it has spread, the probability of a successful treatment is higher than when it is diagnosed at advanced stages. As low-dose computed tomography (CT) imaging becomes more widely adopted, lung cancer screening programs are becoming popular nowadays, leading to a dramatic surge in detected lung nodules.

1.2.1 Pulmonary Nodules

A solitary pulmonary nodule, often referred to as a “spot on the lung”, is defined as a discrete small structure confined within the lung parenchyma. It is not in contact with the root of the lung or mediastinum, and not associated with collapsed lung, enlarged lymph nodes, or

1. Clinical Context

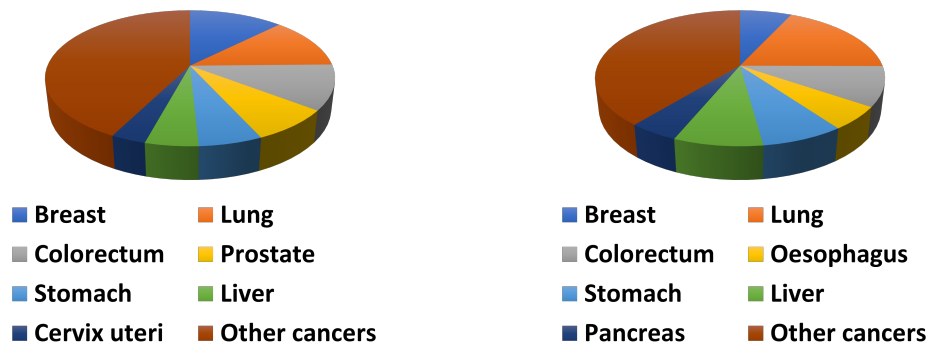


Figure 1.4: Estimated number of new cancer cases (left) and cancer-related deaths (right) in 2020 worldwide for both sexes and all ages. Data source: GLOBOCAN 2020 [2].

pleural effusion. It appears as a well-distinguished rounded or irregular radiographic opacity measuring 3 cm or less in diameter and is entirely surrounded by lung tissues. Pulmonary nodules can have various shapes, sizes, and densities, and can be either benign (noncancerous) or indicators of a malignant (cancerous) disease. Lesions exceeding 3 cm in diameter are considered as masses and are treated as malignant until a thorough diagnosis can prove otherwise.

Depending on their composition, lung nodules can be classified into two main categories (Figure 1.5):

- **Solid nodules (SN):** SN are the most prevalent type of lung nodules. They are dense and do not contain air pockets.
- **Sub-solid nodules (SSN):** SSN which are less dense than SN, are observed in approximately 9% of individuals undergoing lung cancer screening [4, 5]. These nodules can be categorized into two main types: **part-solid nodules (PSN)** and pure **ground glass nodules (GGN)**. GGN are well-circumscribed nodular lesions in the lung parenchyma, exhibiting a blurred appearance on CT scans. They consist of air-filled spaces with lower attenuation compared to surrounding pulmonary vessels. On the other hand, PSN contain a combination of solid and ground-glass components, appearing visually similar in density to pulmonary vessels.

In Figure 1.6 are shown some image examples of the different types of pulmonary nodules.

1.2.2 Pulmonary Nodule Biopsy

Although most of the detected lung nodules have a benign etiology, many frequently require further investigation and tissue diagnosis. Unlike endobronchial nodules, the diagnosis of peripheral pulmonary nodules (PPN) is particularly challenging to interventional pulmonologists due to the difficulty in navigating to the lung periphery, and in accessing and sampling the nodule under direct visualization. The armamentarium for the diagnosis and sampling

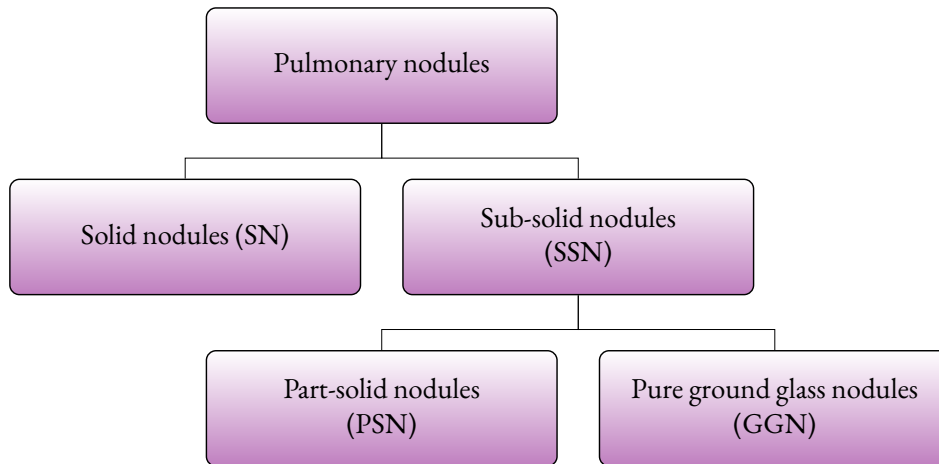


Figure 1.5: Classification of pulmonary nodules.

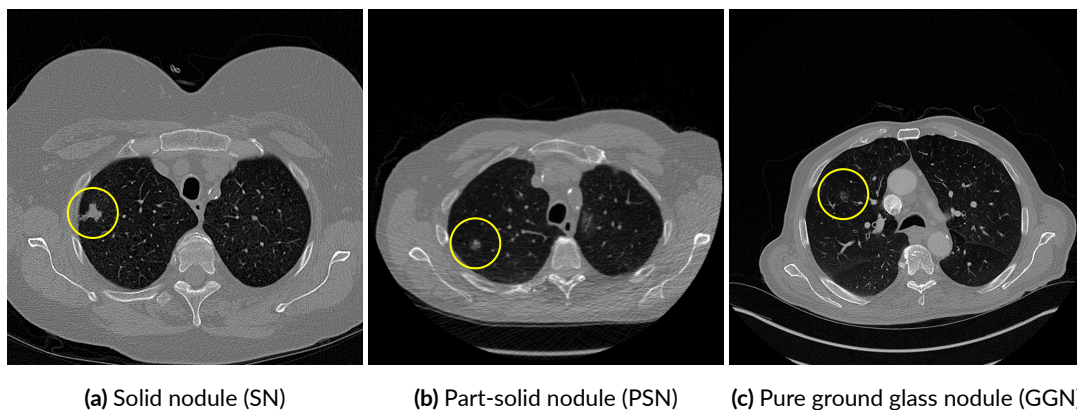


Figure 1.6: Image examples of the different types of pulmonary nodules. The nodules are highlighted in yellow.

of PPN includes multiple modalities ranging from surgery and percutaneous transthoracic needle biopsy (PTNB) to bronchoscopy. Figure 1.7 summarizes the different PPN biopsy modalities currently available. These modalities, along with their diagnostic capabilities and limitations, will be introduced in the following sections, with a particular emphasize on bronchoscopy.

1.2.2.1 Surgical Biopsy

Surgical biopsy of pulmonary nodules is performed by making small cuts in the chest wall and taking samples through the cuts. Surgeons carry out the biopsy in one of the following ways:

- **open surgery**, where the surgeon makes a cut in the skin of the chest and collects lung tissues (Figure 1.8).

1. Clinical Context

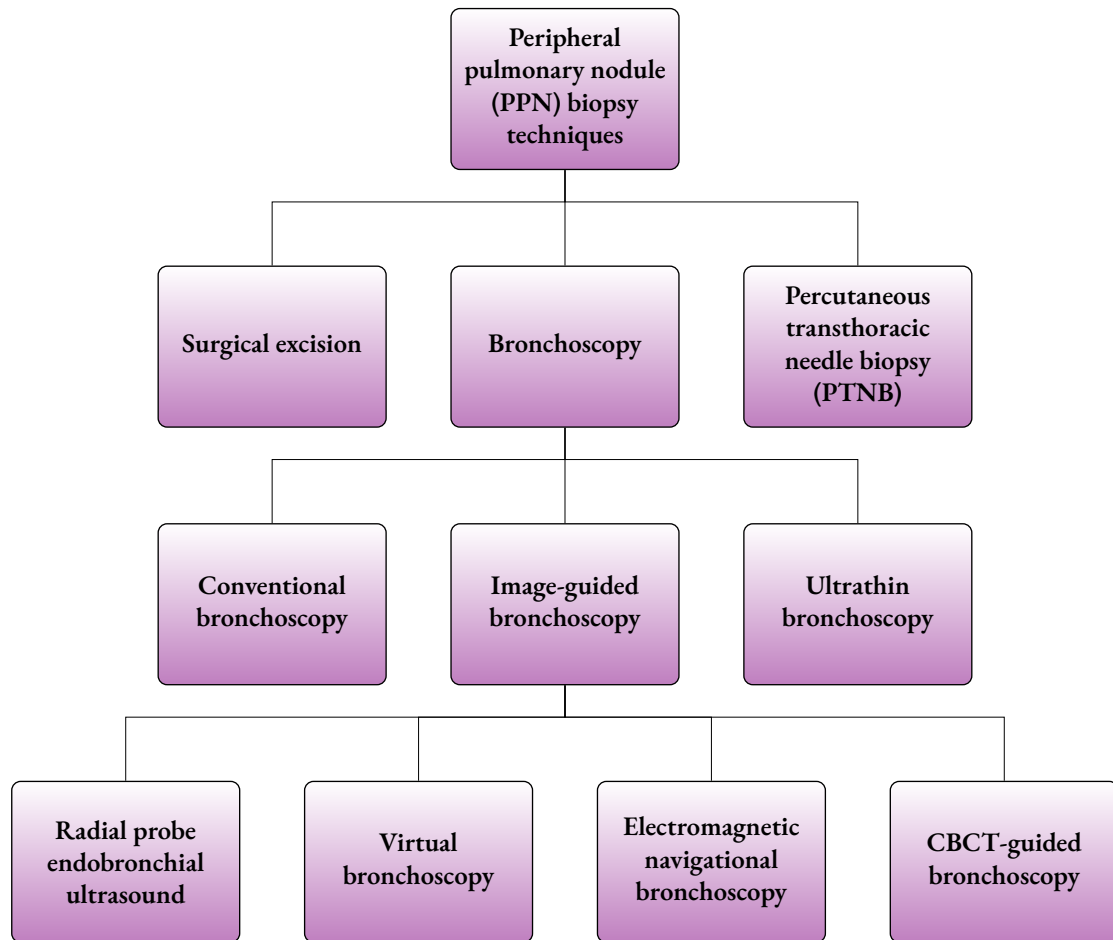


Figure 1.7: Various modalities currently available for the biopsy of peripheral pulmonary nodules PPN.

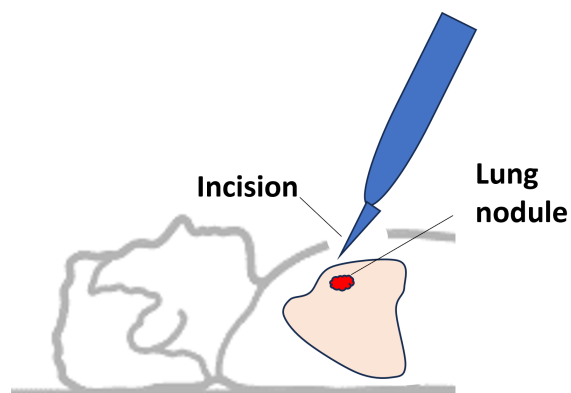


Figure 1.8: Illustration of a surgical biopsy of a lung nodule.

- **keyhole surgery** also known as **video-assisted thoracoscopy surgery (VATS)**, where the surgeon performs several cuts in the chest wall and inserts a tube with a camera through one cut and the biopsy tools through the others.

This approach is primarily utilized for the diagnosis of pulmonary nodules undergoing definitive resection or which previously underwent a non-diagnostic needle biopsy [6]. While such a technique enables a therapeutic procedure to be performed directly during the same operation, it is invasive and poses a significant risk of severe complications such as bleeding, infection, and blood clots [7]. Whereas most of the detected PPN are benign and do not require resection, subjecting all patients with detected PPN to surgical biopsy, with its associated cost and complications, is not reasonable.

1.2.2.2 Percutaneous Transthoracic Needle Biopsy

A less invasive PPN biopsy technique is percutaneous transthoracic needle biopsy (PTNB). During PTNB, the radiologist passes a needle through the chest wall into the suspicious nodule under image guidance (Figure 1.9). Options for image guidance modalities include CT, fluoroscopy, ultrasonography, and magnetic resonance imaging. Whereas the majority of PTNB procedures are conducted under CT guidance, ultrasonography is favored for lesions extending across the chest wall or for subpleural lung lesions [8–10]. Compared to bronchoscopy, CT-guided PTNB has higher sensitivity (up to 90%) and specificity (98% to 100%) for the diagnosis of malignant lesions [11]. However, its complication rates are significantly more elevated. The most common complication is pneumothorax, with reported incidence rates ranging between 10% and 60% [12–17]. It occurs when air escapes from the lung and leaks into the space between the chest wall and the lung, leading to collapsed lungs (Figure 1.10). During PTNB, the development of pneumothorax could be due to crossing a fissure during the biopsy [17], large needle size [15], biopsy of deep or cavitory lesions [18], patient positioning in the lateral position [19], emphysema [14], and multiple pleural punctures [20]. It frequently necessitates the insertion of a chest tube. This condition may force the biopsy procedure to come to a halt before collecting any diagnostic specimen.

1.2.2.3 Bronchoscopy

The safest and most non-invasive PPN biopsy technique is interventional bronchoscopy. During bronchoscopy, the bronchoscopist inserts a narrow lighted tube, known as a bronchoscope, through either the patient's nose or mouth, guiding it down the throat and into the trachea, to the lung airways (Figure 1.11). The tube is usually coupled with a camera and light at the end and has a small channel for histological specimen collection as well. Bron-

1. Clinical Context

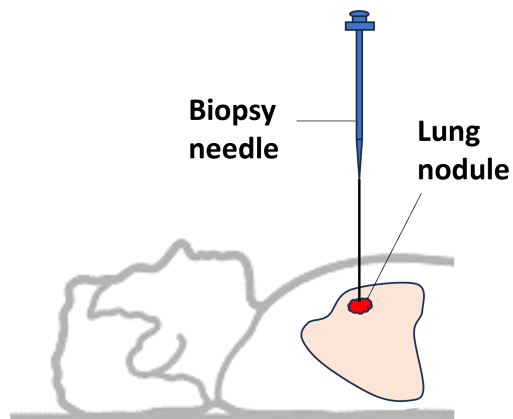


Figure 1.9: Illustration of a percutaneous transthoracic needle biopsy (PTNB) procedure.

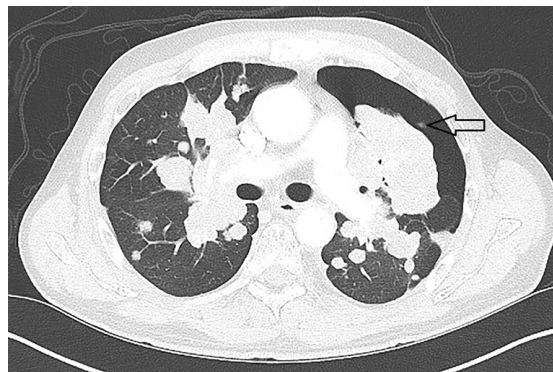


Figure 1.10: CT chest of a patient presenting a left pneumothorax (black arrow). Source: Grosu et al. *Journal of Thoracic Disease*, 2019; <https://doi.org/10.21037/jtd.2019.03.35> [21].

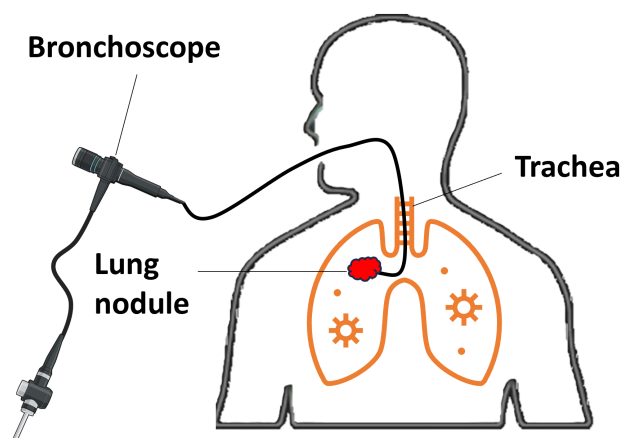


Figure 1.11: Illustration of a bronchoscopy procedure.

choscopy serves both diagnostic and therapeutic purposes. These include airway inspection, removing foreign objects stuck in the airways, diagnosis of airway lesions, therapeutic aspirations of airway secretions, and transbronchial needle biopsy (TBBx) for the diagnosis of lung parenchyma abnormalities [22–24]. Two types of bronchoscopes exist: rigid and flexible. A rigid bronchoscope is a straight tube and can only inspect the large airways (bronchi). A flexible bronchoscope is used in the majority of the cases as it can be moved down into the smaller branches of the bronchi (bronchioles).

The invention of bronchoscopy dates back to 1897 when Gustav Killian, a laryngologist of the University of Freiburg, removed with the bronchoscope the first foreign body via the larynx in a volunteer after he had verified his findings in cadavers that had not undergone tracheotomies (Figure 1.12). He noted afterwards: “*I think I have made an important discovery*”. Following a more thorough and comprehensive series of experiments to confirm his findings, he introduced his discovery, *bronchoscopy*, at the 6th meeting of the Society of South German Laryngologists in Heidelberg on the 29th of May 1898. At Killian’s time, such an invention was very important since most of the patients who aspirated a foreign body fell chronically ill and could not be cured. Killian’s discovery was seen as a miracle. In all but 12 cases of the 703 patients who aspirated a foreign body in the years 1911 to 1921, the foreign body could be removed with bronchoscopy. In the light of his many publications and lectures, he became popular and known as the *father of bronchoscopy*, and Freiburg became the *Mekka of Bronchoscopy* as well. For a detailed history of the genesis of bronchoscopy, interested readers are referred to the first chapter of C. T. Bolliger and P. N. Mathur’s book entitled ‘Interventional Bronchoscopy’ [25].

Conventional Bronchoscopy

Although conventional bronchoscopy and TBBx are successful for endobronchial nodule (nodule in the bronchial lumen mainly) biopsy, their diagnostic yield for PPN is still poor. This yield was reported to range between 43% and 65%, and is particularly lower (14% to 31%) for smaller PPN (< 2 cm) [26]. With the emergence of newer advanced navigational and imaging technologies, conventional bronchoscopy almost phased out from the diagnosis of PPN.

Image-Guided Bronchoscopy

Obstacles to the broader adoption of conventional bronchoscopy have included the avoidance of adjacent blood vessels when performing the biopsy, hurdles in navigating to the lung periphery, and the lack of direct visualization while sampling a lesion. To alleviate these limitations, image-guided bronchoscopy adds real-time imaging techniques to conventional

1. Clinical Context

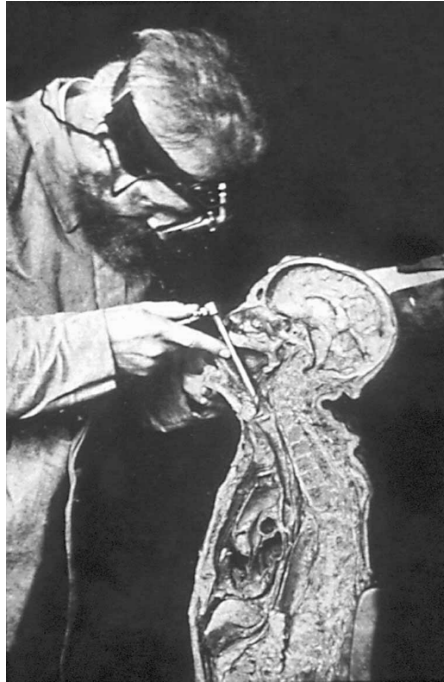


Figure 1.12: Gustav Killian demonstrating bronchoscopy in a half-dissected frozen corpse sitting in a straight position. He is introducing the endoscope using a laryngoscopic spatula with light from an electric head lamp. Source: C. T. Bolliger, P. N. Mathur (eds): *Progress in Respiratory Research. Interventional Bronchoscopy*, Basel, Karger, 2000, vol 30, pp 2-155; <https://doi.org/10.1159/isbn.978-3-318-00415-1> [25].

bronchoscopy. These techniques assist the bronchoscopist with navigational platforms directing them to the target nodule and provide real-time visualization of the lesion during the biopsy procedure. Advancements in imaging and navigational techniques have revolutionized the practice of interventional bronchoscopy and have significantly amplified the diagnostic efficiency of TBBx procedures. Compared to PTNB, image-guided TBBx procedures are safer, pose less complications to the patient, and incur low rate of pneumothorax [27, 28]. In the last ten to fifteen years, these procedures have dominated the scene in the diagnosis of PPN with a wealth of navigational and imaging techniques. These techniques will be presented in Section 1.3 each with its pros and cons.

Ultrathin Bronchoscopy

A significant drawback of conventional bronchoscopy is the inability to navigate the conventional bronchoscope (4.9 mm to 6.1 mm in diameter) beyond the subsegmental bronchi and subsequently the difficulty in reaching the PPN. Biopsy tools have to be thrown from a distance to the target nodule which lessen the diagnostic yield of PPN. Development of ultrathin bronchoscopes (Figure 1.13) with an outer diameter much smaller than that of a standard bronchoscope (2.8–3.5 mm) has allowed a greater maneuverability to reach more

distal bronchi and navigate beyond the fifth or sixth order airways. Thus, biopsy samples can be taken more accurately from the target lesion. When utilized as a standalone technique, ultrathin bronchoscopy has reported diagnostic yields ranging from 57% to 70% [29–31]. Combined with other navigational and imaging techniques, a higher diagnostic yield was reached (74%) [32]. This yield depends on the image guidance modality employed [33–35]. Of the limitations of ultrathin bronchoscopy is the constraint on the size of the collected specimen by the bronchoscope size.



Figure 1.13: Ultrathin bronchoscope (left) and standard bronchoscopes (right). Source: Kalanjeri et al., *Clinics in Chest Medicine*, 2018; <https://doi.org/10.1016/j.ccm.2017.11.007> [36].

1.3 Image-Guided Bronchoscopy Tools

Since their introduction, image guidance modalities coupled with navigational techniques have played a pivotal role in guiding TBBx procedures and have exponentially improved the diagnostic yield of PPN. Various navigational and imaging routines have been adopted and have been combined for an improved access to PPN. The main navigational and imaging modalities will be introduced in the following sections.

1.3.1 Radial Probe Endobronchial Ultrasound

Radial probe endobronchial ultrasound (rEBUS), developed by Olympus Medical Systems, in Tokyo, Japan, is an imaging modality utilized to provide real-time sonographic images for localizing PPN before collecting tissue specimen during bronchoscopy [37]. It employs a miniature mechanical ultrasound probe, operating within a frequency range of 20 to 30 MHz, featuring a rotating tip emitting ultrasound waves in radial pattern and providing a detailed visualization of the target nodule (Figure 1.14). The probe is threaded through the working channel of the bronchoscope, then introduced into the tracheobronchial lumen and is advanced all the way to the PPN. While it provides real-time visualization of the nodule before tissue sampling, the probe cannot take samples itself and must be retracted before the

1. Clinical Context

biopsy tools can be inserted in its place. Navigating these tools through the same route traversed by the probe is not always guaranteed, due to differences in flexibility between the probe and the biopsy tools. To alleviate this limitation, a guide sheath (GS), known as extended working channel as well, is introduced into the working channel of the bronchoscope. Subsequently, the probe is threaded into the GS. The probe is advanced all the way to the PPN. When it is reached, the GS is advanced and positioned in the target location. Having identified the position of the lesion using rEBUS, the probe is retracted, leaving the GS in place. Biopsy tools are then inserted into the GS until reaching its proximal end and tissue samples are collected. While using GS-rEBUS improves the diagnosis accuracy, still it cannot confirm tool-in-lesion since the scanning probe and biopsy tools cannot be inserted together. Moreover, rEBUS-based and GS-rEBUS-based localizations are insufficient as confirmatory techniques due to their lateral-only looking and the high rate of false positives resulting from atelectasis and bleeding [38]. When used as a standalone modality, rEBUS has a diagnostic yield for PPN of 69% [39]. According to a comprehensive meta-analysis, the diagnostic yield of all methods employing rEBUS amounts to approximately 73% for lung cancer [29]. In a recent comprehensive review covering 57 studies and 7872 lesions, the employment of rEBUS demonstrated a diagnostic yield of approximately 70.6% [40].

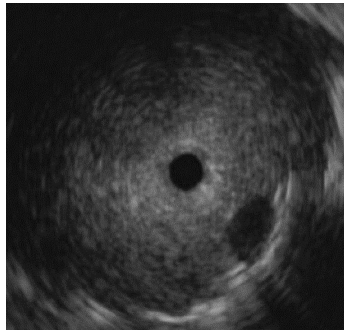


Figure 1.14: A radial probe endobronchial ultrasound (rEBUS) image of a radial probe inserted in the center of a pulmonary lung nodule. Source: Criner et al., *American Journal of Respiratory and Critical Care Medicine*, 2020; <https://doi.org/10.1164/rccm.201907-129250> [41].

1.3.2 Virtual Bronchoscopy

A major challenge in TBBx procedures lies in effectively guiding the bronchoscope and biopsy tools toward the target nodule. To reach the PPN, an accurate guidance of the bronchoscope and biopsy tools all the way along the bronchi is required. The tools have to traverse many bronchial branching sites. Virtual bronchoscopic navigation (VBN) offers a solution by simulating real bronchoscopic images of the bronchial tree from 3D patient-specific preprocedural helical CT data. Based on these images, VBN software creates a virtual tracheobronchial

1.3. Image-Guided Bronchoscopy Tools

tree and a pathway from the central airways to the target lesion in the lung periphery. During bronchoscopy, the bronchoscopist navigates the bronchoscope to the target PPN by displaying the VBN images of the bronchial path in tandem with real-time bronchoscopic images (Figure 1.15).

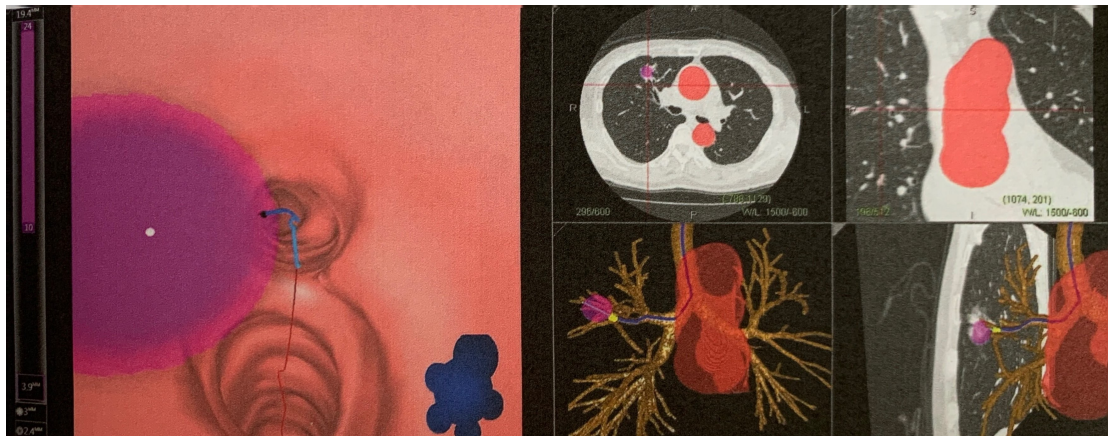


Figure 1.15: Display of a virtual bronchoscopic navigation (VBN) to a peripheral pulmonary nodule (PPN). Left: VBN image. The bronchial centerline to the PPN is shown in light blue. The target PPN is highlighted as a pink circle. Lower image at the center: the bronchial tree with the route to the target highlighted in blue. Right lower image: overlaid sagittal CT slice of the lesion area, the bronchial tree, and the location of the virtual bronchoscope. Source: A. Mehata and P. Jain, *Interventional Bronchoscopy: A clinical Guide*, 2013; <https://doi.org/10.1007/978-1-62703-395-4> [42].

Various VBN platforms have been developed and are commercially available, such as BfNAVI (Cybernet systems, Tokyo, Japan) [30, 43], LungPoint (Broncus Technologies, Inc., Mountain View, CA, USA) [44], and BTPNA (Archimedes System/Broncus Technologies, Inc., Mountain View, CA, USA) [45]. The diagnostic yield for all PPN using VBN ranges between 72% and 74% [29, 46] and is around 67% for smaller lesions (diameter ≤ 2 cm) [46]. One limitation of the VBN platforms is their inability to track the tools in real-time during the actual procedure. Additionally, there may be discrepancies between the expected position of the target lesion on virtual bronchoscopic images and its actual position. This is known as **CT-to-body divergence**. It has been cited as a crucial barrier to a successful lung navigation [47]. The main contributing factors to this divergence are the differences in lung volumes and in patient positioning between the preoperative CT scan and the intraoperative state during bronchoscopy. Planning CT scans are usually performed at full inspiration, in an awake and spontaneous respiration state, prior to the intervention with the patient's arms overhead. However, throughout the procedure, patients are often sedated, mechanically ventilated in tidal or expiratory reserve volume breathing state with the arms at the side in a supine position. The mismatch between the virtual and the actual target position can be misleading and

1. Clinical Context

challenging to the bronchoscopist, adds time to the procedure, and diminishes the diagnostic yield.

1.3.3 Electromagnetic Navigational Bronchoscopy

The incapability of VBN systems of tracking the bronchoscopy tools while navigating to the PPN has led to the development of electromagnetic navigational bronchoscopy (ENB). This navigational technique relies on using a patient-specific planning CT scan and some sensors in a low-frequency electromagnetic field. Compared to VBN, ENB-based systems allow for real-time positional guidance to the PPN. A widely used ENB system is the superDimension by Medtronic in Minneapolis, MN, USA. Using this system, the bronchoscopy procedure is accomplished in three phases (Figure 1.16). First is the planning phase where the planning CT data are loaded to the planning station. The software constructs a dynamic virtual 3D tracheobronchial tree and the target PPN is identified and marked. An approximate pathway to the closest central airway to the target is automatically created. Registration landmarks are identified on the virtual tree and are used in the next phases. Following an examination and validation by the bronchoscopist, the planning data are saved. Second is the registration phase. During this phase, the patient lays on the procedure table and a magnetic board is attached to the table. Sensors are placed on the patient and a locatable guide (LG) is passed through the bronchoscope's working channel. As the bronchoscope is advanced through the airways, the LG passively collects numerous positional data points and syncs them with the virtual landmarks identified in the planning phase, resulting in the creation of a virtual bronchoscopic image. Last is the navigation phase. During this phase, the bronchoscope is inserted into the bronchus leading towards the target PPN. The LG and edge catheter are then advanced as close to the target as possible, following the pathway outlined on the virtual bronchoscopic image. When the desired location is reached, the LG is removed and the catheter is secured near the end of the bronchoscope's biopsy channel. To procure tissue specimen, biopsy accessories (forceps, endobronchial brush, transbronchial aspiration needle, ...) are passed through the catheter.

In a multi-center comprehensive study (NAVIGATE), the diagnostic yield of ENB procedures performed on 1157 patients using the superDimension system was 73% [48]. While fluoroscopy can be utilized to ensure tool-in-lesion at the end of the procedure, it cannot be employed during the navigation since the fluoroscope itself presents ferromagnetic interference with the magnetic board [42]. Therefore, the bronchoscopist will navigate to the lesion relatively blindly. In addition, using fluoroscopy to ensure tool-in-lesion is risky, the lesion may not be visible due to the overlap of the structures in a 2D image. Additionally, CT-to-body divergence is another critical obstacle to ENB procedures. The location of the target PPN

1.3. Image-Guided Bronchoscopy Tools

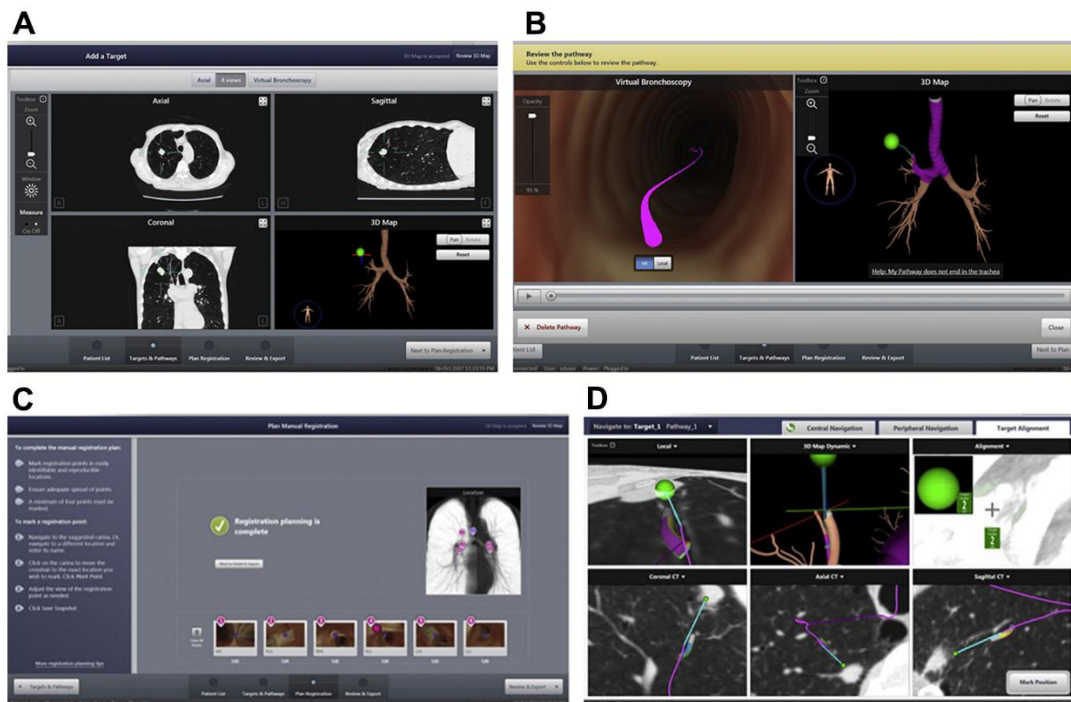


Figure 1.16: SuperDimension ENB-based navigational system. A: planning phase. The planning CT scan is loaded and a dynamic virtual 3D tracheobronchial tree is created. The target lesion is highlighted in green. B: Planning phase. A virtual pathway (violet) to the target is created. C: Registration phase. Registration of prominent landmarks. D: Navigation phase. Multiplanar views of the virtual images. LG approaches the target. Source: S. Kalanjeri et al., *Clinics in Chest Medicine*, 2018; <https://doi.org/10.1016/j.ccm.2017.11.007> [36].

on the virtual maps may be different than its actual location during bronchoscopy [49, 50]. Moreover, respiratory motion, especially in the lower lobe, tends to impede the bronchoscopy procedure [51]. In an attempt to alleviate the impact of respiratory motion on the procedure, SPiN system (Veran Medical Technologies, St Louis, MO, USA) accommodating for respiratory gating technologies has been developed to track moving lesions during bronchoscopy [52]. Besides unresolved CT-to-body divergences, such system poses workflow-related challenges since the planning CT scan has to be done on the same day as the procedure.

1.3.4 CBCT-Guided Bronchoscopy

Despite the broad range of developed navigational and imaging techniques for guiding TBBx procedures, the diagnostic yield for PPN continues to be unsatisfactory and suboptimal, ranging in some studies from 38% to 74% [29, 51, 53, 54]. The remaining aspects of unresolved CT-to-body divergence, which can misguide navigational bronchoscopy, along with the absence of an accurate real-time confirmatory imaging technique, have recently led to the adoption of intraprocedural C-arm-based cone-beam computed tomography (CBCT) by the

1. Clinical Context

bronchoscopy community [38, 55–59]. In contrast to standard fan-beam CT, CBCT is sufficiently compact to be mounted on a moving C-arm. CBCT images are obtained by rotating the C-arm system approximately 200° along a single circular orbit around the patient, and acquiring a large set of 2D X-ray projection images at specific angular intervals while the patient remains stationary (Figure 1.17).

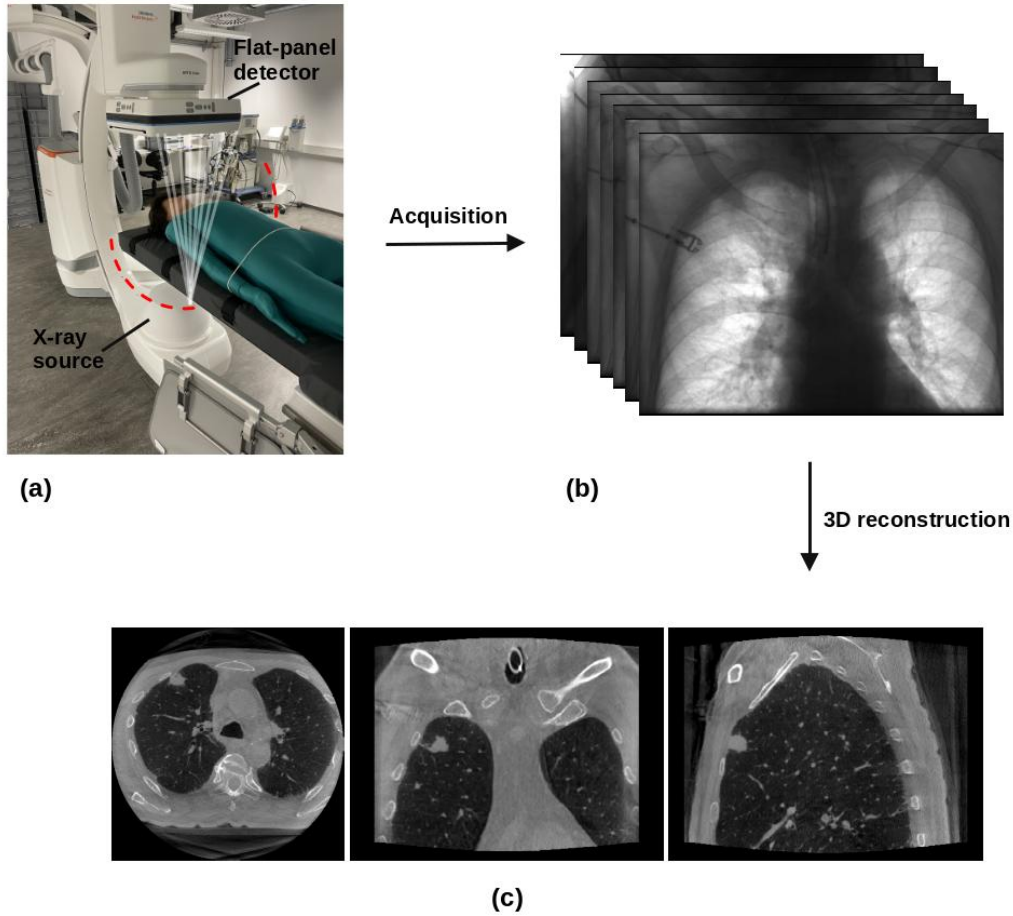


Figure 1.17: Bronchoscopy guidance using a C-arm CBCT system. (a) Illustration of a CBCT system mounted on a C-arm device. The dotted red circle is the circular CBCT scan orbit. The white lines represent an X-ray cone-beam emitted from the X-ray source at one of the angular acquisition intervals and detected by the flat-panel detector. (b) Illustration of a set of acquired projection images. (c) From left to right, an axial, a coronal, and a sagittal slice of the 3D reconstructed CBCT volume.

The reconstruction of the projection images provides a complete 3D stack of axial images covering a large region of interest of the patient anatomy with a sub-millimeter isotropic resolution. Up to 600 projection images are acquired in 3-20 seconds depending on the imaging system specifications and protocols. CBCT imaging is used for guiding the navigation as well as for confirming tool-in-lesion. Once the patient is intubated and before inserting the

1.3. Image-Guided Bronchoscopy Tools

bronchoscope, a CBCT scan is performed to locate the target PPN. Using dedicated segmentation software, the nodule is outlined. During the bronchoscopy procedure, the segmented lesion is overlaid on live fluoroscopic images to visualize the target towards which the bronchoscopist drives during navigation. While navigating to the lesion using live fluoroscopy and/or any of the available navigational techniques, CBCT scans are only performed to obtain a full 3D intraprocedural overview when deemed necessary. Prior to biopsy and after the bronchoscopic biopsy tool has reached the target PPN, a CBCT scan is performed to confirm tool-in-lesion (Figure 1.18). From one to three CBCT acquisitions per patient and per procedure are usually performed in CBCT-guided bronchoscopy procedures. In a large study, a diagnostic yield of 84% has been reached using CBCT-overlaid fluoroscopy besides ENB during navigation [59]. An increase of 25% in navigational yield and an increase of 20% in diagnostic yield were reported when performing the tool-in-lesion confirmation CBCT prior to sampling tissues [38], and, interestingly, while atelectasis were not detected on fluoroscopy alone and were producing false-positive rEBUS images, they were visible on CBCT.

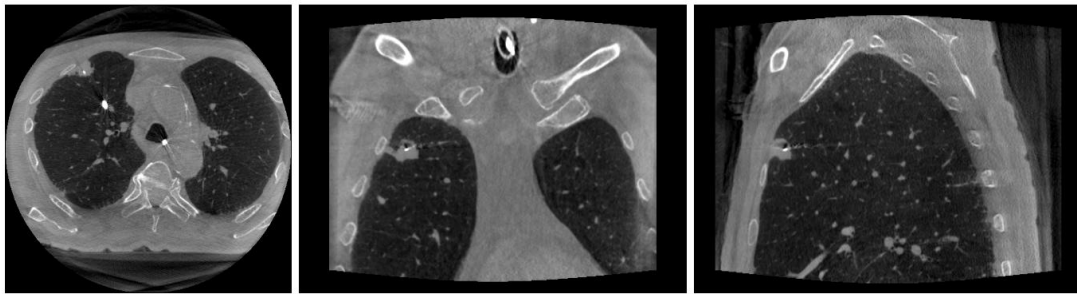


Figure 1.18: Tool-in-lesion confirmation CBCT images. The biopsy tool is in contact with the target PPN. From left to right: an axial, a coronal, and a sagittal slice of the CBCT volume.

Whereas CBCT might look like the ideal imaging modality providing exact intraprocedural 3D images, resolving the CT-to-body divergence, and increasing the diagnostic yield for PPN when utilized in conjunction with the common bronchoscopic navigational techniques, its use is at the cost of serious risks and challenges.

- **Radiation dose:** A major drawback associated with using CBCT for guidance is the harmful excessive high radiation to which patients as well as bronchoscopists and staff are exposed. A high risk of developing cancer has been linked to a high cumulative radiation exposure [60, 61]. Recent studies have shown that one to three CBCT acquisitions are performed per patient and per procedure during CBCT-guided bronchoscopy [38, 59]. Since the total radiation dose increases linearly when CBCT acquisitions are repeated, this poses a serious limitation of using CBCT in such procedures.

1. Clinical Context

- **Workspace restrictions:** To perform a CBCT scan during the bronchoscopy procedure, the C-arm has to be almost fully rotated around the patient ($\sim 200^\circ$). However, the available space in the operating room is limited (Figure 1.19). Many entangled cables, lines, tubes, wires, and other systems block the C-arm trajectory. Additionally, a bronchoscope tower, a robotic arm holding the bronchoscope, and some navigational equipment may interfere with the C-arm motion. This necessitates rearrangement of the tools prior to the scan to avoid collision, disrupting the workflow in the operating room.



Figure 1.19: Representative room setup in a bronchoscopy procedure showing the limited available space for rotating the C-arm. Source: R. Setser et al., *Journal of Thoracic disease*, 2020; <https://doi.org/10.21037/jtd-20-2382> [62].

- **Imaging time:** The abovementioned operations required to perform the scan are time-consuming, and time is a critical factor during bronchoscopy procedures. Moreover, the acquisition of several hundreds of 2D X-ray projection images required to reconstruct each non-ambiguous CBCT volume with the standard reconstruction algorithms available on the commercial C-arm devices further adds to the time required, as C-arm systems are relatively slow.

1.4 Conclusion

To sum up, in this introductory chapter, we have discussed the current global state of lung cancer and its associated burden, emphasized the importance of nodule biopsy in the diagnosis process, explored the challenges encountered when sampling PPN, and outlined the various available approaches for PPN biopsy. We have mainly shed light on navigational bronchoscopy, recognized as the safest and least invasive biopsy technique. Furthermore, we have elucidated the diverse navigational and imaging approaches employed to guide today's bronchoscopy procedures, each with its own set of advantages and drawbacks. After covering the clinical context of bronchoscopy procedures and the challenges associated with the most recently adopted imaging modality for guiding such procedures, i.e., CBCT, we formulate in the next chapter the problems this research work addresses, the research questions it seeks to answer, the motivation and well-defined aims of this thesis, as well as its contributions.

1. Clinical Context

2

Problem Formulation and Aims of the Thesis

Contents

| | | |
|-----|--|----|
| 2.1 | Problem Formulation and Research Questions | 21 |
| 2.2 | Motivation | 23 |
| 2.3 | Research Objectives | 23 |
| 2.4 | Contributions and Significance | 24 |
| 2.5 | Thesis Structure | 25 |
| 2.6 | List of Publications | 26 |

HAVING introduced in the previous chapter the clinical context that frames this research work, this chapter unravels the problem addressed by this research and contextualizes its significance within research and practical applications of bronchoscopy intervention image guidance. Subsequently, it articulates the precise research questions this work seeks to answer and its driving motivations, followed by a clear delineation of research objectives, providing a structured framework for this thesis. Lastly, the distinctive contributions that this research makes to the existing body of knowledge within bronchoscopy image guidance are highlighted, emphasizing its potential impact and relevance in both academic and practical realms.

2.1 Problem Formulation and Research Questions

With the release of current C-arm systems, a co-integration of cone-beam computed tomography (CBCT) and projective fluoroscopy has become possible. For guiding bronchoscopy

2. Problem Formulation and Aims of the Thesis

interventions, a continuous follow-up is provided by fluoroscopic imaging and, from time to time, CBCT imaging is performed providing exact 3D overview of the anatomy and guiding the bronchoscopist towards the target lesion [59]. Whereas projective fluoroscopy poses low radiation dose to the patient and the bronchoscopist, its weakness is in the superposition of the different structures in a 2D image hindering the depiction of intervention targets (e.g., lesions) [63]. While CBCT might look like the perfect guiding modality, offering accurate real-time imaging, solving the CT-to-body divergence, and increasing the diagnostic yield for peripheral pulmonary nodules (PPN) [38, 59], it has failed to reach its wide application in the real clinical routine of bronchoscopy interventions. As detailed in Section 1.3.4, **radiation dose**, **timeliness**, and **workspace limitations** still form significant barriers to the broad adoption of CBCT in guiding bronchoscopy interventions.

The general problem this doctoral work addresses can be formulated as follows:

How to reduce the radiation dose, the imaging time, and the required footprint of CBCT in image-guided bronchoscopy interventions without sacrificing the image quality?

A full CBCT acquisition involves acquiring several hundreds of uniformly distributed X-ray projection images over a full angle of rotation ($\sim 200^\circ$). One way to reduce the radiation dose involved in CBCT is to acquire less X-ray data. Here two approaches rise: the sparse-view approach and the limited-angle approach. The sparse-view approach consists on acquiring only few projection images over a full angle of rotation. The limited-angle approach involves acquiring X-ray data with dense angular sampling over a limited angle of rotation (less than 200°). As the aim while guiding bronchoscopy interventions is to reduce the radiation dose as well as the imaging time and space requirements, this thesis work is focused on combining both approaches, i.e., acquiring few X-ray data over a limited angular range.

In this context, Aboudara et al. proposed recently digital tomosynthesis (DTS) technology as a potential alternative to CBCT for navigational bronchoscopy guidance [64]. Introducing some depth information to projective fluoroscopy on the one hand, and imposing fractions of the radiation dose, imaging time, and space requirements of CBCT on the other hand, DTS appears as a potential candidate for guiding bronchoscopy interventions. DTS is a form of limited-angle tomography that provides quasi-3D images. During DTS, the C-arm performs a fluoroscopic sweep around the patient over a limited angular range and a limited set of X-ray projection images are acquired and reconstructed. Compared to CBCT, the trade-off is in image quality, more specifically, images reconstructed from such kind of incomplete data using the standard conventional reconstruction algorithms, like the Feldkamp–Davis–Kress algorithm (FDK) [65], suffer from severe streaking artifacts and poor depth resolution (resolution in the direction orthogonal to the detector surface). Therefore, they are clinically useless and may make bronchoscopy intervention guidance impossible. The question that

arises here is: *how to compensate for the missing data with DTS to preserve images with a quality sufficient-enough for guiding the intervention?*

2.2 Motivation

The loss of information with DTS can be tackled at three levels: **data acquisition**, **missing data replacement**, and **image reconstruction**. At the acquisition level, the use of complex multidirectional scan orbits might improve DTS image quality compared to the standard unidirectional scan orbits. However, inventing new complex DTS motions is often constrained by logistic circumstances of the specific medical intervention. In bronchoscopy interventions, some devices, in particular robotic bronchoscope holders, are placed in a way that the angulation in the cranial/caudal direction is limited. Therefore, when proposing a new DTS motion profile, special considerations should be taken into account to avoid the collision of the C-arm with the different equipment.

A promising source for missing data replacement is prior information. In bronchoscopy procedures, high quality patient-specific computed tomography (CT) scans are often performed prior to the intervention for planning the intervention or for diagnosis. These prior CT images share a fair amount of information content with the intraoperative DTS images and could provide additional valuable clinical information not apparent in the DTS images. However, CT-to-body divergence poses a significant obstacle that hampers the proper use of the CT images. This divergence is mainly caused by different patient positioning between the prior CT scan and the intraoperative DTS scan, by anatomic changes due to neuromuscular paralysis, and by dynamic changes due to respiratory motion and insertion of the catheters and biopsy tools. Investments in such priors are constrained by a proper registration of the prior CT image to the current anatomy. One way to address the loss of information on the reconstruction level is by properly including this prior knowledge into the DTS reconstruction algorithm compensating for the missing data.

2.3 Research Objectives

Based on the formulated problem and to be able to appropriately answer the research questions raised above, the ultimate research objectives of this doctoral work are defined as:

- **diminution of the ionizing radiation dose,**
- **reduction of the imaging time, and**
- **minimization of the scanning footprints**

2. Problem Formulation and Aims of the Thesis

of X-ray imaging during image-guided bronchoscopy interventions, while providing images with a quality sufficient-enough for a proper guidance.

To achieve the aforementioned goals, the work is mainly focused on finding a DTS scanning protocol customized for bronchoscopy intervention guidance and improving image quality of existing DTS scanning protocols, and on properly including available prior information (i.e., high-quality patient-specific prior CT scan) into the DTS reconstruction algorithm to further improve DTS image quality.

2.4 Contributions and Significance

In the course of this thesis, several contributions to the use of DTS imaging in guiding bronchoscopy interventions have been made. A complete framework starting from the acquisition protocol to the reconstruction algorithm has been developed. These key contributions can be summarized as:

- ✓ **a novel C-arm-based spherical ellipse DTS scanning protocol customized for bronchoscopy interventions**
- ✓ **a novel deformable 3D/3D registration algorithm that aligns prior chest CT images to intraoperative DTS images for bronchoscopy intervention guidance**
- ✓ **a novel prior-aided iterative DTS reconstruction framework including prior CT images into the DTS reconstruction**

This research work has the potential to contribute significantly to both academic understanding and practical advancements in the field of bronchoscopy intervention image guidance. Introducing a customized DTS scanning protocol for guiding bronchoscopy interventions could contribute to the academic field by expanding the understanding of optimized imaging protocols tailored for specific medical procedures. Moreover, the novel scanning protocol has practical implications for bronchoscopy interventions, potentially improving image quality, accuracy, and efficiency during these procedures compared to existing scanning protocols. This could lead to higher diagnostic yields and more precise treatment planning. In existing literature, prior-CT-to-intraoperative-DTS image registration problem has been minimally addressed, primarily because of the complex resolution characteristics of DTS. Furthermore, to the best of the author's knowledge, taking into account in this context deformable motion in a 3D/3D CT-to-DTS registration format has not been explored. In this research work, a registration framework that considers dynamic deformable changes has been successfully developed. This aspect holds significant relevance in the context of bronchoscopy interventions, given the considerable movement exhibited by organs within the chest. Properly

addressing CT-to-body divergence, considered as the major challenge in navigational bronchoscopy guidance, is of great clinical importance, especially that prior CT images are usually of high quality and carry a wealth of useful anatomical information. Being able to properly align these prior CT images to intraoperative DTS images has the potential to significantly improve the accuracy and precision of localizing target lung nodules, thereby increasing the diagnostic yield of these procedures. Of particular note is the prior-aided DTS reconstruction algorithm providing CT-augmented DTS images. Through this algorithm, DTS images can successfully be transformed from a radiography-like quality to a more tomography-like quality, presenting DTS images that are comparable to CBCT images at a fraction of the required radiation dose and footprints. Overall, this research work offers valuable insights and tools for researchers and medical practitioners to introduce DTS as an image guidance modality for bronchoscopy interventions. Moreover, while the work in this thesis was mainly focused on bronchoscopy interventions, all the presented methods can be adopted to other medical interventions.

2.5 Thesis Structure

In **Chapter 1**, the clinical context framing and motivating this research work has been introduced. An overview on the current global state of lung cancer and its associated burden has been presented highlighting the importance of lung nodule biopsies in the diagnosis process and the challenges encountered during the biopsy procedure. A special attention has been given to navigational bronchoscopy since it is recognized as the safest and least invasive biopsy technique, and to the crucial role of imaging techniques in guiding navigational bronchoscopy procedures. Furthermore, the challenges associated with the most recently adopted imaging modality, i.e., CBCT, have been highlighted.

Chapter 2 has formulated the problem addressed by this research work and has motivated the need for adopting a new imaging modality, i.e., DTS, in guiding bronchoscopy interventions. The research questions this doctoral work seeks to answer, the research objectives it tends to achieve, and its contributions have been also revealed.

As DTS is a form of X-ray imaging, the fundamentals of X-ray imaging, from X-ray generation to image formation, will be presented in **Chapter 3**. Subsequently, an in-depth coverage on DTS imaging, from its data acquisition geometries to its image formation and its special kind of artifacts, will be provided.

Chapters 4, 5, and 6 unveil the main contributions of this thesis. In **Chapter 4**, a novel DTS scan orbit customized for bronchoscopy intervention guidance will be disclosed. This orbit will be compared to projective radiography (PR), CBCT, and the available DTS scan orbits, and its advantages will be exposed. **Chapter 5** uncovers a novel deformable 3D/3D

2. Problem Formulation and Aims of the Thesis

CT-to-DTS registration algorithm that aligns prior CT images to intraoperative DTS images in the context of bronchoscopy intervention guidance. In **Chapter 6**, a prior-aided DTS reconstruction algorithm employing registered prior CT images to improve intraoperative DTS image quality will be introduced. The benefits of incorporating prior knowledge into the intraoperative DTS reconstruction algorithm will be demonstrated.

Chapter 7 briefly discusses cases where CT-to-DTS registration might fail and provides insights into an alternative bronchoscopy guidance protocol based on employing CBCT at the very beginning of the procedure and following it with DTS whenever a 3D scan is deemed necessary. This chapter offers perspective on how to use intraoperative CBCT as an alternative to prior CT images employed in earlier chapters.

Chapter 8 summarizes the key findings and achieved contributions of this research. The proposed methods, along with their benefits, limitations, and implications for future research and clinical practice are discussed. Additionally, a list of potential avenues for further development and research in the field is provided.

2.6 List of Publications

The main contributions of this doctoral work have been published in several journal papers and conference proceedings and have been presented in several national and international conferences. These are listed below.

Journal articles

- **Fatima Saad**, Robert Frysch, Sylvia Saalfeld, Stephan Kellnberger, Jessica Schulz, Rebecca Fahrig, Krish Bhadra, Andreas Nürnberger, and Georg Rose. **Deformable 3D/3D CT-to-Digital-Tomosynthesis Image Registration in Image-Guided Bronchoscopy Interventions**. *Computers in Biology and Medicine*, volume 171, pages 108199, 2024.
- **Fatima Saad**, Robert Frysch, Sylvia Saalfeld, Stephan Kellnberger, Jessica Schulz, Rebecca Fahrig, Krish Bhadra, Andreas Nürnberger, and Georg Rose. **CT-Augmented Digital Tomosynthesis Image Reconstruction in Image-Guided Bronchoscopy Interventions**. (submitted)

Conference papers

- **Fatima Saad**, Robert Frysch, Tim Pfeiffer, Sylvia Saalfeld, Jessica Schulz, Jens-Christoph Georgi, Andreas Nürnberger, Guenter Lauritsch, and Georg Rose. **Iterative intraoperative digital tomosynthesis image reconstruction using a prior as initial image**.

In 7th International Conference on Image Formation in X-Ray Computed Tomography, volume 12304, pages 669–674. SPIE, 2022.

- **Fatima Saad**, Robert Frysch, Tim Pfeiffer, Andreas Nürnberger, Guenter Lauritsch, and Georg Rose. **Adjusting the acquisition parameters of spherical ellipse tomosynthesis scan orbit for guiding interventional bronchoscopy.** *In the 5th Conference on Image-Guided Interventions (IGIC 2021)*, Magdeburg, Germany, Oct 13-14, 2021.
- **Fatima Saad**, Robert Frysch, Tim Pfeiffer, Jens-Christoph Georgi, Torsten Knetsch, Roberto F Casal, Andreas Nürnberger, Guenter Lauritsch, and Georg Rose. **Spherical ellipse scan trajectory for tomosynthesis-assisted interventional bronchoscopy.** *In Proceedings of the 16th Virtual International Meeting on Fully 3D Image Reconstruction in Radiology and Nuclear Medicine*, Schramm, G., Rezaei, A., Thielemans, K., and Nuyts, J., eds, pages 352–356, 2021.
- **Fatima Saad**, Robert Frysch, Vojtech Kulvait, Daniel Punzet, and Georg Rose. **Nullspace-constrained modifications of under-sampled interventional ct images using instrument-specific prior information.** *In Medical Imaging 2020: Physics of Medical Imaging*, volume 11312, pages 888–894. SPIE, 2020.
- **Fatima Saad**, Robert Frysch, Vojtech Kulvait, Daniel Punzet, and Georg Rose. **Reconstruction of difference images using the nullspace-constrained modification scheme and instrument-specific prior information.** *In the 4th Conference on Image-Guided Interventions (IGIC 2019)*, Mannheim, Germany, Nov 4-5, 2019.

Further contributions (other topics)

- Soumick Chatterjee*, **Fatima Saad***, Chompunuch Sarasaen*, Suhita Ghosh*, Valerie Krug, Rupali Khatun, Rahul Mishra, Nirja Desai, Petia Radeva, Georg Rose, Sebastian Stober, Oliver Speck, and Andreas Nürnberger. **Exploration of interpretability techniques for deep covid-19 classification using chest x-ray images.** *Journal of Imaging*, volume 10, 2024. (* equal contribution)
- Hana Haseljić, Vojtech Kulvait, Robert Frysch, **Fatima Saad**, Bennet Hensen, Frank Wacker, Inga Brüsich, Thomas Werncke, and Georg Rose. **Time separation technique using prior knowledge for dynamic liver perfusion imaging.** *In 7th International Conference on Image Formation in X-Ray Computed Tomography*, volume 12304, pages 440–445. SPIE, 2022.
- Chompunuch Sarasaen, Soumick Chatterjee, **Fatima Saad**, Mario Bretkopf, Georg Rose, Andreas Nürnberger, and Oliver Speck. **Fine-tuning deep learning model parameters for improved super-resolution of dynamic MRI with prior-knowledge.**

2. Problem Formulation and Aims of the Thesis

In the 29th Annual Meeting and Exhibition of the International Society for Magnetic Resonance in Medicine (ISMRM 2021), online, May 15-20, 2021.

- Lisa Meyer-Bäse, **Fatima Saad**, and Amirhessam Tahmassebi. **Controllability of structural brain networks in dementia.** *In Medical Imaging 2020: Biomedical Applications in Molecular, Structural, and Functional Imaging*, volume 11317, pages 476–483. SPIE, 2020.

3

Technical Background

Contents

| | |
|--|-----------|
| 3.1 X-ray Imaging | 30 |
| 3.1.1 X-ray Generation | 31 |
| 3.1.2 X-ray Transmission | 34 |
| 3.1.3 X-ray Detection | 37 |
| 3.1.4 X-ray Applications | 38 |
| 3.1.5 Image Reconstruction | 40 |
| 3.2 Digital Tomosynthesis: From Data Acquisition to Image Formation . | 48 |
| 3.2.1 History of Tomosynthesis | 49 |
| 3.2.2 History of Tomosynthesis Reconstruction Methods | 51 |
| 3.2.3 Data Acquisition | 55 |
| 3.2.4 Acquisition Geometry Parameters | 57 |
| 3.2.5 Artifacts | 58 |
| 3.3 Conclusion | 61 |

As digital tomosynthesis (DTS) is a form of X-ray imaging, this chapter delves into the fundamentals of X-ray physics and techniques, from X-ray generation to image formation. Subsequently, it provides an in-depth coverage on DTS, its milestones, its history from its earliest beginnings to modern imaging, its reconstruction algorithms, and its special kind of artifacts.

3. Technical Background

3.1 X-ray Imaging

It was on the 8th of November 1895 when the Würzburg physics professor Wilhelm Conrad Röntgen discovered the X-ray. After weeks of tireless work and experiments, he made his discovery public. It was described in the newspapers as a new type of “light” that was used to take “a photograph of a set of weights without opening the wooden box in which the weights were kept”, and of a human hand showing the bones “without the flesh” (Figure 3.1). At that time, his peculiar discovery was thought to be a joke and many scientists could not believe it until his experiments were reproduced and confirmed at many physics laboratories. While invasive surgery was the only way to see inside the human body formerly, X-ray discovery has since revolutionized diagnostic care and has opened up new perspectives in medical diagnosis. X-ray imaging is a non-invasive, but ionizing, technique that allows the visualization of the inside of the human body. X-rays are a form of electromagnetic radiation, similar to visible light but with higher energy and shorter wavelength, able to penetrate optically opaque objects. When they pass through a material (biological tissues of a patient’s body in the case of medical imaging), they are absorbed, scattered, or transmitted depending on the density and composition of the material. In general, a standard X-ray imaging device is composed of a tube that generates the X-ray beam, and a detector that captures the X-rays transmitted or scattered through the object or organ studied. The X-rays are absorbed in varying degrees by different tissues based on their radiological density. Figure 3.2 outlines the basic principles of X-ray imaging. Beyond its medical use, X-ray imaging is widely used as a generic diagnostic tool for non-destructive material testing and 3D visualization, as well as in archaeology.



Figure 3.1: One of the earliest X-ray images: the bones of the hand of Bertha, Wilhelm Röntgen’s wife, showing a wedding ring floating around her finger. Source: German Röntgen museum.

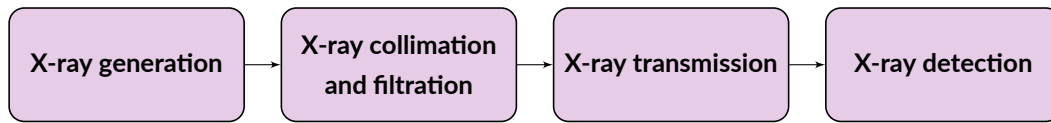


Figure 3.2: Basic principles of X-ray imaging.

3.1.1 X-ray Generation

X-rays lie at the high-energy, short-wavelength segment of the electromagnetic spectrum besides gamma rays (Figure 3.3). They possess enough energy that when they interact with atoms, they can release electrons from the atoms holding them. When an electron is liberated from an atom, a pair is formed: the negatively charged electron (e^-), and the positive atom from which the electron is released. This makes X-rays and gamma rays a form of ionizing radiation and distinguishes them from the rest of the electromagnetic spectrum.

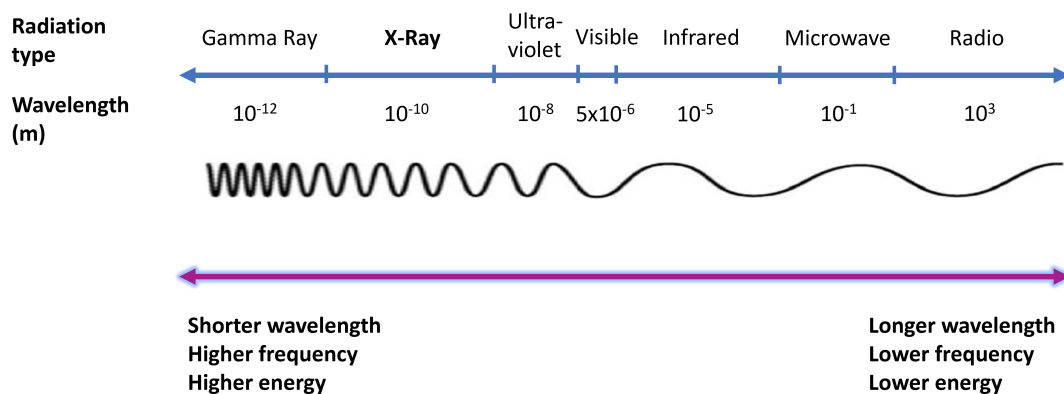


Figure 3.3: Illustration of the electromagnetic spectrum. Comparison of the wavelength, frequency, and energy. X-rays lay at the high-energy short-wavelength end of the spectrum.

The energy E of an electromagnetic wave is proportional to its frequency ν and is determined by Planck's equation

$$E = h \cdot \nu \quad (3.1)$$

where $h = 4.135 \times 10^{-15} \text{ eV} \cdot \text{s}$ is Planck's constant. For chest X-ray imaging, X-ray energies used typically range between 0 and 130 KeV. The wavelength λ of an electromagnetic wave is defined as

$$\lambda = \frac{c}{\nu} \quad (3.2)$$

where $c = 3 \times 10^8 \text{ m/s}$ is the speed of the light. For diagnostic medical X-ray imaging, the wavelengths of X-rays used run from 0.1 nm (at 12.4 KeV) to 0.01 nm (at 124 KeV).

3. Technical Background

Various are the ways to produce X-rays, by free electron lasers, by synchrotrons, by channeling sources, etc. However, the prevalent approach utilized in medical imaging for X-ray production is the standard X-ray tube. An illustration of the different components of a classical X-ray tube is depicted in Figure 3.4. It is mainly composed of an evacuated glass tube with an anode assembly on one side and a cathode assembly on the opposite side. The anode and the cathode are connected through an electrical conductor and are subjected to an electric potential. Inside the cathode, which is the negatively charged pole of the high voltage circuit, are usually two different tungsten wire filaments. When one of the filament is heated up by passing a filament current through it, a stream of electrons are released through a process called thermionic emission and are accelerated towards the anode due to the high voltage potential difference between the anode and the cathode. When the high-speed electrons strike the target anode, they undergo deceleration and their kinetic energy is partially or totally transformed into electromagnetic energy in the form of X-ray photons. The X-rays are generated as a result of interactions between the electrons and the atoms in the anode material and their energy depends on the energy of the incoming electrons, and the atomic structure of the target anode material.

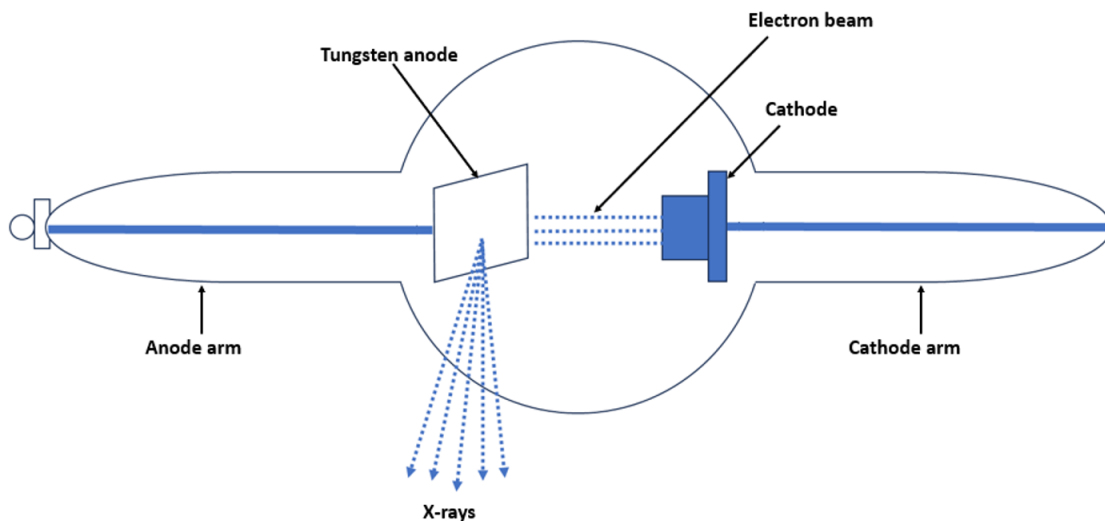


Figure 3.4: Illustration of the functional components of an X-ray tube.

During the collision of the high-speed electrons with the cathode, two main physical effects can be observed, the bremsstrahlung and the characteristic radiation.

Bremsstrahlung: When the incoming electron passes near the nucleus of the anode atoms, it interacts with the Coulomb field of the nucleus, it is slowed down, and its path is deflected. The reduction of its velocity translates into a reduction of its overall energy, and this loss of energy is released by emitting a light quantum, i.e., a bremsstrahlung X-ray photon (Figure 3.5).

The energy of the emitted photon is given by

$$E_{\text{photon}} = E_{\text{before}} - E_{\text{after}} = h \cdot f = h \cdot \frac{c}{\lambda} \quad (3.3)$$

where E_{before} and E_{after} are the energy of the electron before and after deceleration, respectively, and h is Planck's constant. Thus, the energy of the emitted photon, and consequently, the energy of the X-rays, is fully dependent on their frequency or wavelength.

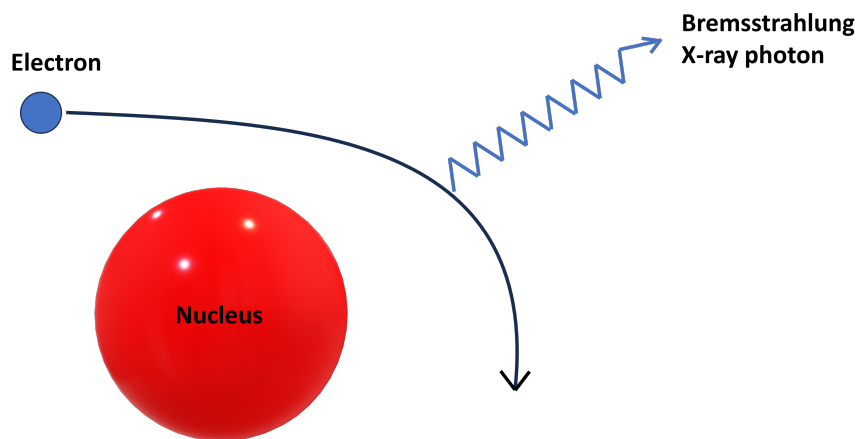


Figure 3.5: Bremsstrahlung X-ray generation.

Characteristic radiation This type of interactions happens when the high-energy fast electron coming from the cathode collides with an inner shell electron of the target anode. In this case both the electrons are ejected from the tungsten atom and a hole is left in the inner shell. An outer shell electron changes its state and fills the free spot (hole) which is energetically more stable. The loss of energy resulting from this transition is emitted as characteristic X-ray photon at distinct energy level (Figure 3.6). The energy of this radiation calculates again as

$$E_{\text{photon}} = E_{\text{outer}} - E_{\text{inner}} = h \cdot f = h \cdot \frac{c}{\lambda} \quad (3.4)$$

where E_{outer} and E_{inner} are the energies the electron has when being at the outer and inner shell, respectively.

A spectrum of X-ray energy is produced within the X-ray beam as a result of bremsstrahlung and characteristic X-ray generation. Figure 3.7 illustrates a plot of the X-ray intensity against the wavelength and depicts the principle drawing of a spectrum of X-ray energy.

3. Technical Background

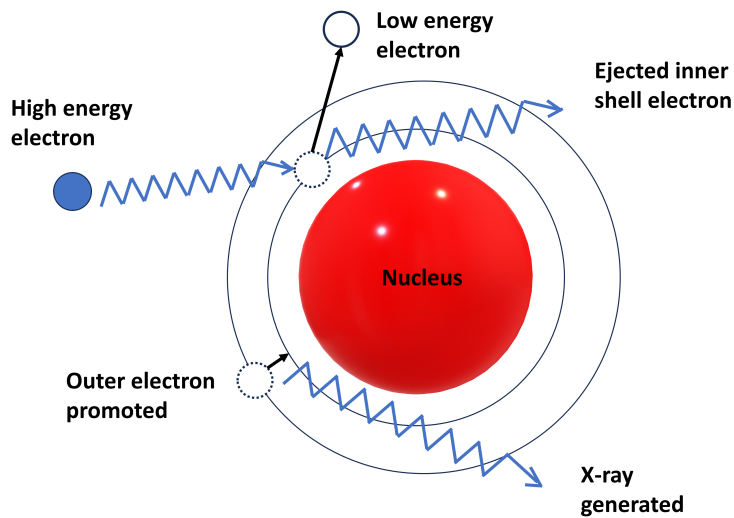


Figure 3.6: Characteristic X-ray generation.

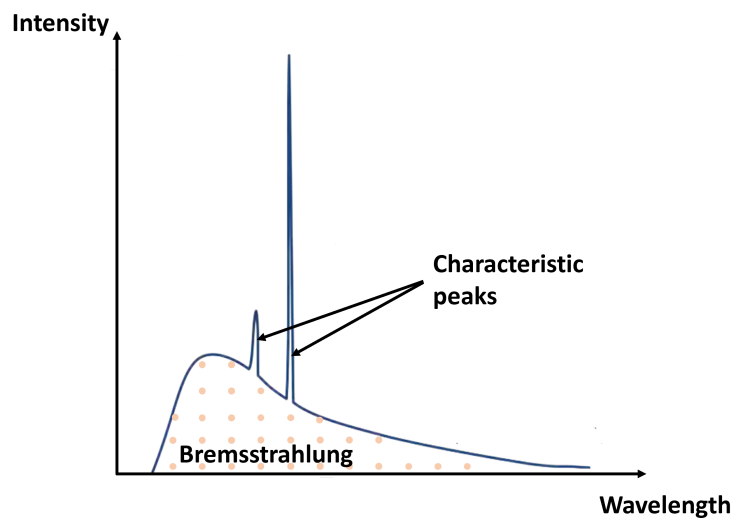


Figure 3.7: Example of an X-ray spectrum generated by an X-ray tube: bremsstrahlung and characteristic peaks.

3.1.2 X-ray Transmission

After emanating from the tube, X-ray photons pass through the imaged object (patient in medical imaging) and, depending on their energy, five different interaction mechanisms with matter may occur. Three interactions are of particular interest in medical imaging: the Compton effect, the photoelectric effect, and the Rayleigh effect. These are illustrated in Figure 3.8 and are briefly described in the following section.

3.1.2.1 Interaction Mechanisms

Compton scattering

Compton scattering happens when an X-ray photon interacts with a loosely bound electron of the outer shell of the atom. In this case, the electron is released and the atom is ionized. As for the X-ray photon, it does not use up all its energy, but it is scattered in a different direction with less energy. Both the ejected Compton electron and the scattered photon may have enough energy left and can cause a cascade of interactions with the matter they encounter. While the scattered photon has no useful information on the radiograph, it has a great impact on the image and reduces the contrast. The photon can be scattered in any direction, when it is scattered back in the same direction, it is called 'back scatter' and it is the primary source of radiation exposure to radiologists. The likelihood of Compton scatter is inversely proportional to the energy of the X-ray, however, unlike photoelectric absorption, it is independent of the atomic number of the material.

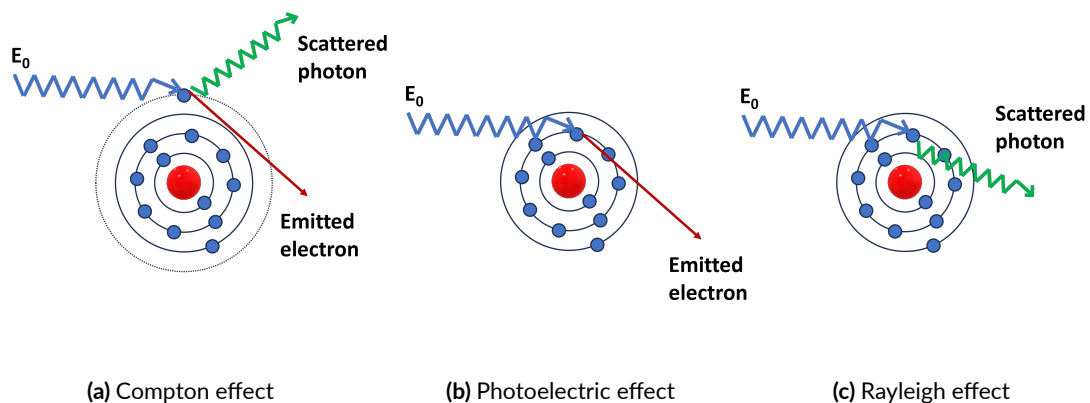


Figure 3.8: X-ray photon interaction mechanisms with matter.

Photoelectric effect

The photoelectric effect occurs when the incident X-ray photon interacts with an electron of the inner shell of the atom. The incident photon completely disappears after transferring all its energy to the electron. Once the electron is kicked off its parent atom, it travels through the material as a photoelectron, the atom is ionized, and a vacancy in one of its electron shells is created. An outer shell electron fills in the inner shell void resulting in the production of characteristic radiation as described in Section 3.1.1. This low-energy secondary radiation does not travel far before being attenuated, it is absorbed locally in adjacent tissue and has no effect on X-ray images. The likelihood of photoelectric absorption depends on the atomic number of the material. The higher the effective atomic number, the greater is the X-ray

3. Technical Background

absorption. Hence, bone structures present greater absorption than fat structures and appear lighter in X-ray images. Moreover, the probability of photoelectric absorption decreases with increasing energy of the X-rays.

Rayleigh scattering

Rayleigh scattering, also referred to as coherent scattering, mostly occurs when a low-energy incident X-ray photon interacts with the whole atom and causes it to be excited. Since the energy of the incident photon is less than the binding energy of the electrons, no electron is emitted and ionization does not occur. The photon is deflected from its original path conserving its incident energy. Compared to Compton scattering, Rayleigh scattering has little effect on the image. However, it cannot be disregarded in mammography and digital breast tomosynthesis, particularly as these techniques employ low energy X-rays to enhance soft tissue contrast.

3.1.2.2 Attenuation Coefficients

The combination of all three X-ray interaction mechanisms described above contributes to the **attenuation** of the incident X-ray beam. Attenuation is defined as the total reduction in number of X-ray photons from the incident X-ray beam by either absorption or scattering after passing through tissues. It mainly depends on three factors:

- the density and chemical composition of the material being radiographed
- the thickness of the material
- the energy of the X-ray beam, determined by the applied voltage of the X-ray equipment

Let us consider a beam, with an incident intensity of I_0 and its rays having the same energy E , is passing through a homogeneous thin slab of material of thickness x and attenuation coefficient μ (Figure 3.9). The attenuation of the rays after passing through the object is approximated as an exponential process and is given by

$$I = I_0 e^{-\mu(E)x} \quad (3.5)$$

where I is the intensity transmitted through the matter of thickness x . μ is the combined linear attenuation coefficient from all the interaction mechanisms, i.e.,

$$\mu(E) = \mu_{photoelectric}(E) + \mu_{Compton}(E) + \mu_{Rayleigh}(E) \quad (3.6)$$

This exponential decay relationship is referred as Beer–Lambert law.

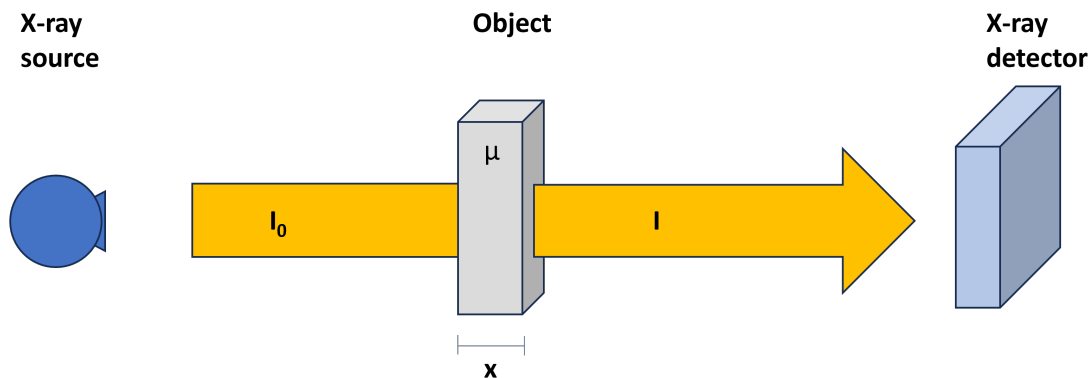


Figure 3.9: Mathematical model of X-ray attenuation.

$\mu(E)$ represents how much the radiation is attenuated per unit thickness of the tissue. From equation 3.5, one can observe that the higher the linear attenuation coefficient is, the more the radiation is attenuated. Moreover, as the radiation travels deeper into the body, it encounters more tissue, leading to greater attenuation. $\mu(E)$ depends on the energy of the X-ray beam and on the medium material as well. At the same photon energy, distinct materials have different attenuation coefficients. A mass attenuation coefficient k can be defined as

$$k = \frac{\mu}{\rho} \quad (3.7)$$

where ρ is the material density. Figure 3.10 shows the mass attenuation coefficients for bone and lung tissues as functions of the X-ray energy.

In X-ray imaging, the goal is to estimate the map of attenuation coefficients of the imaged object.

3.1.3 X-ray Detection

After passing through and interacting with the patient, X-rays transmitted or scattered are captured using X-ray detection systems. These systems convert the X-ray signal into an actual radiograph. A class of advanced X-ray detection systems widely used nowadays are flat panel detectors (FPD). They are used in various medical imaging modalities, including radiography, fluoroscopy, and CT. They have largely replaced traditional film-based imaging systems and image intensifiers due to their higher image quality, faster image acquisition, and digital capabilities. A FPD consists of a flat thin panel containing an array of detector elements that convert X-ray photons into digital signals, enabling the creation of high-resolution digital images.

3. Technical Background

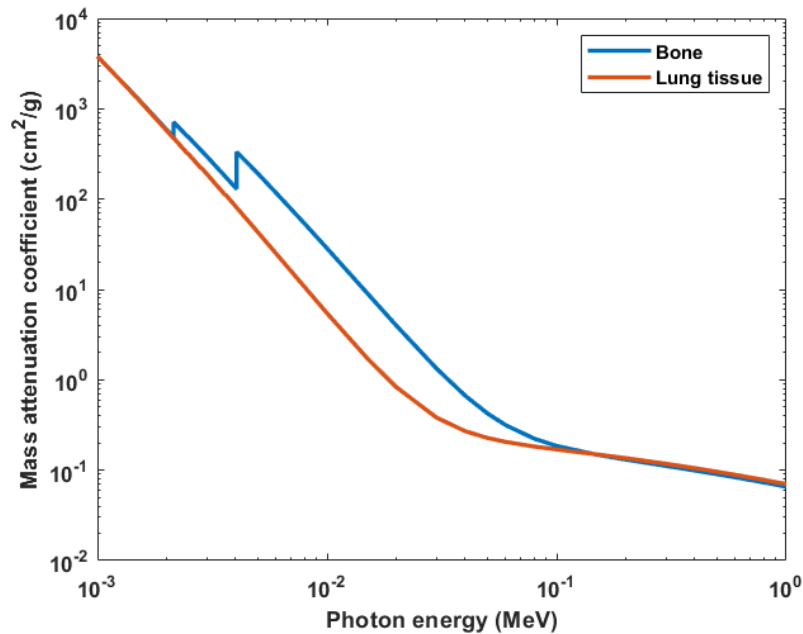


Figure 3.10: Typical profile for the mass attenuation coefficient for bone and lung tissue as a function of X-ray energy. Data source: NIST database [66].

3.1.4 X-ray Applications

Several are the imaging modalities that use X-rays. Some of the key applications include:

Projective Radiography

Projective radiography (PR) refers to the process of creating 2D projection images of the anatomy by passing an X-ray beam through the patient and measuring the attenuation it undergoes through absorption or scattering by the internal structures. The resulting image is often called a radiograph or X-ray image. Radiography is widely prevalent in the field of medicine with X-ray machines being present in the majority of urgent care facilities, hospitals, emergency rooms, and orthopedic surgery clinics. It is applied in various examinations and procedures where there is a need to capture a static image. One of the main applications is the examination of bone fractures. Since bones possess high attenuation coefficients compared to their surrounding soft-tissues, radiographs are able to provide a clear image of the bone and assess the severity of the fracture. Other application examples include: dental examination, mammography, confirmation of accurate placement of surgical markers before invasive interventions, and diagnosis of lung conditions such as pneumonia, emphysema, and lung cancer. In Figure 3.11, a chest PR image showing a large lesion in the right lung lobe of the patient is depicted.



Figure 3.11: Chest X-ray image showing a lesion in the right lung lobe of the patient.

Fluoroscopy

Unlike radiography which produces static images, fluoroscopy involves the use of X-rays to create real-time images of moving internal structures of the body. X-rays are emitted in a pulsed or continuous fashion, and the detector captures the X-rays that pass through the patient's body. The visible light images are displayed on a monitor in real time. Fluoroscopy is particularly useful in image-guided minimally invasive interventions such as angiography, cardiac catheterization, and navigational bronchoscopy. It provides real-time guidance to the physician for an accurate placement of catheters, stents, biopsy tools, and other medical devices without being in direct visual contact with the target region. Fluoroscopy images are generally of much lower quality than conventional radiographs in order to limit the patient's overall exposure to radiation. Figure 3.12 (a) shows an image example from a fluoroscopy sequence taken during a navigational bronchoscopy procedure. During minimally invasive surgeries, fluoroscopy images are often acquired using C-arm CBCT devices where the X-ray source and the detector are mounted on a C-shaped arm and rotated around the patient. Figure 3.12 (b) illustrates an example of a typical C-arm CBCT scanner that can be used in minimally invasive interventions and can be freely positioned around the patient.

Computed tomography

Besides 2D projective images, X-rays can be used to provide 3D volumetric images of the patient. CT is an X-ray imaging technique that yields a stack of detailed cross-sectional views of the patient presented as a collection of slice images. In CT, a set of 2D projection images are acquired from different angles and are reconstructed using dedicated reconstruction algorithms. CT scans are used to diagnose a variety of medical conditions, such as tumors, fractures, infections, and vascular diseases. They provide detailed information about the location, size, and characteristics of abnormalities. Moreover, CT images are valuable for planning surgical procedures, radiation therapy, and other interventions. While CT offers detailed imaging, it involves exposure to ionizing radiation, which can carry potential risks. Figure 3.13

3. Technical Background

shows image examples of axial, coronal, and sagittal slices from a chest CT scan.

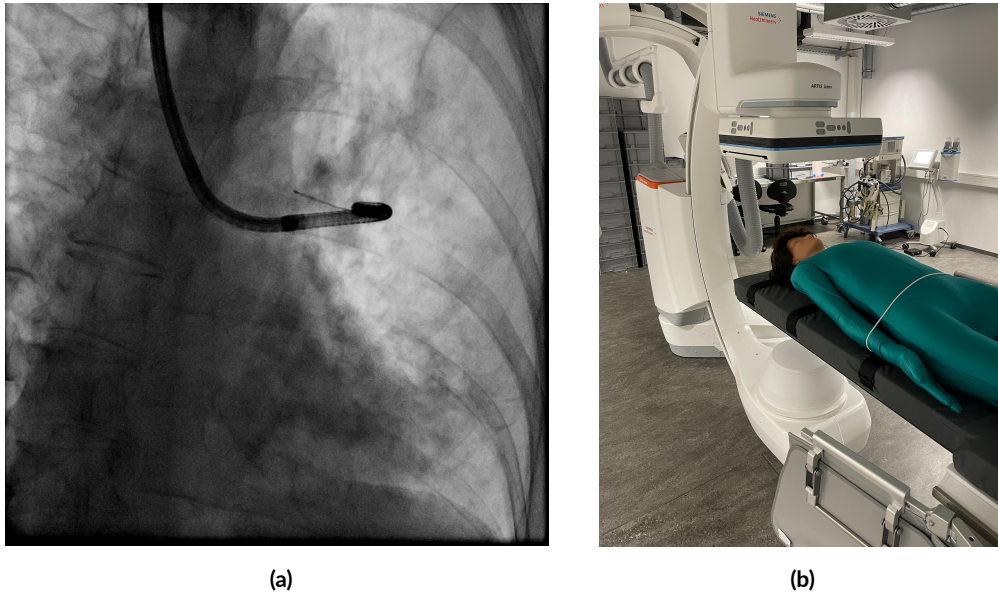


Figure 3.12: (a) Image example from a fluoroscopic sequence taken during a navigational bronchoscopy intervention. (b) Example of a typical C-arm scanner used in minimally invasive interventions.

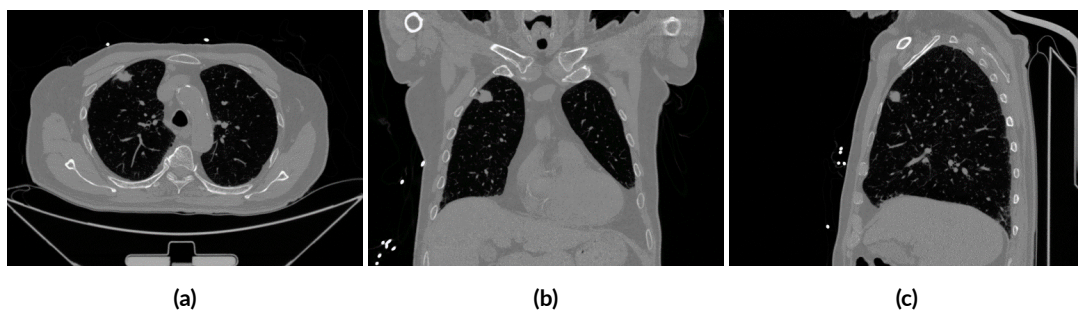


Figure 3.13: Axial (a), coronal (b), and sagittal (c) slice images of a chest CT scan.

3.1.5 Image Reconstruction

Having introduced in the previous sections the processes of X-ray generation, X-ray transmission, and X-ray detection, we cover in this section the fundamentals of image reconstruction. Image reconstruction denotes the process of producing a tomographic image from projections. Any reconstruction algorithm requires as input data the projection images and some related imaging geometry information, and provides a 3D volume as output data. Before

presenting the common reconstruction algorithms, we introduce first some mathematical foundations which are keys for image reconstruction.

3.1.5.1 Radon Transform

Radon transform is the core mathematical principle of image reconstruction. Laid down by the Austrian mathematician Johann Radon, its concept states that any function $f(x, y)$ can be recovered from its linear integrals over all possible lines in a given space. Let us consider a two dimensional object $f(x, y)$ defined on a certain Cartesian system (Figure 3.14) and let us define the line l lying at a distance s from the origin and forming an angle θ between its normal vector and the x-axis (Figure 3.15).

$$\forall M(x, y) \in (l) : \begin{cases} x_M = s \cos \theta \\ y_M = s \sin \theta \end{cases} \quad (3.8)$$

To find out the equation of l in polar coordinates s and θ , let us compute $x_M \cos \theta + y_M \sin \theta$. Using equation 3.8,

$$\begin{aligned} x_M \cos \theta + y_M \sin \theta &= s \cos^2 \theta + s \sin^2 \theta \\ &= s (\cos^2 \theta + \sin^2 \theta) \\ &= s \end{aligned}$$

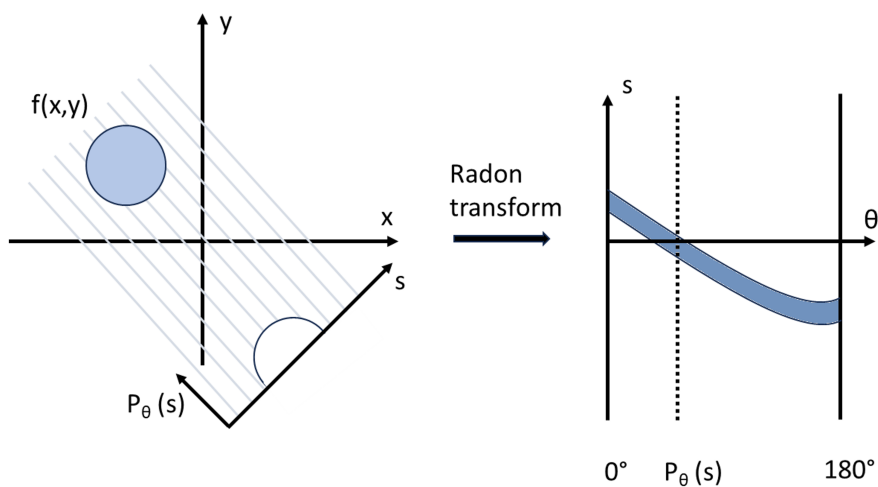


Figure 3.14: Illustration of the Radon transform and the formation of the sinogram.

3. Technical Background

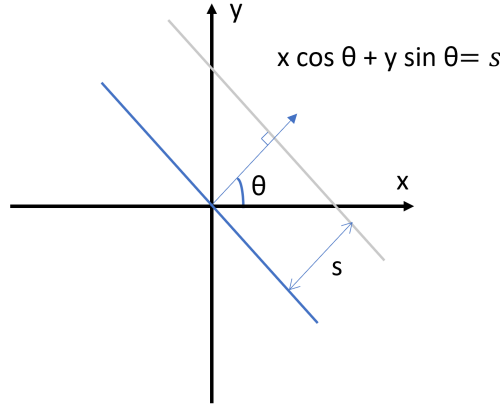


Figure 3.15: Line integral definition.

Hence, a unique representation of l in polar coordinates is given by

$$s = x \cos \theta + y \sin \theta \quad (3.9)$$

The Radon transform of $f(x, y)$ along a line l is defined as

$$p(\theta, s) = \iint_{-\infty}^{+\infty} f(x, y) \delta(x \cos \theta + y \sin \theta - s) dx dy \quad (3.10)$$

where $\delta(t)$ is the Dirac function defined as

$$\delta(t) = \begin{cases} 1, & \text{if } t=0 \\ 0, & \text{otherwise} \end{cases} \quad (3.11)$$

Equation 3.10 represents the line integral of $f(x, y)$ evaluated along the line l . It defines the transformation relating the 2D object $f(x, y)$ to the 1D projection $p(\theta, s)$. Computing $p(\theta, s)$ for all the angles $\theta \in [0^\circ, 180^\circ]$ and distances $s \in [-\infty, +\infty]$ provides the complete set of line integrals and builds the Radon transform. For a fixed angle θ , $p_\theta(s)$ is a one-dimensional function and represents one projection of $f(x, y)$. The combination of all projections side-by-side as a 2D image forms a sinogram (Figure 3.14). In tomographic image reconstruction, the goal is to find $f(x, y)$ from its line integrals $p(\theta, s)$. In other terms, we aim to compute the inverse Radon transform.

3.1.5.2 Fourier Slice Theorem

The Fourier slice theorem is the foundation of tomography. It establishes a relationship between an image and its projections in the Fourier domain. Let $P(w, \theta)$ be the 1D Fourier

transform of $p_\theta(s)$,

$$P(w, \theta) = \int_{-\infty}^{+\infty} p_\theta(s) e^{-2\pi i w s} ds \quad (3.12)$$

Substituting $p_\theta(s)$ by its expression from equation 3.10, we obtain

$$P(w, \theta) = \int_{-\infty}^{+\infty} \int_{-\infty}^{+\infty} f(x, y) \delta(x \cos \theta + y \sin \theta - s) dx dy e^{-2\pi i w s} ds \quad (3.13)$$

Interchanging the order of integration leads to

$$P(w, \theta) = \iint_{-\infty}^{+\infty} f(x, y) \int_{-\infty}^{+\infty} \delta(x \cos \theta + y \sin \theta - s) e^{-2\pi i w s} ds dx dy \quad (3.14)$$

Eliminating the delta function yields

$$P(w, \theta) = \iint_{-\infty}^{+\infty} f(x, y) e^{-2\pi i w (x \cos \theta + y \sin \theta)} dx dy \quad (3.15)$$

Let $u = w \cos \theta$ and $v = w \sin \theta$, performing a variable substitution leads to

$$P(w, \theta) = \iint_{-\infty}^{+\infty} f(x, y) e^{-2\pi i (x u + y v)} dx dy \quad (3.16)$$

Hence

$$P(w, \theta) = F(w \cos \theta, w \sin \theta) \quad (3.17)$$

where $F(u, v)$ denotes the 2D Fourier transform of $f(x, y)$. This equation is the mathematical derivation of the Fourier slice theorem. In 2D, it states that the 1D Fourier transform $P(w, \theta)$ of the projection $p_\theta(s)$ of a 2D function $f(x, y)$ is equal to the 2D Fourier transform $F(u, v)$ of $f(x, y)$ along a radial line through the origin at angle θ . An illustration of this relation is shown in Figure 3.16. Measuring the complete set of projections provides a measure of the entire 2D Fourier transform $F(u, v)$. The original function $f(x, y)$ can be obtained by 2D inverse Fourier transform of $F(u, v)$.

3.1.5.3 Analytic Reconstruction

The aim of reconstruction algorithms is to find a 3D volume that spatially models the linear attenuation coefficients of the imaged material. The 3D imaged volume is generated by reconstructing a stack of 2D axial slices at slightly shifted positions. The unknown function

3. Technical Background

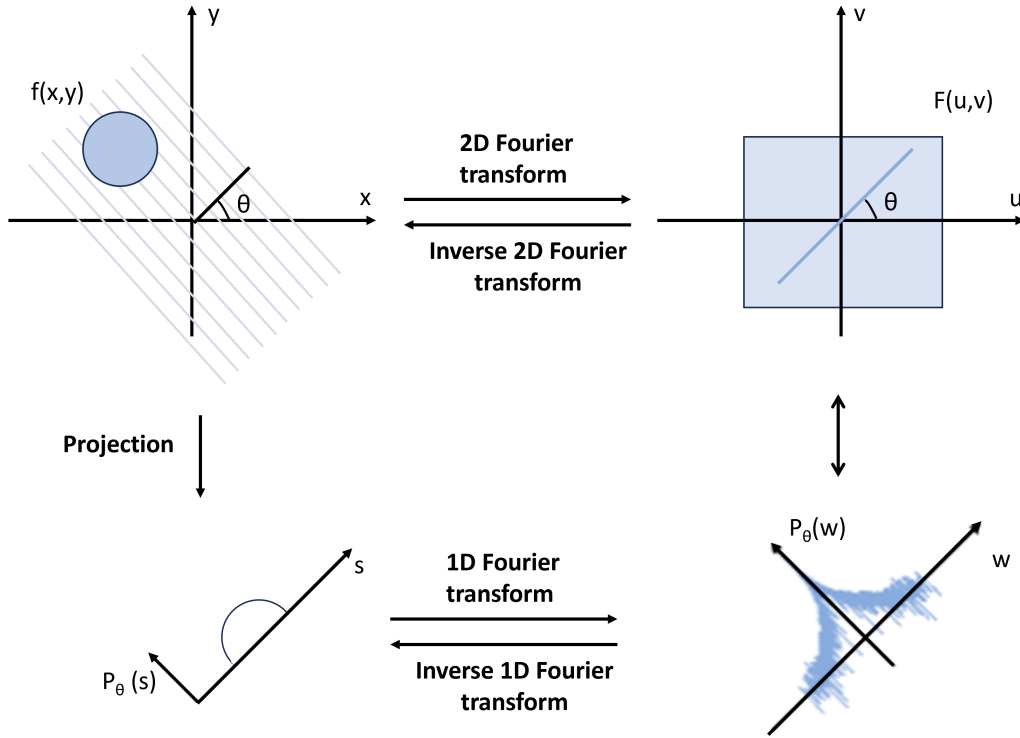


Figure 3.16: Illustration of the Fourier slice theorem.

$f(x, y)$ represents one axial slice. Its values correspond to the linear attenuation coefficients of the imaged material.

Image reconstruction methods can generally be categorized into two broad groups: analytic and algebraic. Analytic reconstruction methods rely on mathematical principles such as the Radon transform and the Fourier slice theorem. The most common analytic reconstruction method is the filtered backprojection (FBP). As stated in the previous section, $f(x, y)$ can be obtained by inverse Fourier transform of $F(u, v)$. The inverse Fourier transform of $F(u, v)$ is given by

$$f(x, y) = \iint_{-\infty}^{+\infty} F(u, v) e^{2\pi i(ux+vy)} du dv \quad (3.18)$$

Writing this equation in polar coordinates by substituting $u = w \cos \theta$ and $v = w \sin \theta$ and performing a change in integration variables from (u, v) to (w, θ) leads to

$$f(x, y) = \int_0^\pi \int_{-\infty}^{+\infty} F(w, \theta) e^{2\pi i w(x \cos \theta + y \sin \theta)} |\det(J)| dw d\theta \quad (3.19)$$

where $|\det(J)|$ is the absolute value of the determinant of the transformation's Jacobian

transform.

$$\begin{aligned} |\det(J)| &= \left| \det \left(\begin{bmatrix} \frac{\partial u}{\partial w} & \frac{\partial u}{\partial \theta} \\ \frac{\partial v}{\partial w} & \frac{\partial v}{\partial \theta} \end{bmatrix} \right) \right| = \left| \det \left(\begin{bmatrix} \cos \theta & -w \sin \theta \\ \sin \theta & w \cos \theta \end{bmatrix} \right) \right| \\ &= |w \cos^2 \theta + w \sin^2 \theta| = |w| \end{aligned} \quad (3.20)$$

Substituting $|\det(J)|$ by its value in equation 3.19 yields

$$f(x, y) = \int_0^\pi \int_{-\infty}^{+\infty} F(w, \theta) |w| e^{2\pi i w(x \cos \theta + y \sin \theta)} dw d\theta \quad (3.21)$$

Using the Fourier slice theorem, equation 3.21 can be written as

$$f(x, y) = \int_0^\pi \int_{-\infty}^{+\infty} P(w, \theta) |w| e^{2\pi i w(x \cos \theta + y \sin \theta)} dw d\theta \quad (3.22)$$

Replacing $x \cos \theta + y \sin \theta$ by s , we obtain

$$f(x, y) = \int_0^\pi \int_{-\infty}^{+\infty} P(w, \theta) |w| e^{2\pi i w s} dw d\theta \quad (3.23)$$

Multiplication of $P(w, \theta)$ by $|w|$ represents a filtering operation by a ramp filter. According to the Fourier transform theory, multiplication in the frequency domain corresponds to a convolution in the spatial domain, hence, equation 3.23 can be written in spatial domain as

$$f(x, y) = \int_0^\pi p_\theta(s) * h(s) d\theta \quad (3.24)$$

where $h(s)$ is the inverse Fourier transform of $|w|$. Thus, finding $f(x, y)$ amounts to backprojecting $p_\theta(s)$ convolved with $h(s)$. This is the principle of the FBP reconstruction method.

3.1.5.4 Algebraic Reconstruction

Instead of analytically reconstructing the image, algebraic reconstruction algorithms solve the reconstruction problem numerically using linear algebra and matrix theory. They model the reconstruction problem as a system of linear equations and tend to invert it and approach the solution. Each linear equation sums up one projection ray and the image pixels it passes through and equalizes it to the measured data. Hence, this system can be modeled as

$$p = Af \quad (3.25)$$

where $p = (p_1, p_2, \dots, p_m)^T \in \mathbb{R}_+^m$ and $f = (f_1, f_2, \dots, f_n)^T \in \mathbb{R}_+^n$ are respectively the measured line integrals and the unknown image pixels numbered sequentially and modeled as

3. Technical Background

vectors in a multidimensional domain. $A \in \mathbb{R}_+^{m \times n}$ is the geometry matrix where each of its elements a_{ij} indicates the weight of the contribution of a particular pixel f_j to a particular detector reading p_i . Many are the possibilities to model A . The most straightforward method is to set a_{ij} to 1 when the ray passes through the pixel and 0 otherwise. Other models include the length of the intersection segment of the projection ray and the pixel, or the area of intersection if the rays are assumed to have non trivial thickness. Figure 3.17 illustrates an example of an image grid and a set of projection rays. If the matrix A is invertible and well-

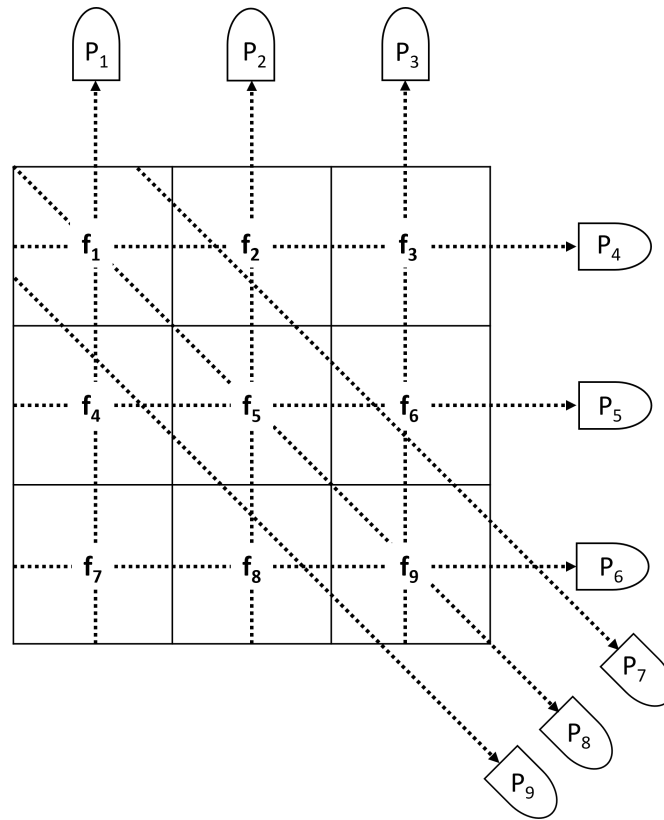


Figure 3.17: Example of an image grid and some projection rays.

conditioned, the unknown image f can be found by direct matrix inversion (e.g., by singular value decomposition). However, this does not hold in tomography problem. Tomographic reconstruction is a typical case of an ill-posed inverse problem in the sense of Hadamard [67], insofar as at least one of the following three conditions is violated:

1. Existence of the solution
2. Uniqueness of the solution
3. Stability of the solution

To solve this linear system of equations, a whole family of iterative reconstruction methods has been developed. The core idea of such methods is to proceed iteratively and make an estimate of the imaged object, perform a projection operation on the estimate, compare the

real projected data with the simulated data, smear the data residual back through the subject volume, and then generate a new estimate. The basic algebraic reconstruction algorithm is the algebraic reconstruction technique (ART), known as Kaczmarz method as well. It updates the estimate of the solution by focusing on one equation at a time. Its fundamental concept revolves around associating each linear equation with a line (in 2D) or a hyperplane (in higher dimensions) within the solution space. The hyperplane's dimension corresponds to the number of unknowns. Any point situated on a hyperplane satisfies its respective equation. Consequently, the accurate solution of the problem is formed at the intersection point of all these hyperplanes. By consistently projecting the current estimate orthogonally onto a plane defined by a different equation, the solution is progressively refined through iterations. For an intuitive explanation of ART, let us consider the following linear system of two equations with two unknown independent variables f_1 and f_2

$$\begin{pmatrix} p_1 \\ p_2 \end{pmatrix} = \begin{pmatrix} a_{11} & a_{12} \\ a_{21} & a_{22} \end{pmatrix} \begin{pmatrix} f_1 \\ f_2 \end{pmatrix} \quad (3.26)$$

Each row of this linear system represents an equation describing a line as illustrated in Figure 3.18. The solution of the linear system is the intersection of the lines. ART involves starting with an initial guess f^0 of the solution, then alternately projecting the current solution estimate onto each line until feasible estimate for the volume f is found or a certain criteria for the residual error is fulfilled.

A single update step of ART is given by

$$f^{k+1} = f^k + \frac{p_j - a_j f^k}{a_j a_j^T} a_j^T \quad (3.27)$$

where a_j denotes the j^{th} row of the system matrix A and k is the number of the current iteration. This update equation states that the updated estimate at iteration $k + 1$ is equal to the current estimate at iteration k plus the backprojection of the error of the current estimation. The error of the current estimation is the difference between the measured data and the estimated data at iteration k . A computational concern with ART is its slow convergence where many steps at each iteration need to be applied to get a good solution. To address this limitation, many variations of ART have been developed, among which is the simultaneous algebraic reconstruction technique (SART). While ART updates the estimate one projection at a time, SART updates the estimate using a weighted combination of all projections, aiming to balance convergence speed and accuracy. The update step of SART is expressed as

$$f^{k+1} = f^k + \lambda_k \sum_j w_{k,j} \frac{p_j - a_j f^k}{a_j a_j^T} a_j^T \quad (3.28)$$

3. Technical Background

with

$$\sum_j w_{k,j} = 1 \quad (3.29)$$

λ_k are the relaxation parameters included at each iteration to control the step size and improve the convergence.

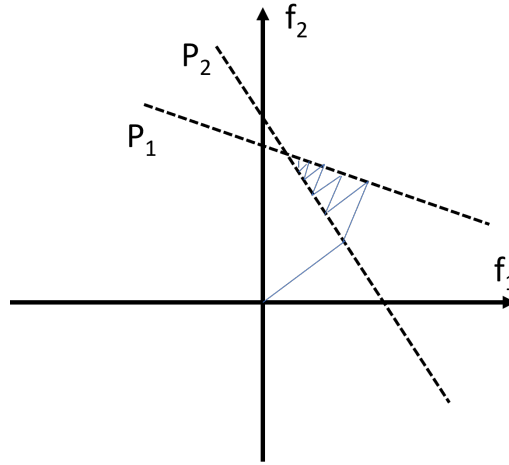


Figure 3.18: Schematic of the ART cycle.

3.2 Digital Tomosynthesis: From Data Acquisition to Image Formation

DTS is a quasi-3D X-ray imaging modality halfway between conventional projective radiography (PR) and CT in its imaging performance. It is a form of limited angle tomography that renders section images of the imaged object from a discrete series of projection images acquired over a restricted angular range. Compared to PR, DTS introduces depth information to the X-ray radiographic image with a scant increase in radiation dose. Its ability of depth localization improves the conspicuity of subtle structures and distinguishes them from the overlying anatomy. Unlike CBCT and due to the limited angle acquisition, the resolution in the resulting tomosynthesis images is not isotropic. More precisely, DTS exhibits poor resolution in image planes perpendicular to the detector surface. Figure 3.19 portrays a posterior-anterior PR image (Figure 3.19 (a)), a coronal CBCT slice (Figure 3.19 (b)), and a coronal DTS slice (Figure 3.19 (c)) of a patient. The CBCT and DTS slices are shown at a similar position. These patient images are acquired intraoperatively during a bronchoscopy intervention. As can be observed, it is difficult to discern the target lesion in the PR image as it is hidden by the overlapping ribs. However, the DTS slice shows clearly the target lesion.

3.2. Digital Tomosynthesis: From Data Acquisition to Image Formation

The low depth resolution of DTS is evident from the apparent ribs insufficiently blurred and showing up in this slice where they should not be present in as confirmed by the CBCT slice.

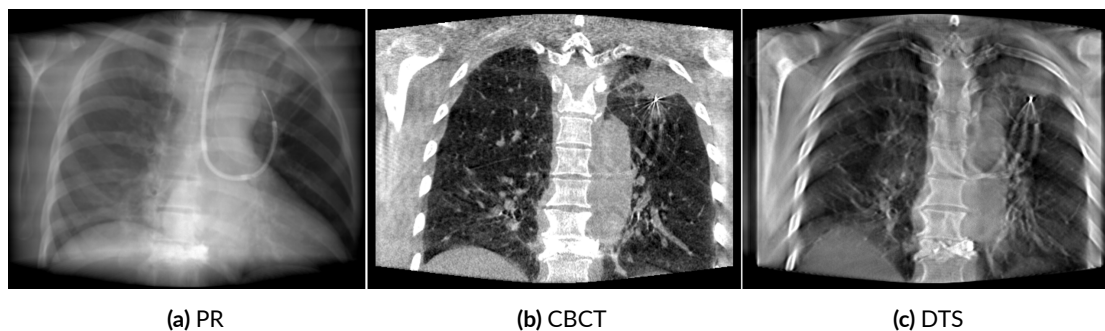


Figure 3.19: Patient chest images acquired during a bronchoscopy intervention. Comparison of a posterior-anterior PR image (a), a coronal CBCT slice (b), and a coronal DTS slice (c). The CBCT and DTS slices are shown at a similar position.

The development of DTS imaging has gone through several stages over the last nine decades. In the following section, we cover the genesis of DTS highlighting its historical milestones and current status.

3.2.1 History of Tomosynthesis

It was in 1917 when Radon published his famous paper laying the mathematical foundation of tomography [68] which enables the visualization of slices internal to an object. With early geometric tomography systems, it was possible to generate only one slice from a single acquisition sequence. To render volumetric data, several acquisitions had to be performed. This was impractical in many examinations due to the time needed to acquire data and the potential exposition of the patient to high radiation levels. Widely acknowledged for pioneering tomosynthesis, the Dutch electrical engineer and neuroradiologist Ziedses des Plantes patented in 1936 a radiographic technique, which he initially referred to as 'seriescopy', that enables the sequential visualization of an infinite series of parallel planes from a single acquisition procedure [69, 70]. While he proved it possible in theory, it took until 1969 for the full implementation of Ziedses des Plantes' theoretical framework to see the light. Garisson et al. constructed a prototype system 'three-dimensional roentgenography', successfully generating a full 3D dataset from a single radiographic acquisition [71]. Shortly after, in 1971, Miller et al. developed a rapid film changer tomosynthesis system and referred to it as 'photographic laminography' [72]. In 1972, Grant built a prototype 3D image projector using a circular image acquisition geometry and he first coined the term 'tomosynthesis' to describe the ability to retrospectively generate an infinite number of arbitrary tomograms [73].

3. Technical Background

One of the notable limitations of Miller's and Grant's devices is the need to change the film between each projection acquisition, resulting in a lengthy and inconvenient imaging procedure in most clinical applications. To shorten the film-based tomosynthesis procedure time, a number of variants have been developed. An interesting tomosynthesis technique of the past is coded aperture imaging developed by Klotz and Weiss from Philips GmbH, Hamburg, Germany, in the 1970s [74–76]. It enables the generation of arbitrary tomosynthesis planes within a matter of milliseconds, making it effective to scan organs prone to motion. Many investigators described coded aperture tomosynthesis under different names, 'short-time tomosynthesis' [75], 'flashing tomosynthesis' [77–82] and 'tomoscopy' [83]. The main concept is to use multiple X-ray sources arranged in a fixed geometry and pulsed either sequentially or simultaneously (Figure 3.20). A single film captures the complete set of sub-images, forming the coded image. Summing a series of shifted versions of the coded image enables the reconstruction of an arbitrary plane within the object. Of the acknowledged drawbacks of this technique is the need to select the distribution of the X-ray sources in a way to avoid the overlapping of the sub-images, otherwise additional tomographic blur adds to the reconstructed image on top of the blur inherent in tomosynthesis images. A wealth of papers have been published on coded aperture tomosynthesis [77–82, 84–87]. This technique proved to be particularly successful in angiography procedures where the superimposition of low contrast structures of the sub-images does not mask the visibility of high contrast vasculature of interest filled with contrast agent.

A significant obstacle in the advancement of tomosynthesis was the lack of appropriate digital detectors to store the acquired projection images. In the work of Dobbins et al. [90], screen-film projection images were acquired, followed by digitization and processing to gener-

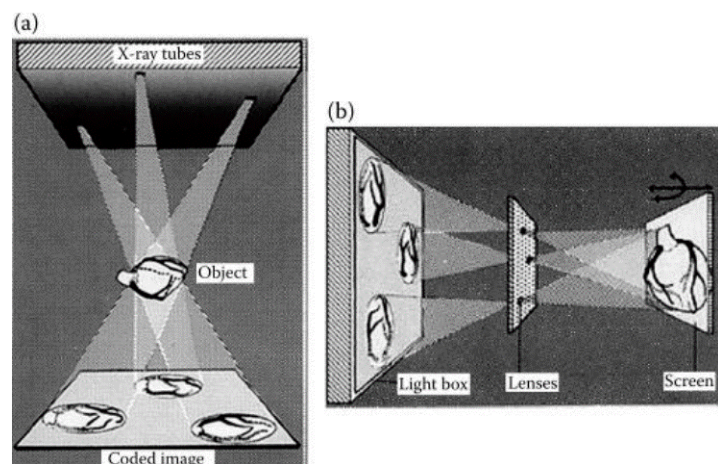


Figure 3.20: Coded aperture tomosynthesis system [88]. Source: I. Reiser and S. Glick (eds), *Tomosynthesis Imaging*, Taylor and Francis Group, 2014 [89].

3.2. Digital Tomosynthesis: From Data Acquisition to Image Formation

ate digital projection images. However, film digitization is time consuming and clinically impractical. Another attempt to shorten the acquisition time of tomosynthesis imaging procedure was the use of image intensifier-TV camera detectors providing high frame rates and improved contrast at low radiation dose [83, 91–98]. The main drawback of image intensifier-based tomosynthesis systems is the geometric distortion, specifically pin cushion distortion, resulting from less effective electron focusing within the image intensifier towards the periphery of the image.

The lack of suitable distortion-free digital detectors for tomosynthesis on one hand, and the advent and popularity of CT in the late 1980s on the other hand, led to a marked interruption in tomosynthesis research and development for about a decade. However, with the introduction of digital FPD in the late 1990s providing high detective quantum efficiency and rapid readout rates, and with the emergence of cost-effective computing power, a renewed interest in tomosynthesis research has risen among investigators. Ever since, digital detector-based tomosynthesis has been applied to a wealth of clinical imaging tasks with the most attention received by breast imaging [99–106] and chest imaging [63, 107, 108].

For a detailed review on the genesis of tomosynthesis the interested reader is encouraged to refer to [89].

3.2.2 History of Tomosynthesis Reconstruction Methods

Unlike CT, in tomosynthesis imaging, only a limited angle is swept out during the acquisition process. This incomplete data acquisition poses a challenge to the reconstruction algorithm. The reconstructed tomosynthesis slices are usually deteriorated with image artifacts manifesting as residual blur of objects lying outside the plane of interest. In other words, each reconstructed tomosynthesis slice does not only contain structures of interest situated within the focal plane, but also incorporates blurred-out structures from every other plane, overlaid on the plane of interest. This residual blur reduces the in-plane contrast and masks subtle structures by the overlying anatomy. Various reconstruction techniques have been proposed with the aim of reducing the artifacts. These techniques can be classified into two categories:

1. **Analytical methods** (transform-based methods): shift-and-add (SAA), backprojection, tuned aperture CT, filtered backprojection, matrix inversion
2. **Iterative methods**: constrained iterative restoration, algebraic techniques, statistical reconstruction

These methods are briefly exposed in the following sections.

3. Technical Background

3.2.2.1 Shift-and-Add

SAA is one of the earliest tomosynthesis reconstruction algorithm which was applied first to film-based systems. As its name suggests, it involves shifting each projection image by a certain amount and then adding the shifted images together. The amount of shifting controls which plane is brought in focus while blurring out out-of-plane structures. Its concept is based on the fact that objects positioned at varying heights above the detector are projected onto different positions on the detector, depending on their relative heights. A simple demonstration of the SAA algorithm is illustrated in Figure 3.21. The figure depicts three X-ray projections acquired at three different positions, a circular object in **plane A** and a triangular object in **plane B**. The projected positions of the circle and the triangle on the detector as the X-ray source moves from position 1 to position 3 are shown in Figure 3.21 (a). Figure 3.21 (b) illustrates the shifted and added projection images to bring either the circle or the triangle in focus while smearing out the other object.

To get an insight on how do objects lying outside the in-focus plane contribute to the blur in the reconstructed tomosynthesis slice of interest, let us consider the imaging geometry depicted in Figure 3.22. Here, we assume that the X-ray tube and the detector are traveling linearly along the x-axis acquiring n projection images. The fulcrum plane around which both the detector and the tube move synchronously is positioned at height $z = z_f$ while the tube is located at height $z = D$ above the detector. At the first position of the tube $x = a_1$, the center of the detector is located at b_1 , such that

$$b_1 = \frac{-Da_1}{D - z_f} + a_1 = a_1(1 - m_f) \quad (3.30)$$

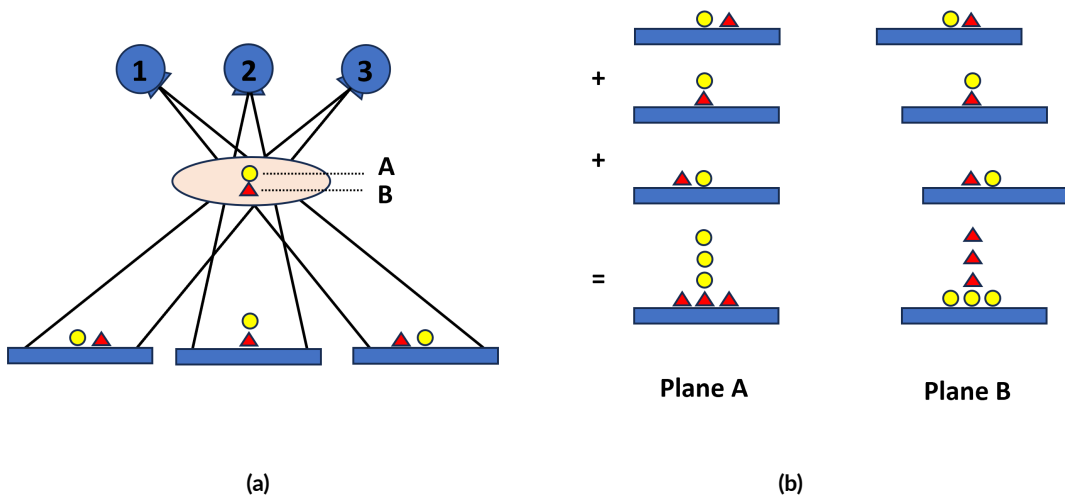


Figure 3.21: Principle of shift-and-add (SAA) tomosynthesis.

3.2. Digital Tomosynthesis: From Data Acquisition to Image Formation

with $m_f = \frac{D}{D-z_f}$.

If we project onto the detector a Dirac delta function located at $x = 0$ and at a height z , its projection location will be

$$x_1(z) = a_1(1 - m_z) \quad (3.31)$$

with $m_z = \frac{D}{D-z}$.

To bring the plane at height z into focus, one must shift the projection image by

$$shift_1(z) = -x'_1(z) = b_1 - x_1(z) = a_1(m_z - m_f) \quad (3.32)$$

Similarly, the k^{th} projection image must be shifted by

$$shift_k(z) = -x'_k(z) = b_k - x_k(z) = a_k(m_z - m_f) \quad (3.33)$$

Therefore, the tomosynthesis image of plane z when an impulse is located at $x = 0$ and height z' is given by

$$T_z(x', y) = \frac{1}{n} \sum_{k=1}^n \delta[x' - shift_k(z) - x'_k(z')] = \frac{1}{n} \sum_{k=1}^n \delta[x' - a_k(m_z - m_{z'})] \quad (3.34)$$

This equation explains how structures located at height z' contribute to the reconstructed tomosynthesis slice at height z . The reconstruction of this in-focus plane depends on the magnifications of the plane z' and the focal plane z , as well as on the relative spacing of the tube locations.

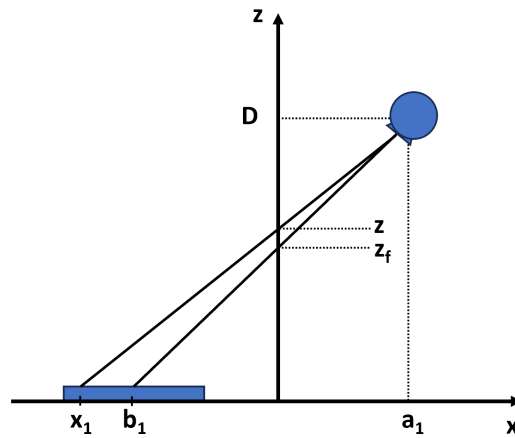


Figure 3.22: Illustration of a linear tomosynthesis imaging geometry.

Basically, SAA is equivalent to unfiltered backprojection. While it seems to be simple and

3. Technical Background

requires little computational effort, relying only on SAA to get high-quality tomosynthesis images is insufficient due to the overlapping blurred anatomical structures from outside the in-focus plane.

3.2.2.2 Tuned Aperture CT

One of the challenges encountered while aligning the structures after SAA shifting is patient motion. A slight movement of the patient during acquisition adds blur to the reconstructed tomosynthesis slice. To address this issue, Webber developed a method called tuned aperture CT (TACT) [100, 102]. It is basically a variant of SAA employing fiducial markers to register the projection images and account for patient motion. TACT has been implemented in many clinical applications including breast imaging [103, 105, 109], chest imaging [63], and dental imaging [110–113].

3.2.2.3 Deblurring Algorithms

In an attempt to separate blur from in-plane structures, many deblurring methods have been developed. Chief among them are **matrix inversion tomosynthesis** (MITS) and **FBP**. MITS utilizes linear algebra to address out-of-plane blur by leveraging the known blurring functions of all other planes during the reconstruction process of a particular plane [90, 107, 108, 114, 115]. MITS was shown to be fast and successful in solving the out-of-plane blur, however, it performed poorly with low-frequency information and exhibited sensitivity to noise [90, 107]. FBP, widely used in CT reconstruction, has been also applied to tomosynthesis. Compared to MITS, FBP performs better in terms of noise properties at low frequencies.

3.2.2.4 Iterative Methods

Another class of algorithms that have also been investigated in tomosynthesis reconstruction are iterative algorithms. Their potential advantage over analytical methods is the possibility to include prior information about the imaging system and the object to be reconstructed into the reconstruction algorithm, which stabilizes the reconstruction process and improves image quality. In 1984, Ruttimann et al. proposed the **constrained iterative restoration** approach which is similar to MITS in solving the tomographic blur by convolving a weighted fraction of the reconstructed planes with their blurring functions [103, 105, 111, 116, 117]. However, it tends to solve the equations iteratively rather than by matrix algebra as MITS. While this technique does not suffer from noise amplification at low frequencies like MITS, it is computationally more expensive. **Algebraic reconstruction methods** have been also adopted from

3.2. Digital Tomosynthesis: From Data Acquisition to Image Formation

CT for tomosynthesis reconstruction [118–120]. In the context of iterative approaches, **statistical reconstruction methods** using probabilistic models to estimate the image and incorporate noise statistics have been also investigated for tomosynthesis reconstruction [121]. Variants include maximum likelihood expectation maximization (MLEM) [122] and maximum likelihood with convex algorithm [106, 123]. An improved image quality was reported using such techniques over analytical methods, however, it is at the cost of significant computational costs. For a detailed review and comparison of tomosynthesis reconstruction algorithms, the interested reader is encouraged to refer to [123–125].

3.2.3 Data Acquisition

Image quality in DTS is mainly dependent upon contrast, noise, and image artifacts. The contrast depends on how well the overlying structures are blurred and the noise depends on the total dose of the acquisition. Structured noise, manifesting as out-of-plane structures in the DTS slices, is considered as image artifacts. Besides image reconstruction, system geometry is a critical factor affecting the image quality. In tomosynthesis imaging, the source and detector are mounted on gantries and one or both are moved relative to the patient. Several motion geometries have been developed and investigated for various tomosynthesis imaging applications, including:

- linear geometry
- pseudo-linear geometry (arc)
- circular geometry
- complex geometry (e.g., two orthogonal arcs, two orthogonal lines, sequence of zigzag lines, hypocycloidal motion)

The direction of motion highly impacts the visualization and blurring of out-of-plane artifacts. Usually, the more complex the source motion, the more effective is the blurring of out-of-plane structures. However, the more complex the motion becomes, the more mechanical constraints in building and maintaining the gantry arise.

To understand the motivation for moving from simple linear motion to more complex motion and before exploring a novel motion in the next chapter, we cover in this section the most common tomosynthesis motion profiles.

3.2.3.1 Linear Geometry

In the linear motion geometry, the X-ray tube moves in one plane parallel to the detector surface in a one dimensional profile. The detector may move in a linear path in opposite to the X-ray source (figure 3.23 (a)) or remain stationary (figure 3.23 (b)). This geometry is similar to conventional geometric tomography [126]. It is used in chest [92, 114] and abdominal [91] tomosynthesis imaging.

3. Technical Background

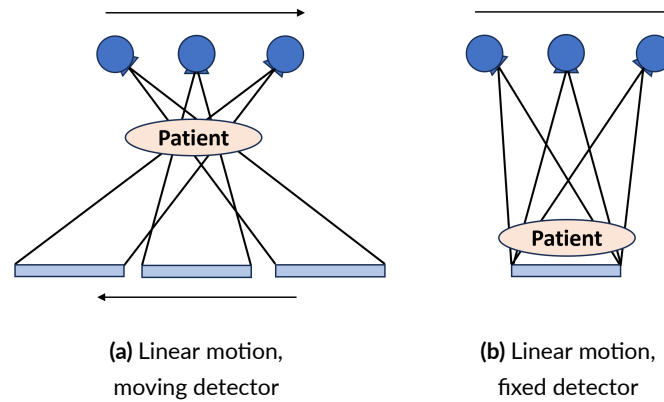


Figure 3.23: Linear tomosynthesis motion geometry. (a) Linear source motion, moving detector. (b) Linear source motion, fixed detector.

3.2.3.2 Pseudo-Linear Geometry

In the pseudo-linear geometry, the X-ray tube moves along an arc trajectory rotating about a fixed central point. Depending on the motion of the detector, this geometry can be full isocentric or partial isocentric. In the full isocentric case, the X-ray tube and the detector are locked rigidly to each other and rotate about a center of motion (Figure 3.24 (a)). In the partial isocentric case, the detector moves in a plane along a linear path (Figure 3.24 (b)) or remains stationary (Figure 3.24 (c)). The partial isocentric geometry is typically used in breast tomosynthesis imaging devices where the detector is fixed beneath the breast [99, 105]. The full isocentric motion is mainly investigated in radiation oncology applications and in image-guided interventions involving a C-arm device [64, 127]. Tomosynthesis imaging is used in such instances for patient positioning, for guiding the intervention, or to confirm tool-in-lesion.

3.2.3.3 Circular Geometry

In circular tomosynthesis, the X-ray source and the detector move in two different planes parallel to the detector surface, one above and one below the patient, along a circular path (Figure 3.25). This type of motion was introduced in early works on tomosynthesis [73] and can be easily implemented on a C-arm device. Circular motion was investigated in several medical applications such as cerebral perfusion imaging [128], breast imaging [129], and cervical spine imaging [129], as well as in industrial applications [130].

3.2.3.4 Complex Geometries

Besides the above described motion geometries, more complex motions have been proposed in the literature in an attempt to improve DTS image quality. Xia et al. proposed moving the

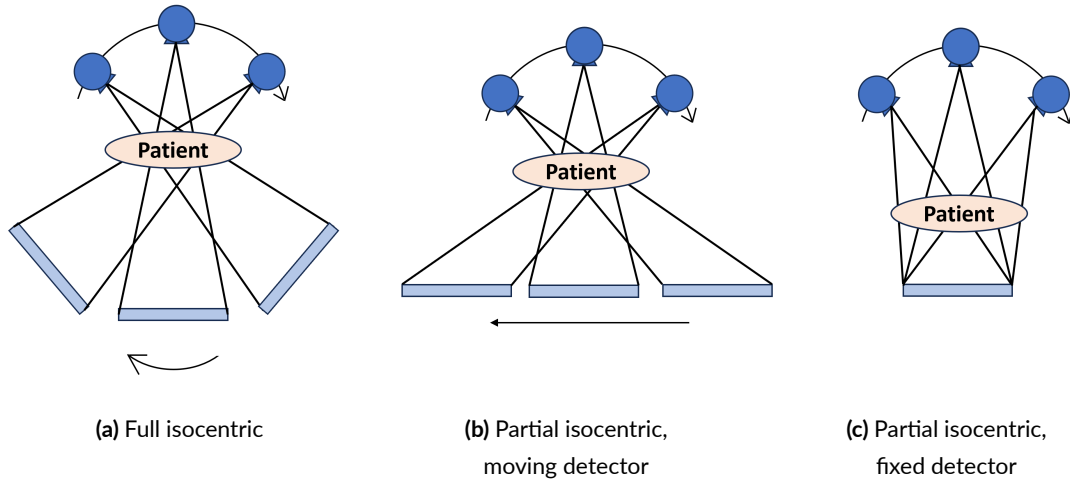


Figure 3.24: Pseudo-linear tomosynthesis motion geometry. (a) Full isocentric. (b) Partial isocentric, moving detector. (c) Partial isocentric, fixed detector.

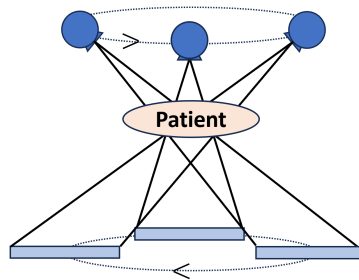


Figure 3.25: Circular tomosynthesis motion geometry.

X-ray source along two orthogonal arcs [131]. A motion formed by a sequence of zigzag lines on a spherical surface above the imaged object was presented by Zhang et al. [132]. Bleuet et al. proposed a cross trajectory formed by two normal lines [133]. Ruttimann et al. proposed a trajectory formed by three concentric circles and demonstrated better artifact removal than with conventional circular tomosynthesis [134]. Carter et al. showed that a hypocycloidal motion, defined as two eccentric circles of the X-ray source provides better imaging performance than the standard linear and circular motions, but at the expense of longer imaging time [135].

3.2.4 Acquisition Geometry Parameters

Due to the limited angle acquisition, image artifacts are inevitable in DTS imaging. However, adjusting the different acquisition parameters according to the imaging task and the anatomic site being examined reduces the appearance of potential artifacts, makes them less clinically confounding, and provides images with a quality sufficient-enough for the exam-

3. Technical Background

ination. The main acquisition parameters affecting image quality in tomosynthesis are the **tomographic angle**, the **number of projection views**, the **projection density**, and the **total radiation dose**. In Figure 3.26 are illustrated the geometry parameters of a pseudo-linear scan acquisition as an example. In this thesis, the tomographic angle θ is defined as half of the total angular range γ ($\gamma = 2\theta$). This means, if the X-ray tube moves from -20° to $+20^\circ$, θ is equal to 20° . In circular tomosynthesis, θ is defined as half of the solid angle drawn by the X-ray tube. The number of projection views N is the number of X-ray projection images acquired during the acquisition over the total angular range. The linear projection density D is defined as the number of projection views divided by the total perimeter of the scan orbit. The total radiation dose is defined as the cumulative sum of doses across all projections.

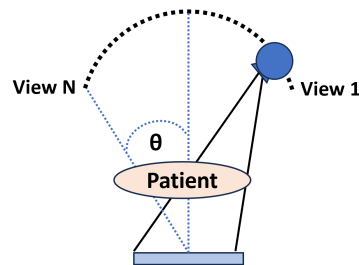


Figure 3.26: Illustration of the geometry parameters of a pseudo-linear scan acquisition.

3.2.5 Artifacts

The appearance of image artifacts in DTS depends largely on the aforementioned acquisition geometry parameters. These artifacts are mainly caused by the missing data due to the limited-angle acquisition. **Out-of-plane artifacts**, known as **blurring artifacts** as well, are the most common and inevitable artifacts in tomosynthesis images. They are due to insufficient blurring of structures lying outside the plane of interest. These structures contribute to the reconstructed slice and create unwanted shadows or structures that can mimic pathology. Moreover, such artifacts may mask subtle anomalies. The range and intensity of out-of-plane artifacts are related to the contrast and size of the out-of-plane structure causing their appearance. The higher the contrast of the structure, the stronger are the artifacts, and the larger the structure, the wider is the spread of the artifacts [136–138]. Figure 3.27 shows examples of blurring artifacts in a patient chest DTS image. These artifacts (yellow arrows) are caused by the bronchoscope and by the ribs located outside of the imaged plane.

The occurrence of **ripple artifacts** is caused by high contrast structures located far away from the plane of interest but not adequately blurred. They are usually due to a low number of projection views over the angular range, in other terms, they are due to a low projec-

3.2. Digital Tomosynthesis: From Data Acquisition to Image Formation

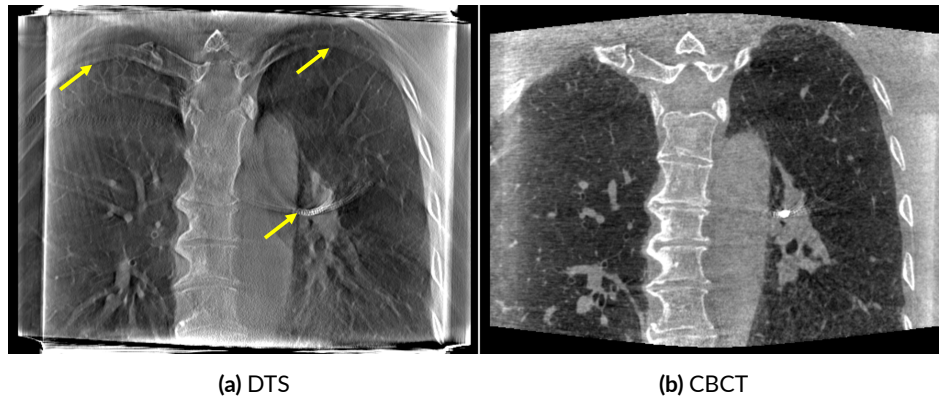


Figure 3.27: Image example of blurring artifacts. (a) DTS image of the chest showing blurring artifacts (yellow arrows) caused by the bronchoscope and by the ribs located outside the imaged plane. (b) CBCT slice at the same position shown as a reference.

tion density. Blurring artifacts transform into ripple artifacts as the distance from the ripple source to the plane of interest exceeds a certain threshold. Figure 3.28 shows an example of ripple artifacts (red arrows) in a chest DTS slice due to the high-contrast bronchoscope located far outside the plane in focus but whose contributions to the imaging plane are not enough blurred.

Another distortions that could be seen in tomosynthesis images are **ghost artifacts**. These artifacts arise from a high-contrast structure lying outside the plane of interest, with its long axis parallel to the sweep direction. Due to the limited angle acquisition, this structure is imaged in all the projections without capturing depth information regarding it. Therefore, it cannot be completely blurred and manifests as faint or ghost artifact in the in-focus plane. Figure 3.29 portrays an example of a patient chest DTS image presenting ghost artifacts (blue arrows) at the clavicle level. The clavicle seems to widen as it moves out of plane.

Metal artifacts seen in CT images are also encountered in DTS images. These artifacts appear as low-density artifacts along the sweep direction and surrounding high attenuation materials such as implants or metallic objects. Figure 3.30 illustrates an example of a patient intraoperative chest DTS image presenting metal artifacts (green arrows) from the high-contrast bronchoscope.

3. Technical Background



Figure 3.28: Example of ripple artifacts (red arrows) in a DTS slice caused by the high-contrast bronchoscope located far outside the imaged plane but whose contributions to the in-focus plane are not sufficiently blurred.



Figure 3.29: Example of ghost artifacts (blue arrows) in a patient chest DTS slice at the clavicle level. The clavicle seems to widen as it moves out of plane.



Figure 3.30: Example of metal artifacts (green arrows) in a patient intraoperative chest DTS slice caused by the high-contrast bronchoscope.

3.3 Conclusion

As DTS is an X-ray imaging modality, we have covered in this chapter the fundamentals of X-rays, from their generation to their transmission until their detection. Moreover, we have highlighted the mathematical foundation of tomographic image formation and the different classes of image reconstruction algorithms. Afterwards, we have provided an in-depth coverage of the genesis of DTS, its data acquisition geometries, and its special kind of artifacts. The next chapter is more dedicated to data acquisition geometries, we explore the pitfalls of the available system geometries in the context of image-guided bronchoscopy interventions and we unveil our novel bronchoscopy-customized scanning geometry protocol.

3. Technical Background

4

Spherical Ellipse Digital Tomosynthesis Scan Orbit

Contents

| | | |
|------------|---|-----------|
| 4.1 | Motivation | 64 |
| 4.2 | Mathematical Definition of a Spherical Ellipse | 66 |
| 4.3 | Design of the Spherical Ellipse DTS Scan Orbit | 67 |
| 4.4 | Materials and Methods | 69 |
| 4.4.1 | Scan Orbits | 69 |
| 4.4.2 | Data | 71 |
| 4.4.3 | Reconstruction Algorithm | 72 |
| 4.4.4 | Experiments | 73 |
| 4.5 | Results | 74 |
| 4.6 | Conclusion | 86 |

AFTER exposing the various available system acquisition geometries for digital tomosynthesis (DTS) imaging in the previous chapter, this chapter dives into the potentials and limitations of these geometries, especially in guiding navigational bronchoscopy procedures, and motivates the need for a bronchoscopy-customized DTS scan geometry. A novel C-arm-based spherical ellipse DTS scan orbit dedicated to bronchoscopy procedure guidance was developed within the scope of this thesis and is unveiled in this chapter. Through experiments on simulated data of numerical phantoms and patients, its advantages over projective radiography (PR), cone-beam computed tomography (CBCT), and the standard DTS scan trajectories are outlined.

4. Spherical Ellipse Digital Tomosynthesis Scan Orbit

Some parts of the research presented in this chapter have been published in the paper titled "Spherical Ellipse Scan Trajectory for Tomosynthesis-Assisted Interventional Bronchoscopy" (in: G. Schramm, A. Rezaei, K. Thielemans, J. Nuyts (Eds.), *Proceedings of the 16th Virtual International Meeting on Fully 3D Image Reconstruction in Radiology and Nuclear Medicine*, 2021, pp. 352–356, <http://dx.doi.org/10.48550/arXiv.2110.04143> [139]).

4.1 Motivation

As presented in Chapter 1 and Chapter 2, current navigational bronchoscopy procedures rely on PR and CBCT to perform biopsies on peripheral pulmonary nodules (PPN). This navigational approach is challenging due to the superimposition of the distinct anatomical structures in radiography in a 2D image, obstructing the visualization of the target lesions. Only the bronchoscopy tools and the ribs can be resolved. On the other hand, while CBCT is considered as the gold standard accurately locating the lesion in 3D, its associated high radiation dose, long imaging time, and large scanning footprints are of great concern. Circumventing the aforementioned shortcomings, DTS emerges as a compelling alternative for guiding bronchoscopy procedures combining the advantages of radiography and CBCT. It provides quasi-3D images and captures the location of both the biopsy needle tip and the lesion. Only the depth resolution cannot match a full CBCT image due to the limited angle acquisition. As we are interested in interventional DTS, and with the wide availability of C-arm devices in intervention departments, we choose to focus in this work on standard DTS trajectories that could be performed on a C-arm device, mainly the pseudo-linear DTS and the circular DTS presented in Section 3.2.3.

One of the most common DTS scan trajectories is the unidirectional full isocentric pseudo-linear scan orbit. Whereas this trajectory is mechanically simple to achieve, it cannot delineate boundaries properly in 3D due to the incomplete data acquisition. The Fourier slice theorem (presented in 2D in Section 3.1.5.2) in 3D dictates that the 2D Fourier transform of the 2D projection image at a certain angle is equal to a 2D slice of the 3D Fourier transform of the projected object at the same angle. In a pseudo-linear scan geometry with the approximation of parallel-beam sampling, only a small portion of Fourier's space formed of planes in a double-wedge domain is sampled as depicted in Figure 4.1. If the X-ray source moves from $-\theta$ to $+\theta$, frequencies $\omega_y > \omega_y^{max} = \omega_x \tan \theta$ are lost. The narrower the angular range, i.e., the smaller the tomosynthesis angle θ , the larger is the region in the Fourier's space where data are not available. This loss of information is responsible for the poor depth resolution along the y axis in the reconstructed DTS images.

Multidirectional scan orbits might improve the depth resolution as data acquired cover a wider portion of the spherical surface above the imaged object. Circular DTS is the most

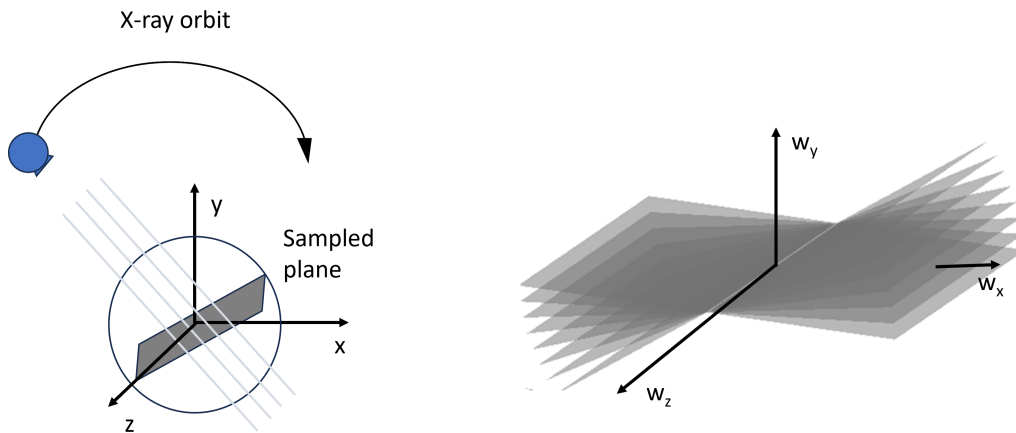


Figure 4.1: Region of Fourier's space sampled with a pseudo-linear DTS acquisition geometry.

prevalent multidirectional DTS data acquisition geometry. As illustrated in Figure 4.2, when the X-ray tube travels along the circular path with a tomographic angle θ , the sampled area in Fourier's space covers a region cut out by a double cone oriented along the w_y axis with a half opening angle equal to $\pi/2 - \theta$. As the tomographic angle θ increases, the opening angle of the cone decreases and subsequently the unsampled region shrinks. Compared to pseudo-linear geometry, it is obvious to see that a larger portion of Fourier's space is covered with circular tomosynthesis for a fixed tomographic angle θ . This translates into more frequencies being sampled and improved depth resolution.

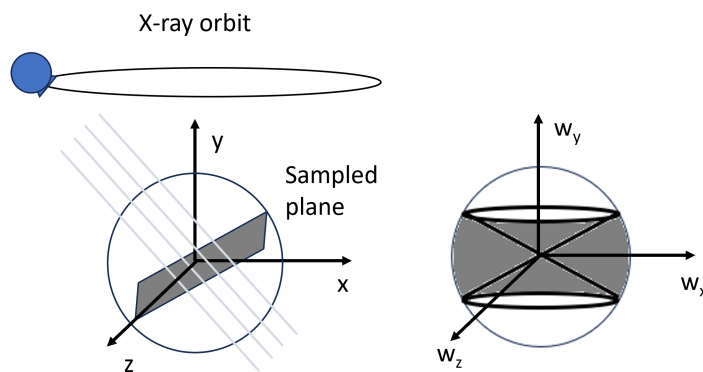


Figure 4.2: Region of Fourier's space sampled with a circular DTS acquisition geometry.

When the number of projection views is infinite, greater tomographic angles result in better reconstruction. However, with a limited number of projection views, increasing the tomographic angle leads to a more noticeable discrete sampling of the Fourier's space, resulting

4. Spherical Ellipse Digital Tomosynthesis Scan Orbit

in more discretely blurred out-of-plane structures. In circular DTS, out-of-plane structures are blurred into discretely sampled circles with the points forming the circle becoming more distant as the distance from the plane of interest gets larger. This kind of out-of-plane artifacts may mask subtle anatomy in DTS images. Therefore, there is a trade-off between the number of projection views and the tomographic angle. If one is restricted to circular trajectories, only a relatively small circle can be used.

Moreover, as discussed in Section 1.3.4, in bronchoscopy interventions, some specific space constraints that limit the movement of the C-arm in certain directions are imposed. Some devices, in particular robotic bronchoscope holders and certain navigational equipment, are placed in a way that the angulation in the cranial/caudal direction are restricted (Figure 1.19). To avoid collision, only a circular trajectory relatively small could be applied.

The aforementioned limitations of the standard pseudo-linear and circular DTS scan geometries drive the motivation to search for an alternative scan geometry suitable for guiding bronchoscopy interventions and that could acquire more data of the object without introducing additional radiation dose and artifacts. In this context and in the course of this doctoral work, we developed a novel C-arm-based spherical ellipse DTS scan trajectory customized for guiding bronchoscopy interventions, and we investigated its added value compared to the standard DTS scan orbits. A spherical ellipse orbit can be obtained by elongating a small circular orbit into a certain direction where space is not limited. If we are restricted to circular trajectories, only a small circle can be performed due to the aforementioned limitations, however, having the spherical ellipse in hand, it could be used for an improved image quality as it permits the acquisition of data covering larger portion of the Fourier's sampling space. The remaining of this chapter mainly investigates which of the two options is more appropriate. In the next section, the theoretical background and the design of the spherical ellipse scan orbit are presented.

4.2 Mathematical Definition of a Spherical Ellipse

A spherical ellipse is a spherical biquadratic belonging to the family of spherical conics. It is defined as the curve of intersection of a sphere with an elliptic cone of the second degree whose vertex is at the midpoint of the sphere (Figure 4.3). It is the spherical analog of a planar ellipse in Euclidean space. Hence, transposing Gardener's method for the planar ellipse to the sphere, a spherical ellipse can be defined as the locus of points on the sphere for which the sum of their great circle distances from two fixed points on the sphere, called foci, is constant. In simpler terms, it is a lift of a planar ellipse on a sphere. Its projection from the midpoint of the sphere onto some plane is a planar conic section. A spherical ellipse is characterized by the greatest and least vertical angles of the cone referred as α and β , respectively, and known

4.3. Design of the Spherical Ellipse DTS Scan Orbit

as the principal angles of the cone. Its Cartesian parametrization is given by

$$\begin{cases} x = d \sin \alpha \cos t \\ z = d \sin \beta \sin t \\ y = \pm d \sqrt{1 - \sin^2 \alpha \cos^2 t - \sin^2 \beta \sin^2 t} \end{cases} \quad (4.1)$$

where d is the radius of the sphere.

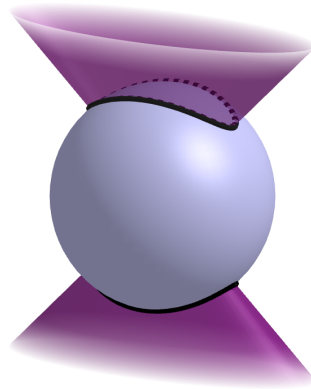


Figure 4.3: An illustration of a spherical ellipse (black curve) defined as the curve of intersection of a sphere with an elliptic cone whose vertex is at the midpoint of the sphere.

4.3 Design of the Spherical Ellipse DTS Scan Orbit

Investigations of the novel spherical ellipse DTS scan trajectory are carried out using numerical simulations. The spherical ellipse scan trajectory is implemented in the *Computed Tomography Library* (CTL)¹ [140]. To construct this orbit, the source positions are evenly spaced per arc length on a 2D ellipse located in a plane parallel to the xz plane and tangent to a sphere of radius d , and are then projected on the surface of the sphere from its midpoint (Figure 4.4). The ellipse is defined by its large radius $a = d \tan \alpha$ and its small radius $b = d \tan \beta$.

On the 2D ellipse, the source sampling positions are given by

$$\vec{T}_i^s = (r(\theta_i^s) \cos \theta_i^s, d, r(\theta_i^s) \sin \theta_i^s) \quad (4.2)$$

where

$$r(\theta_i^s) = \frac{b}{\sqrt{1 - (e \cos \theta_i^s)^2}} \quad (4.3)$$

¹Code available at: <https://gitlab.com/tpfeiffe/ctl>

4. Spherical Ellipse Digital Tomosynthesis Scan Orbit

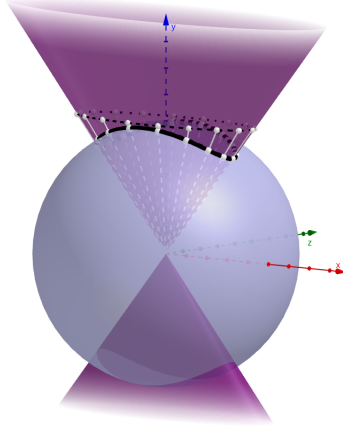


Figure 4.4: Sampling of the spherical ellipse. The points are evenly sampled per arc length on a 2D ellipse, then projected on the surface of the sphere.

and $e = \sqrt{1 - \frac{b^2}{a^2}}$ is the ellipse eccentricity.

To find θ_i^s at position i , the circumference C of the ellipse is computed by

$$C = 4aE(e) \quad (4.4)$$

where E is the complete elliptic integral of the second kind defined by

$$E(k) = \int_0^{\pi/2} \sqrt{1 - k^2 \sin^2 \theta} d\theta = \int_0^1 \frac{\sqrt{1 - k^2 t^2}}{\sqrt{1 - t^2}} dt \quad (4.5)$$

The arc length between each two consecutive source locations on the plane ellipse is given by

$$\Delta l = \frac{C}{N} \quad (4.6)$$

where N is the number of projection views acquired. The arc length from the source at position 0 (located on the large radius of the ellipse) to the source at position i is given by

$$L(\theta_i^s) = i\Delta l = aE(e) - \varepsilon\left(\frac{r(\theta_i^s) \cos \theta_i^s}{a}; e\right) \quad (4.7)$$

where ε is the incomplete elliptic integral of the second kind defined as

$$\varepsilon(\sin \varphi; m) = \int_0^\varphi \sqrt{1 - m \sin^2 \theta} d\theta \quad (4.8)$$

with $\varphi \in [-\pi/2, \pi/2]$ and $m \in [0, 1]$ is the elliptic modulus.

Using 4.7, one can write:

$$\varepsilon\left(\frac{r(\theta_i^s) \cos \theta_i^s}{a}; e\right) = aE(e) - i\Delta l \quad (4.9)$$

θ_i^s can be found by computing the inverse of ε . In this work, Newton's iteration proposed by Boyd in [141] was used to compute this inverse. The inverse $\varphi(z; m) = \varepsilon^{-1}(z; m)$ solves the equation $f(\varphi) = 0$ where $f(\varphi) = \varepsilon(\sin \varphi; m) - z$.

Newton's iteration is given by

$$\varphi^{n+1} = \varphi^n - \frac{\varepsilon(\sin \varphi^n; m) - z}{\sqrt{1 - m \sin^2 \varphi^n}} \quad (4.10)$$

and is initialized with

$$\varphi^0(z; m) = \pi/2 + \sqrt{r}(\theta - \pi/2), \quad (4.11)$$

where

$$\theta = \arctan\left(\frac{\mu}{\zeta}\right), \quad (4.12)$$

$$\mu = 1 - m, \quad (4.13)$$

$$\zeta = 1 - \frac{z}{\varepsilon(1; m)}, \quad (4.14)$$

and

$$r = \sqrt{(1 - m)^2 + \zeta^2}. \quad (4.15)$$

4.4 Materials and Methods

4.4.1 Scan Orbits

Three classes of DTS scan orbits have been evaluated using numerical simulations: **pseudo-linear orbit**, **circular orbit**, and **spherical ellipse orbit**. All three scan trajectories have been implemented in the CTL toolkit. The simulation assumes an X-ray source and a flat-panel detector are mounted on a robotic C-arm with a source to detector distance set to 1200 mm. The source to isocenter distance d is assumed constant by design and is fixed to 785 mm. The flat-panel detector moving above the patient table is composed of 616×480 pixels with a 0.616 mm pixel pitch, and is mounted in opposite to the X-ray source while performing an in-plane rotation in a way its rows are kept tangential to the scan trajectory. Poisson noise

4. Spherical Ellipse Digital Tomosynthesis Scan Orbit

was added to the projection data with a photon flux set to 4.75×10^8 photons per cm^2 . N projection views are acquired on each of the studied trajectories.

For the pseudo-linear scan trajectory, the source sampling positions are evenly spaced on the arc orbit per arc length (Figure 4.5 (a)). The coordinate of the i^{th} X-ray tube position is given by

$$\vec{T}_i^l = (d \sin \theta_i^l, d \cos \theta_i^l, 0) \quad (4.16)$$

where

$$\theta_i^l = -\alpha + i\Delta\theta^l, \quad i = 0, \dots, N-1 \quad (4.17)$$

and

$$\Delta\theta^l = \frac{2\alpha}{N-1}. \quad (4.18)$$

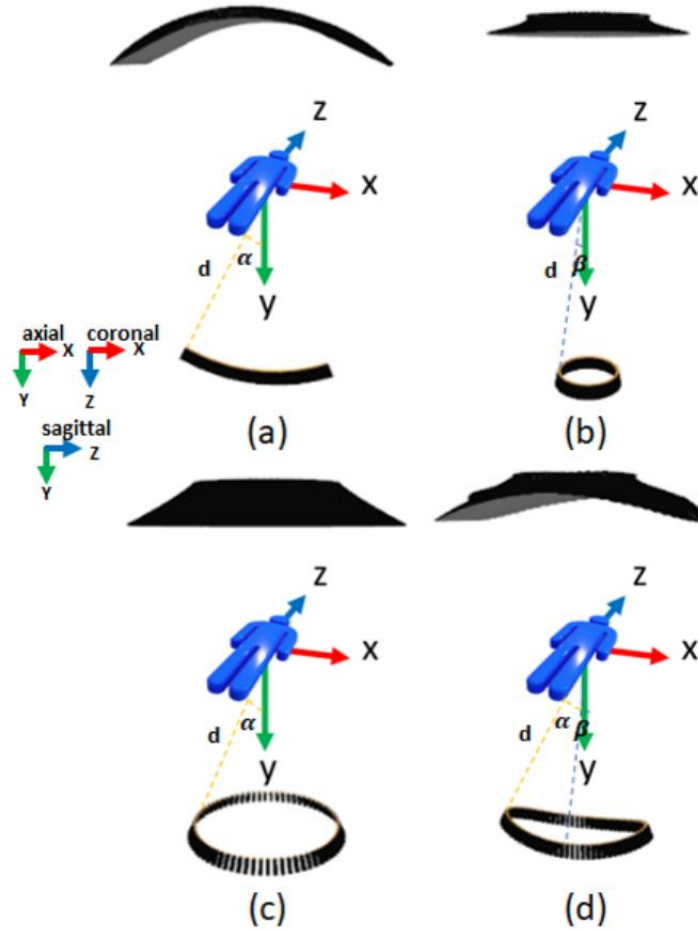


Figure 4.5: Illustration of the different DTS scan orbits: (a) Pseudo-linear (PL), (b) small circle (SC), (c) large circle (LC), and (d) spherical ellipse (SE). The source trajectory is shown below the patient and the detector trajectory is shown above the patient.

For the circular scan trajectory, two cases are considered: a small circle (Figure 4.5 (b)) with an angular range of $\pm\beta$ and a large circle (Figure 4.5 (c)) with an angular range of $\pm\alpha$ ($\alpha > \beta$). The source sampling positions are given by

$$\vec{T}_i^c = (d \sin \eta \cos \theta_i^c, d \cos \eta, d \sin \eta \sin \theta_i^c) \quad (4.19)$$

where

$$\eta = \begin{cases} \alpha, & \text{for the large circle} \\ \beta, & \text{for the small circle} \end{cases} \quad (4.20)$$

$$\theta_i^c = i\Delta\theta^c, \quad i = 0, \dots, N-1, \quad (4.21)$$

and

$$\Delta\theta^c = \frac{360^\circ}{N}. \quad (4.22)$$

For the sake of simplicity, in the rest of this chapter, we will refer to the **pseudo-linear**, **small circular**, **large circular**, and **spherical ellipse** DTS scan orbits as **PL**, **SC**, **LC**, and **SE**, respectively.

Figure 4.6 illustrates the visible and invisible singularities when scanning a homogeneous spherical object with the four DTS scanning protocols. The visible singularities (red covered region on the sphere) refer to the features that could be reconstructed with DTS, while the invisible ones (blue covered region on the sphere) cannot be reconstructed. The tomographic angle for PL and LC is α , and for SC is β . SE has α and β as tomographic angles. Having the same angular range, a larger portion of the sphere is visible with LC compared to PL. LC covers larger region of the sphere than SC due to its larger tomographic angle. The region that can be reconstructed with SE lies between that of LC and SC.

4.4.2 Data

4.4.2.1 Numerical Ball Phantom

In order to qualitatively characterize and compare the spatial resolution of the four DTS scan orbits, a simple numerical phantom featuring a small ball made of polyethylene was constructed. The ball has a diameter of 6.4 mm and is placed at the isocenter. The phantom size is set to $64 \times 64 \times 64$ voxels with a voxel size of $0.5 \text{ mm} \times 0.5 \text{ mm} \times 0.5 \text{ mm}$.

4.4.2.2 Patient Data

In order to take the complex chest anatomy into account, real chest CBCT images acquired using a C-arm device (Axiom Artis dTA, Siemens Healthcare GmbH, Erlangen, Germany)

4. Spherical Ellipse Digital Tomosynthesis Scan Orbit

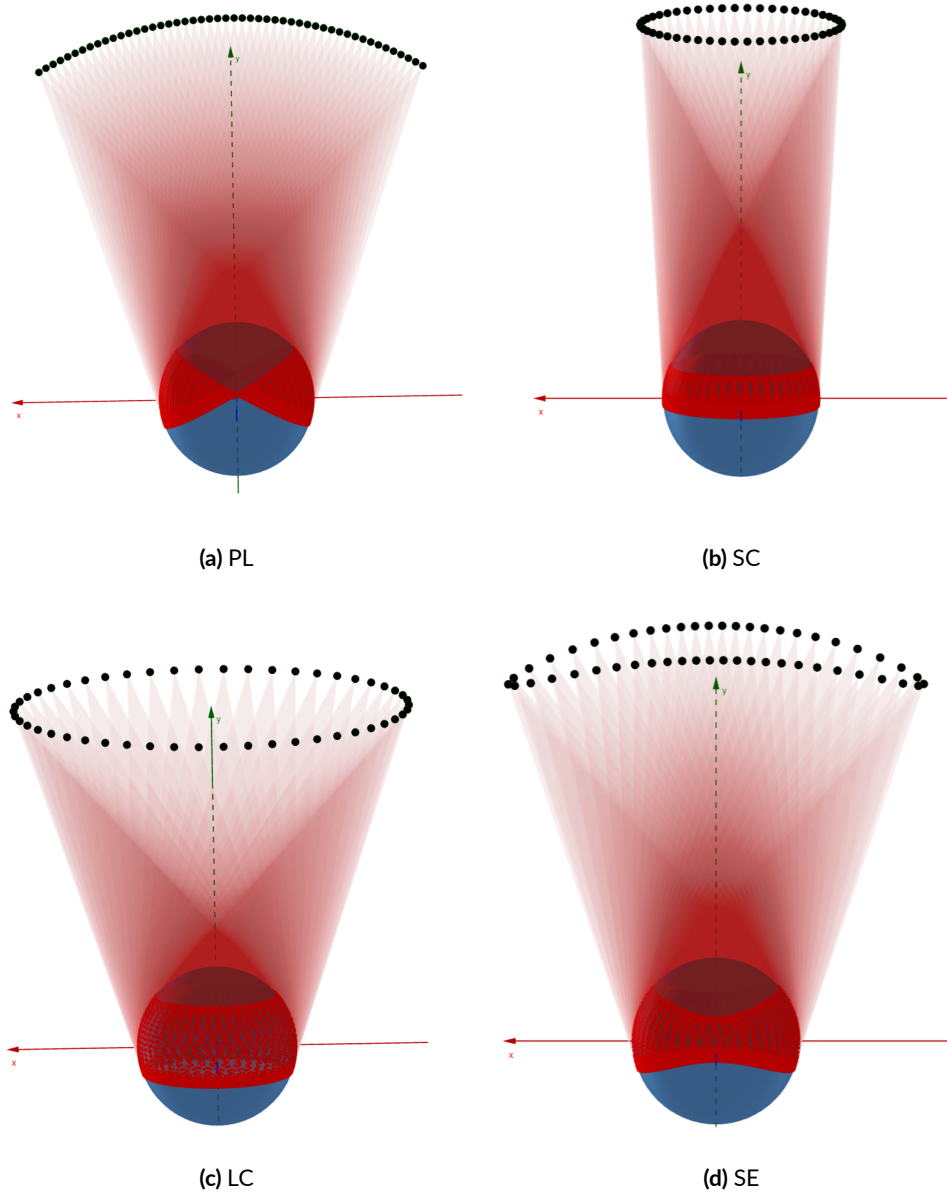


Figure 4.6: Illustration of visible and invisible singularities on a homogeneous sphere for each DTS scan orbit. The region covered in red on the sphere represents the features that can be reconstructed. PL: pseudo-linear, SC: small circle, LC: large circle, and SE: spherical ellipse.

were used. The images were acquired during interventional bronchoscopy procedures held at MD Anderson Cancer Center, Houston, USA, and show a bronchoscope and a trans-bronchial biopsy needle inserted within a target lesion in a patient lung.

4.4.3 Reconstruction Algorithm

Since different scan geometries require distinct filter kernels, and since the design of the filter significantly impacts the reconstructed image quality, we decided to focus in this thesis work

on algebraic and not analytic reconstruction methods in order to fairly compare the different scan protocols. ART algorithm, presented in Section 3.1.5.4, was used to reconstruct the DTS data of the different scan protocols. As ART can be applied to different geometries without requiring major modifications, it makes possible the comparison of the reconstruction results of the different scan geometries. ART was used with an ordered subset scheme [142] and including only the positivity constraint as a regularization term. The ART reconstruction is implemented and openly available in the CTL toolkit [140].

4.4.4 Experiments

Experiment 1

In this experiment, DTS projection images of the ball phantom were simulated according to the four scan protocols: PL, SC, LC, and SE. The simulated data were then reconstructed using ART. The number of iterations was fixed to 50 as iterating further did not result in any significant improvement in image quality. Reconstructed axial, coronal, and sagittal slices were compared and line profiles in each direction were plotted to depict and compare the asymmetry in spatial resolution across the different scan orbits. In order to ensure a fixed dose for each acquisition, the number of projection views N was fixed to 72. We again emphasize here, the tomographic angle of PL and LC is α , the tomographic angle for SC is β , and SE has two tomographic angles α and β . In this experiment, α and β were fixed to 23° and 15° , respectively.

Experiment 2

Having compared the different scan orbits in Experiment 1, we focused in Experiment 2 on the SE scan orbit and studied the change in the depth resolution (along the y direction) when varying the tomographic angle. The ball phantom was used in this experiment as well. Different settings of α ranging from 23° to 46° were tested while keeping β fixed at 15° and N at 72.

Experiment 3

In this experiment, DTS projections were simulated by forwardprojecting the real patient CBCT images according to the four scanning protocols. In this experiment, ART iterations were stopped once the normal equation ($A^T(Af - p) = 0$) was numerically satisfied in order to ensure convergence. The size of the reconstructed images was set to $512 \times 512 \times 382$ voxels with a voxel size of $0.5 \text{ mm} \times 0.5 \text{ mm} \times 0.5 \text{ mm}$. In this experiment, the reconstructions were done with different settings of N , α , and β . Qualitative evaluation by visual inspection

4. Spherical Ellipse Digital Tomosynthesis Scan Orbit

as well as quantitative assessment by computing the Pearson correlation (PC) have been conducted. PC was computed in distinct regions of interest (ROI), focusing on the ability of the different orbits to detect the biopsy needle and the target lung nodule and to resolve the different chest structures. PC of two random variables x and y each having M scalar observations is defined as

$$PC(x, y) = \frac{1}{M-1} \sum_{i=1}^M \left(\frac{x_i - \mu_x}{\sigma_x} \right) \left(\frac{y_i - \mu_y}{\sigma_y} \right) \quad (4.23)$$

where μ_x and σ_x represent the mean and standard deviation of x , respectively, and μ_y and σ_y denote the mean and standard deviation of y , respectively.

4.5 Results

Experiment 1

Figure 4.7 illustrates the reconstruction results using PL (a), SC (b), LC (c), and SE (d) DTS scan orbits. As a ground truth (GT), the simulated ball phantom is shown in (e) as well. Axial (top), coronal (middle), and sagittal (lower) slices at the same positions are shown for each case. The asymmetry in spatial resolution across all trajectories can be clearly noticed. While the ball is faithfully reconstructed in the coronal slices, it is highly geometrically distorted in the axial and sagittal slices demonstrating a loss of resolution in the y direction.

Visual inspection of the different reconstructions suggests higher distortion and, subsequently, higher loss in the depth resolution (in the y direction) with PL and SC, compared to LC and SE. For a more quantitative validation, line profiles along the three directions (yellow lines in Figure 4.7) are visualized in Figure 4.8. In accordance with the visual observations, the full-width at half-maximum (FWHM) in the y direction is higher for PL and SC than for LC and SE. Interestingly, FWHM for LC is just slightly lower than that for SE. The line profiles in the x and z directions suggest no significant differences across the different trajectories.

In order to characterize how the type of blurring of out-of-plane objects depends on the source motion profile during the acquisition, Figure 4.9 shows reconstructed coronal slices at 12.5 mm from the center of the phantom with the different scan protocols. Despite the fact that there exist no object in GT (Figure 4.9 (e)) at this position, out-of-plane artifacts coming from the ball can be depicted in the DTS reconstructions. In accordance with the theory presented in the beginning of this chapter, out-of-plane points are blurred into discrete lines with PL (Figure 4.9 (a)), discrete rings with SC (Figure 4.9 (b)) and LC (Figure 4.9 (c)), and discrete ellipses with SE (Figure 4.9 (d)). The discrete linear artifacts with PL can conceal anatomical details in the DTS images or may be confused for a circumscribed nodule. It

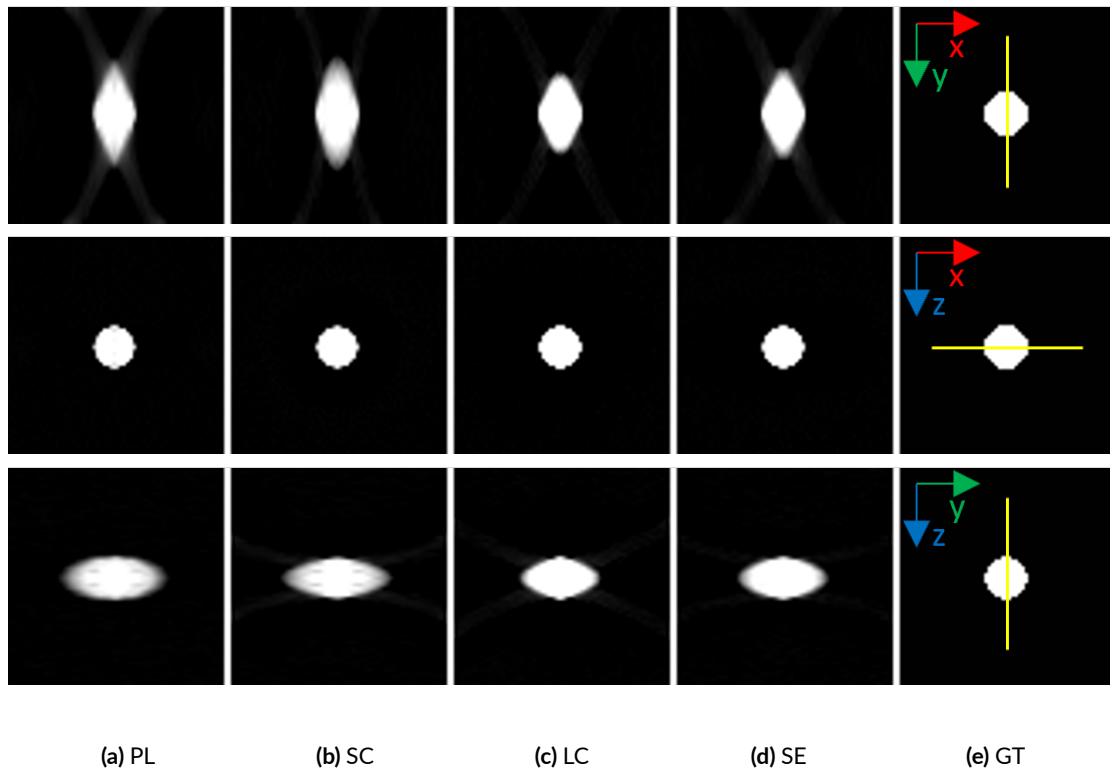


Figure 4.7: Ball phantom reconstructed images with the different DTS scan protocols. PL: pseudo-linear, SC: small circle, LC: large circle, SE: spherical ellipse, and GT: ground truth.

is evident that multidirectional motion profiles provide more effective blurring of out-of-plane objects compared to the unidirectional PL motion profile. Comparison of SC and LC indicates a better blurring of out-of-plane objects with LC as the area of the blurring is larger. This is due to a larger tomographic angle with LC. The blurring with LC and SE are less disturbing to the observer.

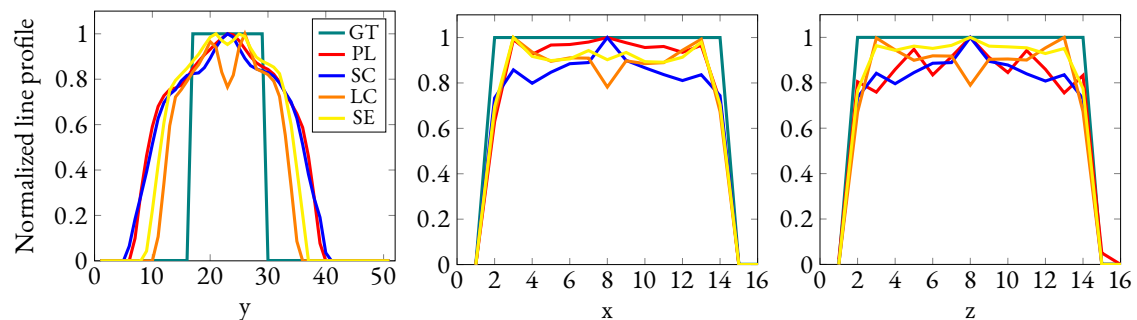


Figure 4.8: Line profiles in the y (left), x (center), and z (right) directions through the center of the sphere. GT: ground truth, PL: pseudo-linear, SC: small circle, LC: large circle, and SE: spherical ellipse.

4. Spherical Ellipse Digital Tomosynthesis Scan Orbit

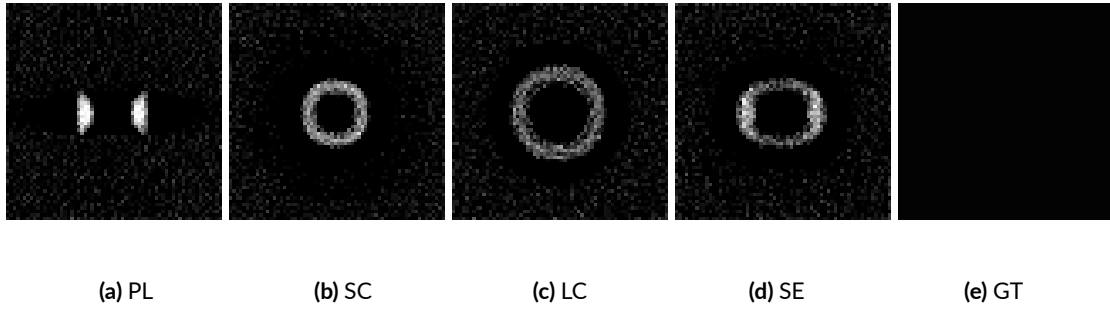


Figure 4.9: Ball phantom reconstructed coronal slices at 12.5 mm from the center of the phantom. Figure illustrating the different types of blurring with the different DTS trajectories. PL: pseudo-linear, SC: small circle, LC: large circle, SE: spherical ellipse, and GT: ground truth.

Experiment 2

Figure 4.10 portrays axial reconstructions of the ball phantom with a SE scan orbit using different values of α . Jointly, Figure 4.11 shows the corresponding line profiles in the y direction. The results suggest that the larger the α , the less is the geometric distortion of the ball in the y direction and the smaller is the FWHM.

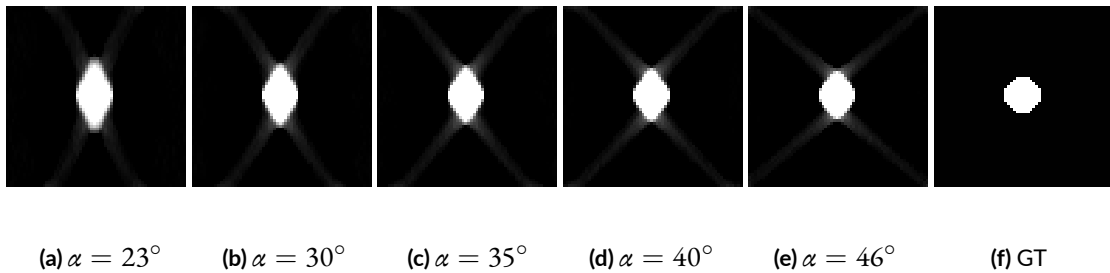


Figure 4.10: Ball phantom axial slices reconstructed using different values of the large tomographic angle α . The small tomographic angle β is fixed at 15° and the number of projection views N is fixed at 72.

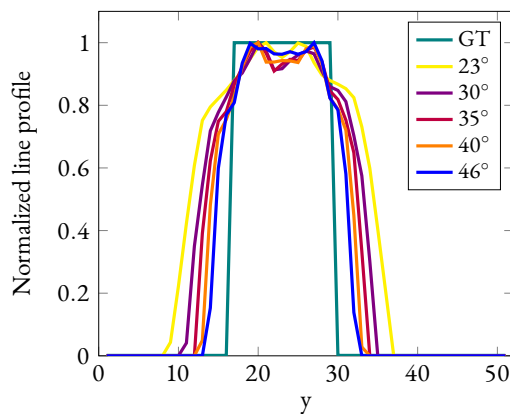


Figure 4.11: Line profiles in the y direction through the center of the sphere in the reconstructed axial slices shown in Figure 4.10.

Experiment 3

Figure 4.12 illustrates DTS coronal slice reconstructions of the patient data with PL (a), SC (b), LC (c), and SE (d). For comparison, a PR image is shown in (e), and a CBCT coronal slice is shown as reference in (f) as well. Coronal slices at the same position are shown for the CBCT and all the DTS reconstructions. DTS reconstructions are shown for N , α , and β set to 72 , 23° , and 15° , respectively. Overall, compared to PR, DTS reconstructions indicate improved conspicuity of the diverse chest structures, including normal pulmonary vasculature and the spine. In the radiographic image, the target nodule, intervertebral discs, and pulmonary vasculature are entirely obscured by the overlapping ribs and the bronchoscope. Compared to the multidirectional orbits, out-of-plane artifacts are more discernible with the unidirectional PL orbit (red arrows), mainly due to the lower spatial resolution. The horizontal edges of the intervertebral discs (black arrows) and the lesion (yellow arrows) are hidden by shadowing artifacts with PL, but are better recovered with SC, LC, and SE.

To focus on the different relevant structures, three regions of interest (ROIs) were selected. These ROIs are defined in the CBCT coronal slice in Figure 4.13 and are highlighted in yellow. ROI#1 surrounds the spine, ROI#2 surrounds the lesion and the tip of the biopsy needle, and ROI#3 covers the spine, lesion, and tip of the needle, together with the ribs and other distinct chest structures.

Figure 4.14 portrays enlarged views of ROI#1 for the different reconstructions shown in Figure 4.12. On top of the strong shadowing artifacts observed with PL, pronounced out-of-focus artifacts generated by the high-attenuation object (bronchoscope) manifest with both PL and SC as multiple ghosting replicas of the bronchoscope (blue arrows), particularly at its edges. Although LC has a larger tomographic angle, strong ripple artifacts emerge along the spine (green arrows). This is primarily attributed to the lower projection density on the LC trajectory in comparison to the other ones. These artifacts do not appear with SE.

Figure 4.15 shows enlarged regions around the lesion and the tip of the needle (ROI#2) for the various reconstructions. The lesion is better distinguishable from the lung background with SC, LC, and SE compared to PL. However, out-of-focus artifacts coming from the bronchoscope are slightly stronger with SC.

4. Spherical Ellipse Digital Tomosynthesis Scan Orbit

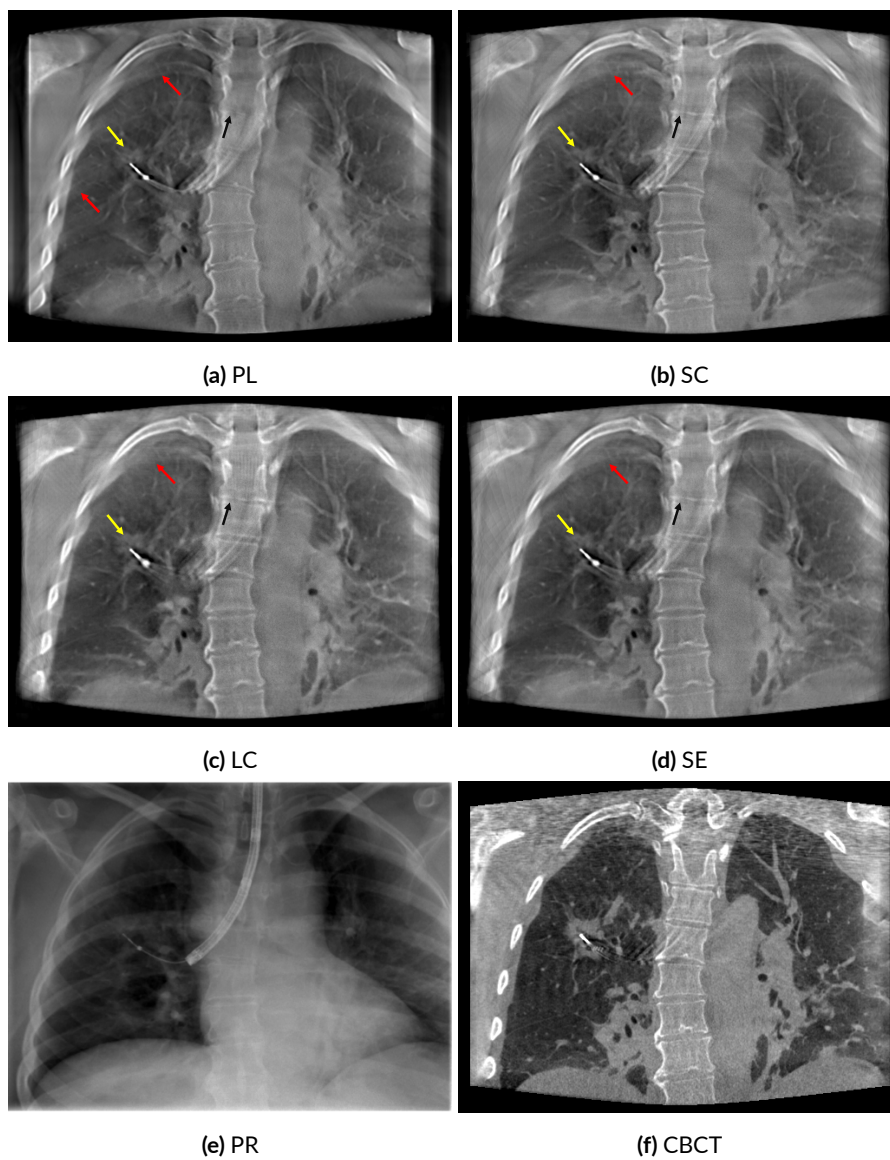


Figure 4.12: Patient data DTS coronal slice reconstructions with the different scan trajectories. (a) PL, (b) SC, (c) LC, and (d) SE. For comparison, (e) PR and (f) CBCT images are shown as well. (displayed window for DTS and CBCT: [-1000 HU, 1000 HU]). PL: pseudo-linear, SC: small circle, LC: large circle, SE: spherical ellipse, PR: projective radiography, and CBCT: cone-beam computed tomography.



Figure 4.13: ROIs defined in the CBCT slice: ROI#1 around the spine, ROI#2 around the lesion, and ROI#3 covering the different structures in the chest.

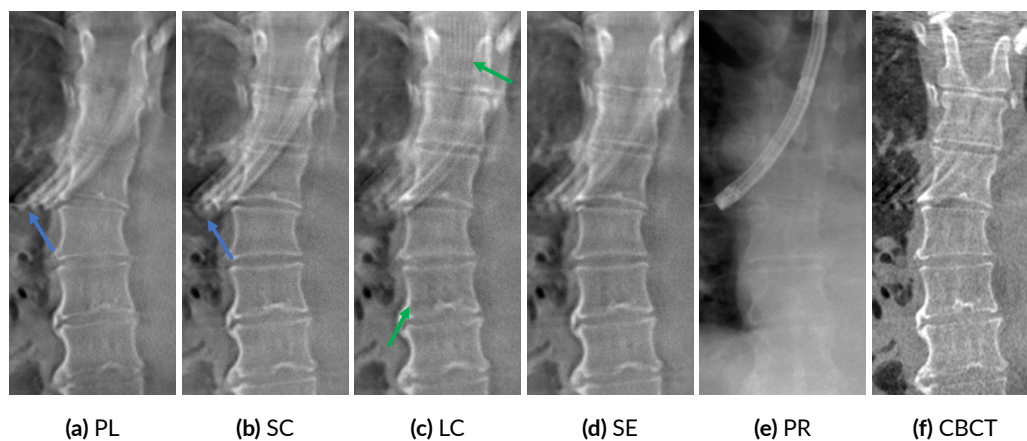


Figure 4.14: Enlarged views around the spine (ROI#1) corresponding to the images shown in Figure 4.12. PL: pseudo-linear, SC: small circle, LC: large circle, SE: spherical ellipse, PR: projective radiography, and CBCT: cone-beam computed tomography.

4. Spherical Ellipse Digital Tomosynthesis Scan Orbit

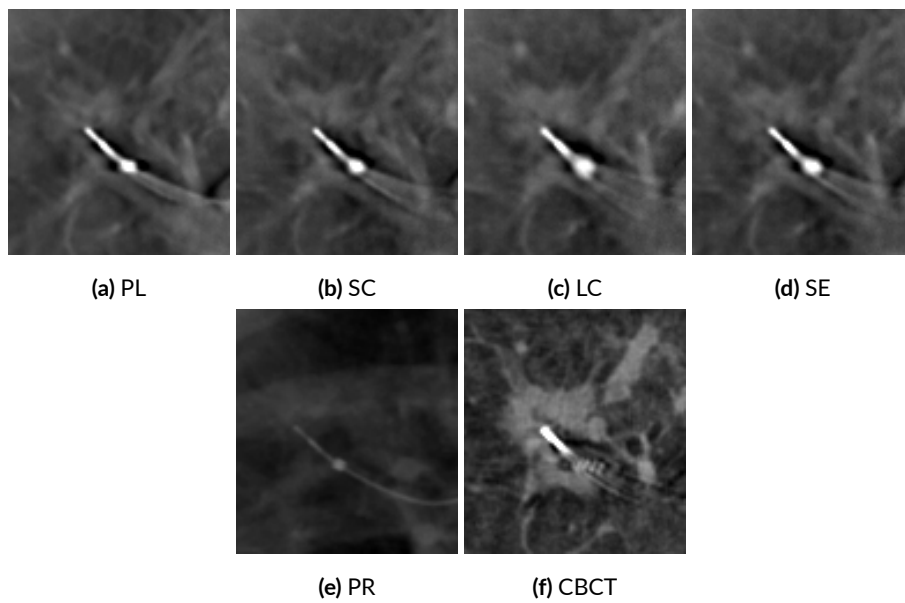


Figure 4.15: Enlarged views around the needle tip and the target lesion (ROI#2) corresponding to the images shown in Figure 4.12. PL: pseudo-linear, SC: small circle, LC: large circle, SE: spherical ellipse, PR: projective radiography, and CBCT: cone-beam computed tomography.

For a quantitative validation of the observations, Figure 4.16 (a), Figure 4.16 (b), and Figure 4.16 (c) show the plots of PC against N for the different scan orbits in ROI#1, ROI#2, and ROI#3, respectively. In accordance with the visual inspection, LC consistently exhibits the highest PC in all ROIs. PC coefficients are higher for SE than for SC and PL in all ROIs, and, interestingly, are just slightly lower than LC in ROI#1. Notably, PC is higher for SC than PL in ROI#1 and ROI#3, but this pattern is reversed in ROI#2. PC may be object-dependent. ROI#1 contains more horizontal edges that cannot be adequately resolved with PL. Increasing N from 36 to 72 indicates higher PC coefficients for almost all reconstructions, but increasing N beyond 72 does not seem to improve PC much. The curves almost exhibit a plateau beyond 72 projections views.

In order to investigate the impact of the tomographic angle on the reconstructions, DTS reconstructions with the various scan orbits with different settings of α and β were performed. N was fixed to 72 in this case. Figure 4.16 (d) shows PC coefficients with PL, SC, LC, and SE for α ranging from 18° to 48° and β ranging from 10° to 40° . In opposite to the behavior with increasing N, increasing the tomographic angle continuously raises the PC for all the scan orbits. LC has the highest PC, with SE just slightly lower. PC for SE is superior to PL and SC, mainly for small tomographic angles.

Since the number of projection views, the tomographic angles, and the projection density are interdependent parameters, let us focus on the SE scan orbit and see how do these parameters together affect the DTS image quality. We define the linear projection density D as the ratio of N to the perimeter p of the SE scan orbit. p is given by

$$p = \frac{4d \tan \beta \sin \beta}{\tan \alpha} \pi(n, k) \quad (4.24)$$

where d is the source-to-isocenter distance in this case and $\pi(n, k)$ is the elliptic integral of the third kind defined as

$$\pi(n, k) = \int_0^{\pi/2} \frac{d\varphi}{(1 - n \sin^2 \varphi) \sqrt{1 - k^2 \sin^2 \varphi}} \quad (4.25)$$

where k is given by

$$k = \frac{\tan^2 \alpha - \tan^2 \beta}{\tan^2 \alpha} \quad (4.26)$$

and n is given by

$$n = \sqrt{\frac{\sin^2 \alpha - \sin^2 \beta}{\sin^2 \alpha}}. \quad (4.27)$$

It is worth noting that the SE scan orbit was not implemented based on an equal linear sampling of the spherical ellipse itself. Instead, it was conducted through an equal linear sam-

4. Spherical Ellipse Digital Tomosynthesis Scan Orbit

pling per arc length of a plane ellipse, with the sampled positions subsequently projected onto a sphere, as elaborated in Section 4.3. Consequently, the assumption of equal sampling on the spherical ellipse does not hold true due to the curvature of the sphere. However, this assumption remains valid for computing D , as any discrepancy in sampling, though present, is nearly negligible owing to the relatively small and close opening angles of the spherical ellipse. Furthermore, the density of the projections on the plane ellipse remains proportional to that on the spherical ellipse, thereby ensuring consistency in the analysis and results. Figure 4.17 illustrates the coronal slice shown in Figure 4.13 reconstructed for various combinations of N and α , with β fixed at 15° , resulting in different values of D . These reconstructed images demonstrate that increasing N while maintaining α at small values (23°) does not significantly enhance image quality (blue arrows), whereas increasing N with larger α values (53°) aids in improving image quality, particularly in reducing ripple artifacts emanating from the bronchoscope (red arrows). These observations are further supported by the quantitative results depicted in Figure 4.18. Figure 4.18 (a) illustrates the dependency of D on the chosen pair N and α while fixing β . For a fixed α , higher N values lead to higher D , indicating that the acquired projection views are closer to each other. Similarly, for a fixed N , larger α values result in lower D . Figure 4.18 (b), Figure 4.18 (c), and Figure 4.18 (d) display contour lines of PC as a function of N and α in ROI#1, ROI#2, and ROI#3, respectively. When traversing a contour line while maintaining D fixed, image quality improves with increasing N and α . Overall, the behavior depicted in these plots aligns with the findings presented in Figure 4.16, underscoring the more significant role of the tomographic angle compared to the number of projection views in DTS image quality.

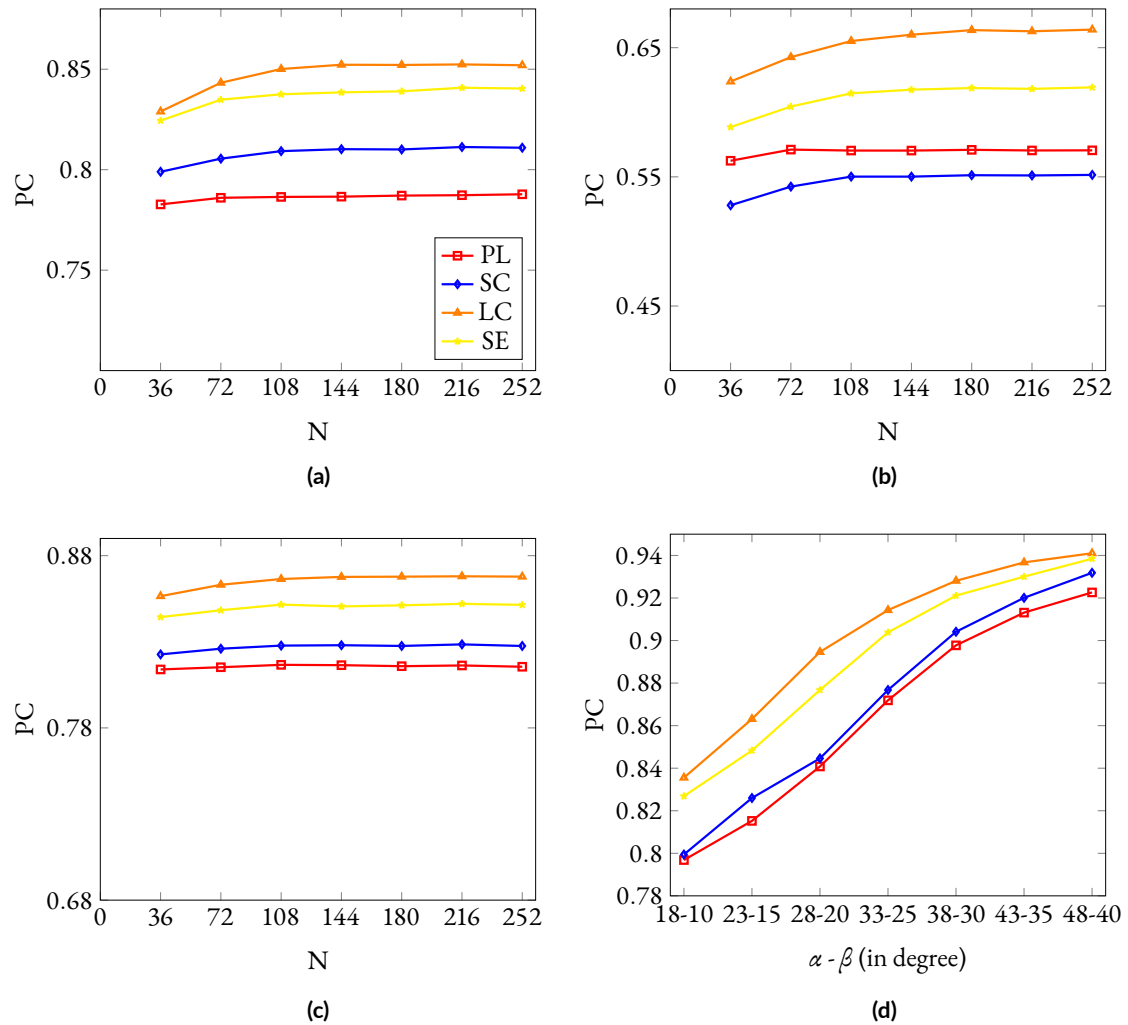


Figure 4.16: Pearson correlation in ROI#1 (a), in ROI#2 (b), and in ROI#3 (c) as a function of the number of projection views computed for the different scan orbits. Pearson correlation in ROI#3 (d) as a function of the tomographic angle computed for the different scan orbits. PL: pseudo-linear, SC: small circle, LC: large circle, and SE: spherical ellipse.

4. Spherical Ellipse Digital Tomosynthesis Scan Orbit

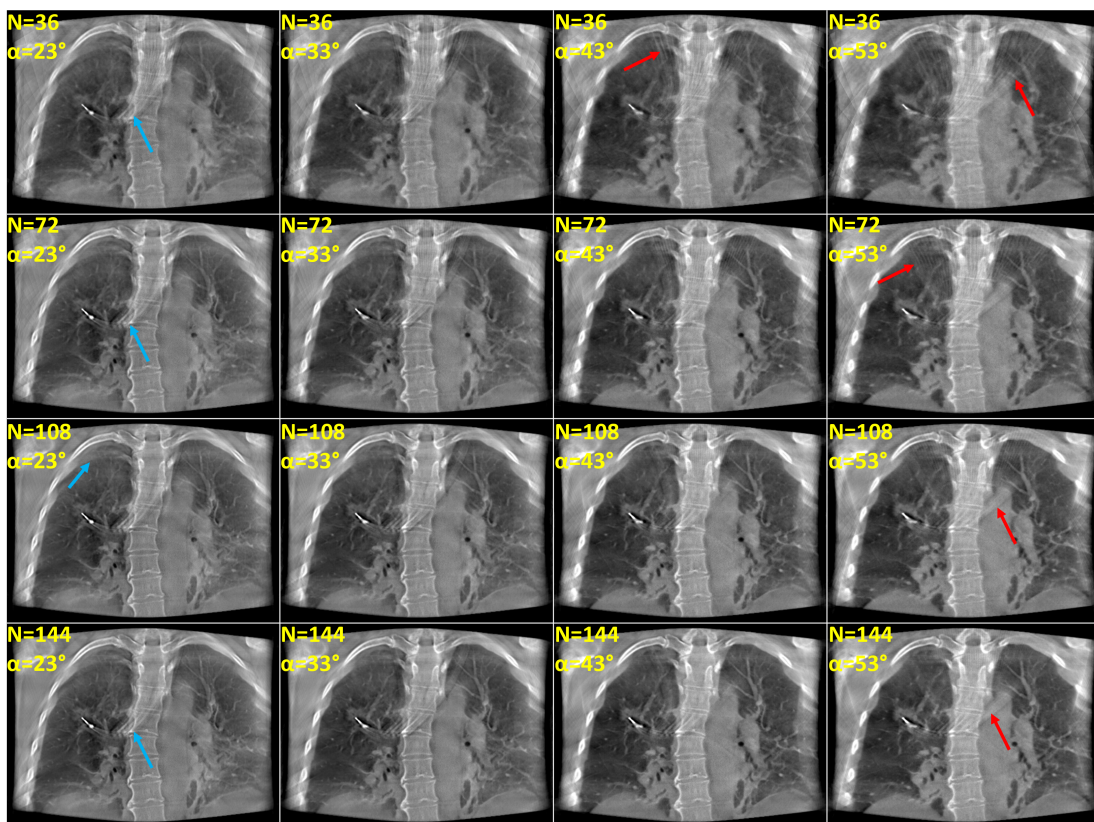


Figure 4.17: Reconstructed coronal slices using a spherical ellipse (SE) scan orbit with different combinations of the number of projection views N and large tomographic angle α .

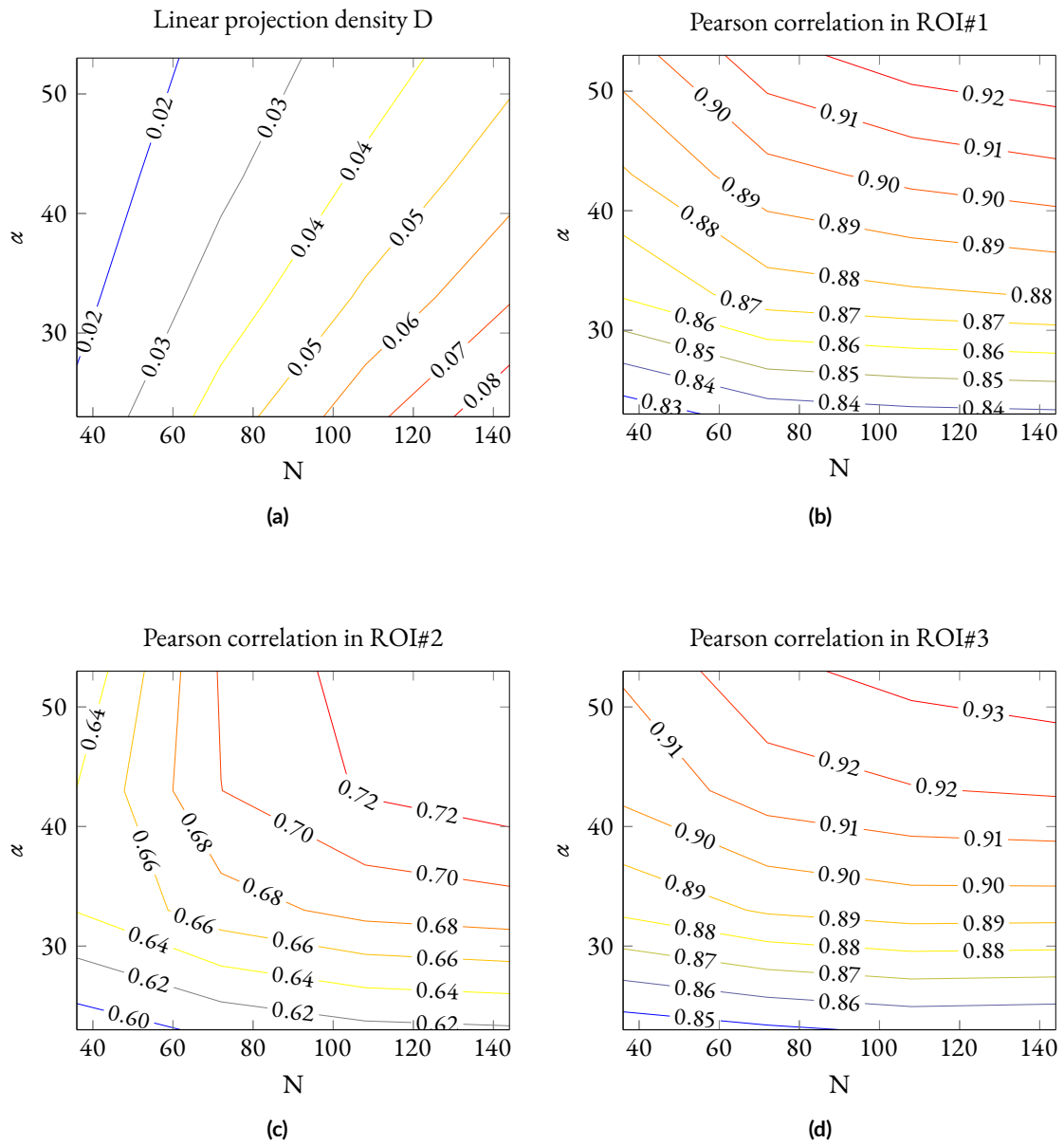


Figure 4.18: Contour plots of the linear projection density D as a function of the number of projection views N and the tomographic angle α (a). Contour plots of the Pearson correlation as a function of N and α computed with respect to the reference CBCT image in ROI#1 (b), ROI#2 (c), and ROI#3 (d).

4.6 Conclusion

In this chapter, we presented a novel C-arm-based spherical ellipse DTS scan orbit customized for bronchoscopy intervention guidance. Its benefits compared to conventional projective radiography (PR) and standard pseudo-linear and circular DTS scan protocols were investigated using simulated phantom and patient data. Our results indicate that the spherical ellipse DTS scan protocol is a promising alternative to PR yielding significantly improved bony and soft structures visibility. This is pivotal in navigational bronchoscopy for a proper navigation and to confirm tool-in-lesion and collect biopsy specimen from the accurate locations. Compared to PL, the proposed orbit suggests better removal of residual blur of objects lying outside the plane of interest. Relative to circular DTS, the spherical ellipse provides a good compromise between image quality and footprint requirements. If one is restricted to circular trajectories, only small circles can be performed due to space constraints in the operating room. Having the spherical ellipse in hand, it can be employed for an improved image quality. Next chapters explore ways to further improve DTS image quality by mainly investing in available patient-specific prior knowledge.

5

Prior CT to Intraoperative Digital Tomosynthesis Image Registration

Contents

| | | |
|------------|---|------------|
| 5.1 | Motivation | 88 |
| 5.2 | Proposed Algorithm | 89 |
| 5.2.1 | Multistage Framework | 89 |
| 5.2.2 | Cost Functions and Multimetric Registration | 92 |
| 5.2.3 | Multiresolution Strategy | 93 |
| 5.3 | Experiments | 94 |
| 5.3.1 | Data | 94 |
| 5.3.2 | DTS Projection Generation | 95 |
| 5.4 | Evaluation Metrics | 97 |
| 5.5 | Results | 97 |
| 5.6 | Conclusion | 109 |

IN the previous chapter, we have revealed a novel C-arm-based spherical ellipse digital tomosynthesis (DTS) scan trajectory and have shown its benefits over projective radiography (PR), cone-beam computed tomography (CBCT), and the standard DTS scan trajectories. In this chapter, we unveil a novel deformable 3D/3D CT-to-DTS registration algorithm to align preoperative CT images to intraoperative DTS images in the context of guiding bronchoscopy interventions. The motivation for registering prior CT images to intraoperative DTS images is first introduced, and then a detailed presentation of the registration algorithm is given. Experiments on simulated and real patient data as well as registration results are exposed and discussed.

5. Prior CT to Intraoperative Digital Tomosynthesis Image Registration

Large part of the research presented in this chapter has been published in the paper entitled "Deformable 3D/3D CT-to-Digital-Tomosynthesis Image Registration in Image-Guided Bronchoscopy Interventions" (in: *Computers in Biology and Medicine* 171 (2024) 108199. <http://dx.doi.org/10.1016/j.combiomed.2024.108199> [143]).

5.1 Motivation

Although DTS yields images with some depth information, there remains an opportunity for enhancement to achieve images with a quality sufficient-enough for a reliable needle biopsy guidance. Preprocedural CT scans are often performed prior to interventions for diagnosis and/or to plan the intervention. These patient-specific CT images usually possess a relatively high spatial resolution and share a fair amount of anatomical similarity with the intraoperative DTS images. Therefore, they can be employed to fill the niche in DTS-based bronchoscopy intervention guidance. However, CT-to-body divergence poses an obstacle to the appropriate use of CT images during the intervention. This divergence is mainly due to differences in patient's positioning and lung volumes between the preoperative and intraoperative states. It includes dynamic changes caused by respiratory motion and by the navigation of catheters and biopsy tools, and anatomic changes due to neuromuscular paralysis and repositioning of interventional tools. To accommodate for this divergence, a CT-to-DTS registration is required.

CT-to-DTS image registration can be addressed according to two approaches: 2D/3D image registration and 3D/3D image registration. 2D/3D image registration seeks to align the 3D CT volume with the 2D projections of the DTS image. Numerous are the techniques for 2D/3D registration that have been proposed in existing literature. Frysck et al. made use of Grangeat's relation to reduce the computational workload associated with the forward and backward projection steps that are commonly used in most 2D/3D registration methods [144]. While this approach significantly enhanced computational efficiency, it is limited to transformations that map planes to other planes. This is not applicable in the chest region, where the potential for fully elastic deformations is high. Additionally, various deep learning-based approaches have been developed to tackle the 2D/3D registration problem. These methods involve constructing regression models using statistical deformation models and performing regression on B-spline transform coefficients through convolutional neural networks, utilizing prior information [145, 146]. Tian et al., for instance, predicted deformation fields based on regression coefficients, but the registration network used in such techniques is patient-specific [147], which may yield inaccurate results in clinical practice. Vijayan et al. recently introduced a 2D/3D registration algorithm designed to align 3D volumes (preoperative CT or intraoperative CBCT) with intraoperative 2D projective fluoroscopy for

image-guided transbronchial interventions [148]. Their algorithm relies on conducting a series of locally rigid registrations within regions of interest surrounding various targets. Nevertheless, local rigidity is not a realistic assumption for lesions located at the lung periphery or in regions characterized by sliding motion. During the period between the prior CT scan and the intervention, complex local and global deformations may occur.

The second approach centers on 3D/3D registration, involving the alignment of the 3D CT volume with the 3D DTS volume. This approach presents challenges due to the blurred and smeared anatomical structures in DTS images, and as a result, less research has been dedicated to this method. Godfrey et al. conducted a study on the registration of preoperative CT images with on-board DTS images for target localization in external beam radiotherapy [149]. However, their work focused solely on rigid motion and did not account for tissue deformations.

CT-to-CT registration of chest images is already a complex endeavor, primarily because of the intricate and distinctive lung structure, its high deformability, and its nonuniform changes in intensity associated with breathing. This process becomes even more demanding when attempting to register CT images to DTS images due to the complex anisotropic resolution characteristics of DTS. Godfrey et al. demonstrated that prior CT data lack sufficient similarity to intraoperative DTS data, making precise registration challenging, and suggested a DTS-to-DTS registration approach [149].

Therefore, in the light of above, we have proposed over the course of this doctoral work a novel deformable 3D/3D CT-to-DTS registration algorithm spatially aligning preoperative CT images to intraoperative DTS images for image-guided transbronchial needle biopsy interventions. The multistage, multiresolution registration algorithm relies on simulating a prior DTS image from the prior CT image and subsequently registering it to the intraoperative DTS image. A comprehensive presentation of the proposed algorithm is detailed in the subsequent sections, including details on experiments conducted using both simulated and real patient bronchoscopy data, along with the corresponding observed results.

5.2 Proposed Algorithm

5.2.1 Multistage Framework

A parametric registration algorithm can be expressed as an optimization problem in the following form:

$$\hat{T}_\mu = \underset{T_\mu}{\operatorname{argmin}} C(T_\mu; I_f, I_m) \quad (5.1)$$

5. Prior CT to Intraoperative Digital Tomosynthesis Image Registration

where I_f is the fixed image, I_m is the moving image, C is the cost function or metric that defines the quality of alignment, T_μ is the transformation spatially aligning I_m to I_f , and μ is the vector enclosing the transformation parameters. The cost function is commonly expressed in the following form:

$$C(T_\mu; I_f, I_m) = -S(T_\mu; I_f, I_m) + \gamma P(T_\mu) \quad (5.2)$$

where S is a similarity measure, P is a penalty term introduced to force some constraints on T_μ , and γ is a coefficient weighting the similarity against the regularization.

The proposed registration framework is depicted in Figure 5.1. It involves two key inputs: a preoperative CT image, and an intraoperative DTS image. As mentioned in the previous section, given the challenges associated with CT-to-DTS registration, we generate a prior DTS image by simulating a DTS image from the preprocedural CT data. This is achieved by forward projecting the preprocedural CT image using the same system geometry employed for the intraoperative DTS scan. The digitally reconstructed radiographs (DRRs) are then reconstructed to produce the prior DTS image. The intraoperative DTS image serves as the fixed image (I_f) of the registration algorithm, while the prior DTS image serves as the moving image (I_m).

The registration of the prior DTS image to the intraoperative DTS image is integrated into a multistage framework comprising four distinct stages as illustrated in Figure 5.1. These stages are outlined as follows:

1. Stage 1: Affine registration using a bone mask. Given the diversity of structures within the chest region, each with distinct intensity (e.g., ribs and vessels), the registration process may be biased towards certain structures, potentially neglecting others (e.g., the rib cage can have a strong influence on the similarity metric and be well aligned at the cost of the small vessels). To address this, a bone mask for the fixed image is employed at this stage. This initial registration step serves to account for overall pose differences between the two volumes and primarily aligns the rib cage.
2. Stage 2: Affine registration using a lung mask for the fixed image. This stage is focused on aligning the soft tissues within the lungs. These initial two affine registrations are crucial for providing a solid starting point for subsequent deformable registrations.
3. Stage 3: Elastic registration using the lung mask for the fixed image. This step considers elastic deformations in the lung region.
4. Stage 4: Elastic registration using a mask for the fixed image defined as a ROI surrounding the target lesion. The registration is concentrated on this specific ROI, as precise alignment is primarily required for the lesion and its vicinity.

5.2. Proposed Algorithm

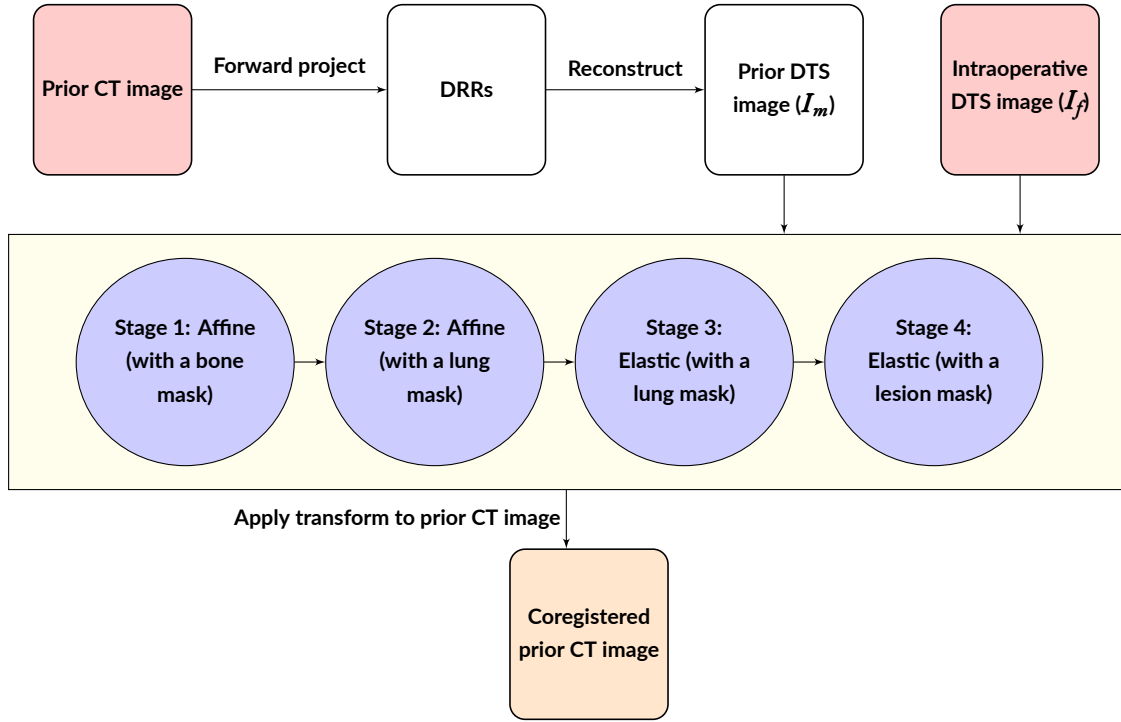


Figure 5.1: Illustration of the proposed deformable 3D/3D CT-to-DTS registration algorithm. The digitally reconstructed radiographs (DRRs) are computed by forward projecting the prior CT image according to the same DTS acquisition geometry as the intraoperative DTS image, and are then reconstructed to obtain the prior DTS image. The inputs of the registration are the intraoperative DTS image (fixed image) and the prior DTS image (moving image). The registration is performed at four stages. At stage 1: affine registration using a bone mask for the fixed image. At stage 2: affine registration using a lung mask for the fixed image. At stage 3: elastic registration modeled by a coarse B-spline transform using the lung mask for the fixed image. At stage 4: elastic registration modeled by a finer B-spline transform using a mask for the fixed image defined as a cuboid surrounding the target lesion. To obtain the registered prior CT image, the composition of all four transforms is applied to the prior CT image [143].

The elastic transformations at stage 3 and stage 4 are modeled as cubic B-splines [150]. These registration steps are executed sequentially, with the output transformation from one stage serving as input for the next. To obtain the registered prior CT image, the composition of all the transforms is applied to the prior CT image.

The mask used at stage 4 is a simple cuboid defined around the lesion, and excluding bones and the bronchoscope. All registration steps are carried out using the Elastix software [151, 152]. Precise mask definition in DTS images is challenging due to factors such as geometric distortions, streaking artifacts, inaccuracies of CT values, and the overlapping of structures from different DTS slices. In this study, the bone mask and lung mask for the intraoperative DTS images are determined by thresholding the intraoperative CBCT images.

5. Prior CT to Intraoperative Digital Tomosynthesis Image Registration

It is important to note that the automatic generation of such masks for DTS images without the use of CBCT images is a topic beyond the scope of this thesis and is a subject for future research.

5.2.2 Cost Functions and Multimetric Registration

Various cost functions are specified for the different stages of the registration process. The normalized correlation coefficient (NCC) is employed as a similarity metric for the affine registrations at stage 1 and stage 2, and no regularization is incorporated. NCC accommodates for global intensity variations stemming from the distinct spectral characteristics of CT and C-arm CBCT devices, including differences in X-ray spectra, X-ray filters, and detector responses. It is defined as

$$NCC(\mu; I_f, I_m) = \frac{\sum_{x_i \in \Omega_f} (I_f(x_i) - \bar{I}_f) (I_m(T_\mu(x_i)) - \bar{I}_m)}{\sqrt{\sum_{x_i \in \Omega_f} (I_f(x_i) - \bar{I}_f)^2 \sum_{x_i \in \Omega_f} (I_m(T_\mu(x_i)) - \bar{I}_m)^2}} \quad (5.3)$$

where x_i are the samples drawn from I_f , $\bar{I}_f = \frac{1}{|\Omega_f|} \sum_{x_i} I_f(x_i)$ and $\bar{I}_m = \frac{1}{|\Omega_m|} \sum_{x_i} I_m(x_i)$ are the average values for I_f and I_m , respectively. At stage 3, a combination of multiple metrics is utilized to form a multimetric cost function, which is expressed as follows

$$C(T_\mu; I_f, I_m) = \frac{1}{\sum_{i=1}^N w_i} \sum_{i=1}^N w_i C_i(T_\mu; I_f, I_m) \quad (5.4)$$

where w_i are user-defined weights. At this stage, a combination of NCC and the sum of squared tissue volume differences (SSTVD) [153, 154] is employed. SSTVD is defined as

$$SSTVD(\mu; I_f, I_m) = \sum_{x_i \in \Omega_f} [V_{I_f}(x_i) - V_{I_m}(T_\mu(x_i))]^2 \quad (5.5)$$

where $V_{I_f}(x_i)$ and $V_{I_m}(x_i)$ are tissue volumes in a voxel in I_f and its corresponding region in I_m , respectively, and Ω is the overlapping lung region between the two images. This metric reduces the disparity in the local tissue volumes within the lungs between matched regions. Additionally, a regularization term in the form of bending energy (BE) penalty is introduced

at this stage. BE is defined as

$$\begin{aligned}
 BE(\mu) = \frac{1}{V} \sum_x \sum_y \sum_z \left(\frac{\partial^2 T}{\partial x^2} \right)^2 + \left(\frac{\partial^2 T}{\partial y^2} \right)^2 + \left(\frac{\partial^2 T}{\partial z^2} \right)^2 \\
 + 2 \left(\frac{\partial^2 T}{\partial x \partial y} \right)^2 + 2 \left(\frac{\partial^2 T}{\partial x \partial z} \right)^2 + 2 \left(\frac{\partial^2 T}{\partial y \partial z} \right)^2 \quad (5.6)
 \end{aligned}$$

where V is the volume of I_f . This component involves the calculation of second-order spatial derivatives of the transformation. Although computationally demanding, it is essential to penalize abrupt deviations and prevent folding, which are highly probable in lung registration. At stage 4, NCC is utilized as a similarity metric, and the BE penalty term is incorporated as well.

The weights assigned to the similarity metrics and the penalty term are patient-specific and vary depending on the specific application. In this work, a heuristic approach was adopted to determine these weights and strike a balance of the conflicting deformations of the different metrics, promoting a compromise that upholds both the smoothness of the deformation field and the requisites of the multiple metrics. The automated selection of such weights, especially tailored for bronchoscopy data registration, was beyond the scope of this thesis and is an area of exploration in future research. The adaptive stochastic gradient descent serves as the optimizer in this process [155, 156]. A total of one thousand iterations are carried out at each stage, and the remaining parameters are kept in their default settings in the Elastix software [151, 152].

5.2.3 Multiresolution Strategy

Since the likelihood of successful registration is greater when dealing with less complex data, a multiresolution approach for the image data with a Gaussian image pyramid is employed. Five resolution levels are defined and different pyramid schedules are applied at the various stages of the registration. Five levels are needed because the initial alignment of the fixed and moving images is relatively poor. The pyramid schedule defines the amount of blurring and downsampling performed at each resolution level in all three dimensions. The smoothing and downsampling factors f used at each resolution level and each stage are provided in Table 5.1. Given that DTS image resolution is highly anisotropic and predominantly low in the depth dimension, blurring and downsampling are exclusively applied in the in-plane directions. At stage 3 and stage 4, in addition to the image pyramid schedule, we employ a multigrid strategy. This strategy initiates with a coarse control point grid at the first level and progressively refines it at subsequent resolution levels for the B-spline transforms. This way, coarse deformations are modeled first, aligning large structures elastically deformed, then at higher levels

5. Prior CT to Intraoperative Digital Tomosynthesis Image Registration

smaller structures are accommodated. The grid spacings s at the various levels and stages are summarized in Table 5.1.

| <i>Level</i> | | 0 | 1 | 2 | 3 | 4 |
|--------------|-----|----|----|----|----|---|
| Stage 1 | f | 16 | 8 | 4 | 2 | 1 |
| Stage 2 | f | 16 | 8 | 4 | 2 | 1 |
| Stage 3 | f | 16 | 8 | 4 | 2 | 1 |
| | s | 64 | 64 | 32 | 16 | 8 |
| Stage 4 | f | 4 | 3 | 2 | 1 | 1 |
| | s | 40 | 40 | 20 | 10 | 5 |

Table 5.1: Downsampling factors f and control point grid spacings s (in mm) used at the different stages and different resolution levels [143].

5.3 Experiments

5.3.1 Data

In order to take the complex chest anatomy into account, experiments on real patient bronchoscopy data were conducted. Datasets comprising six pairs of planning CT images and intraoperative CBCT scans (including projection images and reconstructed images) of six patients have been selected to evaluate the performance of the proposed registration algorithm. These datasets were collected while planning and monitoring CBCT-guided bronchoscopy procedures conducted at CHI Memorial’s Buz Standefer Lung Center in Chattanooga, TN, USA. Random samples including detected lesions of different types, sizes, shapes, and locations were selected. Only cases where patients developed atelectasis during the intervention were excluded from the original dataset, since their CBCT scans do not show the target lesion to be registered. Patient demographics and lesion characteristics for the six cases are portrayed in Table 5.2. These selected cases showcase a diverse range of bronchoscopy scenarios as the average lesion size for all patients included in this study is 20.2 mm and the percentages of RUL, RLL, RML and LUL lesion locations are 32%, 32%, 2%, and 21%, respectively (RUL: right upper lobe, RLL: right lower lobe, RML: right middle lobe, LUL: left upper lobe). The planning CT images were acquired four days to seven weeks (three weeks on average) before the bronchoscopy interventions, using CT devices from various manufacturers. All the intraoperative CBCT images were obtained using the same C-arm device (AXIOM Artis dTA, Siemens Healthcare GmbH, Erlangen, Germany). During each procedure, two to three CBCT scans were performed at different time points. For this study, we exclusively utilized

5.3. Experiments

the CBCT scans performed at the very end of the procedure to confirm tool-in-lesion. These CBCT images depict a flexible bronchoscope inserted throughout the patient's trachea and directed towards a target lesion, along with a transbronchial biopsy needle inserted into the lesion. Figure 5.2 illustrates image examples featuring a coronal slice of a CBCT image, along with the corresponding masks for the bones, lung, and lesion, utilized in the registration process.

| Case | Sex | Height (m) | Weight (Kg) | BMI (Kg/m ²) | Size (mm) | Location | Diagnosis (Pathology) |
|------|-----|------------|-------------|--------------------------|-----------|----------|--|
| 1 | M | 1.73 | 78.4 | 26.3 | 9.2 | RUL | Adenocarcinoma |
| 2 | M | 1.78 | 64.4 | 20.4 | 18 | RLL | Fibroelastosis with focal foreign material |
| 3 | M | 1.68 | 59.6 | 21.2 | 15 | RUL | Adenocarcinoma |
| 4 | F | 1.63 | 59.0 | 22.3 | 52 | RML | Necroinflammatory debris |
| 5 | M | 1.75 | 81.6 | 26.6 | 21 | LUL | Mycobacterium Gordonae |
| 6 | M | 1.78 | 56.7 | 17.9 | 37 | RUL | Adenocarcinoma |

Table 5.2: Patient demographics and lesion characteristics of each case. M: male, F: female, BMI: body mass index, RUL: right upper lobe, RLL: right lower lobe, RML: right middle lobe, LUL: left upper lobe.

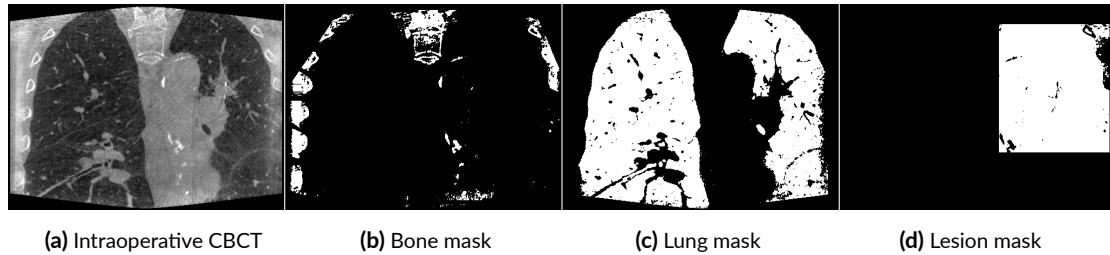


Figure 5.2: Image examples of an intraoperative CBCT coronal slice (a) and its associated bone (b), lung (c), and lesion masks (d).

5.3.2 DTS Projection Generation

To generate the intraoperative DTS projection images, we examined three different scenarios:

1. "*sim_SE*": Simulated spherical ellipse DTS scan
2. "*real_PL*": Real pseudo-linear DTS scan
3. "*sim_PL*": Simulated pseudo-linear DTS scan

5. Prior CT to Intraoperative Digital Tomosynthesis Image Registration

"**sim_SE**": DTS projection images were simulated by forward projecting the CBCT images according to the C-arm-based spherical ellipse scan geometry introduced in Chapter 4 [139]. The source-to-isocenter distance and the source-to-detector distance are kept constant and set to 785 mm and 1200 mm, respectively. A flat-panel detector of 616×480 pixels was assumed with a pixel pitch of 0.616 mm. Poisson noise was added to the projection data with a photon flux set to 4.75×10^8 photons per cm^2 . Limited detector dynamics were also included in the simulation manifesting as a saturation effect, preventing all extinction values from exceeding 20.

"**real_PL**": Since real DTS data using the spherical ellipse scan orbit are unavailable, and in order to assess the performance of the proposed registration algorithm in realistic conditions, we opted to use the original projection images from the CBCT scans. Specifically, we selected a limited set of projection images acquired over a limited angular range of $\pm\alpha$. This emulates a real pseudo-linear DTS scan. To be able to reconstruct the DTS image, the set of projection data was processed using the same preprocessing pipeline (Siemens Healthcare GmbH, Erlangen, Germany) employed on the original projection images at the AXIOM Artis dTA workstation. The processing pipeline encompasses several steps, including the conversion of raw intensity data into extinction values and a series of correction steps mainly aiming to compensate for scatter and beam-hardening distortions.

"**sim_PL**": Given that it would be unfair to compare simulated DTS data generated using a spherical ellipse acquisition geometry with real DTS data obtained using a pseudo-linear acquisition geometry, and considering the unavailability of real spherical ellipse data, we considered the use of DTS data simulated using a pseudo-linear scan geometry. We emphasize here that the main objective was not to compare the performance of the registration algorithm across different scan geometries but rather to evaluate whether the algorithm's performance with simulated data remains consistent when applied to real data. We compare the registrations of simulated and real pseudo-linear data and anticipate a similar behavior with simulated and real spherical ellipse data. To simulate the DTS projection images, the intraoperative CBCT volume was forward-projected according to a pseudo-linear scan protocol. It is noteworthy that the source-to-isocenter distance, the source-to-detector distance, the dimensions of the flat-panel detector, the photon flux, and the saturation effect limit were all maintained at the same values as in the simulated spherical ellipse case. In the rest of this chapter, the large tomographic angle α was set to 23° , the small tomographic angle β was set to 15° , and the number of projection views N was fixed to 72, unless otherwise stated.

5.4 Evaluation Metrics

The evaluation of the registration results is conducted through both qualitative and quantitative assessments as described below. The difference images between the registered prior CT images and the intraoperative CBCT images are computed and qualitatively evaluated by visual inspection. Given that the main objective is to achieve an accurate registration particularly in the vicinity of the lesion, a ROI surrounding the lesion is delineated. Segmentation of the lesion in the registered prior CT image, V_{reg} , and in the intraoperative CBCT image, V_{ref} (presenting the ground truth), is performed. Since the lesions in our datasets exhibit high contrast with their surroundings, lesion segmentation is carried out through a straightforward thresholding method. The same threshold level is consistently applied across all three scenarios for each patient dataset. To quantitatively evaluate the proposed registration algorithm, the Dice coefficient (DC) and the average symmetric surface distance (ASSD) are computed. These metrics are defined as follows:

$$DC(V_{ref}, V_{reg}) = \frac{2|V_{ref} \cap V_{reg}|}{|V_{ref}| + |V_{reg}|} \quad (5.7)$$

where $|\cdot|$ denotes the cardinality, and

$$ASSD(V_{ref}, V_{reg}) = \frac{1}{|B_{V_{ref}}| + |B_{V_{reg}}|} \times \left(\sum_{x \in B_{V_{ref}}} d(x, B_{V_{reg}}) + \sum_{y \in B_{V_{reg}}} d(y, B_{V_{ref}}) \right) \quad (5.8)$$

where $B_{V_{ref}}$ and $B_{V_{reg}}$ are the border voxel sets of V_{ref} and V_{reg} respectively, $d(x, B) = \min_{y \in B} d(x, y)$ is defined as the distance of voxel x to a set of voxels B , and $d(x, y)$ is the Euclidean distance between the voxels x and y .

DC assesses the degree of matching between V_{ref} and V_{reg} , whereas ASSD quantifies the distance between their respective boundaries.

5.5 Results

The proposed registration algorithm was evaluated on patient bronchoscopy data to reflect real clinical conditions. For each dataset, the registration algorithm was assessed across all three scenarios, as described in Section 5.3.2. Table 5.3 provides an overview of the acquisition and reconstruction parameters for the prior CT image and intraoperative CBCT image for each patient. The volume size and voxel size for all intraoperative CBCT images are $512 \times 512 \times 379$ voxels and $0.5 \text{ mm} \times 0.5 \text{ mm} \times 0.5 \text{ mm}$, respectively. Given that the

5. Prior CT to Intraoperative Digital Tomosynthesis Image Registration

field of view (FOV) of the CT volume significantly exceeds that of the intraoperative CBCT volume and since the two volumes do not initially sufficiently overlap, preprocessing steps were applied to the prior CT volumes for a better initialization of the registration algorithm. The preprocessing includes resampling the prior CT volume to the same voxel size of the intraoperative CBCT volume. As the prior CT images include the abdominal region but the intraoperative CBCT images do not, a simple graphical user interface was utilized to crop the coronal and axial slices of the prior CT volume, excluding the abdomen. Additionally, a circular mask with a diameter of 512 voxels was applied to each axial slice to match the FOV of the CT volume with that of the CBCT volume. In the subsequent sections, the registration results of one of the cases will be shown, but the results from the other cases will be included in the quantitative analysis of the outcomes.

| Case | Prior CT | | | | | Intraoperative CBCT | | Duration (days) |
|------|--------------------|----------------------------|-----------------------------|------|-----------------------------|---------------------|---------------------|-----------------|
| | Tube voltage (kVp) | Scanner | Volume (voxels) | size | Voxel size (mm) | Tube voltage (kVp) | Scanner | |
| 1 | 120 | GE Optima | $512 \times 512 \times 203$ | | $0.7 \times 0.7 \times 1.5$ | 101.6 | Siemens AXIOM Artis | 4 |
| 2 | 120 | Siemens SOMATOM Definition | $512 \times 512 \times 372$ | | $0.8 \times 0.8 \times 1.0$ | 90 | Siemens AXIOM Artis | 4 |
| 3 | 120 | Philips Brilliance 64 | $512 \times 512 \times 369$ | | $0.8 \times 0.8 \times 0.8$ | 109 | Siemens AXIOM Artis | 9 |
| 4 | 100 | Siemens SOMATOM Definition | $512 \times 512 \times 390$ | | $0.7 \times 0.7 \times 0.8$ | 109 | Siemens AXIOM Artis | 46 |
| 5 | 120 | Siemens SOMATOM Definition | $512 \times 512 \times 404$ | | $0.8 \times 0.8 \times 0.8$ | 112.6 | Siemens AXIOM Artis | 32 |
| 6 | 120 | Siemens SOMATOM Definition | $512 \times 512 \times 478$ | | $0.8 \times 0.8 \times 0.8$ | 90 | Siemens AXIOM Artis | 22 |

Table 5.3: Acquisition parameters for the prior CT images and for the intraoperative CBCT images of each of the six patients. The duration in days between the two image acquisitions is shown for each patient.

Figure 5.3 illustrates the original prior CT image (a) of a patient (case 5) and the preprocessed prior CT image (b), and Figure 5.4 depicts the corresponding intraoperative CBCT image (a). For each image, we present one axial slice in the upper row, one coronal slice in the middle row, and one sagittal slice in the lower row. For the intraoperative CBCT image, the slices where the biopsy needle exists are illustrated, and the corresponding slices at the same

positions are shown for the preprocessed prior CT image. In order to depict the extent of deformations between the prior CT image and the intraoperative CBCT image, the difference between the preprocessed prior CT image and the intraoperative CBCT image is shown in Figure 5.4 (b). This image highlights the substantial geometric changes between the prior CT image and the intraoperative CBCT image, particularly within the lesion's region. Additionally, significant degrees of patient and respiratory motion artifacts are clearly discernible.

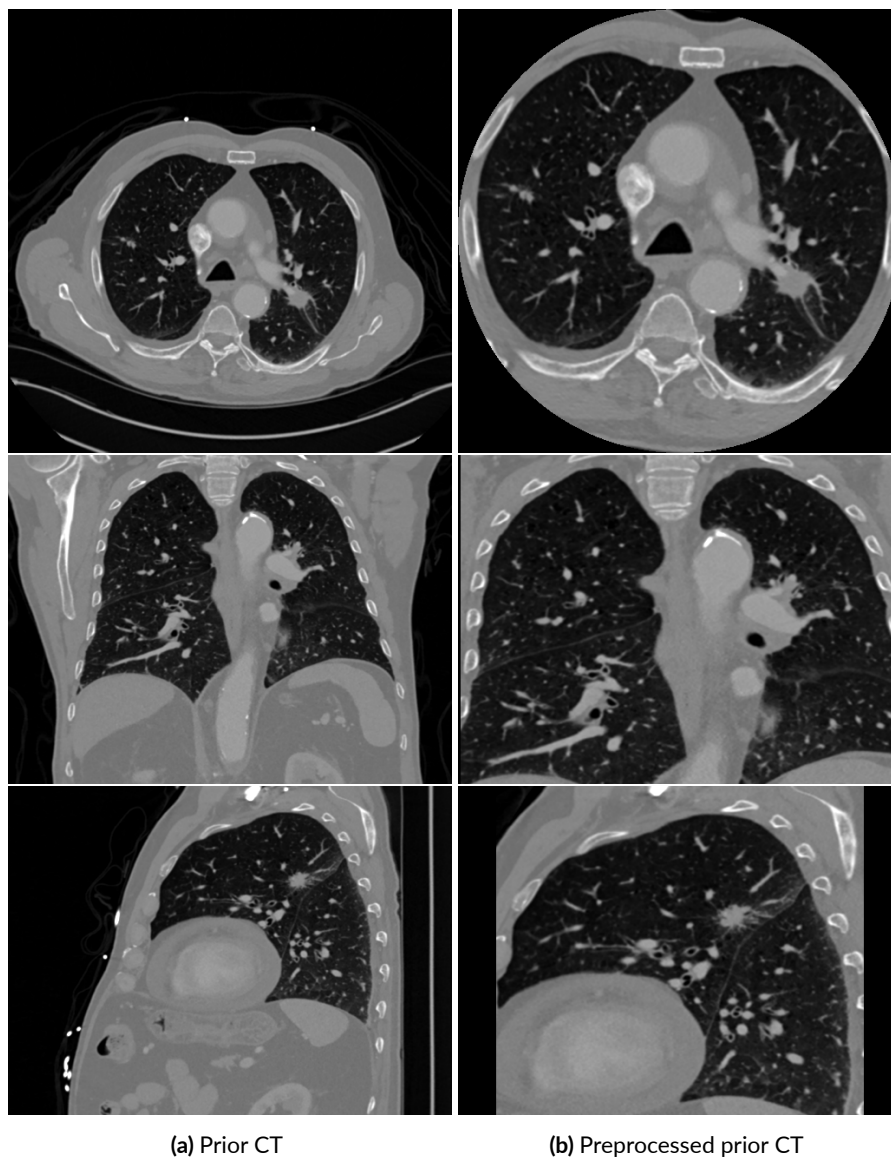


Figure 5.3: Image examples of a prior CT scan of a patient (case 5). One axial slice (top), one coronal slice (middle), and one sagittal slice (bottom) are shown. (a) Original prior CT image. (b) Preprocessed prior CT image.

5. Prior CT to Intraoperative Digital Tomosynthesis Image Registration

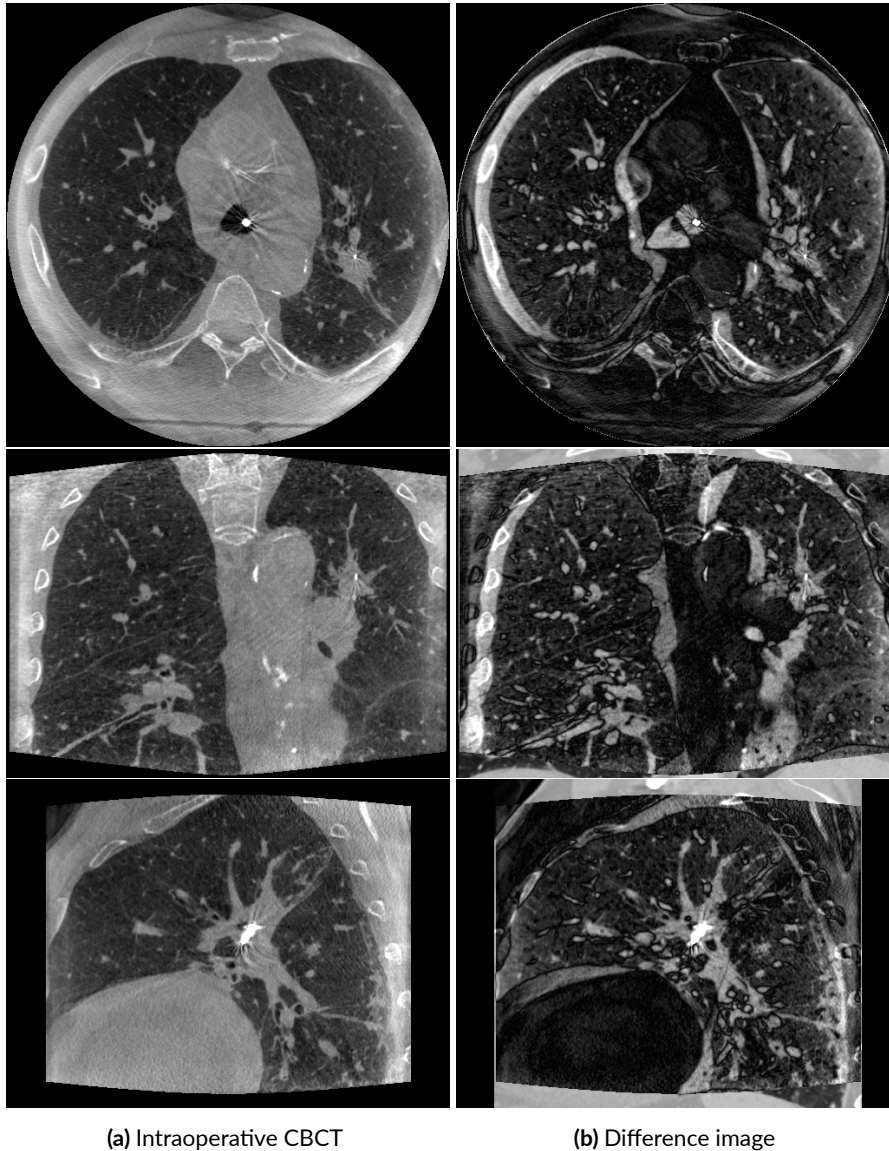


Figure 5.4: (a) Intraoperative CBCT image of the patient (case 5). (b) Difference image between the preprocessed prior CT image and the intraoperative CBCT image. One axial slice (top), one coronal slice (middle), and one sagittal slice (bottom) are shown. The slices with the same numbers are shown for the preprocessed prior CT in Figure 5.3 (b) and the intraoperative CBCT. The difference image in (b) reflects the large mismatch and deformation between the prior CT image and the intraoperative CBCT image.

In Figure 5.5 and Figure 5.6, the intraoperative DTS images and the prior DTS images are respectively shown for all three scenarios described in Section 5.3.2: simulated spherical ellipse acquisition "**sim_SE**" (a), simulated pseudo-linear acquisition "**sim_PL**" (b), and real pseudo-linear acquisition "**real_PL**" (c). The registration algorithm aligns the prior DTS image (moving image) to the intraoperative DTS image (fixed image). It is worth noting here the severe truncation and metal artifacts in the intraoperative DTS_{real_PL} image (Figure 5.5 (c)). These artifacts originate from surgical devices outside the FOV placed on the patient during

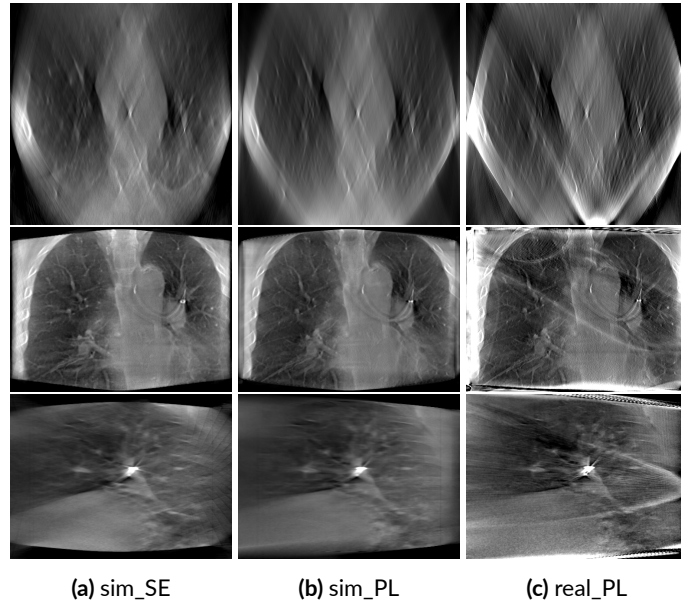


Figure 5.5: Intraoperative DTS images used as fixed images for the registration algorithm. (a) DTS_{sim_SE} data obtained assuming a simulated spherical ellipse scan geometry. (b) DTS_{sim_PL} data obtained assuming a simulated pseudo-linear scan geometry. (c) DTS_{real_PL} data obtained assuming a real pseudo-linear scan geometry.

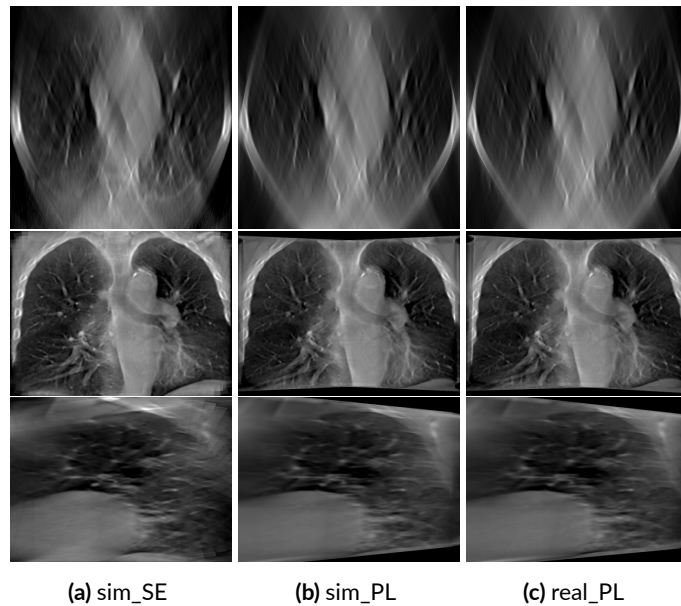


Figure 5.6: Prior DTS images used as moving images for the registration algorithm. (a) DTS_{sim_SE} data obtained assuming a simulated spherical ellipse scan geometry. (b) DTS_{sim_PL} data obtained assuming a simulated pseudo-linear scan geometry. (c) DTS_{real_PL} data obtained assuming a real pseudo-linear scan geometry.

5. Prior CT to Intraoperative Digital Tomosynthesis Image Registration

the intervention and are much less prominent in the intraoperative DTS_{sim_SE} (Figure 5.5 (a)) and DTS_{sim_PL} (Figure 5.5 (b)).

The registered prior DTS_{sim_SE} image at each stage of the registration process is illustrated in Figure 5.7. For comparison purposes, the corresponding slices from the intraoperative DTS_{sim_SE} image (e) are depicted as a reference. At each stage i , the composition of all the transformations from stages 1 to i is applied to the prior DTS_{sim_SE} image. For instance, at stage 4, the composition of the registration transforms from stages 1, 2, 3, and 4 is applied to the prior DTS_{sim_SE} image. Despite the notably poor resolution of the DTS images, a match between the registered prior DTS_{sim_SE} image at the last stage of the registration and the intraoperative DTS_{sim_SE} image can be clearly observed.

Due to the suboptimal image quality of the DTS_{sim_SE} images and their pronounced degradation with severe artifacts, and given that our primary interest lies in the registration of the prior CT image rather than the prior DTS_{sim_SE} image, we applied the registration transformations at the various stages to the preprocessed prior CT image. Figure 5.8 shows the registered prior CT image at the different stages. For reference, the same slices of the intraoperative CBCT image are presented in Figure 5.8 (e). At the last stage of the registration, there is a clear and accurate alignment of the different chest structures in the registered prior CT image with those in the intraoperative CBCT image. This alignment extends beyond the lung

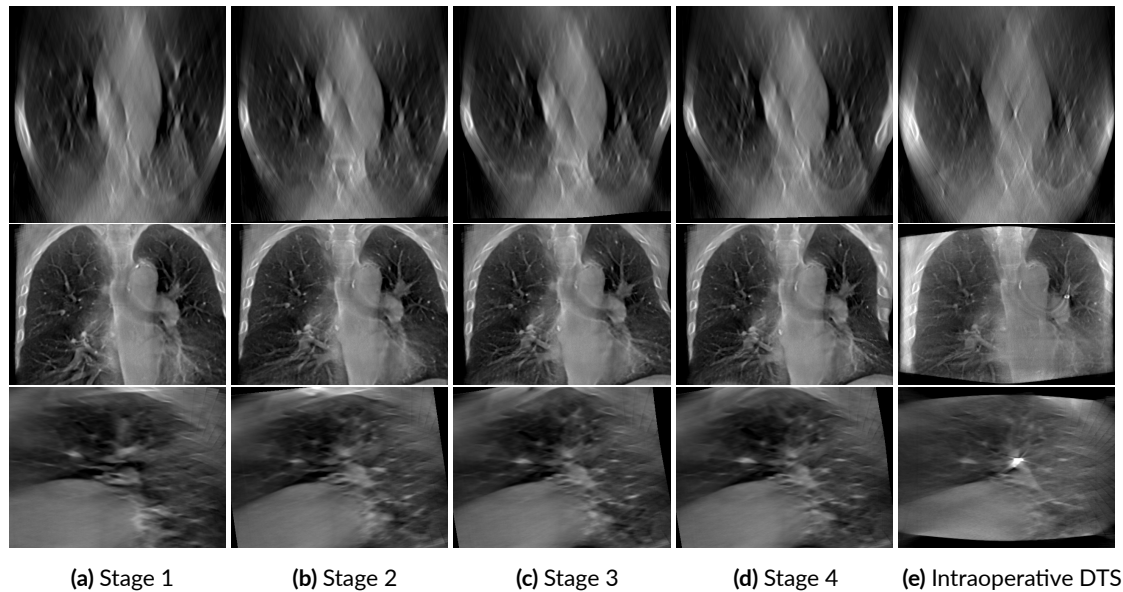


Figure 5.7: Registered prior DTS image at the different stages of the registration algorithm using the DTS_{sim_SE} data. (a) Registered prior DTS_{sim_SE} image at stage 1. (b) Registered prior DTS_{sim_SE} image at stage 2. (c) Registered prior DTS_{sim_SE} image at stage 3. (d) Registered prior DTS_{sim_SE} image at stage 4. (e) Intraoperative DTS_{sim_SE} image shown as the ground truth for the registration. At each stage, the composition of the registration transforms of the previous stages was applied to the prior DTS_{sim_SE} image.

boundaries, encompassing critical structures such as airways, vessels, and notably, the lesion, all of which are sufficiently well aligned.

In navigational bronchoscopy procedures, the bronchoscopist’s primary focus is on visualizing the target suspicious lesion and its surrounding anatomy. Less attention is directed toward the spine, bones, or even the pulmonary structures in the lobes other than those where the lesion is. Consequently, Figure 5.9 illustrates enlarged regions specifically including the lesion and its vicinity (ROIs highlighted in yellow in the intraoperative CBCT slices shown in Figure 5.8) at the different registration stages. To evaluate how closely the registered prior CT image aligns with the intraoperative CBCT image, we compute the difference of these two images. The set of the difference images corresponding to the various registration stages is presented on the right-hand side of Figure 5.9. In the case of a successful registration, we would anticipate a sparse difference image that predominantly displays the interventional tool. As evident, at stage 4 the lesion and all its adjacent structures in the registered prior CT image exhibit a remarkable alignment with the intraoperative CBCT image. In the difference image, nearly only the interventional tool is discernible, with no other edges or structures.

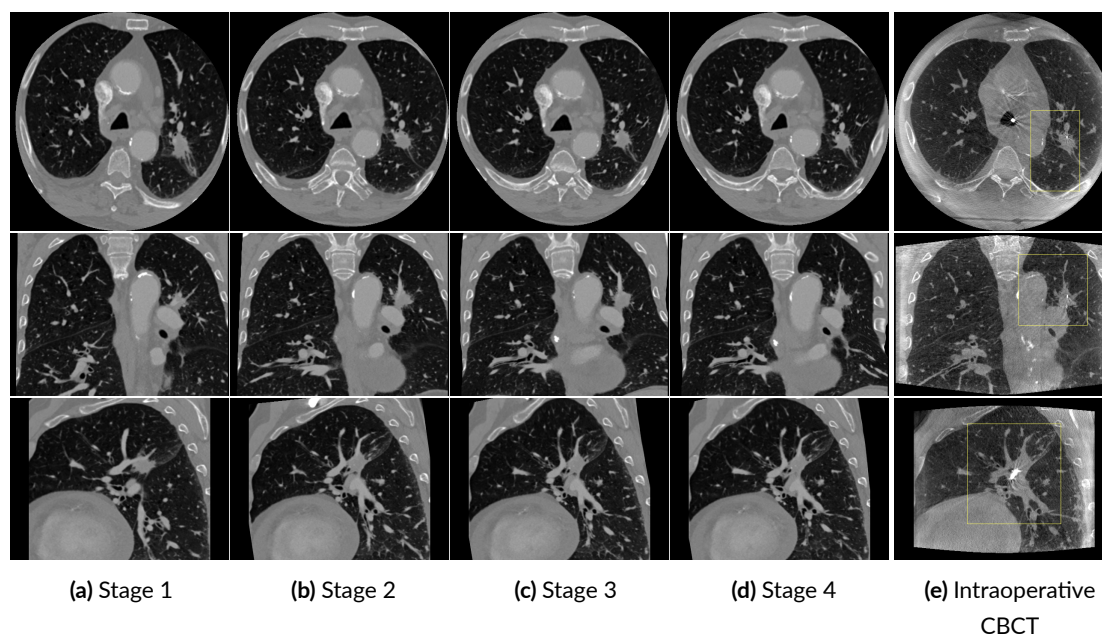


Figure 5.8: Registered prior CT image at the different stages of the registration algorithm using the $DTS_{sim,SE}$ data. (a) Registered prior CT image at stage 1. (b) Registered prior CT image at stage 2. (c) Registered prior CT image at stage 3. (d) Registered prior CT image at stage 4. (e) Intraoperative CBCT image shown as the ground truth for the registration. At each stage, the composition of the registration transforms of the previous stages was applied to the prior CT image.

5. Prior CT to Intraoperative Digital Tomosynthesis Image Registration

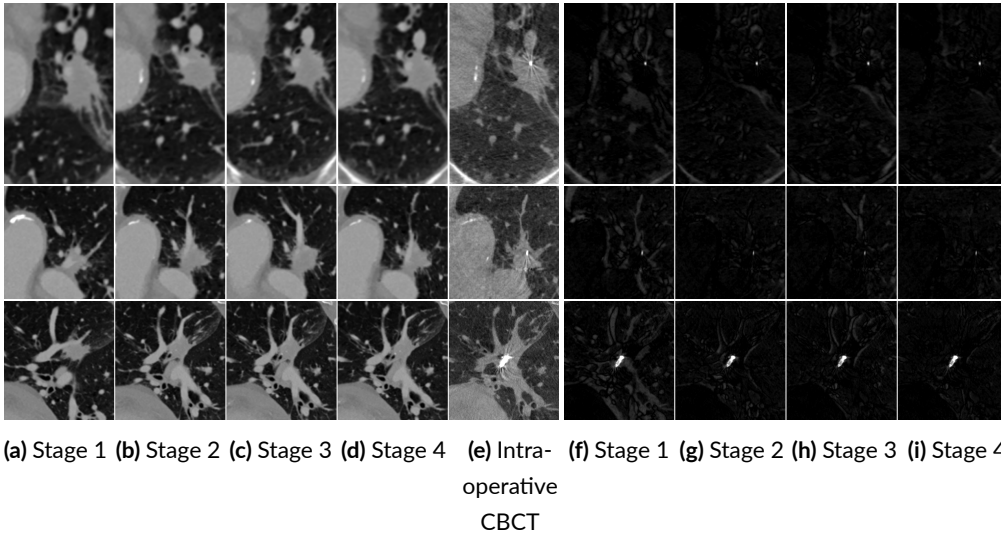


Figure 5.9: On the left: enlarged views of the ROIs highlighted in yellow in Figure 5.8 at the different stages of the registration algorithm using the DTS_{sim_SE} data. (a) Registered prior CT image at stage 1. (b) Registered prior CT image at stage 2. (c) Registered prior CT image at stage 3. (d) Registered prior CT image at stage 4. (e) Intraoperative CBCT image shown as the ground truth for the registration. Displayed window: [-1000 HU, 1000 HU]. On the right: the corresponding difference images of the registered prior CT image and the intraoperative CBCT image. Displayed window: [80 HU, 4400 HU].

In Figure 5.10 and Figure 5.11 are illustrated the prior CT registration results at the different stages using the DTS_{sim_PL} data. These figures showcase the same sets of axial, coronal, and sagittal slices as previously displayed for the sim_SE data. Similar to the results obtained with the sim_SE data, the registered image at stage 4 (Figure 5.10 (d)) exhibits a reasonably robust alignment with the target intraoperative CBCT image across the axial, coronal, and sagittal slices. This alignment is further corroborated by the difference images presented in Figure 5.11. Notably, the difference image at stage 4 is nearly sparse, except for the interventional tool, with only a few discernible edges along the contour of the lesion. These edges were not observed with the DTS_{sim_SE} data.

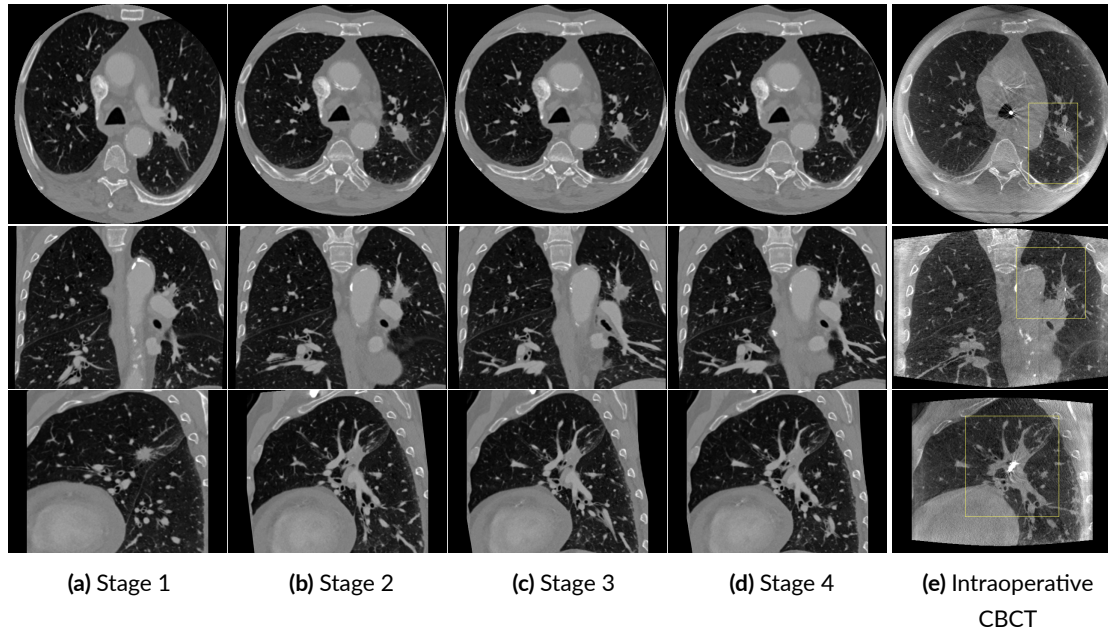


Figure 5.10: Registered prior CT image at the different stages of the registration algorithm using the DTS_{sim_PL} data. (a) Registered prior CT image at stage 1. (b) Registered prior CT image at stage 2. (c) Registered prior CT image at stage 3. (d) Registered prior CT image at stage 4. (e) Intraoperative CBCT image shown as the ground truth for the registration. At each stage, the composition of the registration transforms of the previous stages was applied to the prior CT image.

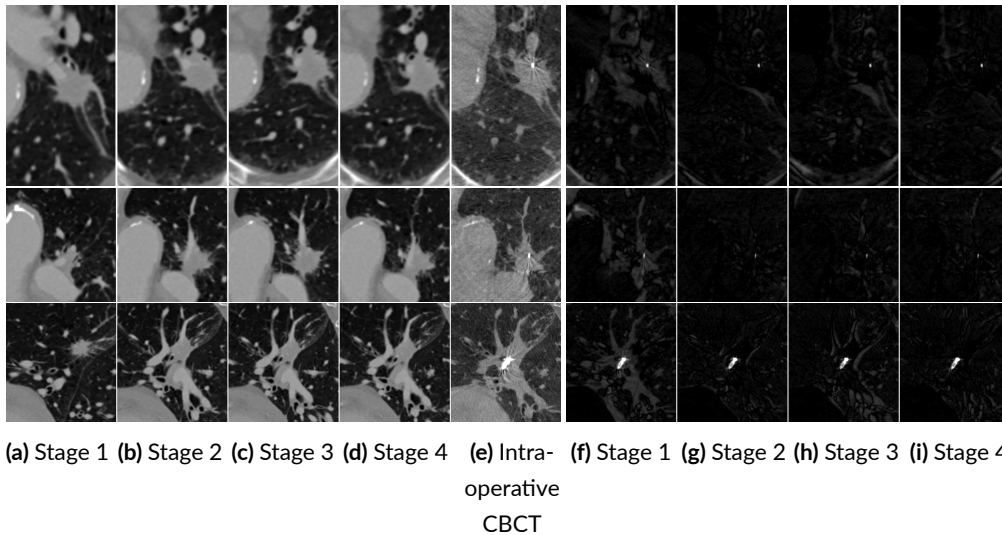


Figure 5.11: On the left: enlarged views of the ROIs highlighted in yellow in Figure 5.8 at the different stages of the registration algorithm using the DTS_{sim_PL} data. (a) Registered prior CT image at stage 1. (b) Registered prior CT image at stage 2. (c) Registered prior CT image at stage 3. (d) Registered prior CT image at stage 4. (e) Intraoperative CBCT image shown as the ground truth for the registration. Displayed window: [-1000 HU, 1000 HU]. On the right: the corresponding difference images of the registered prior CT image and the intraoperative CBCT image. Displayed window: [80 HU, 4400 HU].

5. Prior CT to Intraoperative Digital Tomosynthesis Image Registration

To evaluate the effectiveness of our proposed registration algorithm in a realistic clinical environment where various physical factors can degrade the quality of the data (e.g., truncation, cables and devices lying outside the FOV), we applied the registration algorithm to the DTS_{real_PL} data, obtained as described in Section 5.3.2. Figure 5.12 and Figure 5.13 show the registered prior CT images and the corresponding enlarged ROIs and difference images, respectively. Overall, the results demonstrate a close alignment of the registered prior CT image and the target intraoperative CBCT image. This alignment is particularly evident in the registered prior CT image at stage 4 as depicted in Figure 5.12 and further verified in the corresponding difference image shown in Figure 5.13. It is worth noting that the registration performance with real data is slightly less accurate compared to simulated data, as a few additional edges are noticeable in the difference images. This is expected due to the presence of significant truncation and pronounced metal and streaking artifacts in the intraoperative DTS_{real_PL} image. These artifacts, as shown in Figure 5.5 (c), result from devices positioned on the patient during the intervention and lying outside the FOV.

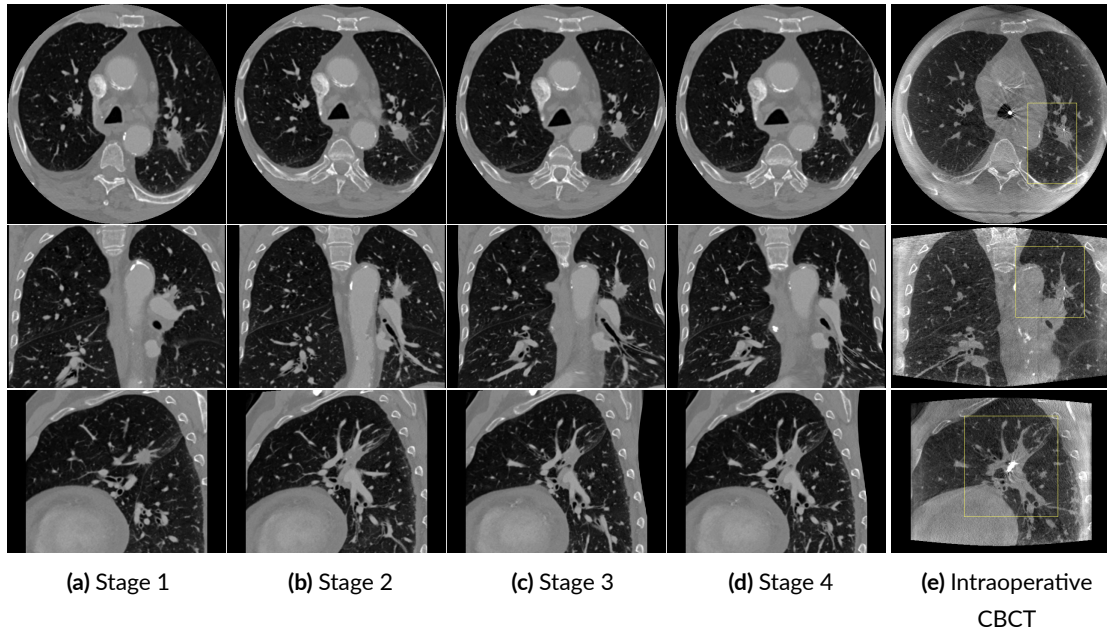


Figure 5.12: Registered prior CT image at the different stages of the registration algorithm using the DTS_{real_PL} data. (a) Registered prior CT image at stage 1. (b) Registered prior CT image at stage 2. (c) Registered prior CT image at stage 3. (d) Prior CT image at stage 4. (e) Intraoperative CBCT image shown as the ground truth for the registration. At each stage, the composition of the registration transforms of the previous stages was applied to the prior CT image.

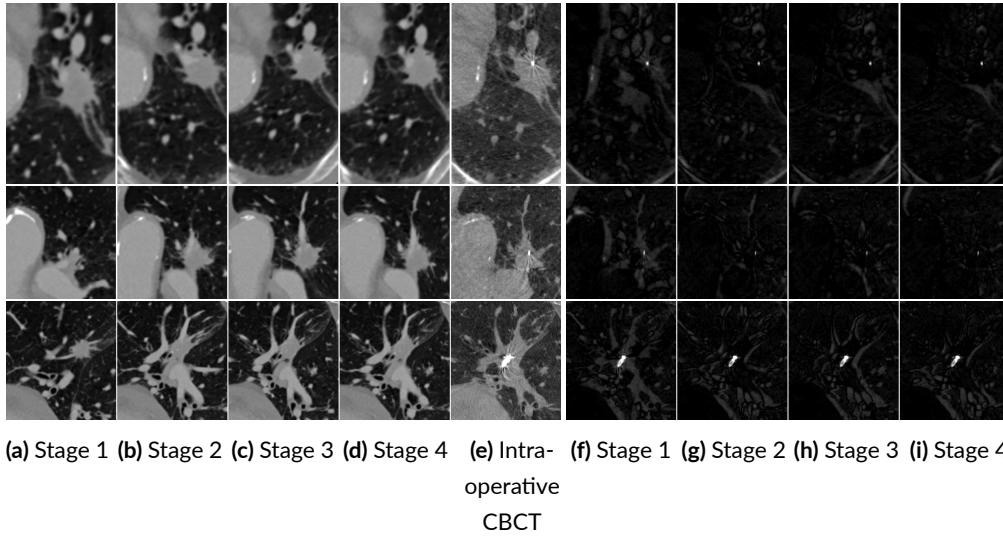


Figure 5.13: On the left: enlarged views of the ROIs highlighted in yellow in Figure 5.8 at the different stages of the registration algorithm using the DTS_{real_PL} data. (a) Registered prior CT image at stage 1. (b) Registered prior CT image at stage 2. (c) Registered prior CT image at stage 3. (d) Registered prior CT image at stage 4. (e) Intraoperative CBCT image shown as the ground truth for the registration. Displayed window: [-1000 HU, 1000 HU]. On the right: the corresponding difference images of the registered prior CT image and the intraoperative CBCT image. Displayed window: [80 HU, 4400 HU].

To quantitatively assess the performance of the registration algorithm, we computed the DC and the ASSD for all six cases and across all three scenarios, as detailed in Section 6.4. The results of this quantitative analysis are presented in Table 5.4. The DC measures the degree of overlap between the two volumes, with values closer to 1 indicating higher overlap. Conversely, the ASSD evaluates the alignment of the boundaries of the two volumes, with values closer to 0 signifying better alignment. Across the six patients, the mean DC values were as follows: 0.83 ± 0.03 , 0.80 ± 0.06 , and 0.74 ± 0.05 for the DTS_{sim_SE} data, the DTS_{sim_PL} data, and the DTS_{real_PL} data, respectively. On the other hand, the mean ASSD values were as follows: 0.61 ± 0.28 mm, 0.69 ± 0.33 mm, and 0.93 ± 0.43 mm for the DTS_{sim_SE} data, the DTS_{sim_PL} data, and the DTS_{real_PL} data, respectively. These reported quantitative measures align with the qualitative observations made during the visual inspection. Specifically, they indicate that the registration accuracy was slightly higher when using the simulated spherical ellipse data compared to simulated pseudo-linear data. The registration with real data exhibited a slightly lower level of accuracy compared to simulated data.

To evaluate the impact of different acquisition parameter configurations on the sensitivity of our proposed registration algorithm, Figure 5.14 (a) depicts the DC and ASSD plots for N fixed at 72 and varying α and β . In Figure 5.14 (b), the DC and ASSD plots are presented as functions of N , with α and β held constant at 23° and 15° , respectively. The results are showcased for case 5 using sim_SE data. It is evident that increasing the tomographic an-

5. Prior CT to Intraoperative Digital Tomosynthesis Image Registration

| Case | Metric | sim_SE | sim_PL | real_PL |
|------|--------------|--------|--------|---------|
| 1 | DC | 0.83 | 0.77 | 0.75 |
| | ASSD (in mm) | 0.32 | 0.42 | 0.47 |
| 2 | DC | 0.87 | 0.88 | 0.80 |
| | ASSD (in mm) | 0.24 | 0.23 | 0.36 |
| 3 | DC | 0.80 | 0.71 | 0.68 |
| | ASSD (in mm) | 0.86 | 0.99 | 1.14 |
| 4 | DC | 0.82 | 0.79 | 0.71 |
| | ASSD (in mm) | 0.86 | 1.05 | 1.38 |
| 5 | DC | 0.82 | 0.80 | 0.71 |
| | ASSD (in mm) | 0.55 | 0.62 | 0.96 |
| 6 | DC | 0.86 | 0.86 | 0.8 |
| | ASSD (in mm) | 0.84 | 0.84 | 1.28 |

Table 5.4: Quantitative results: the Dice coefficients (DC) and the average symmetric surface distances (ASSD) in mm computed on the target lesion segmented after the registration for each of the six patients' data and in all three scenarios. The segmentation of the lesion in the intraoperative CBCT is considered as the ground truth.

gles enhances the registration accuracy, while variations in the number of projections, within constant tomographic angles, have a relatively negligible effect. These observations align with the findings presented in Chapter 4, indicating that increasing N beyond 72 while holding tomographic angles at low values does not lead to further improvements in DTS image quality, elucidating the plateau observed in registration accuracy beyond this threshold.

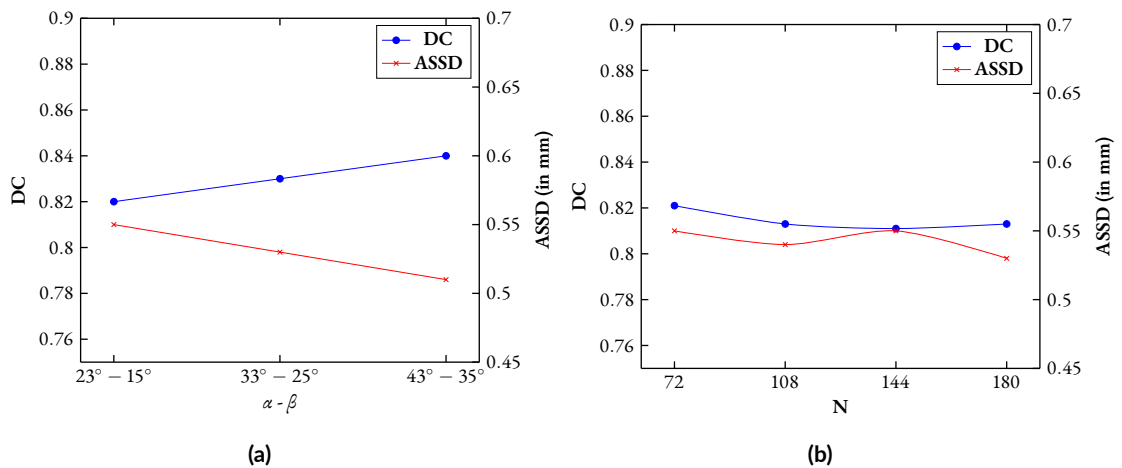


Figure 5.14: The Dice coefficient (DC) and the average symmetric surface distance (ASSD) computed on the target lesion segmented after the registration of case 5 for different settings of α and β while fixing N at 72 (a), and for different values of N while fixing α and β at 23° and 15°, respectively (b).

5.6 Conclusion

In this chapter, we presented a novel deformable 3D/3D registration algorithm designed to align prior CT images to intraoperative DTS images for guiding bronchoscopy interventions. The registration algorithm operates in a multistage, multiresolution manner, employing four stages that integrate both affine and elastic B-spline transformation models. These stages are designed to gradually align the diverse anatomical structures found within the chest region. Evaluations of the registration algorithm were conducted using both simulated and real bronchoscopy data of six patients. We considered simulated DTS data with a spherical ellipse scan geometry and both simulated and real DTS data with a pseudo-linear scan geometry. The evaluation encompassed both qualitative assessments through visual inspection and quantitative assessments using metrics such as the Dice coefficient and the average symmetric surface distance. The findings indicate a successful and accurate-enough registration mainly in the target nodule region and its vicinity. This registration algorithm paves the way for a novel prior-aided DTS reconstruction algorithm that uses the registration results to enhance intraoperative DTS image quality. This will be the subject of the next chapter.

5. Prior CT to Intraoperative Digital Tomosynthesis Image Registration

6

Prior-Aided Digital Tomosynthesis Image Reconstruction

Contents

| | | |
|-------|-------------------------------------|-----|
| 6.1 | Motivation | 112 |
| 6.2 | Proposed Algorithm | 115 |
| 6.3 | Experiments | 116 |
| 6.3.1 | Physical Phantoms | 117 |
| 6.3.2 | Patient Bronchoscopy Data | 119 |
| 6.4 | Evaluation Metrics | 119 |
| 6.5 | Results | 119 |
| 6.6 | Conclusion | 127 |

IN the previous chapter, we presented a deformable registration algorithm suitable for aligning preoperative computed tomography (CT) images to intraoperative digital tomosynthesis (DTS) images in the context of image-guided bronchoscopy interventions. The current chapter is dedicated to introduce a novel prior-aided DTS image reconstruction algorithm employing registered preoperative CT scans to enhance intraoperative DTS image quality. This chapter is initiated by exposing the motivations driving to this reconstruction algorithm, then the proposed algorithm is introduced. Experiments carried out on physical phantoms as well as on real patient bronchoscopy data are presented before revealing the observed results and their significance.

6.1 Motivation

As we have seen in the previous chapters, DTS imaging involves acquiring a limited number of discrete projection radiographs spanning a limited angular range. Relative to cone-beam computed tomography (CBCT), DTS is restricted in both its angular coverage and its angular sampling rate. Even in the best-case scenario of ideal computer simulations, reconstructing an accurate image under such acute data insufficiency is almost impossible without a priori information about the object to be reconstructed.

Preoperative CT scans are often performed days or weeks prior to bronchoscopy interventions for diagnosis or to plan the intervention. These patient-specific CT images are often of high quality and high spatial resolution compared to DTS images. A key observation is that there is a substantial overlap in anatomical information between these prior CT images and the intraoperative DTS images. Moreover, planning CT images could provide additional valuable clinical information not apparent in the intraoperative DTS ones due to the deterioration of DTS images with severe limited-angle artifacts. The deformations between prior scans and intraoperative scans stem solely from patient and respiratory movements, and the placement of the surgical tools. Therefore, prior CT scans, when incorporated properly, accommodate intraoperative DTS image reconstruction with potential prior knowledge.

Many are the iterative prior-based image reconstruction (PBIR) approaches that have been proposed in the literature for CT problems with data insufficiency. One important work in this context has been developed by Chen et al [157]. They introduced the Prior Image Constraint Compressed Sensing (PICCS) algorithm. The main idea is to minimize an objective function seeking a sparse reconstructed image as well as a sparse difference between the reconstructed image and a previously acquired prior image (L1 norm minimization). This algorithm was applied on sparse-view CT image reconstruction. In the same context, Stayman et al. [158] developed the Prior-Image-Registered Penalized-Likelihood Estimator (PIRPLE), a technique for integrating prior images into a model-based penalized likelihood reconstruction of sparse-view projection datasets. Jointly, since some changes between the prior and current image can arise from motion between scans, a rigid registration step of the prior to the current anatomy was included in the reconstruction. Dang et al. [159] extended the PIRPLE to the deformable PIRPLE (dPIRPLE) including a proper 3D elastic deformation model into the model-based iterative reconstruction method. In several sequential imaging scenarios, the main goal is to check for the difference between two consecutive scans, for example in measuring the tumor growth or visualizing the region of surgical change. In this context, Lee et al. [160] proposed a strategy for region of change (ROC) reconstruction. This strategy is based on the computation of the difference between the forward projections of a prior CT or CBCT image and the measured projections, after registering the prior image to the

current anatomy. The difference image is then reconstructed using a penalized-likelihood reconstruction technique with a compressed sensing-based regularization, highlighting the surgical change which occurred in the patient. This algorithm was also applied to sparse-view data. In the same spirit, Pourmorteza et al. [161] proposed a method called Reconstruction of Difference (RoD). They have included the prior image into the data fidelity term of the penalized-likelihood cost function and not just in the regularization term, in contrast to the conventional PBIR techniques. In the context of 4D intervention guidance, Kuntz et al. [162] developed an iterative reconstruction algorithm called Prior Image Dynamic Interventional Computed Tomography (PrIDICT). Using PrIDICT, it is possible to continuously reconstruct the time frame images from sparse-view datasets and a high quality prior image. It combines FDK reconstruction iteratively with the constraint that only few voxels of the image with high absolute values contain the desired information. PrIDICT has been extended to take into account the mismatching between different scans due to patient motion. Flach et al. [163] proposed the running prior technique which is composed of two steps: registration of the prior to the current anatomy then replacement of outdated projections by newly acquired projections. In the registration step a 3D/3D registration is performed. In [164], Flach et al. re-extended their work to a deformable 2D/3D registration. Most of the aforementioned PBIR algorithms have been applied to sparse-view CT or CBCT data and not to limited-angle or DTS data. Moreover, the priors have been always included in the body of the iteration of the reconstruction algorithm whereas the initialization has been overlooked.

DTS image reconstruction is characterized by an underdetermined system of linear equations where the number of voxels to be reconstructed is significantly higher than the number of projection data acquired. This translates to having more unknowns than equations and having many solutions that may fit the available data. Given that we are addressing a severely underdetermined problem in DTS image reconstruction, characterized by a vast nullspace and the measurement of only a small fraction of image information, the selection of the initial image is of significant importance. To clarify this importance, let us examine the reconstruction problem algebraically as a system of linear equations with just two independent variables for the sake of simplicity

$$\begin{pmatrix} p_1 \\ p_2 \end{pmatrix} = \begin{pmatrix} a_{11} & a_{12} \\ a_{21} & a_{22} \end{pmatrix} \begin{pmatrix} f_1 \\ f_2 \end{pmatrix} \quad (6.1)$$

Applying the ART algorithm to solve this system is intuitively illustrated in Figure 6.1. Each row of this linear system represents an equation depicting a line. The solution to this system is found at the intersection of these lines. In the ART process, an initial approximation of the solution is made (zero for f_1 and f_2 in the case shown in the graph), and is fol-

6. Prior-Aided Digital Tomosynthesis Image Reconstruction

lowed by iterative steps of projecting the current estimate onto each line alternately. In the inner ART loop, the process entails projecting the current estimate onto a single line from the system's equations. Conversely, in the outer ART loop, a step involves projecting the current estimate onto all lines (in this case, both). The system shown above is an ideal square consistent system having a unique solution. However, as mentioned previously, DTS image reconstruction is characterized by an underdetermined linear system having less equations than variables. Therefore, considering the two-variable system, we would have just one equation. This system is illustrated in Figure 6.2 (a). In this particular scenario, it is evident that the ART concludes after just one projection, and the final solution is dependent upon the first guess. Besides underdeterminedness, ill-conditionedness is another property that holds significance in DTS image reconstruction. Figure 6.2 (b) depicts a schematic of the ART cycle tailored for an ill-conditioned system featuring two variables. The system's condition is tied to the angle formed between the two lines representing its equations. A smaller angle indicates poorer conditioning of the system. The cycle exhibits slow progress towards the intersection of the lines, which represents the system's solution. Considering that we aim for a solution with just few iterations and that truncated iterations are a common practice, the ill-conditioned nature behaves comparably to underdeterminedness. In such instances, ART cycles display slow advancements in refining the solution estimate. The deviation from the outcome of the initial projection cycle is gradual, indicating a slow convergence towards an accurate solution. Consequently, this yields a solution estimate that heavily relies on the initial guess.

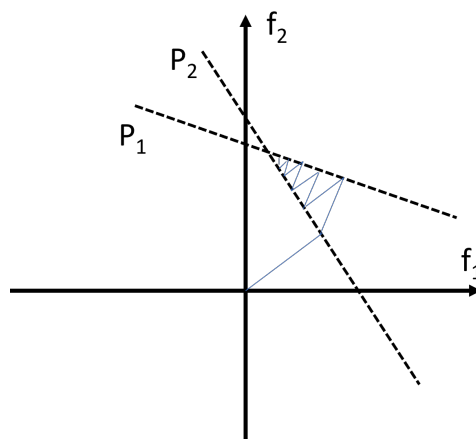


Figure 6.1: Illustration of the ART cycle in the case of a consistent square system having a unique solution.

Different choices of the initial values of the iterative process have been suggested in the literature, ranging from a uniform distribution of zero values or extremely small positive val-

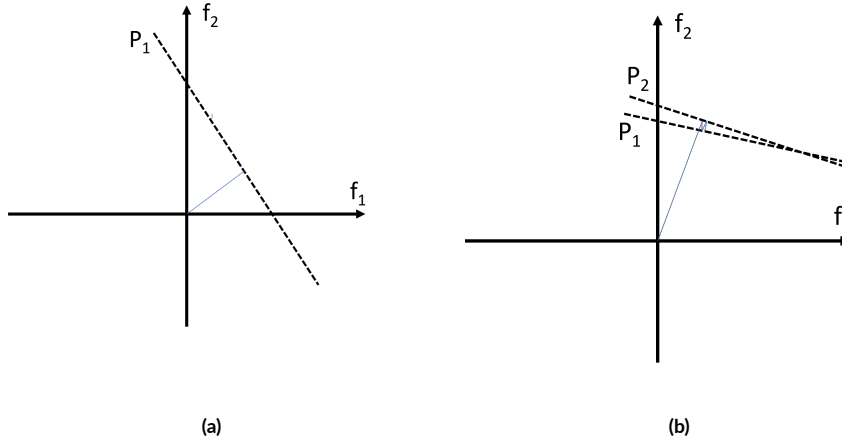


Figure 6.2: (a) Illustration of the ART cycle in the case of an underdetermined system. (b) Illustration of the ART cycle in the case of an ill-conditioned system.

ues to a uniform distribution of averaged attenuation coefficients [165] or even utilizing reconstruction outcomes from alternative methods like the backprojection method [165, 166]. In [167], an optimal initial image exploiting object’s contour symmetry was used. However, object’s contour symmetry assumption does not hold true in many medical CT images and the symmetry axis of the object often does not match the scanner axis due to positioning errors.

Having a patient-specific prior CT image at hand and a promising deformable registration algorithm aligning this prior CT image to the intraoperative DTS image as exposed in the previous chapter, this properly registered prior CT image is a precious candidate for a first guess of the iterative ART reconstruction. To the best of our knowledge, this kind of initialization in DTS image reconstruction has not been explored earlier in the literature and is the subject of this chapter.

6.2 Proposed Algorithm

The proposed prior-aided DTS reconstruction algorithm is illustrated in Figure 6.3. As revealed in the previous chapter, digitally reconstructed radiographs (DRRs) are generated from the prior CT image by forward projecting it using the same scan geometry of the intraoperative DTS scan. The reconstruction of the DRRs provides the prior DTS image. An intermediate intraoperative DTS image is reconstructed from the available intraoperative DTS projections. At this stage, ART with an ordered-subset scheme is used with the relaxation parameter estimated as in [168] and with the initial guess of the voxels set to zero. The registration of the prior DTS image to the intermediate intraoperative DTS image and the application of

6. Prior-Aided Digital Tomosynthesis Image Reconstruction

the registration transform to the prior CT image provide the coregistered prior CT image. By iteratively re-reconstructing the intraoperative DTS projections using the coregistered prior CT as a first guess, an improved intraoperative DTS image is obtained. This enhanced image will be referred to as the prior-aided DTS image throughout the remainder of this chapter.

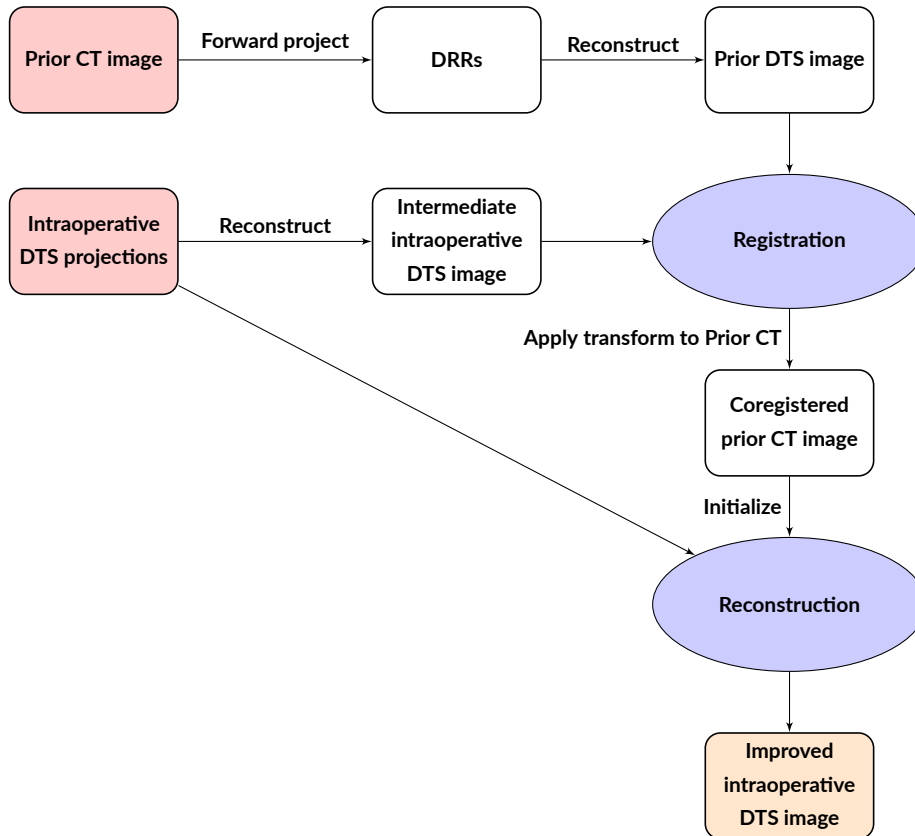


Figure 6.3: Flowchart of the proposed prior-aided DTS reconstruction method.

6.3 Experiments

Experiments on physical phantom data and on patient bronchoscopy data are conducted to assess the performance of the proposed prior-aided DTS reconstruction algorithm. To demonstrate the benefit of incorporating prior information in the initialization of the iterative reconstruction algorithm, the proposed algorithm is compared to zero-initialized reconstruction. As in the previous chapter, when the real projection images and matrices from the scanner are available, the DTS projection data are generated according to three different scenarios as described and motivated in Section 5.3.2.

6.3.1 Physical Phantoms

As a proof of concept, experiments have been carried out first on two physical phantoms to evaluate the performance of the proposed prior-aided DTS reconstruction algorithm.

- a. **Experiment 1:** In this experiment we used the Quant CT-Training phantom from Cascination ¹ (Figure 6.4). This phantom encompasses a liver with some lesions, a spine, ribs, and a portal vein. The prior CT volume was acquired at 70 KVp through a Siemens SOMATOM X.cite scanner (Siemens Healthcare GmbH, Erlangen, Germany). The acquired image had dimensions of $768 \times 768 \times 266$ voxels, with a voxel size of $0.479 \text{ mm} \times 0.479 \text{ mm} \times 1 \text{ mm}$. The intraoperative CBCT volume was acquired using a Siemens ARTIS Icono C-arm scanner (Siemens Healthcare GmbH, Erlangen, Germany) at 87.5 KVp, and the CBCT image dimensions were $512 \times 512 \times 368$ voxels, with a voxel size of $0.49 \text{ mm} \times 0.49 \text{ mm} \times 0.49 \text{ mm}$. In order to replicate an interventional scenario, an ablation needle was introduced into the phantom prior to acquiring the intraoperative CBCT volume. In this experiment, DTS projection images were simulated by forwardprojecting the intraoperative CBCT image using the CTL toolkit and assuming a spherical ellipse imaging geometry (sim_SE). The small and large tomographic angles of the spherical ellipse were set to 15° and 23° , respectively, and the number of projection views was fixed to 72. Table 6.1 summarizes the different acquisition and reconstruction parameters assumed in the simulation. The number of iterations was set to 50 since no significant improvements in the reconstructed images were observed when iterating more. As the structures in this phantom are static, a simple rigid registration was used in this case to align the prior CT image to the intraoperative DTS image.



Figure 6.4: Quant CT-training phantom from Cascination.

¹<https://www.cascination.com/en/quant-training-phantom>

6. Prior-Aided Digital Tomosynthesis Image Reconstruction

| Acquisition parameters | Reconstruction parameters |
|--|---|
| Photon flux: 4.75×10^8 photons per cm^2 | Reconstruction algorithm: ART with ordered subsets |
| Source-to-isocenter distance: 785 mm | Regularization: positivity constraint |
| Source-to-detector distance: 1200 mm | Stopping criteria: 50 iterations |
| Detector dimensions: 616×480 pixels | Volume dimension: $512 \times 512 \times 368$ voxels |
| Pixel dimensions: $0.616 \text{ mm} \times 0.616 \text{ mm}$ | Voxel size: $0.49 \text{ mm} \times 0.49 \text{ mm} \times 0.49 \text{ mm}$ |

Table 6.1: Acquisition and reconstruction parameters used in the simulation of DTS data in Experiment 1.

- b. **Experiment 2:** The Lungman chest phantom from Kyoto Kagaku Co., Ltd, Japan, was used in this experiment (Figure 6.5). This multipurpose chest phantom is a life-size anatomical model of a human torso and possesses a comprehensive anatomical representation, including pulmonary arteries and airways. A network of tiny structures mimicking bronchial and vascular structures are connected to the heart. The phantom lacks a substance that mimics lung parenchyma, but is instead filled with air. It provides radiographs that closely resemble real clinical images. With dimensions of 43 cm in width, 46 cm in height, and 20 cm in depth, and an approximate weight of 18 kg, this chest phantom accurately simulates the human torso. Various arrangements of synthetic spherical nodules were inserted into its vascular model. Same as in the previous experiment, this phantom was first scanned with the Siemens SOMATOM X.cite scanner (Siemens Healthcare GmbH, Erlangen, Germany) at 80 KVp providing a prior CT volume. The acquired image had dimensions of $768 \times 768 \times 473$ voxels, with a voxel size of $0.433 \text{ mm} \times 0.433 \text{ mm} \times 0.7 \text{ mm}$. To mimic an intraoperative scenario, a guide wire with a stent was inserted into the phantom, then the latter was scanned with the Siemens ARTIS Icono C-arm scanner (Siemens Healthcare GmbH, Erlangen, Germany) at 90 KVp providing an intraoperative CBCT scan. The reconstructed CBCT image consists of $512 \times 512 \times 368$ voxels, with a voxel size of $0.49 \text{ mm} \times 0.49 \text{ mm} \times 0.49 \text{ mm}$. In order to test the performance of the proposed prior-aided DTS reconstruction algorithm with real DTS data and as motivated in Section 5.3.2, the three scenarios, *sim_SE*, *real_PL*, and *sim_PL*, were considered in this experiment. For the simulation of the DTS images, the acquisition and reconstruction parameters were kept as in Experiment 1. A rigid registration with a bone mask of the fixed image followed by a rigid registration with a lung mask were used in this experiment to align the prior CT image to the intraoperative DTS image.



Figure 6.5: Anthropomorphic Lungman thoracic phantom from Kyoto Kagaku, Japan.

6.3.2 Patient Bronchoscopy Data

In order to take the complex chest anatomy into account, the proposed prior-aided DTS reconstruction algorithm was tested on real patient bronchoscopy data. The same patient datasets introduced in the previous chapter and described in Table 5.2 and Table 5.3 were used. While only the results of case 6 will be exposed in the next sections, similar outcomes were observed across all cases. The registration of these data was accomplished according to the deformable registration algorithm presented in the previous chapter, and the three scenarios, *sim_SE*, *real_PL*, and *sim_PL*, were considered. Same as in Experiment 1 and Experiment 2, the small and large tomographic angles were set to 15° and 23° , respectively, the number of projection views was fixed to 72, and the same number of iterations was used.

6.4 Evaluation Metrics

The reconstruction results are evaluated qualitatively by visual inspection and quantitatively by computing Pearson correlation (PC) (introduced in Chapter 4) in selected regions of interest (ROIs).

6.5 Results

Experiment 1

Figure 6.6 illustrates the prior CT image (a) and the intraoperative CBCT image (b) used in Experiment 1. One axial slice, one coronal slice, and one sagittal slice are shown for each image. Figure 6.7 (a) portrays the intraoperative DTS image reconstructed using zero-initialized ART, without including prior information. The proposed prior-aided DTS reconstruction

6. Prior-Aided Digital Tomosynthesis Image Reconstruction

is shown in Figure 6.7 (b) with the intraoperative CBCT image illustrated in (c) for comparison. The slices at exactly the same position are shown in all three images. The shown slices are chosen where a liver lesion and the ablation needle exist. As anticipated, without including the prior CT, DTS exhibits poor depth resolution mainly observed in the axial and sagittal slices. The lesion and the spine are blurred and barely discernible. However, a considerable enhancement in image quality is evident with the prior-aided reconstruction. The resulting images closely resemble the intraoperative CBCT. For a quantitative validation of these observations, ROIs in the axial, coronal, and sagittal slices were selected and are highlighted in yellow in Figure 6.7 (c). PC coefficients were computed in each of these ROIs and are reported in Table 6.2. In accordance with the visual inspection, prior-aided ART reconstructions exhibit considerably higher PC coefficients than zero-initialized ART in all three slices.

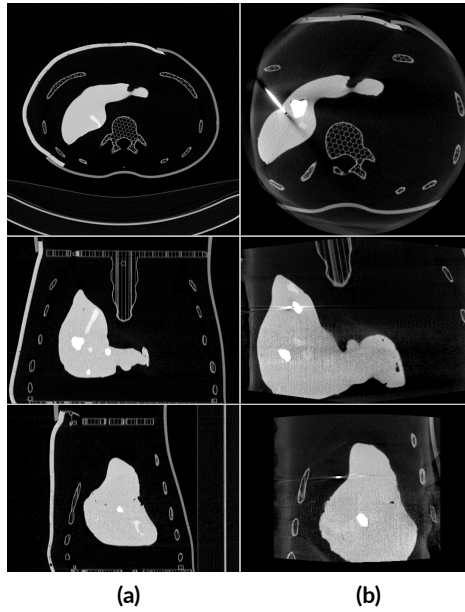


Figure 6.6: Experiment 1 data. (a) Prior CT and (b) intraoperative CBCT. Upper row: one axial slice. Middle row: one coronal slice. Lower row: one sagittal slice. The display window range is [-1000 HU, 700 HU].

| ROI | Zero-initialized ART | Prior-aided ART |
|-----|----------------------|-----------------|
| 1 | 0.6657 | 0.8721 |
| 2 | 0.8232 | 0.9609 |
| 3 | 0.7891 | 0.9618 |

Table 6.2: Experiment 1 quantitative results. Pearson correlation (PC) computed in the different ROIs highlighted in yellow in Figure 6.7.

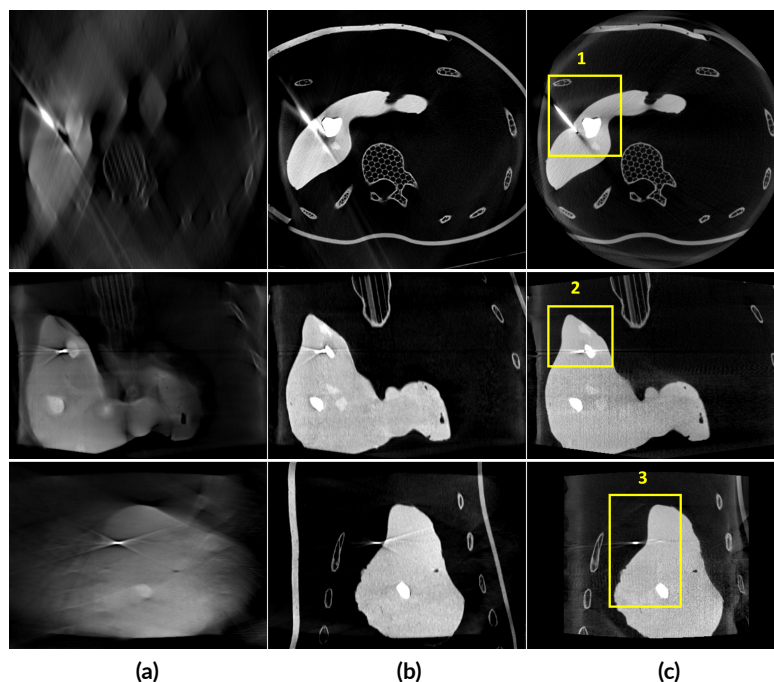


Figure 6.7: Experiment 1 reconstruction results. (a) zero-initialized ART, (b) prior-aided ART, and (c) intraoperative CBCT. Upper row: one axial slice. Middle row: one coronal slice. Lower row: one sagittal slice. Slices at the same position are shown in (a), (b), and (c). The display window range is [-1000 HU, 700 HU].

Experiment 2

In Figure 6.8 are portrayed the prior CT (a) and the intraoperative CBCT (b) of the Lungman phantom. Slices of the intraoperative CBCT volume where a lesion (green arrows) and/or the guide wire (blue arrows) exist are shown. Figure 6.9, Figure 6.10, and Figure 6.11 illustrate the reconstruction results using DTS_{sim_SE} , DTS_{sim_PL} , and DTS_{real_PL} data, respectively. In each case, zero-initialized ART reconstruction (a), prior-aided ART reconstruction (b), and the reference CBCT (c) are shown. ROIs including a lesion and/or a guide wire are selected and their enlarged views are shown in the corner of each image. Same as in Experiment 1, zero-initialized reconstructions exhibit poor depth resolution and are deteriorated with severe artifacts. The target lesions are barely visible and are difficult to be correctly localized in the depth direction. This is of special concern in transbronchial needle biopsy procedures where an accurate localization of target lesions is critical for the success of the procedure. In contrast, prior-aided reconstructions yield images with significant improvements in the depth resolution and drastically resembling the CBCT images. No significant difference is observed using simulated or real DTS data. These visual observations are further validated by the quantitative evaluation in Table 6.3, which reports the PC coefficients.

6. Prior-Aided Digital Tomosynthesis Image Reconstruction

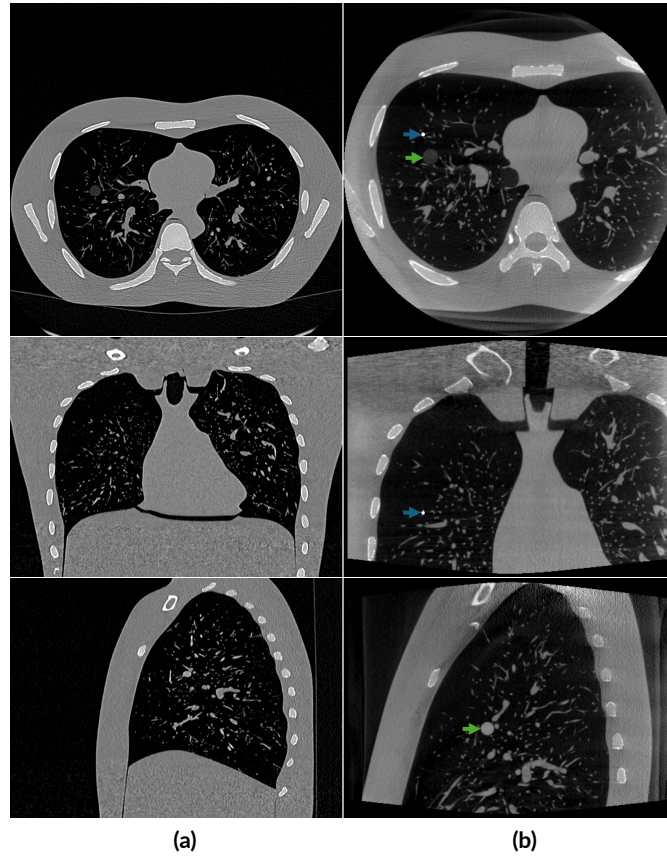


Figure 6.8: Experiment 2 data. (a) Prior CT and (b) intraoperative CBCT. Upper row: one axial slice. Middle row: one coronal slice. Lower row: one sagittal slice. The display window range is [-1000 HU, 1000 HU].

| | | <i>sim_SE</i> | <i>sim_PL</i> | <i>real_PL</i> |
|-------|------------------|---------------|---------------|----------------|
| ROI#1 | zero-initialized | 0.563 | 0.496 | 0.501 |
| | prior-aided | 0.658 | 0.644 | 0.643 |
| ROI#2 | zero-initialized | 0.598 | 0.542 | 0.568 |
| | prior-aided | 0.724 | 0.720 | 0.729 |
| ROI#3 | zero-initialized | 0.563 | 0.471 | 0.507 |
| | prior-aided | 0.881 | 0.871 | 0.857 |

Table 6.3: Experiment 2 quantitative results. Pearson correlation (PC) computed in the different ROIs highlighted in yellow in Figure 6.9.

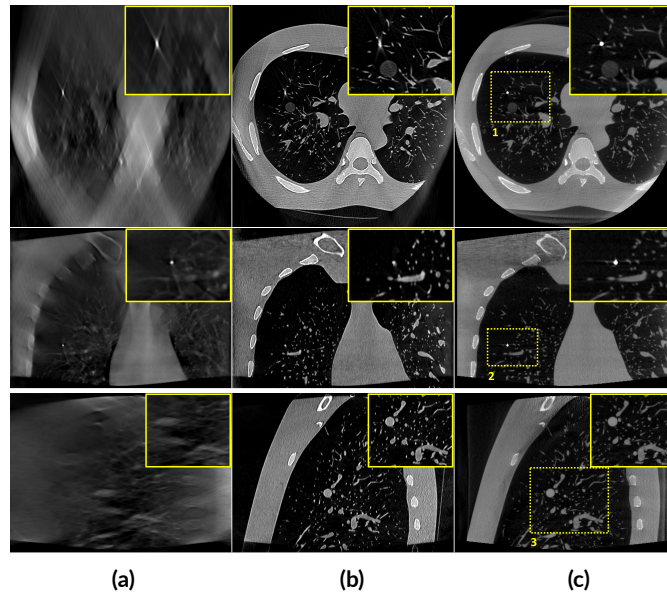


Figure 6.9: Experiment 2 reconstruction results using $DTS_{sim_{SE}}$. (a) zero-initialized ART, (b) prior-aided ART, and (c) intraoperative CBCT. Upper row: one axial slice. Middle row: one coronal slice. Lower row: one sagittal slice. Slices at the same position are shown in (a), (b), and (c). The display window range is [-1000 HU, 1000 HU].

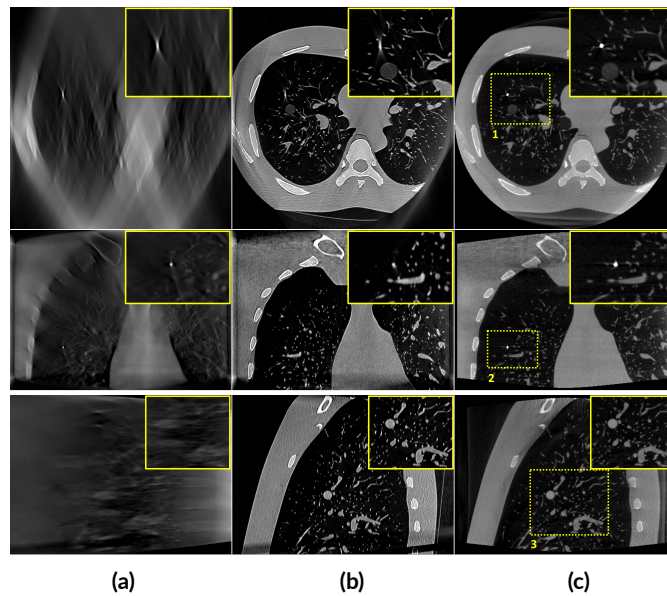


Figure 6.10: Experiment 2 reconstruction results using $DTS_{sim_{PL}}$. (a) zero-initialized ART, (b) prior-aided ART, and (c) intraoperative CBCT. Upper row: one axial slice. Middle row: one coronal slice. Lower row: one sagittal slice. Slices at the same position are shown in (a), (b), and (c). The display window range is [-1000 HU, 1000 HU].

6. Prior-Aided Digital Tomosynthesis Image Reconstruction

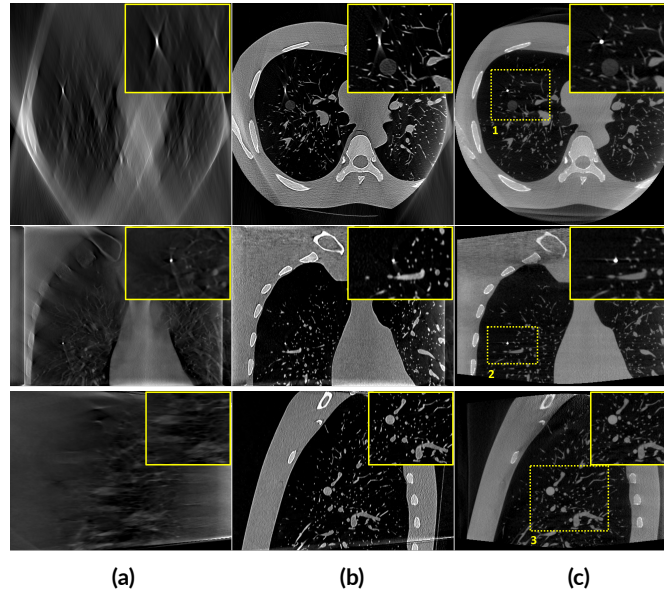


Figure 6.11: Experiment 2 reconstruction results using DTS_{real_PL} . (a) zero-initialized ART, (b) prior-aided ART, and (c) intraoperative CBCT. Upper row: one axial slice. Middle row: one coronal slice. Lower row: one sagittal slice. Slices at the same position are shown in (a), (b), and (c). The display window range is [-1000 HU, 1000 HU].

Patient bronchoscopy data

To assess the performance of the algorithm in real clinical conditions where more complex data are encountered and where dynamic changes occur between prior CT scans and intraoperative DTS scans, we investigated it on real patient bronchoscopy data. Figure 6.12 illustrates an example of a patient prior CT scan and its corresponding intraoperative CBCT scan. Figure 6.13, Figure 6.14, and Figure 6.15 portray the reconstructed images using DTS_{sim_SE} , DTS_{sim_PL} , and DTS_{real_PL} data, respectively. Same as with the previous experiments, zero-initialized ART (a), prior-aided ART (b), and the reference CBCT (c) images are shown with enlarged views of ROIs highlighted in yellow. In accordance with the results of the phantom-based experiments, zero-initialized ART yields reconstructions with a poor depth resolution. The target lesion, pulmonary vasculature, and intervertebral disks are completely obscured by overlapping structures mainly in the axial and sagittal slices. However, prior-aided ART reconstructions provide improved visibility of the different chest structures, and more importantly of the target lesion. The lesion contour is much better distinguished from the lung background compared to zero-initialized ART reconstructions and much fewer out-of-focus artifacts are evident. The results with DTS_{sim_SE} , DTS_{sim_PL} , and DTS_{real_PL} are comparable. Table 6.4 lists the PC coefficients of the different reconstructions. Consistent with the visual inspection, prior-aided reconstructions yield higher PC, and PC using the real data is just slightly lower compared to simulated data. This is expected as we have demonstrated in

the previous chapter that the registration of real data is only slightly less accurate than that of simulated data.

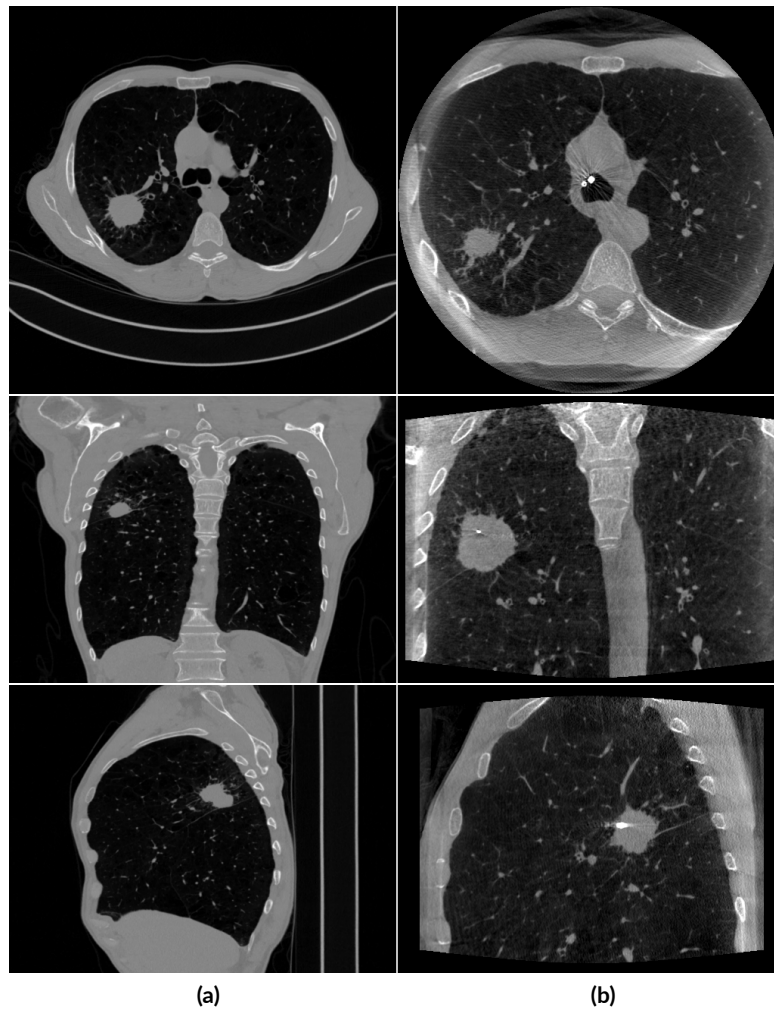


Figure 6.12: Patient bronchoscopy data. (a) Prior CT and (b) intraoperative CBCT. Upper row: one axial slice. Middle row: one coronal slice. Lower row: one sagittal slice. The display window range is [-1000 HU, 1000 HU].

6. Prior-Aided Digital Tomosynthesis Image Reconstruction

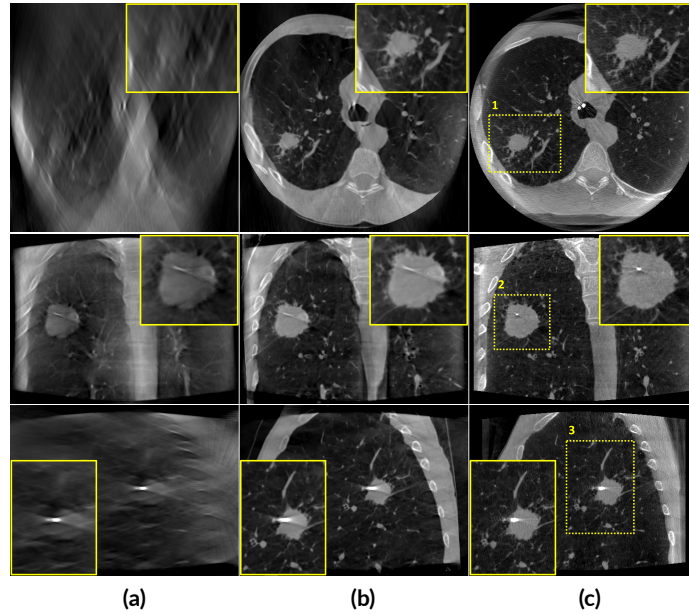


Figure 6.13: Patient bronchoscopy data reconstruction results using $DTS_{sim_{SE}}$. (a) zero-initialized ART, (b) prior-aided ART, and (c) intraoperative CBCT. Upper row: one axial slice. Middle row: one coronal slice. Lower row: one sagittal slice. Slices at the same position are shown in (a), (b), and (c). The display window range is [-1000 HU, 1000 HU].

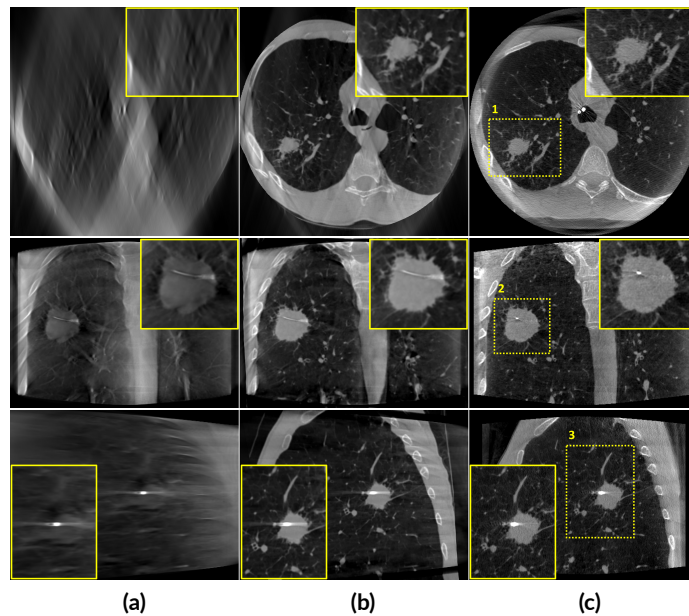


Figure 6.14: Patient bronchoscopy data reconstruction results using $DTS_{sim_{PL}}$. (a) zero-initialized ART, (b) prior-aided ART, and (c) intraoperative CBCT. Upper row: one axial slice. Middle row: one coronal slice. Lower row: one sagittal slice. Slices at the same position are shown in (a), (b), and (c). The display window range is [-1000 HU, 1000 HU].

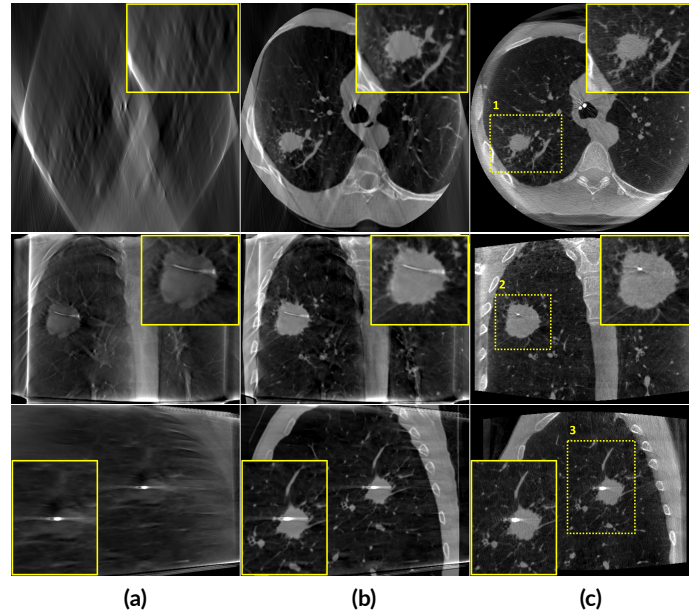


Figure 6.15: Patient bronchoscopy data reconstruction results using DTS_{real_PL} . (a) zero-initialized ART, (b) prior-aided ART, and (c) intraoperative CBCT. Upper row: one axial slice. Middle row: one coronal slice. Lower row: one sagittal slice. Slices at the same position are shown in (a), (b), and (c). The display window range is [-1000 HU, 1000 HU].

| | | sim_SE | sim_PL | $real_PL$ |
|-------|------------------|--------------|--------------|--------------|
| ROI#1 | zero-initialized | 0.707 | 0.746 | 0.606 |
| | prior-aided | 0.903 | 0.908 | 0.844 |
| ROI#2 | zero-initialized | 0.813 | 0.782 | 0.689 |
| | prior-aided | 0.933 | 0.930 | 0.867 |
| ROI#3 | zero-initialized | 0.681 | 0.668 | 0.605 |
| | prior-aided | 0.800 | 0.804 | 0.719 |

Table 6.4: Patient bronchoscopy data quantitative results. Pearson correlation (PC) computed in the different ROIs highlighted in yellow in Figure 6.13.

6.6 Conclusion

In this chapter, we unveiled a prior-aided DTS reconstruction algorithm employing prior CT images to improve intraoperative DTS images. The proposed algorithm is mainly based upon the deformable CT-to-DTS registration algorithm we presented in Chapter 5 and primarily investigates the initialization of the iterative ART reconstruction algorithm with a well-registered prior CT image. While the first guess of the iterative algorithm is often overlooked, we proved in this chapter how important it is, especially when working with highly underdetermined problems like in DTS image reconstruction. Moreover, we demonstrated

6. Prior-Aided Digital Tomosynthesis Image Reconstruction

the benefits of incorporating prior information into the DTS reconstruction. A significant enhancement in the visibility of the different structures was successfully achieved, and DTS images closely resembling CBCT images were rendered. In the next chapter, we briefly discuss cases where CT-to-DTS registration, and subsequently CT-aided DTS reconstruction, might fail. Additionally, we propose an alternative protocol to deal with such cases.

7

Alternative to Failed CT-Augmented Digital Tomosynthesis

Contents

| | | |
|-----|---|-----|
| 7.1 | Motivation | 129 |
| 7.2 | CBCT-to-DTS Registration Algorithm | 131 |
| 7.3 | CBCT-Aided DTS Reconstruction Algorithm | 131 |
| 7.4 | Results | 131 |
| 7.5 | Conclusion | 136 |

IN Chapter 5, we introduced a registration algorithm aimed at aligning prior CT images to intraoperative DTS images in image-guided bronchoscopy interventions. Subsequently, in Chapter 6, we presented a prior-aided DTS reconstruction algorithm employing registered prior CT images to elevate the quality of intraoperative DTS images. This brief chapter will delve into scenarios where CT-to-DTS registration might fail and offer insights into a promising alternative protocol.

7.1 Motivation

In the preceding chapters, our focus has primarily centered on leveraging prior CT images—often obtained prior to bronchoscopy interventions for diagnostic or planning purposes—to augment the quality of intraoperative DTS images. Our goal has been to establish a bronchoscopy guidance protocol reliant solely on prior CT scans and intraoperative DTS scans, effectively replacing intraoperative CBCT scans commonly used in today’s bronchoscopy interventions. However, certain challenges may arise, particularly in the realm of CT-to-DTS image registration. In some instances, complications such as atelectasis—a condition where

7. Alternative to Failed CT-Augmented Digital Tomosynthesis

the entirety of the lung or an area of it collapses—may occur during the procedure making it difficult to align prior CT images, which do not show atelectasis, to intraoperative DTS images. Additionally, DTS images are more susceptible to truncation artifacts compared to CT images due to the limited field-of-view of C-arm systems. Highly truncated DTS images can present challenges for the registration algorithm, particularly if the rib structures are absent as these are often considered as a good guide for the registration. Furthermore, significant movements or deformations of the lesions between the time of the CT scan and the intraoperative DTS scan may fall outside the registration algorithm’s capture range, leading to inadequate alignment.

In today’s bronchoscopy procedures, two to three CBCT scans are typically conducted for intervention guidance, with the first scan often performed before the biopsy tool insertion, and the last scan performed at the end of the procedure to confirm tool-in-lesion. An alternative guidance protocol that could be employed when CT-to-DTS registration fails, involves initiating the procedure with a CBCT scan followed by subsequent DTS scans whenever a 3D overview of the anatomy is required during the intervention. Figure 7.1 portrays this alternative guidance protocol. The CBCT image could be registered to the subsequent DTS images and used to enhance DTS image quality.



Figure 7.1: Alternative CBCT-coupled DTS-guided bronchoscopy protocol.

CBCT-to-DTS registration is notably simpler compared to CT-to-DTS registration. This is primarily because both CBCT and DTS images are acquired using the same device, with similar patient positioning, and during the same procedure. In contrast, prior CT scans are performed with a different device and different patient positioning, and are obtained days or weeks before the intervention, allowing for potential significant changes in the patient’s condition. Moreover, differences in respiratory motion between CBCT and DTS images are typically smaller compared to those between prior CT and DTS images, as both CBCT and DTS scans are performed under the same breathing protocol.

In the forthcoming sections of this chapter, we will illustrate scenarios where CT-to-DTS registration might fail and demonstrate how the alternative CBCT-based guidance protocol can address such challenges.

7.2 CBCT-to-DTS Registration Algorithm

During bronchoscopy interventions, both intraoperative CBCT and DTS images are obtained with the same patient positioning. The primary disparity between the CBCT and DTS images arises from respiratory motion. Therefore, only stage 4 of the CT-to-DTS registration algorithm outlined in Chapter 5 is needed to register the CBCT images to the DTS images. Elastic transformations, represented by cubic B-splines, are utilized. The registration process employs the normalized correlation coefficient (NCC) as a similarity metric and incorporates the bending energy (BE) as a regularity term. Additionally, a mask for the fixed image (intraoperative DTS image) is applied, delineating a cuboid surrounding the target lesion. This mask aids in directing the registration process toward the target lesion and its immediate vicinity.

7.3 CBCT-Aided DTS Reconstruction Algorithm

Like the previously introduced prior-aided DTS reconstruction algorithm presented in Chapter 6, the CBCT-aided DTS reconstruction algorithm leverages the registered CBCT image to improve the quality of the DTS image. The registered CBCT image serves as the initial approximation in the ART reconstruction process.

7.4 Results

Similar to Chapter 5 and Chapter 6, datasets used in this chapter are patient bronchoscopy data acquired during some bronchoscopy interventions. For each case, two to three intraoperative CBCT scans are available. In this chapter, DTS images are simulated based on the CBCT images according to a spherical ellipse scan geometry as thoroughly described in Section 5.3.2.

Case A

Figure 7.2 portrays a patient's prior CT image (a) and two intraoperative CBCT images, (b) and (c), acquired to guide a bronchoscopy intervention. As can be observed, the intraoperative data are noisy and large deformations between the prior CT image and the intraoperative

7. Alternative to Failed CT-Augmented Digital Tomosynthesis

CBCT image (subsequently the DTS image) exist. That is why, CT-to-DTS registration in this case is challenging, and the alternative CBCT-based guidance protocol could be beneficial.

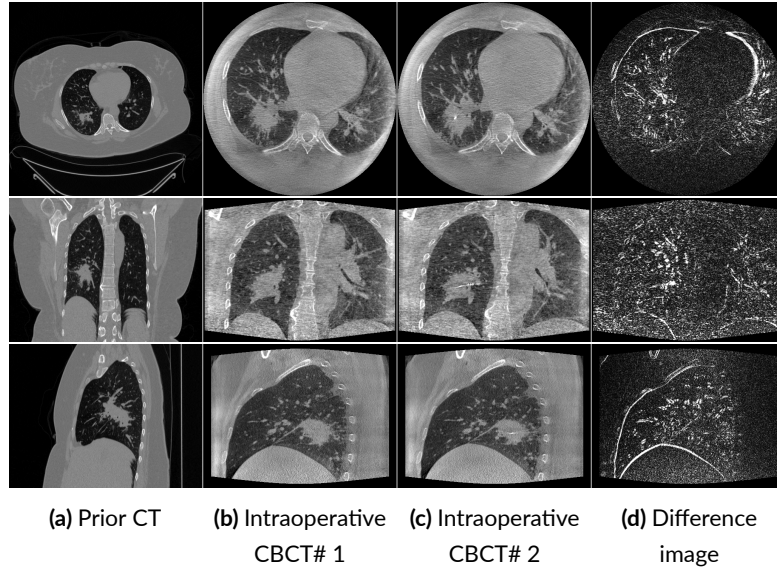


Figure 7.2: Image examples of a prior CT scan of a patient (Case A) and its corresponding intraoperative CBCT scans. One axial slice (top), one coronal slice (middle), and one sagittal slice (bottom) are shown. (a) Prior CT image, (b) intraoperative CBCT image# 1, (c) intraoperative CBCT image# 2, and (d) difference image between (b) and (c). Displayed window for (a), (b), and (c) is [-1000 HU, 1000 HU]. Displayed window for (d) is [0 HU, 600 HU].

Figure 7.2 (d) illustrates the difference image between the two consecutive intraoperative CBCT images, showing a negligible movement of the ribs. That is why we mainly focused the registration on the target lesion and its vicinity. Figure 7.3 shows the CBCT image (a) from which a DTS image was simulated to serve as the moving image of the registration, the intraoperative DTS image (b), representing the fixed image of the registration, the registered CBCT image (c), and its difference to the intraoperative CBCT# 2 (d). If the registration process is successful, we expect to see a sparse difference image mainly highlighting the interventional tool with no other edges. It is evident that the lesion and its surrounding are well registered, the enlarged views highlighted in yellow around the lesion show no edges other than the biopsy needle.

Figure 7.4 portrays the CBCT-aided DTS reconstruction results. In Figure 7.4 (a), Figure 7.4 (b), and Figure 7.4 (c) are shown the zero-initialized ART, CBCT-initialized ART, and the reference CBCT#2, respectively. In accordance with the results presented in the previous chapter, zero-initialized reconstruction demonstrates low depth resolution and is marred by severe artifacts, resulting in deformed and barely visible target lesion. Conversely,

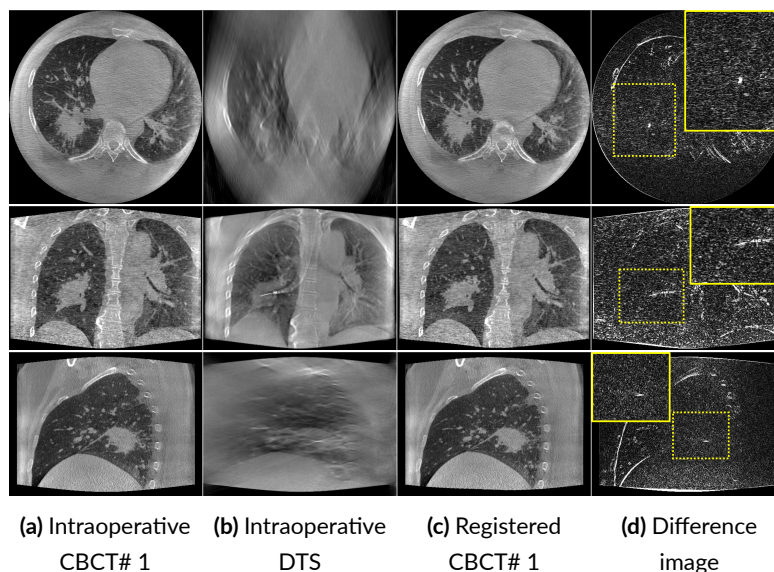


Figure 7.3: Case A registration results: (a) Intraoperative CBCT#1 from which a DTS image is simulated acting as the moving image, (b) intraoperative DTS acting as the fixed image, (c) registered CBCT image, and (d) difference image between the registered CBCT and the intraoperative CBCT#2. One axial slice (top), one coronal slice (middle), and one sagittal slice (bottom) are shown. Displayed window for (a), (b), and (c) is [-1000 HU, 1000 HU]. Displayed window for (d) is [0 HU, 600 HU].

CBCT-aided reconstruction shows substantial enhancements in the depth resolution and provides a DTS image closely resembling the CBCT image.

Case B

Figure 7.5 illustrates another case where the CT-to-DTS registration could fail due to the high truncation of the intraoperative data as portrayed in Figure 7.5 (b) and Figure 7.5 (c). Figure 7.5 (d) shows the difference image between the two consecutive intraoperative CBCT scans. It reveals some deformations in the lesion's region.

Figure 7.6 displays the registration results of Case B, following the same order as those of Case A. It is evident from the comparison that the coregistered CBCT image aligns sufficiently well with the DTS image. This is demonstrated by the minimal presence of edges other than those of the biopsy needle and its metal artifacts in the difference image (Figure 7.6 (d)).

Similarly, Figure 7.7 illustrates the reconstruction results of Case B, mirroring the order of presentation used for Case A. Consistent with the findings from Case A, the CBCT-aided reconstruction notably enhances the depth resolution and the visibility of the target lesion and various chest structures compared to the zero-initialized reconstruction.

7. Alternative to Failed CT-Augmented Digital Tomosynthesis

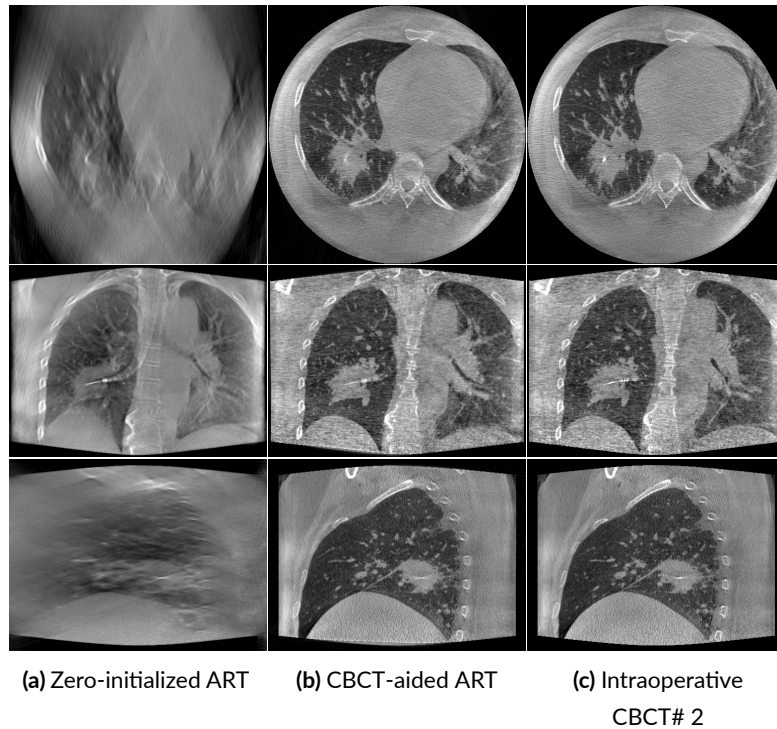


Figure 7.4: Case A reconstruction results: (a) Zero-initialized ART, (b) CBCT-aided ART, and (c) intraoperative CBCT# 2 representing the reference. One axial slice (top), one coronal slice (middle), and one sagittal slice (bottom) are shown. Displayed window is [-1000 HU, 1000 HU].

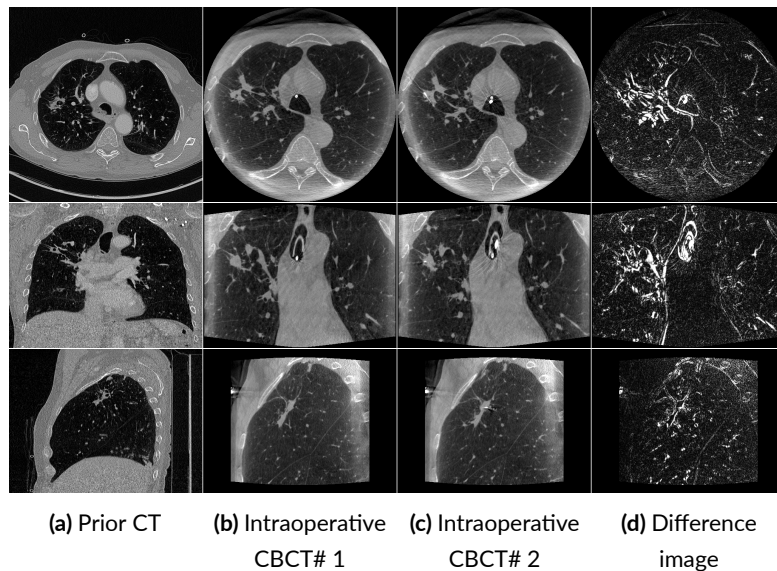


Figure 7.5: Image examples of a prior CT scan of a patient (Case B) and its corresponding intraoperative CBCT scans. One axial slice (top), one coronal slice (middle), and one sagittal slice (bottom) are shown. (a) Prior CT image, (b) intraoperative CBCT image# 1, (c) intraoperative CBCT image# 2, and (d) difference image between (b) and (c). Displayed window for (a), (b), and (c) is [-1000 HU, 1000 HU]. Displayed window for (d) is [0 HU, 600 HU].

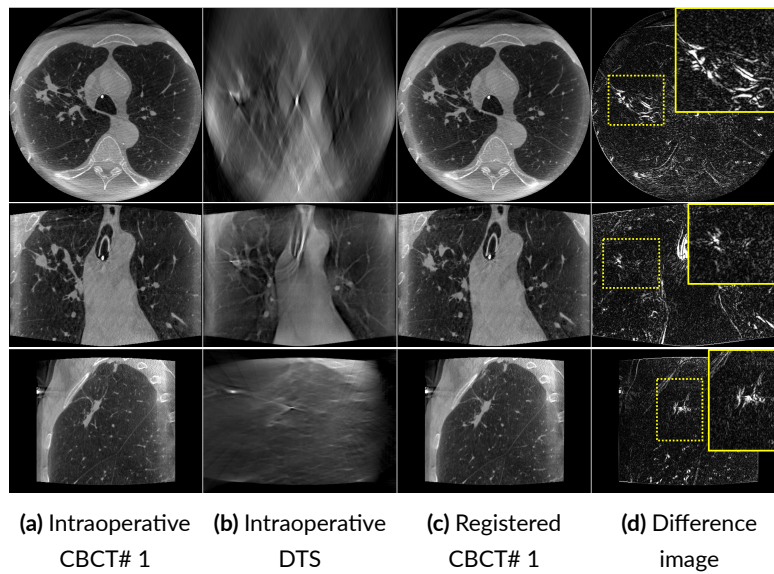


Figure 7.6: Case B registration results: (a) Intraoperative CBCT #1 from which a DTS image is simulated acting as the moving image, (b) intraoperative DTS acting as the fixed image, (c) registered CBCT image, and (d) difference image between the registered CBCT and the intraoperative CBCT#2. One axial slice (top), one coronal slice (middle), and one sagittal slice (bottom) are shown. Displayed window for (a), (b), and (c) is [-1000 HU, 1000 HU]. Displayed window for (d) is [0 HU, 600 HU].

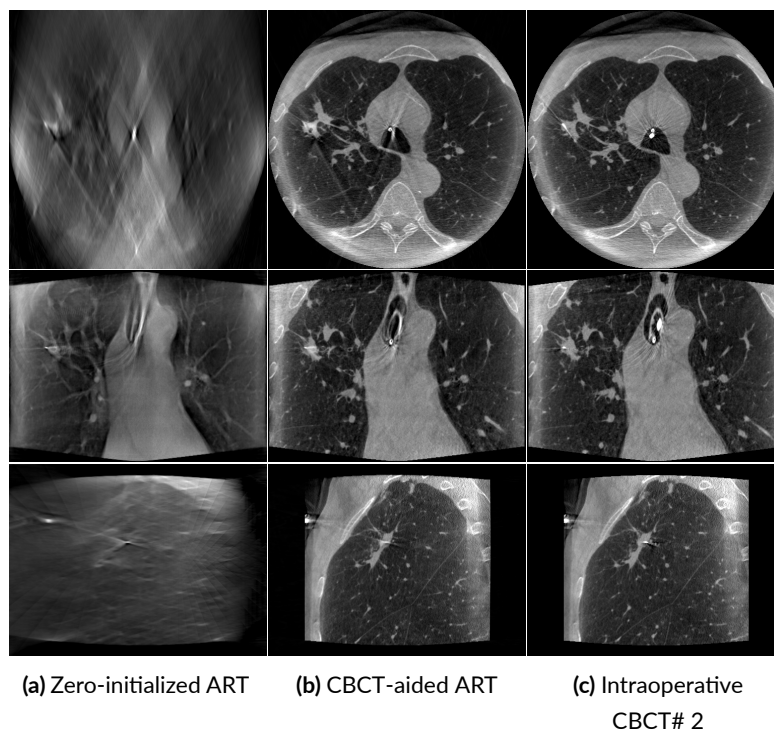


Figure 7.7: Case B reconstruction results: (a) Zero-initialized ART, (b) CBCT-aided ART, and (c) intraoperative CBCT# 2 representing the reference. One axial slice (top), one coronal slice (middle), and one sagittal slice (bottom) are shown. Displayed window is [-1000 HU, 1000 HU].

7.5 Conclusion

In this concise chapter, we have explored scenarios where CT-to-DTS image registration poses challenges and we have provided insights into a promising alternative guidance protocol designed to overcome these challenges. Our proposed protocol involves initiating the intervention with a CBCT scan before introducing the biopsy tools, and utilizing the CBCT volume instead of the prior CT volume to assist subsequent DTS scans during later stages of the intervention. Additionally, we have introduced a CBCT-to-DTS registration algorithm and a CBCT-aided DTS reconstruction technique, both aimed at delivering high-quality intraoperative DTS images. The promising outcomes showcased in this chapter pave the way for future research endeavors, focusing on bronchoscopy guidance protocols that integrate various modalities—such as prior CT, intraoperative CBCT, and intraoperative DTS—as required during the intervention.

8

Conclusion, Discussion, and Perspectives

Contents

| | |
|---------------------------------------|-----|
| 8.1 Summary and Discussion | 137 |
| 8.2 Limitations and Outlook | 141 |

IN this final chapter, we provide a comprehensive overview of the key findings and contributions presented throughout this dissertation. A detailed summary of the research outcomes and their implications will be presented, followed by an in-depth discussion that delves into the significance of the results within the broader context of bronchoscopy intervention image guidance, elucidating the potential impact on the academic community and practical applications. Additionally, we acknowledge the inherent limitations of our work, offering critical insights into the constraints and potential areas for improvement. Finally, we outline avenues for future research, providing a roadmap for scholars and practitioners to build upon the foundations laid in this study, further advancing the understanding of digital tomosynthesis-guided bronchoscopy interventions.

8.1 Summary and Discussion

The ultimate aim of this doctoral work was to address the high radiation dose, long imaging time, and large footprints of cone-beam computed tomography (CBCT) imaging on the one hand, and the lack of depth information in 2D projective radiography (PR) on the other hand, both imaging modalities used nowadays in guiding bronchoscopy interventions. An excellent alternative in this context is digital tomosynthesis (DTS) providing quasi-3D images at a fraction of the radiation dose, imaging time, and footprints required for CBCT. While

8. Conclusion, Discussion, and Perspectives

DTS provides some depth information, its image quality in its conventional standard form is significantly many steps away from being sufficient to properly guide bronchoscopy interventions, mainly due to its poor depth resolution. This is why the focus in this work was devoted to pave the way for a proper introduction of DTS in the clinical routine of guiding bronchoscopy interventions.

The low depth resolution of DTS images is mainly due to data acquisition over limited angular ranges. To tackle this loss of information, the work revolved around three points: data acquisition, replacement of missing data, and data reconstruction. At the data acquisition level, we proposed a novel C-arm-based spherical ellipse DTS scan trajectory suitable and customized for bronchoscopy intervention guidance. Our experiments on simulated numerical phantoms and patient bronchoscopy data indicate that this trajectory provides improved visibility of the tool-in-lesion and of the different chest structures compared to conventional unidirectional pseudo-linear DTS scan orbits, and demonstrates a good compromise between image quality and footprint requirements relative to conventional multidirectional circular DTS scan orbits.

At the missing data replacement level, a promising source to compensate for these data are the patient-specific preoperative CT scans often performed days or weeks prior to bronchoscopy procedures for diagnosis or to plan the intervention. These images share a considerable amount of anatomical information with the intraoperative scans and could be used to compensate for the missing data of the intraoperative DTS scans. To properly use this prior knowledge, we had to address the CT-to-body divergence, cited as one of the major obstacles to successful lung navigation, and which is mainly due to differences in patient positioning, dynamic changes caused by respiratory motion, and anatomic changes caused by neuromuscular paralysis and insertion of interventional tools. In this context, we presented a novel deformable 3D/3D CT-to-DTS registration algorithm suitable for aligning prior CT images to intraoperative DTS images. Our experiments on simulated as well as real patient bronchoscopy data demonstrated promising and sufficiently-enough accurate registration with a reported mean Dice coefficient (DC) of 0.82 ± 0.05 and 0.74 ± 0.05 , and a reported mean average symmetric surface distance (ASSD) of 0.65 ± 0.29 mm and 0.93 ± 0.43 mm for the simulated and real data, respectively.

This proposed registration algorithm laid the groundwork at the data reconstruction level. DTS image reconstruction problem is characterized by a severely underdetermined system of linear equations having more unknowns than equations, and subsequently having many solutions that may fit the measured data. Due to this fact and having to encounter truncated iterations in common practice, the choice of the first guess of the iterative reconstruction scheme is of great importance. In this context, we proposed a novel prior-aided DTS reconstruction algorithm based on the algebraic reconstruction technique (ART) and accommodating the

initial estimate with a properly registered prior CT image. Experiments were carried out on simulated and real data of phantoms and patients, and the results were evaluated qualitatively and quantitatively. Compared to conventional zero-initialized ART reconstruction, the proposed algorithm yielded images with significantly improved depth resolution and improved visibility of the target lesions and their vicinities. The reconstructed images drastically resembled intraoperative CBCT images. These observations were validated by the computed Pearson correlation (PC) coefficients.

We have aimed to develop a bronchoscopy guidance protocol that relies exclusively on pre-operative CT scans and intraoperative DTS scans, with the intention of replacing the conventional use of intraoperative CBCT scans in bronchoscopy procedures. Nonetheless, various cases may be challenging to the CT-to-DTS image registration algorithm. Examples of the identified challenges include complications such as atelectasis, strong truncation artifacts, and large movements or deformations of lesions between the scans. An alternative guidance protocol, involving the integration of CBCT scans, performed at the very beginning of the procedure, with subsequent DTS scans has been proposed and proved to be promising in addressing registration failures of the challenging cases and enhancing DTS image quality during bronchoscopy interventions.

The presented work has potential clinical utility and could advance intervention guidance, especially in transbronchial needle biopsy procedures. Rather than relying on intraoperative 2D PR and navigating relatively blindly to the target lesion, or resorting to intraoperative CBCT with its drawbacks of high cumulative radiation exposure, prolonged imaging duration, and challenging footprint requirements, bronchoscopists can now leverage DTS imaging providing images with a quality sufficient-enough for the guidance. Compared to PR, DTS yields improved bony and soft structures visibility. This is highly crucial in navigational bronchoscopy to verify tool-in-lesion and gather biopsy samples from the accurate location. Hence, DTS improves the precision of localizing target lung nodules and subsequently contributes to an improved diagnostic yield of such procedures.

In this work, we were able to provide adequate DTS images involving only 72 projection images, as opposed to the 397 required for CBCT. This results in a remarkable 81.8% reduction in radiation dose. While an almost 200° angular rotation of the C-arm is required for a single CBCT image acquisition, satisfactory DTS images were obtained with a spherical ellipse scan orbit with only a 23° large tomographic angle and 15° small tomographic angle. This is of great importance in bronchoscopy interventions, since a full rotation of the C-arm requires some considerable logistic efforts. In the operating room, the space is limited, many entangled cables, lines, tubes, and other systems block the C-arm trajectory, and these need to be rearranged before performing the scan, thus obstructing the workflow in the operating room. Moreover, a C-arm system is known to be slow while time is a critical factor during

8. Conclusion, Discussion, and Perspectives

interventions. By limiting the angular rotation of the C-arm and acquiring fewer projections compared to a CBCT acquisition, DTS offers a time-saving option.

The proposed spherical ellipse DTS scan orbit indicates improvements in the depth resolution and better removal of out-of-plane artifacts compared to the standard pseudo-linear DTS scan orbit. While the larger circular scan orbit exhibits a tiny enhancement in image quality compared to the spherical ellipse, this minor advantage comes at the expense of requiring significantly more space for the scan. As stated in the previous paragraph, space is restricted in the operating room, executing a large circle becomes impractical. If constrained to circular DTS trajectories, opting for the smaller circular orbits may be the only feasible option. However, with the availability of the spherical ellipse, it provides an opportunity for achieving improved image quality. Whereas building complex DTS scan orbits was always avoided due to increased challenges in constructing and maintaining gantries, spherical ellipse scan orbits do not necessitate new gantries and can be implemented on standard C-arm systems already available in medical centers. An advantage of the spherical ellipse scan orbit is its versatility: its larger opening angle can be selected in the direction where more space is available.

While DTS image quality is already adequate for navigational bronchoscopy intervention guidance with the spherical ellipse scan trajectory, this guidance can be further enhanced when prior CT images are available. Addressing CT-to-body divergence, the major challenge of navigational bronchoscopy procedure guidance, the proposed registration algorithm holds significant clinical promise. Typically, preoperative CT images exhibit high quality and provide a wealth of anatomical information. The precise alignment of these prior CT images with intraoperative DTS images could substantially enhance the accuracy and precision of localizing target lung nodules, subsequently elevating the diagnostic yield of such procedures. In the literature, few works tackled CT-to-DTS image registration problem due to the complexity of DTS resolution characteristics, and, to the best of our knowledge, deformable motion was never considered in a 3D/3D CT-to-DTS registration format. In this work, we were able to provide a successful registration framework taking into account dynamic deformable changes. This is of great importance in bronchoscopy interventions, as the chest contains organs with substantial movement.

Most interestingly, the prior-aided DTS reconstruction algorithm captured the attention and took center stage in our pursuit as it was able to move DTS images from radiography-like to tomography-like images. It provided DTS images comparable to CBCT images. We emphasize here again, this was possible with only 72 projection images acquired with a maximal tomographic angle of 23° , besides a prior CT image. Compared to the prior-based reconstruction algorithms proposed in the literature, the proposed algorithm employs the priors only in the initialization step, which is often overlooked, with a simple ART reconstruction

instead of adding the prior as a regularization term and including it in the body of the iteration. This makes the proposed algorithm computationally less demanding. Besides indicating the importance of adding prior knowledge into DTS reconstructions, the proposed algorithm suggests that the choice of the initialization is critical in such highly underdetermined systems.

8.2 Limitations and Outlook

Spherical ellipse DTS scan trajectory

In this work, the performance of the spherical ellipse DTS scan orbit compared to the standard pseudo-linear and circular DTS scan orbits was assessed only based on simulated data, as real data acquired according to circular or spherical ellipse scan geometries were unavailable. Validating whether the made observations and results hold true when using real data is essential for the transition of the proposed scanning protocol to real clinical routine. Real data often contain noise, artifacts, and imperfections inherent to the imaging process and these cannot be fully modeled with the simulations. The primary challenges faced in DTS imaging are mainly attributed to sampling insufficiency, marked by a constrained angular scanning range and a low angular sampling rate. These challenges take precedence over inconsistencies arising from physical factors. That is why the simulations performed in this work deliberately avoided detailed physical imaging models. Instead, we employed the standard monochromatic approximate model for transmitted X-ray intensity, disregarding factors such as X-ray scatter and partial volume averaging. Taking into account all these physical factors is necessary to verify the robustness and pertinence of the results with real data. Future works should include the implementation of the pseudo-linear, circular, and spherical ellipse DTS scanning protocols on a real C-arm system.

CT-to-DTS registration algorithm

One of the recognized limitations of the current version of the proposed registration algorithm pertains in the generation of the bone and lung masks for the intraoperative DTS images. Given the substantial degradation in the quality of these images due to geometric and streaking artifacts, creating precise and accurate bone and lung masks, as typically achieved with CT or CBCT images, is unattainable. In this work, these masks were derived from the intraoperative CBCT images through a straightforward thresholding process. However, this hinders the seamless integration of the registration algorithm into clinical practice. To address this limitation, the development of deep learning-based techniques for the automated generation of such masks for DTS images is a potential avenue for exploration. These deep

8. Conclusion, Discussion, and Perspectives

learning models could be trained using a dataset comprising CBCT images, corresponding annotated bone and lung masks, and DTS images simulated from the CBCT data. Leveraging neural network architectures, these models could learn to extract features (masks) directly from the DTS images, obviating the need for manual mask creation.

Another challenge in the automation of the registration algorithm involves the heuristic setting of the weights assigned to various metrics and regularization terms at stage 3 and stage 4 of the registration process. The appropriate weight for the regularization against similarity depends on the degree of deformation between the fixed image and the moving image. A potential solution to automate this process involves incorporating information about the patient's respiratory phases during both the CT scan and the DTS scan.

While we have demonstrated robust and effective registration performance with real patient bronchoscopy data, quantifying the degree of deformation and mismatch between the prior CT image and the intraoperative DTS image, at which successful registration can still be achieved, remains challenging. Information regarding respiratory phases was unavailable, and even if accessible, quantifying it in real patient data is a complex task. Using mathematical phantoms such as the XCAT phantom [169] which incorporates a respiratory model into the image data, could be advantageous for assessing the registration algorithm's capture range.

For clinical integration, the runtime of the registration algorithm is of high importance. Currently, the computation times for the registration stages fall within the following ranges: approximately 31 seconds for stage 1, 34 seconds for stage 2, 3 minutes for stage 3, and 6 minutes for stage 4, resulting in a total registration time of nearly 10 minutes. This long processing time of the registration algorithm is a limitation to its seamless integration into clinical practice. It is noteworthy that all registrations were conducted on a 64-bit version of a typical desktop computer equipped with an Intel(R) Core(TM) i7 CPU @ 3.60 GHz, 32 GB RAM. Transferring these computations to GPUs, using optimizers with faster convergence characteristics, and taking advantage of future advancements, we anticipate a reduction in computation time, enabling real-time registration during the intervention.

Future work could include assessing the registration algorithm's efficacy in scenarios involving common bronchoscopy-induced atelectasis. While our current focus has been primarily on large solid lung nodules, which constitute the most prevalent type, delving into the algorithm's performance when dealing with smaller ground-glass nodules is a potential for future works.

In this work, we employed ART reconstruction method to generate the DTS images. Investigating alternative reconstruction algorithms, that may offer improved speed and efficiency in mitigating out-of-plane artifacts [170], and their impact on the accuracy of the registration process is required.

Prior-aided DTS reconstruction algorithm

One of the raised questions about the proposed prior-aided DTS reconstruction algorithm is its sensitivity to mis-registration errors. By the design of the method, information obtained from the tomosynthesis acquisition are incorporated in the prior-aided ART reconstruction, while any missing information is inherited from the co-registered prior CT image. In instances of inaccuracies in the registration process, this could potentially result in erroneous conclusions during image interpretation. Hence, to mitigate this risk, clinical experts should be involved in the evaluation process in future work.

Introduction of a new imaging modality, like DTS, in the clinical practice of transbronchial needle biopsy procedures might be hindered by the lack of expertise by health professionals in interpreting such images. While we have achieved DTS reconstructions resembling CBCT reconstructions, additional training for DTS interpretation might still be required to achieve proficiency.

Undoubtedly, before adopting DTS as a guiding imaging modality in bronchoscopy procedures, clinical studies comparing the diagnostic yield of CBCT-guided bronchoscopy and DTS-guided bronchoscopy are essential. Moreover, the diagnostic yield when using electromagnetic navigation besides DTS image guidance should be evaluated.

A potential future work could be the application of the nullspace-constrained modification scheme to reconstruct DTS images. We have proposed this reconstruction technique in a previous work [171]. Our experiments on simulated phantom data indicated that this technique is promising for the reconstruction of intraoperative images using undersampled datasets. Its advantage lies in the simplification of the reconstruction process to an unconstrained ART, which is computationally more efficient than regularized algorithms, and the ability to incorporate seamlessly prior information regarding the object to be reconstructed as a post-processing step. Besides using preoperative CT images as prior knowledge, prior information about the interventional tool (e.g., volume, shape, or material of the bronchoscope in the case of bronchoscopy interventions) could be exploited. It would be interesting to compare the behavior of this technique to the prior-aided ART reconstruction.

Finally, while we have mainly focused on bronchoscopy interventions, all methods presented in this thesis could be adopted to other medical intervention scenarios, like external beam radiation therapy, prostate brachytherapy, and partial breast irradiation treatment. Moreover, the adoption of DTS to intervention guidance could potentially lead to the invention of more complex interventions as well as the development of new implants and instruments.

Bibliography

- [1] J. Ferlay, M. Ervik, F. Lam, M. Colombet, L. Mery, M. Piñeros, A. Znaor, I. Soerjomataram, F. Bray, Global cancer observatory: cancer today. Lyon: International Agency for Research on Cancer; 2020, Cancer Tomorrow (2021).
- [2] H. Sung, J. Ferlay, R. L. Siegel, M. Laversanne, I. Soerjomataram, A. Jemal, F. Bray, Global cancer statistics 2020: GLOBOCAN estimates of incidence and mortality worldwide for 36 cancers in 185 countries, *CA: a cancer journal for clinicians* 71 (3) (2021) 209–249. doi:10.3322/caac.21660.
- [3] F. C. Detterbeck, D. J. Boffa, A. W. Kim, L. T. Tanoue, The eighth edition lung cancer stage classification, *Chest* 151 (1) (2017) 193–203. doi:10.1016/j.chest.2016.10.010.
- [4] D. F. Yankelevitz, R. Yip, J. P. Smith, M. Liang, Y. Liu, D. M. Xu, M. M. Salvatore, A. S. Wolf, R. M. Flores, C. I. Henschke, et al., CT screening for lung cancer: nonsolid nodules in baseline and annual repeat rounds, *Radiology* 277 (2) (2015) 555–564. doi:10.1148/radiol.2015142554.
- [5] C. I. Henschke, R. Yip, J. P. Smith, A. S. Wolf, R. M. Flores, M. Liang, M. M. Salvatore, Y. Liu, D. M. Xu, D. F. Yankelevitz, et al., CT screening for lung cancer: part-solid nodules in baseline and annual repeat rounds, *American Journal of Roentgenology* 207 (6) (2016) 1176–1184. doi:10.2214/AJR.16.16043.
- [6] C. J. Lettieri, G. R. Veerappan, D. L. Helman, C. R. Mulligan, A. F. Shorr, Outcomes and safety of surgical lung biopsy for interstitial lung disease, *Chest* 127 (5) (2005) 1600–1605. doi:10.1378/chest.127.5.1600.
- [7] M. E. Kreider, J. Hansen-Flaschen, N. N. Ahmad, M. D. Rossman, L. R. Kaiser, J. C. Kucharczuk, J. B. Shrager, Complications of video-assisted thoracoscopic lung biopsy in patients with interstitial lung disease, *The Annals of thoracic surgery* 83 (3) (2007) 1140–1144. doi:10.1016/j.athoracsur.2006.10.002.
- [8] J. S. Klein, M. A. Zarka, Transthoracic needle biopsy: an overview, *Journal of thoracic imaging* 12 (4) (1997) 232–249. doi:10.1097/00005382-199710000-00002.
- [9] E. H. Moore, Technical aspects of needle aspiration lung biopsy: a personal perspective, *Radiology* 208 (2) (1998) 303–318. doi:10.1148/radiology.208.2.9680552.
- [10] W.-Y. Liao, M.-Z. Chen, Y.-L. Chang, H.-D. Wu, C.-J. Yu, P.-H. Kuo, P.-C. Yang, US-guided transthoracic cutting biopsy for peripheral thoracic lesions less than 3 cm in diameter, *Radiology* 217 (3) (2000) 685–691. doi:10.1148/radiology.217.3.r00dc21685.
- [11] M. Sachdeva, R. Ronaghi, P. K. Mills, M. W. Peterson, Complications and yield of computed tomography-guided transthoracic core needle biopsy of lung nodules at a high-volume academic center in an endemic coccidioidomycosis area, *Lung* 194 (2016) 379–385. doi:10.1007/s00408-016-9866-3.

- [12] L. B. Haramati, J. Austin, Complications after CT-guided needle biopsy through aerated versus nonaerated lung, *Radiology* 181 (3) (1991) 778–778. doi:10.1148/radiology.181.3.1947096.
- [13] M. D. Guimarães, M. Q. de Andrade, A. C. Da Fonte, G. Benevides, R. Chojniak, J. L. Gross, Predictive complication factors for CT-guided fine needle aspiration biopsy of pulmonary lesions, *Clinics* 65 (9) (2010) 847–850. doi:10.1590/S1807-59322010000900006.
- [14] T. Hiraki, H. Mimura, H. Gohara, K. Shibamoto, D. Inoue, Y. Matsui, S. Kanazawa, Incidence of and risk factors for pneumothorax and chest tube placement after CT fluoroscopy-guided percutaneous lung biopsy: retrospective analysis of the procedures conducted over a 9-year period, *American Journal of Roentgenology* 194 (3) (2010) 809–814. doi:10.2214/AJR.09.3224.
- [15] J. D. Kuban, A. L. Tam, S. Y. Huang, J. E. Ensor, A. S. Philip, G. J. Chen, J. Ahrar, R. Murthy, R. Avritscher, D. C. Madoff, et al., The effect of needle gauge on the risk of pneumothorax and chest tube placement after percutaneous computed tomographic (CT)-guided lung biopsy, *Cardiovascular and interventional radiology* 38 (2015) 1595–1602. doi:10.1007/s00270-015-1097-0.
- [16] F. Laspas, A. Roussakis, R. Efthimiadou, D. Papaioannou, S. Papadopoulos, J. Andreou, Percutaneous CT-guided fine-needle aspiration of pulmonary lesions: results and complications in 409 patients, *Journal of medical imaging and radiation oncology* 52 (5) (2008) 458–462. doi:10.1111/j.1440-1673.2008.01990.x.
- [17] N.-E. A. Nour-Eldin, M. Alsubhi, A. Emam, T. Lehnert, M. Beeres, V. Jacobi, T. Gruber-Rouh, J.-E. Scholtz, T. J. Vogl, N. N. Naguib, Pneumothorax complicating coaxial and non-coaxial CT-guided lung biopsy: comparative analysis of determining risk factors and management of pneumothorax in a retrospective review of 650 patients, *Cardiovascular and interventional radiology* 39 (2016) 261–270. doi:10.1007/s00270-015-1167-3.
- [18] M. Anzidei, B. Sacconi, F. Fraioli, L. Saba, P. Lucatelli, A. Napoli, F. Longo, D. Vitolo, F. Venuta, M. Anile, et al., Development of a prediction model and risk score for procedure-related complications in patients undergoing percutaneous computed tomography-guided lung biopsy, *European Journal of Cardio-Thoracic Surgery* 48 (1) (2015) e1–e6. doi:10.1093/ejcts/ezv172.
- [19] A. M. Rozenblit, J. Tuvia, G. N. Rozenblit, A. Klink, CT-guided transthoracic needle biopsy using an ipsilateral dependent position, *American Journal of Roentgenology* 174 (6) (2000) 1759–1764. doi:10.2214/ajr.174.6.1741759.
- [20] C. C. Wu, M. M. Maher, J.-A. O. Shepard, Complications of CT-guided percutaneous needle biopsy of the chest: prevention and management, *American Journal of Roentgenology* 196 (6) (2011) W678–W682. doi:10.2214/AJR.10.4659.

- [21] H. B. Grosu, M. R. Vial, M. Hernandez, L. Li, R. F. Casal, G. A. Eapen, D. E. Ost, Secondary spontaneous pneumothorax in cancer patients, *Journal of Thoracic Disease* 11 (4) (2019) 1495. doi:10.21037/jtd.2019.03.35.
- [22] A. Biswas, H. J. Mehta, P. Sriram, Diagnostic yield of the virtual bronchoscopic navigation system guided sampling of peripheral lung lesions using ultrathin bronchoscope and protected bronchial brush, *Turkish Thoracic Journal* 20 (1) (2019) 6. doi:10.5152/TurkThoracJ.2018.18030.
- [23] A. Mohan, K. Harris, M. R. Bowling, C. Brown, W. Hohenforst-Schmidt, Therapeutic bronchoscopy in the era of genotype directed lung cancer management, *Journal of Thoracic Disease* 10 (11) (2018) 6298. doi:10.21037/jtd.2018.08.14.
- [24] E. Shostak, Foreign body removal in children and adults: review of available techniques and emerging technologies, *AME Medical Journal* 3 (2018). doi:10.21037/amj.2018.07.02.
- [25] C. T. Bolliger, P. N. Mathur, *Interventional bronchoscopy*, Vol. 30, Karger Medical and Scientific Publishers, 2000. doi:10.1159/isbn.978-3-318-00415-1.
- [26] J. F. Beamis, P. N. Mathur, A. C. Mehta, *Interventional pulmonary medicine*, Informa Healthcare, 2010. doi:10.1201/b14203.
- [27] K. M. Bhatt, Y. K. Tandon, R. Graham, C. T. Lau, J. K. Lempel, J. T. Azok, P. J. Mazzone, E. Schneider, N. A. Obuchowski, M. A. Bolen, Electromagnetic navigational bronchoscopy versus CT-guided percutaneous sampling of peripheral indeterminate pulmonary nodules: a cohort study, *Radiology* 286 (3) (2018) 1052–1061. doi:10.1148/radiol.2017170893.
- [28] U. Topala, Y. M. Berkmanb, Effect of needle tract bleeding on occurrence of pneumothorax after transthoracic needle biopsy, *European journal of radiology* 53 (3) (2005) 495–499. doi:10.1016/j.ejrad.2004.05.008.
- [29] J. S. W. Memoli, P. J. Nietert, G. A. Silvestri, Meta-analysis of guided bronchoscopy for the evaluation of the pulmonary nodule, *Chest* 142 (2) (2012) 385–393. doi:10.1378/chest.11-1764.
- [30] F. Asano, Y. Matsuno, N. Shinagawa, K. Yamazaki, T. Suzuki, T. Ishida, H. Moriya, A virtual bronchoscopic navigation system for pulmonary peripheral lesions, *Chest* 130 (2) (2006) 559–566. doi:10.1378/chest.130.2.559.
- [31] M. Oki, H. Saka, C. Kitagawa, Y. Kogure, K. Mori, S. Kajikawa, Endobronchial ultrasound-guided transbronchial biopsy using novel thin bronchoscope for diagnosis of peripheral pulmonary lesions, *Journal of Thoracic Oncology* 4 (10) (2009) 1274–1277. doi:10.1097/JTO.0b013e3181b623e1.
- [32] M. Oki, H. Saka, M. Ando, F. Asano, N. Kurimoto, K. Morita, C. Kitagawa, Y. Kogure, T. Miyazawa, Ultrathin bronchoscopy with multimodal devices for peripheral pulmonary lesions. A randomized trial, *American journal of respiratory and critical care medicine* 192 (4) (2015) 468–476.

- [33] N. Shinagawa, K. Yamazaki, Y. Onodera, K. Miyasaka, E. Kikuchi, H. Dosaka-Akita, M. Nishimura, CT-guided transbronchial biopsy using an ultrathin bronchoscope with virtual bronchoscopic navigation, *Chest* 125 (3) (2004) 1138–1143. doi:10.1378/chest.125.3.1138.
- [34] N. Shinagawa, K. Yamazaki, Y. Onodera, H. Asahina, E. Kikuchi, F. Asano, K. Miyasaka, M. Nishimura, Factors related to diagnostic sensitivity using an ultrathin bronchoscope under CT guidance, *Chest* 131 (2) (2007) 549–553. doi:10.1378/chest.06-0786.
- [35] F. Asano, N. Shinagawa, T. Ishida, J. Shindoh, M. Anzai, A. Tsuzuku, S. Oizumi, S. Morita, Virtual bronchoscopic navigation combined with ultrathin bronchoscopy. A randomized clinical trial, *American journal of respiratory and critical care medicine* 188 (3) (2013) 327–333. doi:10.1164/rccm.201211-21040C.
- [36] S. Kalanjeri, R. C. Holladay, T. R. Gildea, State-of-the-art modalities for peripheral lung nodule biopsy, *Clinics in Chest Medicine* 39 (1) (2018) 125–138. doi:10.1016/j.ccm.2017.11.007.
- [37] F. Herth, A. Ernst, H. Becker, Endobronchial ultrasound-guided transbronchial lung biopsy in solitary pulmonary nodules and peripheral lesions, *European Respiratory Journal* 20 (4) (2002) 972–974. doi:10.1183/09031936.02.00032001.
- [38] R. F. Casal, M. Sarkiss, A. K. Jones, J. Stewart, A. Tam, H. B. Grosu, D. E. Ost, C. A. Jimenez, G. A. Eapen, Cone beam computed tomography-guided thin/ultrathin bronchoscopy for diagnosis of peripheral lung nodules: a prospective pilot study, *Journal of thoracic disease* 10 (12) (2018) 6950. doi:10.21037/jtd.2018.11.21.
- [39] A. Chen, P. Chenna, A. Loiselle, J. Massoni, M. Mayse, D. Misselhorn, Radial probe endobronchial ultrasound for peripheral pulmonary lesions. A 5-year institutional experience, *Annals of the American Thoracic Society* 11 (4) (2014) 578–582. doi:10.1513/AnnalsATS.201311-3840C.
- [40] M. S. Ali, W. Trick, B. I. Mba, D. Mohananey, J. Sethi, A. I. Musani, Radial endobronchial ultrasound for the diagnosis of peripheral pulmonary lesions: A systematic review and meta-analysis, *Respirology* 22 (3) (2017) 443–453. doi:10.1111/resp.12980.
- [41] G. J. Criner, R. Eberhardt, S. Fernandez-Bussy, D. Gompelmann, F. Maldonado, N. Patel, P. L. Shah, D.-J. Slebos, A. Valipour, M. M. Wahidi, et al., Interventional bronchoscopy, *American Journal of Respiratory and Critical Care Medicine* 202 (1) (2020) 29–50. doi:10.1164/rccm.201907-129250.
- [42] A. C. Mehta, P. Jain, *Interventional bronchoscopy: a clinical guide*, Springer, 2013. doi:10.1007/978-1-62703-395-4.
- [43] F. Asano, Y. Matsuno, A. Tsuzuku, M. Anzai, N. Shinagawa, K. Yamazaki, T. Ishida, H. Moriya, Diagnosis of peripheral pulmonary lesions using a bronchoscope insertion guidance system combined with endobronchial ultrasonography with a guide sheath, *Lung Cancer* 60 (3) (2008) 366–373. doi:10.1016/j.lungcan.2007.10.022.

- [44] E. Edell, D. Krier-Morrow, Navigational bronchoscopy: overview of technology and practical considerations—new current procedural terminology codes effective 2010, *Chest* 137 (2) (2010) 450–454. doi:10.1378/chest.09-2003.
- [45] F. J. Herth, R. Eberhardt, D. Sterman, G. A. Silvestri, H. Hoffmann, P. L. Shah, Bronchoscopic transparenchymal nodule access (BTPNA): first in human trial of a novel procedure for sampling solitary pulmonary nodules, *Thorax* 70 (4) (2015) 326–332. doi:10.1136/thoraxjnl-2014-206211.
- [46] F. Asano, R. Eberhardt, F. J. Herth, Virtual bronchoscopic navigation for peripheral pulmonary lesions, *Respiration* 88 (5) (2014) 430–440. doi:10.1159/000367900.
- [47] M. A. Pritchett, K. Bhadra, M. Calcutt, E. Folch, Virtual or reality: divergence between preprocedural computed tomography scans and lung anatomy during guided bronchoscopy, *Journal of thoracic disease* 12 (4) (2020) 1595. doi:10.21037/jtd.2020.01.35.
- [48] E. E. Folch, M. A. Pritchett, M. A. Nead, M. R. Bowling, S. D. Murgu, W. S. Krimsky, B. A. Murillo, G. P. LeMense, D. J. Minnich, S. Bansal, et al., Electromagnetic navigation bronchoscopy for peripheral pulmonary lesions: one-year results of the prospective, multicenter NAVIGATE study, *Journal of Thoracic Oncology* 14 (3) (2019) 445–458. doi:10.1016/j.jtho.2018.11.013.
- [49] D. S. Wilson, R. J. Bartlett, Improved diagnostic yield of bronchoscopy in a community practice: combination of electromagnetic navigation system and rapid on-site evaluation, *Journal of Bronchology & Interventional Pulmonology* 14 (4) (2007) 227–232. doi:10.1097/LBR.0b013e31815a7b00.
- [50] D. Karnak, A. Ciledağ, K. Ceyhan, Ç. Atasoy, S. Akyar, O. Kayacan, Rapid on-site evaluation and low registration error enhance the success of electromagnetic navigation bronchoscopy, *Annals of Thoracic Medicine* 8 (1) (2013) 28. doi:10.4103/1817-1737.105716.
- [51] R. Eberhardt, D. Anantham, A. Ernst, D. Feller-Kopman, F. Herth, Multimodality bronchoscopic diagnosis of peripheral lung lesions: a randomized controlled trial, *American journal of respiratory and critical care medicine* 176 (1) (2007) 36–41. doi:10.1164/rccm.200612-18660C.
- [52] L. B. Yarmus, S. Arias, D. Feller-Kopman, R. Semaan, K. P. Wang, B. Frimpong, K. O. Burgess, R. Thompson, A. Chen, R. Ortiz, et al., Electromagnetic navigation transthoracic needle aspiration for the diagnosis of pulmonary nodules: a safety and feasibility pilot study, *Journal of thoracic disease* 8 (1) (2016) 186. doi:10.3978/j.issn.2072-1439.2016.01.47.
- [53] D. P. Steinfort, Y. H. Khor, R. L. Manser, L. B. Irving, Radial probe endobronchial ultrasound for the diagnosis of peripheral lung cancer: systematic review and meta-analysis, *European Respiratory Journal* 37 (4) (2011) 902–910. doi:10.1183/09031936.00075310.

- [54] D. E. Ost, A. Ernst, X. Lei, K. L. Kovitz, S. Benzaquen, J. Diaz-Mendoza, S. Greenhill, J. Toth, D. Feller-Kopman, J. Puchalski, et al., Diagnostic yield and complications of bronchoscopy for peripheral lung lesions. Results of the AQuIRE registry, *American journal of respiratory and critical care medicine* 193 (1) (2016) 68–77. doi:10.1164/rccm.201507-13320C.
- [55] W. Hohenforst-Schmidt, P. Zarogoulidis, T. Vogl, J. F. Turner, R. Browning, B. Linsmeier, H. Huang, Q. Li, K. Darwiche, L. Freitag, et al., Cone beam computed tomography (CBCT) in interventional chest medicine-high feasibility for endobronchial real-time navigation, *Journal of Cancer* 5 (3) (2014) 231. doi:10.7150/jca.8834.
- [56] M. R. Bowling, C. Brown, C. J. Anciano, Feasibility and safety of the transbronchial access tool for peripheral pulmonary nodule and mass, *The Annals of Thoracic Surgery* 104 (2) (2017) 443–449. doi:10.1016/j.athoracsur.2017.02.035.
- [57] C. S. Ng, S. C. Yu, R. W. Lau, A. P. Yim, Hybrid DynaCT-guided electromagnetic navigational bronchoscopic biopsy, *European Journal of Cardio-Thoracic Surgery* 49 (suppl_1) (2016) i87–i88. doi:10.1093/ejcts/ezv405.
- [58] S. C. Park, C. J. Kim, C. H. Han, S. M. Lee, Factors associated with the diagnostic yield of computed tomography-guided transbronchial lung biopsy, *Thoracic Cancer* 8 (3) (2017) 153–158. doi:10.1111/1759-7714.12417.
- [59] M. A. Pritchett, S. Schampaert, J. A. De Groot, C. C. Schirmer, I. van der Bom, Cone-beam CT with augmented fluoroscopy combined with electromagnetic navigation bronchoscopy for biopsy of pulmonary nodules, *Journal of Bronchology & Interventional Pulmonology* 25 (4) (2018) 274. doi:10.1097/LBR.0000000000000536.
- [60] D. J. Brenner, C. D. Elliston, E. J. Hall, W. E. Berdon, et al., Estimated risks of radiation-induced fatal cancer from pediatric CT, *American journal of roentgenology* 176 (2) (2001) 289–296. doi:10.2214/ajr.176.2.1760289.
- [61] G. X. Ding, C. W. Coffey, Radiation dose from kilovoltage cone beam computed tomography in an image-guided radiotherapy procedure, *International Journal of Radiation Oncology* Biology* Physics* 73 (2) (2009) 610–617. doi:10.1016/j.ijrobp.2008.10.006.
- [62] R. Setser, G. Chintalapani, K. Bhadra, R. F. Casal, Cone beam CT imaging for bronchoscopy: a technical review, *Journal of Thoracic Disease* 12 (12) (2020) 7416. doi:10.21037/jtd-20-2382.
- [63] J. T. Dobbins III, H. P. McAdams, J.-W. Song, C. M. Li, D. J. Godfrey, D. M. DeLong, S.-H. Paik, S. Martinez-Jimenez, Digital tomosynthesis of the chest for lung nodule detection: Interim sensitivity results from an ongoing NIH-sponsored trial, *Medical physics* 35 (6Part1) (2008) 2554–2557. doi:10.1118/1.2937277.
- [64] M. Aboudara, L. Roller, O. Rickman, R. J. Lentz, J. Pannu, H. Chen, F. Maldonado, Improved diagnostic yield for lung nodules with digital tomosynthesis-corrected navigational bronchoscopy: initial experience with a novel adjunct, *Respirology* 25 (2) (2020) 206–213. doi:10.1111/resp.13609.

- [65] L. A. Feldkamp, L. C. Davis, J. W. Kress, Practical cone-beam algorithm, *Josa a* 1 (6) (1984) 612–619. doi:10.1364/JOSA.1.000612.
- [66] J. H. Hubbell, S. M. Seltzer, Tables of X-Ray Mass Attenuation Coefficients and Mass Energy-Absorption Coefficients 1 keV to 20 meV for Elements Z = 1 to 92 and 48 Additional Substances of Dosimetric Interest, NIST, <https://www.osti.gov/biblio/76335> (accessed 2023).
- [67] J. Hadamard, Le problème de Cauchy et les équations aux dérivées partielles linéaires hyperboliques, *Paris* 11 (1932) 243–264. doi:10.1090/S0002-9904-1934-05815-4.
- [68] J. Radon, 1.1 über die bestimmung von funktionen durch ihre integralwerte längs gewisser mannigfaltigkeiten, *Classic papers in modern diagnostic radiology* 5 (21) (2005) 124.
- [69] B. Z. des Plantes, Seriescopy, Een Rontgenographische method welke het mogelijk maakt achtereenvolgens een oneindig aantal evenwijdige vlakken van het te onderzoeken voorwerp afzonderlijk te bechouwen (Seriescopy, a Roentgenographic method which allows an infinite number of successive parallel planes of the test object to be considered separately)(English translation), *Ned. Tijdschr. Geneeskd.* 51 (1935) 5852–5856.
- [70] B. G. Z. des Plantes, Serieskopie: eine r ntgenographische methode, welche erm glicht, mit hilfe einiger aufnahmen eine unendliche reihe paralleler ebenen in reihenfolge gesondert zu betrachten, *Fortshtr Rntgenstr* 57 (1938) 605–616.
- [71] J. Garrison, D. Grant, W. Guier, R. Johns, Three dimensional roentgenography, *American Journal of Roentgenology* 105 (4) (1969) 903–908. doi:10.2214/ajr.105.4.90.
- [72] E. R. Miller, E. M. MoCurry, B. Hruska, An infinite number of laminagrams from a finite number of radiographs, *Radiology* 98 (2) (1971) 249–255. doi:10.1148/98.2.249.
- [73] D. G. Grant, Tomosynthesis: a three-dimensional radiographic imaging technique, *IEEE Transactions on Biomedical Engineering* (1) (1972) 20–28. doi:10.1109/TBME.1972.324154.
- [74] E. Klotz, H. Weiss, Three-dimensional coded aperture imaging using nonredundant point distributions, *Optics Communications* 11 (4) (1974) 368–372. doi:10.1016/0030-4018(74)90238-7.
- [75] E. Klotz, H. Weiss, Short-time tomosynthesis The New Image in Tomography: Proc, in: *Symp. Actualitatis Tomographiae (Genoa, Italy, 11-13 Sept. 1975)*, 1976, pp. 65–70.
- [76] H. Weiss, E. Klotz, R. Linde, G. Rabe, U. Tiemens, Coded aperture imaging with X-rays (flashing tomosynthesis), *Optica Acta: International Journal of Optics* 24 (4) (1977) 305–325. doi:10.1080/713819562.

- [77] M. Nadjmi, H. Weiss, E. Klotz, R. Linde, Flashing tomosynthesis—A new tomographic method, *Neuroradiology* 19 (1980) 113–117. doi:[10.1007/BF00342384](https://doi.org/10.1007/BF00342384).
- [78] H. Becher, P. Hanrath, M. Schluter, W. Bleifeld, E. Klotz, P. Haaker, R. Linde, H. Weiss, Selective Coronary Angiography with Flashing Tomosynthesis in Patients with Coronary-Artery Disease, in: *Circulation*, Vol. 68, 1983, pp. 178–178.
- [79] H. Becher, M. Schlüter, D. Mathey, W. Bleifeld, E. Klotz, P. Haaker, R. LINDE, H. Weiss, Coronary angiography with flashing tomosynthesis, *European Heart Journal* 6 (5) (1985) 399–408. doi:[10.1093/oxfordjournals.eurheartj.a061878](https://doi.org/10.1093/oxfordjournals.eurheartj.a061878).
- [80] P. Haaker, E. Klotz, R. Koppe, R. Linde, D. Mathey, First clinical results with digital flashing tomosynthesis in coronary angiography, *European Heart Journal* 6 (11) (1985) 913–920. doi:[10.1093/oxfordjournals.eurheartj.a061788](https://doi.org/10.1093/oxfordjournals.eurheartj.a061788).
- [81] P. Haaker, E. Klotz, R. Koppe, R. Linde, H. Möller, A new digital tomosynthesis method with less artifacts for angiography, *Medical physics* 12 (4) (1985) 431–436. doi:[10.1118/1.595705](https://doi.org/10.1118/1.595705).
- [82] G. M. Stiel, L. S. Stiel, E. Klotz, C. A. Nienaber, Digital flashing tomosynthesis: a promising technique for angiocardigraphic screening, *IEEE transactions on medical imaging* 12 (2) (1993) 314–321. doi:[10.1109/42.232261](https://doi.org/10.1109/42.232261).
- [83] H. Sklebitz, J. Haendle, Tomoscopy: dynamic layer imaging without mechanical movements, *American journal of roentgenology* 140 (6) (1983) 1247–1252. doi:[10.2214/ajr.140.6.1247](https://doi.org/10.2214/ajr.140.6.1247).
- [84] G. Groh, Tomosynthesis and coded aperture imaging: new approaches to three-dimensional imaging in diagnostic radiography, *Proceedings of the Royal Society of London. Series B. Biological Sciences* 195 (1119) (1977) 299–306. doi:[10.1098/rspb.1977.0010](https://doi.org/10.1098/rspb.1977.0010).
- [85] G. Stiel, L. Stiel, K. Donath, J. Schofer, P. Haaker, E. Klotz, R. Koppe, R. Linde, D. Mathey, Digital flashing tomosynthesis (DFTS)—a technique for three-dimensional coronary angiography, *The International Journal of Cardiac Imaging* 5 (1989) 53–61. doi:[10.1007/BF01745232](https://doi.org/10.1007/BF01745232).
- [86] G. M. Stiel, L. S. Stiel, C. A. Nienaber, Potential of digital flashing tomosynthesis for angiocardigraphic evaluation, *Journal of Digital Imaging* 5 (1992) 194–205. doi:[10.1007/BF03167770](https://doi.org/10.1007/BF03167770).
- [87] P. Haaker, E. Klotz, R. Koppe, R. Linde, Real-time distortion correction of digital X-ray II/TV-systems: An application example for digital flashing tomosynthesis (DFTS), *The International Journal of Cardiac Imaging* 6 (1990) 39–45. doi:[10.1007/BF01798431](https://doi.org/10.1007/BF01798431).
- [88] H. Woelke, P. Hanrath, M. Schlueter, W. Bleifeld, E. Klotz, H. Weiss, D. Waller, J. von Weltzien, Work in progress. Flashing tomosynthesis: a tomographic technique for quantitative coronary angiography, *Radiology* 145 (2) (1982) 357–360. doi:[10.1148/radiology.145.2.7134435](https://doi.org/10.1148/radiology.145.2.7134435).

- [89] I. Reiser, S. Glick, Tomosynthesis imaging, Taylor & Francis, 2014. doi:10.1201/b16583.
- [90] J. Dobbins III, A. Powell, Y. Weaver, Matrix inversion tomosynthesis: Initial image reconstruction, Abstract Summaries of the RSNA 165 (1987) 333.
- [91] S. Sone, T. Kasuga, F. Sakai, J. Aoki, I. Izuno, Y. Tanizaki, H. Shigeta, K. Shibata, Development of a high-resolution digital tomosynthesis system and its clinical application, Radiographics 11 (5) (1991) 807–822. doi:10.1148/radiographics.11.5.1947318.
- [92] S. Sone, T. Kasuga, F. Sakai, H. Hirano, K. Kubo, M. Morimoto, K. Takemura, M. Hosoba, Chest imaging with dual-energy subtraction digital tomosynthesis, Acta Radiologica 34 (4) (1993) 346–350. doi:10.1177/028418519303400407.
- [93] S. Sone, T. Kasuga, F. Sakai, K. Oguchi, A. Itoh, F. Li, Y. Maruyama, K. Kubo, T. Honda, M. Haniuda, et al., Digital tomosynthesis imaging of the lung, Radiation Medicine 14 (2) (1996) 53–63.
- [94] R. Kruger, J. Nelson, D. Ghosh-Roy, F. Miller, R. Anderson, P. Liu, Dynamic tomographic digital subtraction angiography using temporal filtration, Radiology 147 (3) (1983) 863–867. doi:10.1148/radiology.147.3.6342037.
- [95] R. Kruger, M. Sedaghati, D. G. Roy, P. Liu, J. Nelson, W. Kubal, P. Del Rio, Tomosynthesis applied to digital subtraction angiography, Radiology 152 (3) (1984) 805–808. doi:10.1148/radiology.152.3.6379747.
- [96] K. R. Maravilla, R. C. Murry, M. Deck, S. Horner, Clinical application of digital tomosynthesis: a preliminary report, American Journal of Neuroradiology 4 (3) (1983) 277–280. doi:0195-6108/83/0403-0277.
- [97] K. R. Maravilla, R. C. Murry, S. Horner, Digital tomosynthesis: technique for electronic reconstructive tomography, American journal of neuroradiology 4 (4) (1983) 883–888. doi:0195-6108/83/0404-0883.
- [98] K. Maravilla, R. Murry Jr, J. Diehl, R. Suss, L. Allen, K. Chang, J. Crawford, R. McCoy, Digital tomosynthesis: technique modifications and clinical applications for neurovascular anatomy, Radiology 152 (3) (1984) 719–724. doi:10.1148/radiology.152.3.6379745.
- [99] L. T. Niklason, B. T. Christian, L. E. Niklason, D. B. Kopans, D. E. Castleberry, B. Opsahl-Ong, C. E. Landberg, P. J. Slanetz, A. A. Giardino, R. Moore, et al., Digital tomosynthesis in breast imaging, Radiology 205 (2) (1997) 399–406. doi:10.1148/radiology.205.2.9356620.
- [100] R. L. Webber, Self-calibrated tomosynthetic, radiographic-imaging system, method, and device, uS Patent 5,359,637 (Oct. 25 1994).
- [101] R. L. Webber, Self-calibrated tomosynthetic, radiographic-imaging system, method, and device, uS Patent 5,668,844 (Sep. 16 1997).

- [102] R. Webber, R. Horton, D. Tyndall, J. Ludlow, Tuned-aperture computed tomography (TACT). Theory and application for three-dimensional dento-alveolar imaging, *Dentomaxillofacial Radiology* 26 (1) (1997) 53–62. doi:10.1038/sj.dmf.4600201.
- [103] R. L. Webber, H. R. Underhill, R. I. Freimanis, A controlled evaluation of tuned-aperture computed tomography applied to digital spot mammography, *Journal of digital imaging* 13 (2) (2000) 90–97. doi:10.1007/BF03168373.
- [104] M. Lehtimäki, M. Pamilo, L. Raulisto, M. Roiha, M. Kalke, S. Siltanen, T. Ihamäki, Diagnostic clinical benefits of digital spot and digital 3D mammography following analysis of screening findings, in: *Medical Imaging 2003: Visualization, Image-Guided Procedures, and Display*, Vol. 5029, SPIE, 2003, pp. 698–706. doi:10.1117/12.479578.
- [105] S. Suryanarayanan, A. Karellas, S. Vedantham, S. J. Glick, C. J. D’Orsi, S. P. Baker, R. L. Webber, Comparison of tomosynthesis methods used with digital mammography, *Academic Radiology* 7 (12) (2000) 1085–1097. doi:10.1016/S1076-6332(00)80061-6.
- [106] T. Wu, A. Stewart, M. Stanton, T. McCauley, W. Phillips, D. B. Kopans, R. H. Moore, J. W. Eberhard, B. Opsahl-Ong, L. Niklason, et al., Tomographic mammography using a limited number of low-dose cone-beam projection images, *Medical physics* 30 (3) (2003) 365–380. doi:10.1118/1.1543934.
- [107] J. DOBBINS III, Tomosynthesis for improved pulmonary nodule detection, *Radiology* 209 (1998) 280.
- [108] D. J. Godfrey, H. McAdams, J. T. Dobbins III, Optimization of the matrix inversion tomosynthesis (MITS) impulse response and modulation transfer function characteristics for chest imaging, *Medical physics* 33 (3) (2006) 655–667. doi:10.1118/1.2170398.
- [109] S. Suryanarayanan, A. Karellas, S. Vedantham, S. P. Baker, S. J. Glick, C. J. D’Orsi, R. L. Webber, Evaluation of linear and nonlinear tomosynthetic reconstruction methods in digital mammography, *Academic Radiology* 8 (3) (2001) 219–224. doi:10.1016/S1076-6332(03)80530-5.
- [110] D. A. Tyndall, T. L. Clifton, R. L. Webber, J. B. Ludlow, R. A. Horton, TACT imaging of primary caries, *Oral Surgery, Oral Medicine, Oral Pathology, Oral Radiology, and Endodontology* 84 (2) (1997) 214–225. doi:10.1016/S1079-2104(97)90072-X.
- [111] P. Van der Stelt, U. Ruttimann, R. Webber, Enhancement of tomosynthetic images in dental radiology, *Journal of Dental Research* 65 (7) (1986) 967–973. doi:10.1177/00220345860650071.
- [112] R. Vandre, R. Webber, R. Horton, C. Cruz, J. Pajak, Comparison of TACT with film for detecting osseous jaw lesions, *J Dent Res* 74 (1995) 18.

- [113] R. Webber, R. Horton, T. Underhill, Tuned-aperture computed-tomography for diagnosis of crestal defects around implants, in: *Journal of Dental Research*, Vol. 74, AMER ASSOC DENTAL RESEARCH 1619 DUKE ST, ALEXANDRIA, VA 22314, 1995, pp. 18–18.
- [114] D. J. Godfrey, R. J. Warp, J. T. Dobbins III, Optimization of matrix inverse tomosynthesis, in: *Medical Imaging 2001: Physics of Medical Imaging*, Vol. 4320, SPIE, 2001, pp. 696–704. doi:10.1117/12.430908.
- [115] D. J. Godfrey, A. Rader, J. T. Dobbins III, Practical strategies for the clinical implementation of matrix inversion tomosynthesis (MITS), in: *Medical Imaging 2003: Physics of Medical Imaging*, Vol. 5030, SPIE, 2003, pp. 379–390. doi:10.1117/12.480352.
- [116] U. E. Ruttimann, R. A. Groenhuis, R. L. Webber, Restoration of digital multiplane tomosynthesis by a constrained iteration method, *IEEE transactions on Medical Imaging* 3 (3) (1984) 141–148. doi:10.1109/TMI.1984.4307670.
- [117] W. Engelke, U. E. Ruttimann, M. Tsuchimochi, J. D. Bacher, An experimental study of new diagnostic methods for the examination of osseous lesions in the temporomandibular joint, *Oral surgery, oral medicine, oral pathology* 73 (3) (1992) 348–359. doi:10.1016/0030-4220(92)90134-c.
- [118] J. G. Colsher, Iterative three-dimensional image reconstruction from tomographic projections, *Computer Graphics and Image Processing* 6 (6) (1977) 513–537. doi:10.1016/S0146-664X(77)80014-2.
- [119] G. T. Herman, Two direct methods for reconstructing pictures from their projections: a comparative study, in: *Proceedings of the May 16-18, 1972, spring joint computer conference*, 1971, pp. 971–984. doi:10.1145/1478873.1479004.
- [120] P. Bleuet, R. Guillemaud, I. E. Magnin, Resolution improvement in linear tomosynthesis with an adapted 3D regularization scheme, in: *Medical Imaging 2002: Physics of Medical Imaging*, Vol. 4682, SPIE, 2002, pp. 117–125. doi:10.1117/12.465549.
- [121] K. Lange, J. A. Fessler, Globally convergent algorithms for maximum a posteriori transmission tomography, *IEEE Transactions on Image Processing* 4 (10) (1995) 1430–1438. doi:10.1109/83.465107.
- [122] M. Das, H. C. Gifford, J. M. O’Connor, S. J. Glick, Penalized maximum likelihood reconstruction for improved microcalcification detection in breast tomosynthesis, *IEEE Transactions on Medical Imaging* 30 (4) (2010) 904–914. doi:10.1109/TMI.2010.2089694.
- [123] T. Wu, R. H. Moore, E. A. Rafferty, D. B. Kopans, A comparison of reconstruction algorithms for breast tomosynthesis, *Medical physics* 31 (9) (2004) 2636–2647. doi:10.1118/1.1786692.

- [124] J. T. Dobbins III, D. J. Godfrey, Digital x-ray tomosynthesis: current state of the art and clinical potential, *Physics in medicine & biology* 48 (19) (2003) R65. doi:10.1088/0031-9155/48/19/R01.
- [125] Y. Zhang, H.-P. Chan, B. Sahiner, J. Wei, M. M. Goodsitt, L. M. Hadjiiski, J. Ge, C. Zhou, A comparative study of limited-angle cone-beam reconstruction methods for breast tomosynthesis, *Medical physics* 33 (10) (2006) 3781–3795. doi:10.1118/1.2237543.
- [126] B. Z. Des Plantes, Eine neue methode zur differenzierung in der roentgenographie (planigraphie), *Acta Radiologica* (2) (1932) 182–192.
- [127] D. J. Godfrey, F.-F. Yin, M. Oldham, S. Yoo, C. Willett, Digital tomosynthesis with an on-board kilovoltage imaging device, *International Journal of Radiation Oncology* Biology* Physics* 65 (1) (2006) 8–15. doi:10.1016/j.ijrobp.2006.01.025.
- [128] B. E. Claus, D. A. Langan, O. Al Assad, X. Wang, Circular tomosynthesis for neuro perfusion imaging on an interventional C-arm, in: *Medical Imaging 2015: Physics of Medical Imaging*, Vol. 9412, SPIE, 2015, pp. 556–564. doi:10.1117/12.2082695.
- [129] G. M. Stevens, R. L. Birdwell, C. F. Beaulieu, D. M. Ikeda, N. J. Pelc, Circular tomosynthesis: potential in imaging of breast and upper cervical spine—preliminary phantom and in vitro study, *Radiology* 228 (2) (2003) 569–575. doi:10.1148/radiol.2282020295.
- [130] U. Hassler, M. Rehak, R. Hanke, Carbon fibre preform inspection by circular x-ray tomosynthesis, in: *2008 IEEE Nuclear Science Symposium Conference Record*, IEEE, 2008, pp. 590–592. doi:10.1109/NSSMIC.2008.4775123.
- [131] D. Xia, S. Cho, J. Bian, E. Y. Sidky, C. A. Pelizzari, X. Pan, Tomosynthesis with source positions distributed over a surface, in: *Medical Imaging 2008: Physics of Medical Imaging*, Vol. 6913, SPIE, 2008, pp. 776–782. doi:10.1117/12.772687.
- [132] J. Zhang, C. Yu, A novel solid-angle tomosynthesis (SAT) scanning scheme, *Medical physics* 37 (8) (2010) 4186–4192. doi:10.1118/1.3460341.
- [133] P. Bleuet, Reconstruction 3D par tomosynthèse généralisée: application à l'imagerie médicale par rayons, Ph.D. thesis, Lyon, INSA (2002).
- [134] U. E. Ruttimann, X.-L. Oi, R. L. Webber, An optimal synthetic aperture for circular tomosynthesis, *Medical Physics* 16 (4) (1989) 398–405. doi:10.1002/j.2473-4209.1989.tb36310.x.
- [135] S. Carter, J. Martin, J. Middlemiss, F. Ross, Polytome tomography, *Clinical Radiology* 14 (4) (1963) 405–413. doi:10.1016/S0009-9260(63)80029-x.
- [136] I. Reiser, J. Bian, R. M. Nishikawa, E. Y. Sidky, X. Pan, Comparison of reconstruction algorithms for digital breast tomosynthesis (2009). arXiv:0908.2610.

- [137] Y.-H. Hu, B. Zhao, W. Zhao, Image artifacts in digital breast tomosynthesis: investigation of the effects of system geometry and reconstruction parameters using a linear system approach, *Medical physics* 35 (12) (2008) 5242–5252. doi:10.1118/1.2996110.
- [138] T. Svahn, M. Ruschin, B. Hemdal, L. Nyhlén, I. Andersson, P. Timberg, S. Mattsson, A. Tingberg, In-plane artifacts in breast tomosynthesis quantified with a novel contrast-detail phantom, in: *Medical Imaging 2007: Physics of Medical Imaging*, Vol. 6510, SPIE, 2007, pp. 1511–1522. doi:10.1117/12.709591.
- [139] F. Saad, R. Frysich, T. Pfeiffer, J.-C. Georgi, T. Knetsch, R. F. Casal, A. Nürnberger, G. Lauritsch, G. Rose, Spherical ellipse scan trajectory for tomosynthesis-assisted interventional bronchoscopy, in: *Proceedings of the 16th Virtual International Meeting on Fully 3D Image Reconstruction in Radiology and Nuclear Medicine*, Schramm, G., Rezaei, A., Thielemans, K., and Nuyts, J., eds, 2021, pp. 352–356. doi:10.48550/arXiv.2110.04143.
- [140] T. Pfeiffer, R. Frysich, R. N. Bismark, G. Rose, CTL: modular open-source C++-library for CT-simulations, in: *15th International Meeting on Fully Three-Dimensional Image Reconstruction in Radiology and Nuclear Medicine*, Vol. 11072, SPIE, 2019, pp. 269–273. doi:10.1117/12.2534517.
- [141] J. P. Boyd, Numerical, perturbative and Chebyshev inversion of the incomplete elliptic integral of the second kind, *Applied Mathematics and Computation* 218 (13) (2012) 7005–7013. doi:10.1016/j.amc.2011.12.021.
- [142] D. Kim, D. Pal, J.-B. Thibault, J. A. Fessler, Improved ordered subsets algorithm for 3D X-ray CT image reconstruction, *Proc. 2nd Intl. Mtg. on image formation in X-ray CT* (2012) 378–81.
- [143] F. Saad, R. Frysich, S. Saalfeld, S. Kellnberger, J. Schulz, R. Fahrig, K. Bhadra, A. Nürnberger, G. Rose, Deformable 3D/3D CT-to-digital-tomosynthesis image registration in image-guided bronchoscopy interventions, *Computers in Biology and Medicine* 171 (2024) 108199. doi:10.1016/j.combiomed.2024.108199.
- [144] R. Frysich, T. Pfeiffer, G. Rose, A novel approach to 2D/3D registration of X-ray images using Grangeat’s relation, *Medical Image Analysis* 67 (2021) 101815. doi:10.1016/j.media.2020.101815.
- [145] Y. Pei, Y. Zhang, H. Qin, G. Ma, Y. Guo, T. Xu, H. Zha, Non-rigid craniofacial 2D-3D registration using CNN-based regression, in: *Deep Learning in Medical Image Analysis and Multimodal Learning for Clinical Decision Support: Third International Workshop, DLMIA 2017, and 7th International Workshop, ML-CDS 2017, Held in Conjunction with MICCAI 2017, Québec City, QC, Canada, September 14, Proceedings 3*, Springer, 2017, pp. 117–125. doi:10.1007/978-3-319-67558-9_14.
- [146] J. Van Houtte, X. Gao, J. Sijbers, G. Zheng, 2D/3D registration with a statistical deformation model prior using deep learning, in: *2021 IEEE EMBS international conference on biomedical and health informatics (BHI)*, IEEE, 2021, pp. 1–4. doi:10.1109/BHI50953.2021.9508540.

- [147] L. Tian, Y. Z. Lee, R. San José Estépar, M. Niethammer, LiftReg: Limited Angle 2D/3D Deformable Registration, in: *Medical Image Computing and Computer Assisted Intervention–MICCAI 2022: 25th International Conference, Singapore, September 18–22, 2022, Proceedings, Part VI*, Springer, 2022, pp. 207–216. doi: [10.1007/978-3-031-16446-0_20](https://doi.org/10.1007/978-3-031-16446-0_20).
- [148] R. Vijayan, N. Sheth, L. Mekki, A. Lu, A. Uneri, A. Sisniega, J. Magaraggia, G. Kleinszig, S. Vogt, J. Thiboutot, et al., 3D–2D image registration in the presence of soft-tissue deformation in image-guided transbronchial interventions, *Physics in Medicine & Biology* 68 (1) (2022) 015010. doi: [10.1088/1361-6560/ac9e3c](https://doi.org/10.1088/1361-6560/ac9e3c).
- [149] D. J. Godfrey, L. Ren, H. Yan, Q. Wu, S. Yoo, M. Oldham, F. F. Yin, Evaluation of three types of reference image data for external beam radiotherapy target localization using digital tomosynthesis (DTS), *Medical physics* 34 (8) (2007) 3374–3384. doi: [10.1118/1.2756941](https://doi.org/10.1118/1.2756941).
- [150] D. Rueckert, L. I. Sonoda, C. Hayes, D. L. Hill, M. O. Leach, D. J. Hawkes, Nonrigid registration using free-form deformations: application to breast MR images, *IEEE transactions on medical imaging* 18 (8) (1999) 712–721. doi: [10.1109/42.796284](https://doi.org/10.1109/42.796284).
- [151] S. Klein, M. Staring, K. Murphy, M. A. Viergever, J. P. Pluim, Elastix: a toolbox for intensity-based medical image registration, *IEEE transactions on medical imaging* 29 (1) (2009) 196–205. doi: [10.1109/TMI.2009.2035616](https://doi.org/10.1109/TMI.2009.2035616).
- [152] D. P. Shamonin, E. E. Bron, B. P. Lelieveldt, M. Smits, S. Klein, M. Staring, Alzheimer’s Disease Neuroimaging Initiative, Fast parallel image registration on CPU and GPU for diagnostic classification of Alzheimer’s disease, *Frontiers in neuroinformatics* 7 (2014) 50. doi: [10.3389/fninf.2013.00050](https://doi.org/10.3389/fninf.2013.00050).
- [153] C. L. Guy, E. Weiss, G. E. Christensen, N. Jan, G. D. Hugo, CALIPER: A deformable image registration algorithm for large geometric changes during radiotherapy for locally advanced non-small cell lung cancer, *Medical physics* 45 (6) (2018) 2498–2508. doi: [10.1002/mp.12891](https://doi.org/10.1002/mp.12891).
- [154] Y. Yin, E. A. Hoffman, C.-L. Lin, Mass preserving nonrigid registration of CT lung images using cubic B-spline, *Medical physics* 36 (9Part1) (2009) 4213–4222. doi: [10.1118/1.3193526](https://doi.org/10.1118/1.3193526).
- [155] S. Klein, J. P. Pluim, M. Staring, M. A. Viergever, Adaptive stochastic gradient descent optimisation for image registration, *International journal of computer vision* 81 (2009) 227–239. doi: [10.1007/s11263-008-0168-y](https://doi.org/10.1007/s11263-008-0168-y).
- [156] Y. Qiao, B. van Lew, B. P. Lelieveldt, M. Staring, Fast automatic step size estimation for gradient descent optimization of image registration, *IEEE transactions on medical imaging* 35 (2) (2015) 391–403. doi: [10.1109/TMI.2015.2476354](https://doi.org/10.1109/TMI.2015.2476354).
- [157] G.-H. Chen, J. Tang, S. Leng, Prior image constrained compressed sensing (PICCS): a method to accurately reconstruct dynamic CT images from highly undersampled projection data sets, *Medical physics* 35 (2) (2008) 660–663. doi: [10.1118/1.2836423](https://doi.org/10.1118/1.2836423).

- [158] J. W. Stayman, H. Dang, Y. Ding, J. H. Siewerdsen, PIRPLE: a penalized-likelihood framework for incorporation of prior images in CT reconstruction, *Physics in Medicine & Biology* 58 (21) (2013) 7563. doi:10.1088/0031-9155/58/21/7563.
- [159] H. Dang, A. Wang, M. S. Sussman, J. Siewerdsen, J. Stayman, dPIRPLE: a joint estimation framework for deformable registration and penalized-likelihood CT image reconstruction using prior images, *Physics in Medicine & Biology* 59 (17) (2014) 4799. doi:10.1088/0031-9155/59/17/4799.
- [160] J. Lee, J. W. Stayman, Y. Otake, S. Schafer, W. Zbijewski, A. J. Khanna, J. L. Prince, J. H. Siewerdsen, Volume-of-change cone-beam CT for image-guided surgery, *Physics in Medicine & Biology* 57 (15) (2012) 4969. doi:10.1088/0031-9155/57/15/4969.
- [161] A. Pourmorteza, H. Dang, J. H. Siewerdsen, J. W. Stayman, Reconstruction of difference using prior images and a penalized-likelihood framework, in: *Proc. Int. Meeting on Fully Three-Dimensional Image Reconstruction in Radiology and Nuclear Medicine*, 2015, pp. 252–5.
- [162] J. Kuntz, B. Flach, R. Kueres, W. Semmler, M. Kachelrieß, S. Bartling, Constrained reconstructions for 4D intervention guidance, *Physics in Medicine & Biology* 58 (10) (2013) 3283. doi:10.1088/0031-9155/58/10/3283.
- [163] B. Flach, J. Kuntz, M. Brehm, R. Kueres, S. Bartling, M. Kachelrieß, Low dose tomographic fluoroscopy: 4D intervention guidance with running prior, *Medical Physics* 40 (10) (2013) 101909. doi:10.1118/1.4819826.
- [164] B. Flach, M. Brehm, S. Sawall, M. Kachelrieß, Deformable 3D–2D registration for CT and its application to low dose tomographic fluoroscopy, *Physics in Medicine & Biology* 59 (24) (2014) 7865. doi:10.1088/0031-9155/59/24/7865.
- [165] G. T. Herman, Image reconstruction from projections, *The fundamentals of computerized tomography* 316 (1980).
- [166] K. Jensen, A. C. T. Martinsen, A. Tingberg, T. M. Aaløkken, E. Fosse, Comparing five different iterative reconstruction algorithms for computed tomography in an ROC study, *European radiology* 24 (2014) 2989–3002. doi:10.1007/s00330-014-3333-4.
- [167] J. Guo, H. Qi, Y. Xu, Z. Chen, S. Li, L. Zhou, et al., Iterative image reconstruction for limited-angle CT using optimized initial image, *Computational and mathematical methods in medicine* 2016 (2016). doi:10.1155/2016/5836410.
- [168] S. Bannasch, R. Frysck, R. Bismark, G. Warnecke, G. Rose, An Optimal relaxation of the Algebraic Reconstruction Technique for CT Imaging, *Fully Three-Dimensional Image Reconstruction in Radiology and Nuclear Medicine* (2015) 622–625.
- [169] W. P. Segars, G. Sturgeon, S. Mendonca, J. Grimes, B. M. Tsui, 4D XCAT phantom for multimodality imaging research, *Medical physics* 37 (9) (2010) 4902–4915. doi:10.1118/1.3480985.

- [170] M. Wu, S. Yoon, E. G. Solomon, J. Star-Lack, N. Pelc, R. Fahrig, Digital Tomosynthesis System Geometry Analysis Using Convolution-Based Blur-and-Add (BAA) Model, *IEEE Transactions on Medical Imaging* 35 (1) (2015) 131–143. doi:[10.1109/TMI.2015.2458983](https://doi.org/10.1109/TMI.2015.2458983).
- [171] F. Saad, R. Frysch, V. Kulvait, D. Punzet, G. Rose, Nullspace-constrained modifications of under-sampled interventional CT images using instrument-specific prior information, in: *Medical Imaging 2020: Physics of Medical Imaging*, Vol. 11312, SPIE, 2020, pp. 888–894. doi:[10.1117/12.2549773](https://doi.org/10.1117/12.2549773).